



Annual Report 2015

MLZ is a cooperation between:

Bayerisches Staatsministerium für
Bildung und Kultus, Wissenschaft und Kunst



SPONSORED BY THE



Federal Ministry
of Education
and Research

The Heinz Maier-Leibnitz Zentrum (MLZ):

The Heinz Maier-Leibnitz Zentrum is a leading centre for cutting-edge research with neutrons and positrons. Operating as a user facility, the MLZ offers a unique suite of high-performance neutron scattering instruments. This cooperation involves the Technische Universität München, the Forschungszentrum Jülich and the Helmholtz-Zentrum Geesthacht. The MLZ is funded by the German Federal Ministry of Education and Research, together with the Bavarian State Ministry of Education, Science and the Arts and the partners of the cooperation.

The Forschungs-Neutronenquelle Heinz-Maier-Leibnitz (FRM II):

The Forschungs-Neutronenquelle Heinz-Maier-Leibnitz provides neutron beams for the scientific experiments at the MLZ. The FRM II is operated by the Technische Universität München and is funded by the Bavarian State Ministry of Education, Science and the Arts.

Joint Annual Report 2015
of the MLZ and FRM II

Directors' Report

Eager for the coming decades of user operation.....	9
New buildings for the Heinz Maier-Leibnitz Zentrum (MLZ)	10
The year in pictures	12
Workshops, Conferences and Schools	18

Instrumental Upgrades & Services

News of the Instruments.....	22
Behind the Scenes – Service groups and Labs	36
Support for the MLZ from Jülich: Engineering and Electronics	48

Scientific Highlights

Quantum Phenomena

Static and quasi-elastic properties of the spiral magnet	
$\text{Ba}_2\text{CuGe}_2\text{O}_7$ studied by NRSE spectroscopy.....	54
Controlling the DMI to alter the chiral link between structure and magnetism for $\text{Fe}_{1-x}\text{Co}_x\text{Si}$	56
Band structure of helimagnons in MnSi resolved by inelastic neutron scattering	58
Structural and magnetic phase transitions near optimal superconductivity in $\text{BaFe}_2(\text{As}_{1-x}\text{P}_x)_2$	60
Magnetic and structural phase transitions in $\text{La}_{0.4}\text{Na}_{0.6}\text{Fe}_2\text{As}_2$ single crystals	62
Interplanar magnetic correlations in a high-temperature superconductor	64
Morphology of the intermediate mixed state in a bulk niobium type-II superconductor.....	66

Soft Matter

Contrast matching SANS reveals structural properties in protein-gold hybrid materials.....	68
Biomimetic multifunctional magnetite/gel composites	70
Chain exchange in polymeric micelles: Effect of core crystallization and conformational entropy	72
Effect of proteins on calcium mineralization in solutions associated with wastewater desalination	74
Dynamic phase diagram of soft nanocolloids – A recipe book	76
Influence of Ibuprofen on phospholipid layers.....	78
Photoactivation reduces side-chain dynamics of a LOV photoreceptor	80
Near surface dynamics in thin adsorbed layers of thermoresponsive microgel particles.....	82
$\text{SrC}(\text{NH})_3$: Structure and properties of a nitrogen-based carbonate analogue	84

Structure Research

Low temperature oxygen diffusion in $(\text{Nd/Pr})_2\text{NiO}_{4+\delta}$ explored using single crystal neutron diffraction	86
Magnetic ground state of superconducting $\text{Eu}(\text{Fe}_{0.88}\text{Ir}_{0.12})_2\text{As}_2$	88
Anisotropy in the magnetocaloric effect of MnFe_4Si_3	90
Illuminating the function of a biofuels enzyme with neutrons	92

Materials Science

Depth sensitive morphology of model battery anodes – using the TOF-GISANS method	94
In situ neutron experiments on a sodium metal halide battery	96
Transition metal deposition and capacity fade in lithium ion batteries using PGAA, XRD, AC impedance	98
Macroscopic and microscopic residual stresses in friction stir welded metal matrix composites	100
Scattering influences in fission neutron radiography for in-situ analysis of hydrogen storage tanks	102
Detection and imaging of the oxygen deficiency in single crystalline $\text{YBa}_2\text{Cu}_3\text{O}_{7-\delta}$ films using NEPOMUC	104
Ferrofluid magnetic nanoparticles aggregation driven by electric forces	106

Reactor & Industry

Safe operation and future challenges	110
Thermal conductivity of fresh and spent high-density U-Mo fuels	112
N.c.a. Lu-177 as a pharmaceutical drug precursor: From manufacture to new cancer treatment	114

Facts & Figures

Ten Years of the User Office	118
From science to media: The public relations office	120
Organisation	122
Staff	124
Budget	126
Publications & Theses	127
Committees	129
Partner institutions	134
Imprint	138

View of the FRM II (page 7) together with its surroundings
on the Campus Garching (page 8).



Directors' Report



Eager for the coming decades of user operation

On 4th May 2005, Klaus Habicht of the Helmholtz-Zentrum Berlin carried out his experiment at the instrument TRISP as the very first external user. This was the official starting point of user operation which has now been running for 10 years, serving thousands of scientists working on projects ranging over numerous different scientific disciplines. This stream has been uninterrupted and all instruments are always maintained to the highest standard, thanks to the expertise and know-how of our instrument scientists and service groups.

Since 2011, user operation and scientific use of the FRM II has been organized under the auspices of the Heinz Maier-Leibnitz Zentrum (MLZ). The MLZ has become the neutron science centre where “Big Science” and University merge. The committed involvement in instrument construction and operation, in addition to user support, of all partners from various German universities, the Helmholtz Centres in Jülich and Geesthacht, as well as the Max Planck Society, make the MLZ and its user structure unique.

The strong engagement by the different universities is also seen from the large number of Collaborative Project (Verbundforschung) proposals that were submitted to the German Federal Ministry of Education and Research (BMBF) last year. For this reason, the 1st meeting of the MLZ Instrumentation Advisory Committee (IAC) was held in November 2015 and was dedicated to the evaluation of the MLZ-relevant proposals for the BMBF „Verbundforschung“ 2016/19 and their suitability to the existing suite of instrumentation, as well as the further needs of the MLZ. The IAC recommendations support the comments of the MLZ directors to the BMBF. The scientific review of all “Verbund/BMBF”-proposals is organized by the BMBF independently.

In the course of the last decade, we have become the national neutron source, and of ever-growing international importance. This is also demonstrated by our involvement in diverse, major European projects under Horizon 2020. Within the SINE2020 project, the MLZ is one of 18 European partners that aim to further develop the innovation potential of Eu-

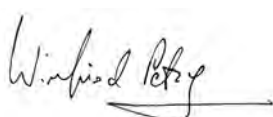
ropean neutron facilities and to pave the way for the neutron scatterer's dream: the European Spallation Source (ESS) in Lund. The MLZ partners will be responsible for the German in-kind contribution to the instrumentation of the ESS. Together with partners from Switzerland, France and the Czech Republic, they will develop and build seven new instruments, four instruments by the FZ Jülich, two instruments by the TUM (FRM II), and one by HZG.

Moreover, the MLZ is among other European partners also involved in another big project, CREMLIN, which promotes Russian and European collaboration for large-scale research infrastructures.

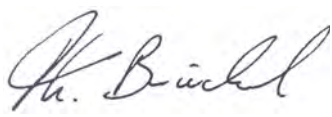
Within the TUM/FRM II-led HERACLES-CP project, European efforts are joint to reduce the risk of proliferation by minimising the use of highly enriched uranium. A new research reactor fuel based on uranium-molybdenum (UMo) alloys is being developed by the HERACLES group. As is evident, when it comes to research, Europe is working ever more closely together.

However, here at the MLZ, we are keen to come back to our main focus – cutting-edge research and first class instrumentation. Energy materials, understanding superconductivity, the location and function of hydrogen in proteins, quantum materials for information technology, residual stresses in engineering components are a few typical examples of questions tackled and answered using the instrumentation of the MLZ, and not only in the past year. One decade of successful user operation makes us proud, but we keep striving to strengthen and expand the scientific appeal for our users. A major step is the exchange of the plug SR5 that was designed by the FZ Jülich. The existing beam plug with two slots will be replaced by one with three slots which will supply the instruments TOPAS, POWTEX and SAPHiR with neutrons in the guide hall east in the future. A longer maintenance break for the exchange began in 2015 and will extend into the early part of 2016.

In this regard, we look forward to an eventful 2016 and take this opportunity to thank all our users for their continued trust and cooperation over the years.



Winfried Petry



Thomas Brückel



Klaus Seebach



Anton Kastenmüller

New buildings for the Heinz Maier-Leibnitz Zentrum (MLZ)

R. Bruchhaus¹, D. Schlotmann², K. Seebach³

¹Jülich Centre for Neutron Science (JCNS) at MLZ, Forschungszentrum Jülich GmbH, Garching, Germany

²JCNS/PGI-TA, Forschungszentrum Jülich GmbH, Jülich, Germany

³Heinz Maier-Leibnitz Zentrum (MLZ), Technische Universität München, Garching, Germany

The continuous expansion of neutron scattering instrument operation and services for scientific users has resulted in a growing number of staff working at the MLZ and the FRM II. Currently, about 413 in total (FRM II: 320, JCNS: 80, HZG: 9 and Max Planck Society: 4) are employed on site and this number is expected to grow even further as 6 new instruments in the new guide hall east go into operation within the coming years. In order to accommodate all these staff, container offices were built and some groups had to be transferred to the campus of the neighboring Max-Planck-Institute for Plasma Physics as an interim solution. Furthermore, more laboratory space and workshop area is urgently needed to meet the future requirements of the international scientific user community, our own scientists and the neutron source operation.

Recently, huge steps were undertaken to meet these requirements and provide more space for laboratories, the workshop and office space for the scientists. Two old laboratory buildings in the west-



Figure 1: The axis between workshop and office building (left) and laboratory and office building (right) affords a view of the heritage-listed "Atomic Egg".

ern part of the FRM II campus, dating from the early days of the "Atomic Egg", were demolished. The first part of the building project occurred underground. A new chute to supply the two new buildings with heat, electricity, water and gas was constructed. In 2015, the planning of a new office and laboratory building, the responsibility of the Forschungszentrum Jülich, and a new science and workshop building, the responsibility of the Technische Universität München (TUM), made considerable progress. The two four-storey buildings will have a floor space of some 9,300 m².

The Bavarian public construction office in Rosenheim ("Staatliches Bauamt Rosenheim") is overseeing the construction of both buildings. The architectural firm HENN GmbH in Munich designed the buildings, Fig. 1.

Due to their recesses and the staggered projections, the two buildings appear like twins establishing, although distant, a connection and the impression of an integrated and interlocked structure. The rectangular concrete panels forming the face of the buildings are balanced by the rounded metal surface of the Atomic Egg, forming a successful ensemble of the historic building and the future hosting modern science facilities.

The science and workshop building will host a large two-storey workshop on the ground and 1st floor levels. This will end the period of a workshop infrastructure housed in different buildings distributed over the FRM II campus. This workshop is urgently needed to meet the requirements for the manufacture of mechanical parts to sustain reliable operation of the neutron source. The two upper storeys contain offices for the reactor operation staff and the instrument teams. In addition, meeting rooms are planned to provide space for scientific discussions. The basement, ground floor and 1st floor of

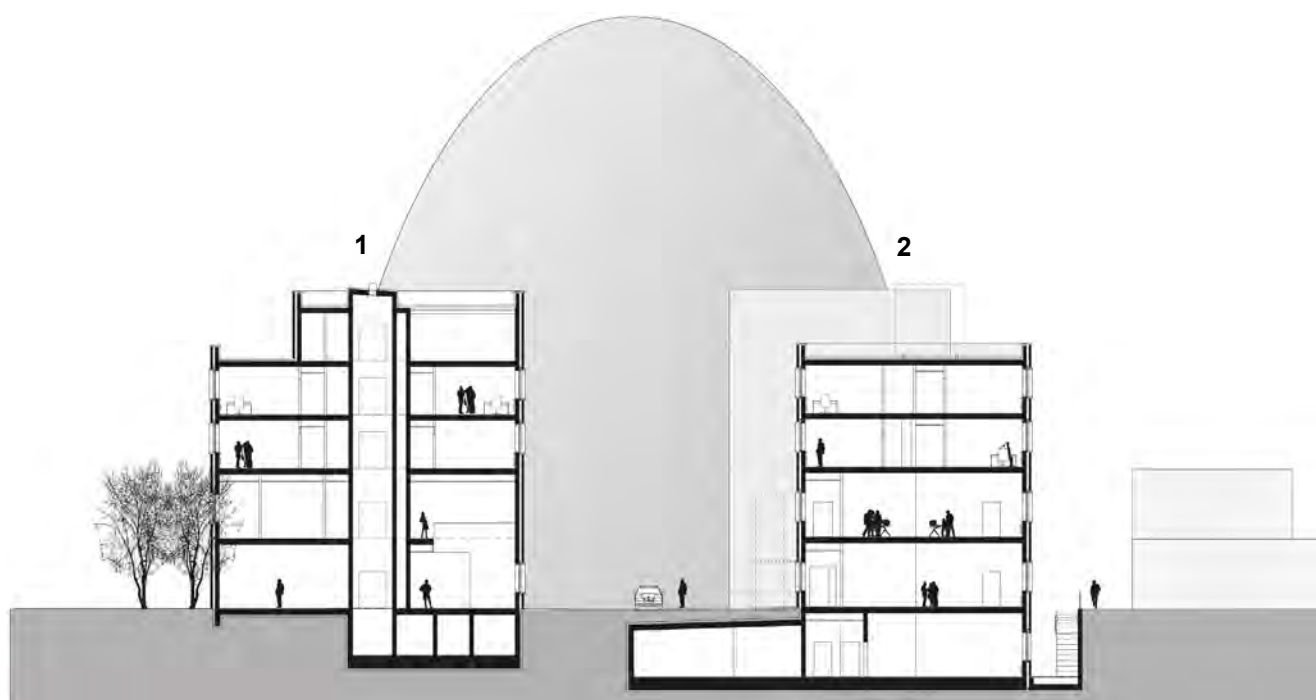


Figure 2: Cross section of the laboratory and office building (2) of the Forschungszentrum Jülich and the science and workshop building (1) of the TUM.

the laboratory building provide space for the sample environment group and the detector laboratories, including a clean room for detector fabrication under optimal conditions. The space designated for the sample environment group is a two storey area with sufficient head-room to move and operate tall and heavy magnets and cryostats. Other laboratories include a chemistry and biology lab equipped for sample preparation and pre-characterization capabilities such as UV-VIS spectroscopy, rheometry etc. The staff of the cooperation partner Helmholtz-Zentrum Geesthacht (HZG) join the JCNS-team in the same building, with their own office space and two laboratories for materials preparation and characterization and the possibility of testing equipment before it is used at the instruments. The building will host the thin film lab with the advanced Molecular Beam Epitaxy (MBE) system for film preparation and the laboratory for the transmission electron microscope. A Small Angle X-ray Scattering system SAXS will be installed in the basement of the building for our own research, and as a complementary method for the user community. The team of technicians will operate a small workshop for the fast and efficient manufacture of mechanical parts such as sample-holders and an electronics laboratory to review and repair the control electronics of the instruments. Different, separable meeting rooms and a larger seminar room, Fig. 3, together with some open floor areas for communication will provide opportunities for intense scientific exchange and discussion.

Two large rooms in close proximity to the office space of the instrument teams are reserved for the scientific users who are on-site during their experiments. These rooms are equipped with data lines to the neutron scattering instruments so that the scientists can remotely track and control their experiments and evaluate the raw data together with the instrument teams.

The total cost of the construction project is in the region of 30 Mio €, shared by the MLZ cooperation partners TUM and Forschungszentrum Jülich. Planning will be finalized in late spring 2016. Construction will start in early spring 2017. The buildings will be put into full operation between late autumn 2018 and spring 2019.



Figure 3: A look into the seminar room.

The year in pictures

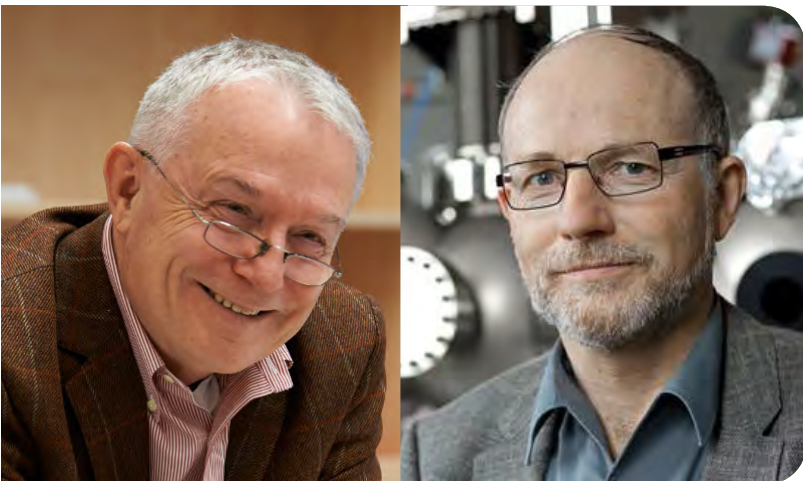


February 5th

VIP visit: Ulrike Scharf, Bavarian State Minister of the Environment and Consumer Protection (2nd from right) paid her inaugural visit to the MLZ.

February 27th

Busy: We are not the only one on the Campus Garching busy with constructing new buildings. In fact, there are several construction sites on and around the FRM II premises, which eventually will attract even more interesting science projects, students and visitors worldwide.



March 31st

Welcome & Goodbye: Prof. Dr. Dieter Richter of the Forschungszentrum Jülich (left) not only retires, but also passes his position as MLZ Director on to Prof. Dr. Thomas Brückel (right).

April 15th

Great: These are the participants in the last round of the National Physics Olympics. Five of them competed in the international round, winning silver and bronze medals.



April 23rd

Major Honour: The Nuclear and Radiological Security Sub-Working Group of the Global Partnership visited the MLZ during their meeting.

April 29th

Anniversary: User operation at the FRM II was officially launched 10 years ago. The first external user was Klaus Habicht of the Helmholtz Centre Berlin (left), who carried out experiments on the instrument TRISP on 4th May 2005.



The year in pictures



June 1st

Well accommodated: The new parent-child room, that is provided by the FRM II, is ready, so that parents can work there and at the same time can keep an eye on their children.

June 27th

Adventurous: This year, the open door day was a Long Night of Science in summer, from 6 pm to midnight at the Garching campus with about 11,000 visitors. Trying to operate a reactor at the computer at the stand of the radiation protection group of FRM II was not only a challenge for Prof. Dr. Winfried Petry (front).



July 1st

Delighted: Dr. Peter Müller, Administrative Head of the Bavarian State Ministry for Education (middle), Science and the Arts, and Dr. Ulrike Kirste of the same ministry (2nd from right) pays a visit to the MLZ.

July 10th

Tasty break: Entrepreneurs have breakfast at the MLZ at the invitation of the Chamber of Commerce of Munich and Upper Bavaria.



July 29th

Locally: The new City Council and the new Mayor, Dietmar Gruchmann (left), visit and gather information on the FRM II.

July 3rd

Happy: Dr. Marina Khanef was awarded the Christian Friedrich Schönbein prize for the best poster during the European Fuel Cell Forum.



The year in pictures



August 8th

Newly arrived: Dr. Kazuhisa Kakurai (middle), this year's winner of the Helmholtz International Fellow Award, arrived at the MLZ. His stay and the experiments he conducts here at the research neutron source are part of the award.

September 7th

Unforgotten: Shortly before his 93rd birthday, Prof. Dr. Lothar Köster passed away. He was Technical Director of the first German research reactor München (FRM) for 27 years – from 1960 until 1987.



September 12th

Congratulations: Prof. Dr. med. habil. Dr. rer. nat. Peter Kneschaurek of the Klinikum rechts der Isar (TUM) received the Glocker Medal for his many years of dedication to medical physics.

October 21st

Online: The first local mass storage for renewable energy was taken online by the Bavarian State Minister of Economic Affairs, Ilse Aigner (4th from left) in the Moosham district of Kirchdorf in Upper Bavaria. The FRM II is one of 13 TUM departments and institutions, which is involved in this innovative bulk storage project together with Varta Storage, Kraftwerke Haag and the ZAE Bayern.



November 23rd

Honoured: The Institute of Physics (IOP) and the German Physical Society (DPG) jointly awarded the Max Born Prize to Christian Pfeleiderer of the TUM's Physik-Department (left). He receives the award „for his fundamental contributions towards novel forms of magnetic ordering, especially of lattices of Skyrmions and their manipulation by electric currents.“

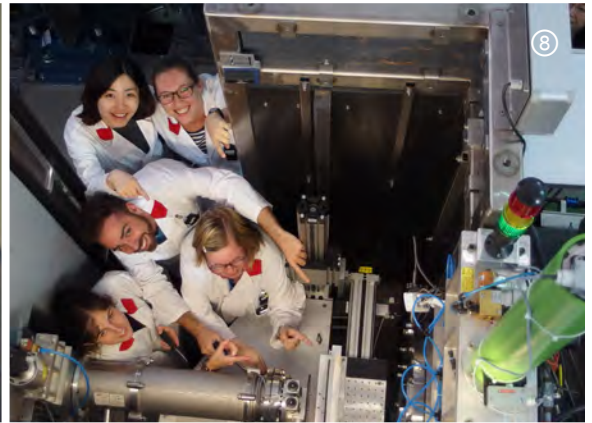
December 10th

Successful: Kick-Off-Event of the HERACLES-CP project in Brussels, a large European project towards the conversion of high performance research reactors in Europe, supporting the international non-proliferation efforts to minimise the use of highly enriched uranium by developing a new fuel based on uranium-molybdenum (UMo) alloys.



Workshops, Conferences and Schools

①	Neutrons in Research and Industry, weekly seminar	12 January – 14 December	Garching, MLZ, TUM
②	Trends in Neutron Science, MLZ User Meeting	23 – 24 February	Ismaning, MLZ
③	Polymers and Neutrons: Past and Future, Workshop	13 March	Jülich, JCNS
④	FullProf Workshop	11 – 12 June	Garching, MLZ
⑤	Internal Science Meeting	15 – 18 June	Grainau, MLZ
⑥	Workshop on „Public Awareness of Research Infrastructures“	18 – 19 June	Garching, ERF-AISBL, ESO, MLZ
⑦	35 th International Symposium on Dynamical Properties of Solids (DyProSo 2015)	13 – 17 September	Freising, MLZ

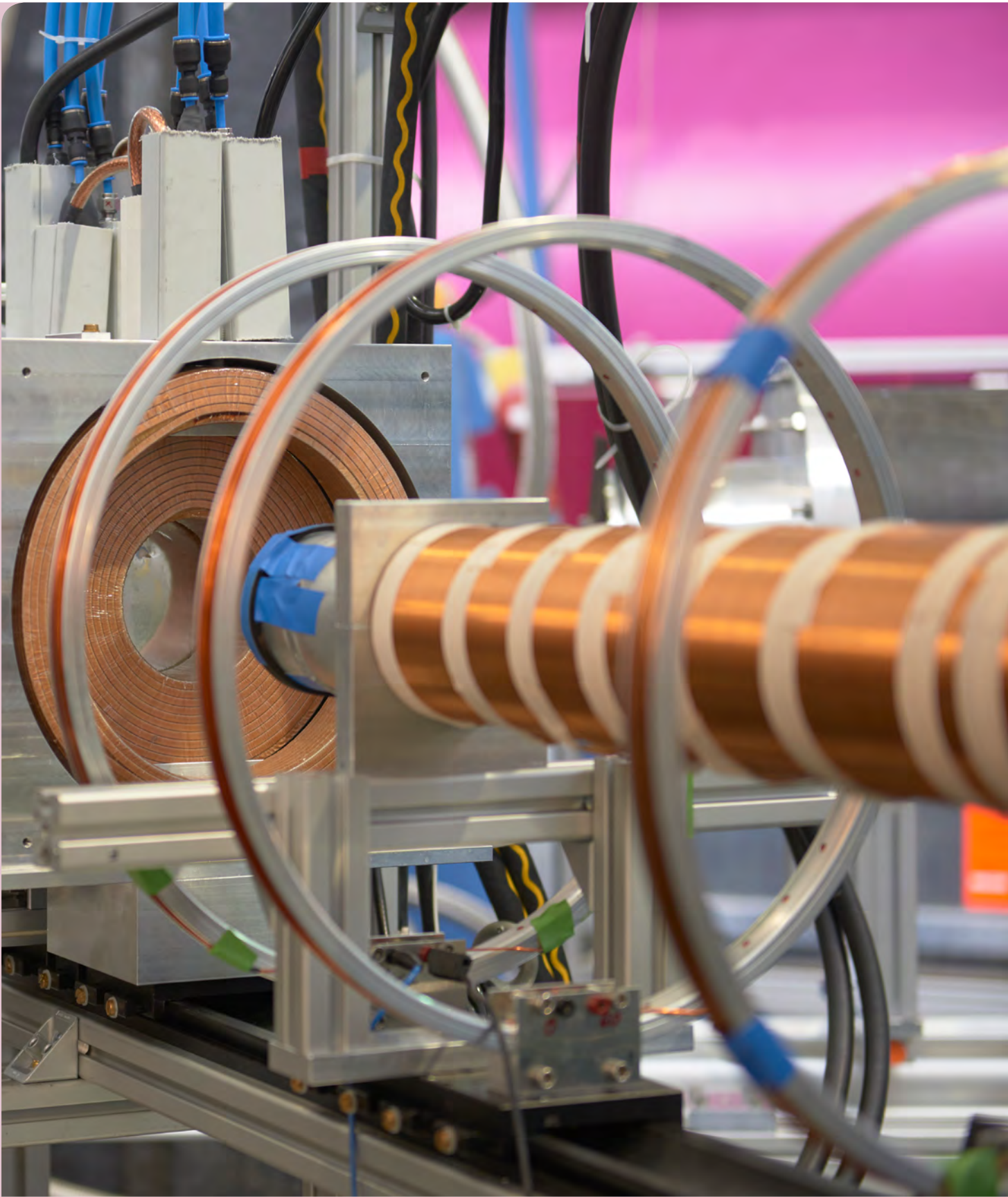


⑧	19 th JCNS Laboratory Course - Neutron Scattering 2015	7 – 18 September	Garching, JCNS
⑨	MATRAC (Application of Neutrons and Synchrotron Radiation in Engineering Materials Science), summer school 2015	21 – 25 September	Hamburg, GEMS
⑩	JCNS Workshop 2015	5 – 8 October	Tutzing, JCNS, DIPC
⑪	Practical training for TUM students	5 – 10 October	Garching, MLZ, TUM
⑫	Soft Matter & Neutrons GO Energy Workshop	8 – 9 October	Feldafing, JCNS
⑬	Workshop on NICOS and future plans for instrument control at the ESS	12 – 13 November	Garching, MLZ
⑭	Fox Workshop	1 December	Garching, MLZ



Detailed reports on the workshops, conferences and schools can be found in the Newsletter MLZ News 14 and 15 and at www.mlz-garching.de/englisch/news-und-media/brochures-und-films/newsletter.html.

The image depicts a view along the secondary spectrometer arm of RESEDA, which is undergoing an upgrade from transversal to longitudinal resonance spin echo spectroscopy (LNRSE). In contrast to transversal NRSE, LNRSE does not need a complex μ -metal shielding but only guide fields. Next to many applicational advantages, this allows this fantastic view of the B_0 -coils containing a RF spin flipper.



Instrumental Upgrades & Services

News of the Instruments

C. Genreith¹, R. Georgii¹, M. Hofmann¹, A. Houben², C. Hugenschmidt¹, V. Hutanu^{2,3}, W. Lohstroh¹, M. Meven^{2,3}, K. Nemkovskiy², B. Pedersen¹, A. Radulescu², O. Soltwedel⁴, E. Vezhlev², J. Voigt², M. Zamponi²

¹Heinz Maier-Leibnitz Zentrum (MLZ), Technische Universität München, Garching, Germany

²Jülich Centre for Neutron Science (JCNS) at MLZ, Forschungszentrum Jülich GmbH, Garching, Germany

³Institute of Crystallography, RWTH Aachen at MLZ, Garching, Germany

⁴Max Planck Institut für Festkörperforschung, Stuttgart, Germany

Successful experiments are heavily dependent on the performance and reliability of the instruments. Be it a boost in neutron signal detection, a decisive upgrade of the sample environment, or an update of the instrument control software, it is this continuous effort which keeps the instrument suite of the MLZ attractive. New instruments and methods contribute further to the potential for scientific progress.

Flux Gain for small samples: focusing the beam nose at TOFTOF

At TOFTOF, the adaptive focusing guide has been reinstalled in the last section of the beam transport system after some necessary modifications to the positioning system. The curvature of the four supermirror plates of the focusing device can be individually adjusted by piezo motors and the resulting geometry approaches a parabolic shape. The focusing can thus be optimized for each wavelength of the broad wavelength range available at TOFTOF. Both the standard linear tapered guide and the focusing guide are now installed in the motorized lift system in the last section of the neutron guide, still within the vacuum system of the primary spectrometer.

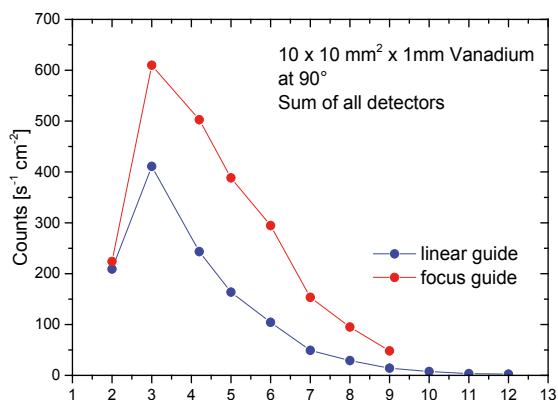


Figure 1: Scattering intensity of a 1 x 1 cm² vanadium plate (oriented at 90° with respect to the incoming beam) measured for the linear guide and the focusing guide at TOFTOF.

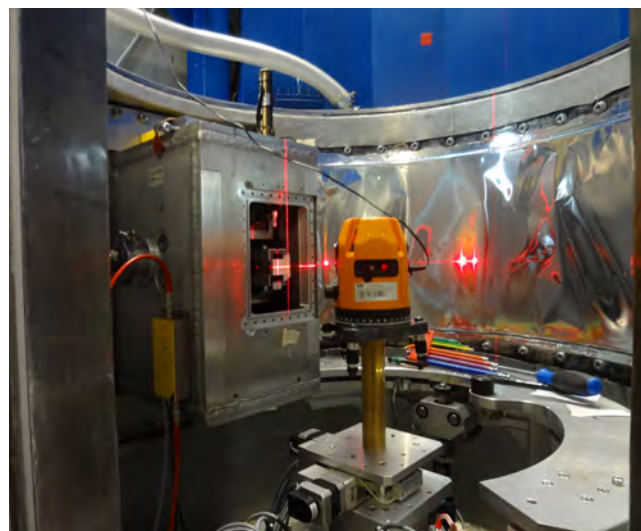


Figure 2: Installing the focusing guide into the beam nose at TOFTOF.

The change from one guide configuration to the other is fully automated and integrated into the instrument control software NICOS, and can be routinely chosen for any experiment at TOFTOF that benefits from a smaller beam spot with higher intensity. Depending on the wavelength, the intensity gain at the sample position (measured with a 1 cm²-vanadium plate) is in the order of 3.

Up-to-date gauge volume defining units at STRESS-SPEC

A new automatic slit system defining the incoming beam just before the sample was installed. The new primary slits are fully motorised and allow defining gauge dimensions continuously from 0.1 (horizontal) × 0.1 (vertical) mm² up to 7 × 17 mm². In combination with a sample tilting device such as the robot or the large Eulerian cradle available at STRESS-SPEC, these slits will enable fully automatic tri-axial strain measurements on engineering components even in the case where, in the course of the experiment, the gauge volume needs to be resized after sample reorientation.



Figure 3: New slit system of STRESS-SPEC.

With the new system, it is also possible to adjust the position of the slits with respect to the beam axis and sample centre in a more efficient and reproducible way. In addition, due to the use of a precision safety clutch, the slit can be repositioned without further realignment in the case of accidental collision with the sample.

Finally, on the diffracted beam side, the oscillation unit for the radial collimators was improved with respect to reproducibility and sturdiness and a new large opening radial collimator (field of view FOV = 10 mm) was designed and manufactured in cooperation with the technical services of the Helmholtz-Zentrum Geesthacht (HZG). With this addition, the available suite of radial collimators for defining the third dimension of the measurement gauge volume on STRESS-SPEC now ranges from FOV = 1 mm up to 10 mm, covering a wide range of possible applications in strain and texture experiments.

New detector system for the NECTAR radiography station

During 2015, ten years after its initial construction at the FRM II, the detector system of NECTAR (**NE**utron **C**omputed **T**omography **A**nd **R**adiography) was thoroughly upgraded to better serve user needs. The basis for the new set-up is the existing rail system for positioning both the sample manipulator and detector system in beam direction, on which a new solid support structure for the new detector system

has been mounted. The support structure allows for the additional mounting of heavy gamma and neutron radiation shielding, which has already been partially realized. A 5 cm thick layer of borated polyethylene, the base for the new camera box, shields the CCD detector from scattered neutron radiation from below. The new L-shaped camera box consists of a fixed and a movable part. The fixed part is built from overlapping aluminum sheets painted with a light-absorbing photo coating from the inside to ensure maximum light tightness and minimum reflectivity. It also houses the scintillator and a foil mirror. The scintillator is now positioned with a simple sliding mechanism in a cassette frame, making a quick and easy scintillator exchange possible. Perpendicular to the neutron beam axis, the CCD detector is mounted on a linear translation stage, allowing a flexible remote controlled selection of the camera's field of view directly from the instrument computer (ranging from 180 x 180 mm² to 300 x 300 mm² with the standard 85 mm lens system). In addition, a remotely controlled focusing unit was constructed, so that the lens focus can easily be adjusted from the



Figure 4: Picture of the new NECTAR detector system. The turn table of the sample manipulator is visible on the lower left in front of the new scintillator (lower center) and the fixed aluminum part of the detector box. The backing of the foil mirror can be seen on the right-hand side of the picture at the "elbow" of the box. On the upper left the new bellows surrounding the movable part of the box can be seen shielded against scattered radiation from the samples by a vertically fixed borated PE plate.

instrument computer without removing the light-tight bellow encasing the movable part. An auto-focus software solution is currently under development. At the moment, both an ANDOR DV 434 and a DV 934 iKon-M CCD camera are available for measurements with the new detector set-up and a support unit for a pco.1600 camera is under construction.

In addition to the hardware upgrade, the control software was also exchanged, such that NICOS is used for the operation of NECTAR. Thus, after being introduced to the system at either ANTARES or NECTAR, users can start experiments much faster at the respective alternative facility. For tomography, the golden angle method was implemented, which allows for better usage of the beam time and creates usable results even if measurements are interrupted.

The upgraded NECTAR facility offers users much more flexibility while increasing the signal-to-noise ratio and enables an adjustment of the resolution of the detector system to meet the individual experimental needs of the users.

Hot polarized neutrons at POLI

As reported previously, during 2014, a new Cu 220 variably double-focusing monochromator for the POLI diffractometer was developed and produced in cooperation between the Institute of Crystallography, RWTH Aachen University and the Institute of Physical Chemistry, University Göttingen (Fig. 5).

This monochromator has been successfully installed and commissioned on the POLI instrument in 2015. It has been optimized to provide high intensity neutron beams with short wavelength of 0.9 Å and 0.55 Å, respectively. It consists of 117 single crystal Cu blocks (individually oriented) forming a 9 x 13 matrix mounted in the mechanics permitting both variable vertical and horizontal focusing. For optimal vertical focusing, a flux increase up to 6.8 times compared to the flat plate geometry has been measured. The variable horizontal focusing allows for resolution optimization, depending on the used sample, experiment geometry and wavelength. The monochromator is fully implemented in the NICOS instrument control software and, in 2015, became a standard part of the diffractometer POLI.

As a first step towards the implementation of flipping ratio measurements on POLI, a detailed investigation of the potential usability of the new 2.2 T high T_c superconducting MLZ magnet for polarized neutron diffraction was undertaken. Using the typical set-up for spherical neutron polarimetry at POLI with a ^3He spin filter polarizer, analyzer and the nutator as spin flipper, neutron polarization could be passed through the magnet almost without losses, at least up to magnetic fields of 1.5 T. These results demonstrate the feasibility of the flipping ratio measurements using this magnet on POLI and serves as a very promising starting point for future optimization of the guide fields in order to reach the full available field region.

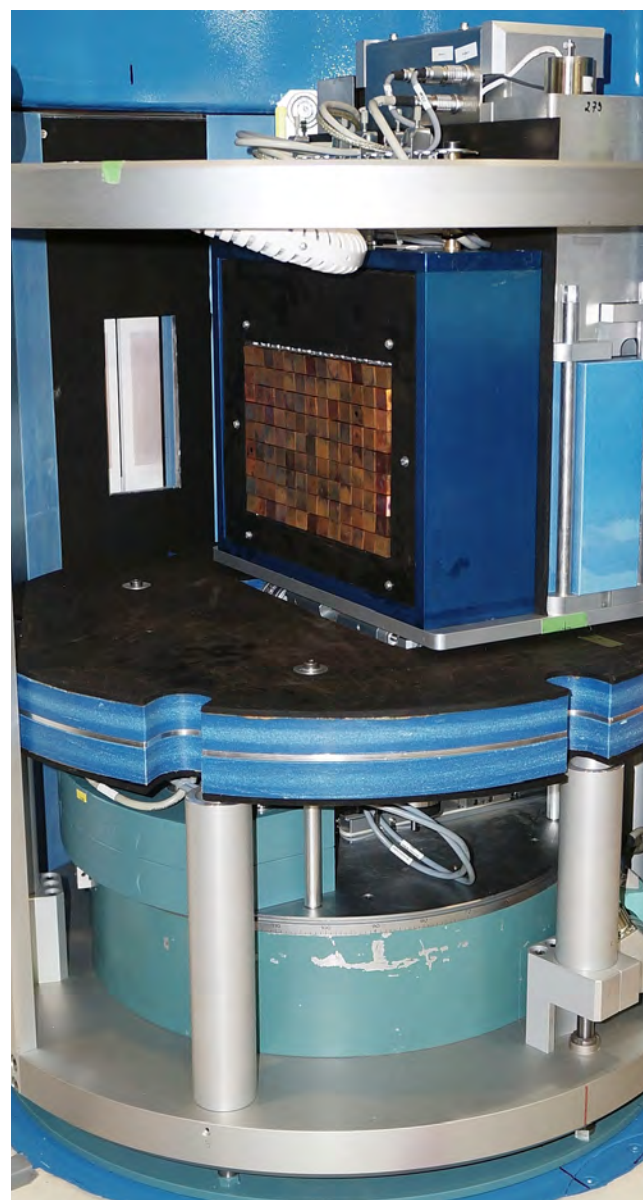


Figure 5: The monochromator table with the Cu220 monochromator installed.

HEIDI: new slits reduce background

At the single crystal diffractometer HEIDI at the hot source of the FRM II, the remote control slit system of the detector has been successfully commissioned and transferred to user operation. An additional beam tube directly in front of the sample with various manually selectable BN slits now allows the signal-to-background ratio to be improved, especially for tiny samples with diameters below 2 mm².

Neutron depth profiling at the focused beam of MARIA

Recently, a series of tests of the neutron depth profiling (NDP) technique was carried out at the cold neutron beams of the reflectometers TREFF and MARIA. The NDP technique allows for the determination of the in-depth distributions of appropriate light elements in a few micrometers of solids. It is based on the energy analysis of charged particles produced following a neutron induced reaction in several light elements with a large neutron absorption cross-section (e.g. Li and B). The energy losses of charged particles through the layer of a host material are defined by their path length, so that the depth distributions of emitting elements can be reconstructed from the measured energy spectra.

There are two typical approaches for the NDP instruments: either placed as close to the reactor source as possible, or as far away from the source at the guided neutron beams. The latter approach is preferable as it allows one to deliver a high neutron flux to the sample, while keeping the background from fast neutrons and γ -rays very low. The idea behind the experimental setup at the MLZ is to use focusing optics to provide an extremely high intensity of the beam at the sample position of the NDP setup. This is possible as the NDP technique does not impose any requirements on the beam collimation, and therefore the whole phase space can be used.

For the first NDP experiments at the MLZ, we used a simple setup borrowed from the Nuclear Physics Institute (Rez, Czech Republic). The aim of the test experiments at the beam of TREFF was to benchmark the possibilities of the NDP techniques at the MLZ with respect to the facilities worldwide in terms of intensity and background. The experiments were performed with standard calibration samples and showed an extremely low background component

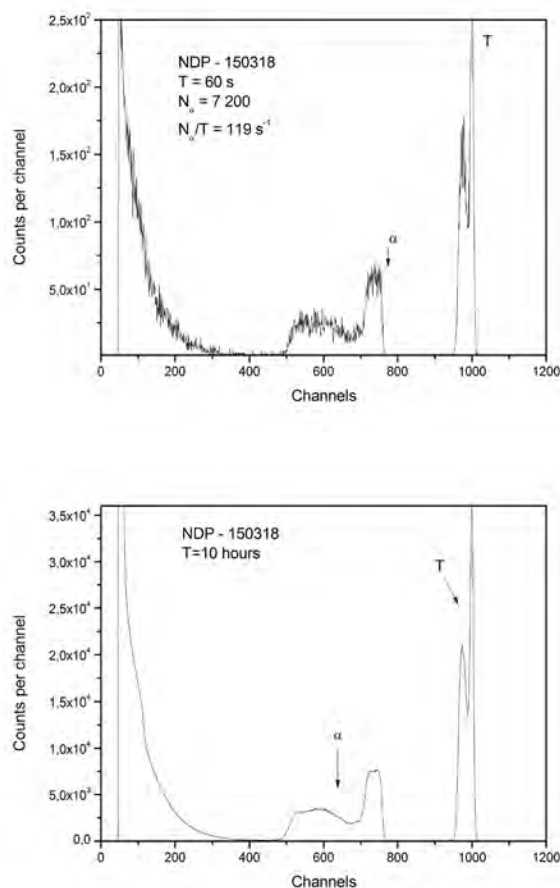


Figure 6: NDP spectra collected from the $\text{TiO}_2/\text{Li}_4\text{Ti}_5\text{O}_{12}/\text{Li}_3\text{PO}_4$ sample at MARIA in 1 minute (a) and 10 hours (b).

from the environment (γ -rays and fast neutrons) and a high data collection rate similar to that at the NDP facility at NPI.

Subsequently, the NDP experiments were performed at the reflectometer MARIA, which provides an extremely high neutron flux at the sample - about 10^8 n/s/cm² for 4.5 Å wavelength neutrons. The data collection rate achieved is about 2 orders of magnitude higher than at TREFF and measurements with real samples demonstrated that reliable data can be obtained within 1 minute. Two example spectra (with the thin-film Li containing a sample provided by P. Notten, TU Eindhoven) taken for different times are shown on Fig. 6.

Historically, NDP has been used with a single detector for charged particles. This approach works well so long as a relatively long time is available for the accumulation of statistics. However, modern chemistry is now engaged in kinetics studies. For example, there is a keen interest in the study of Li

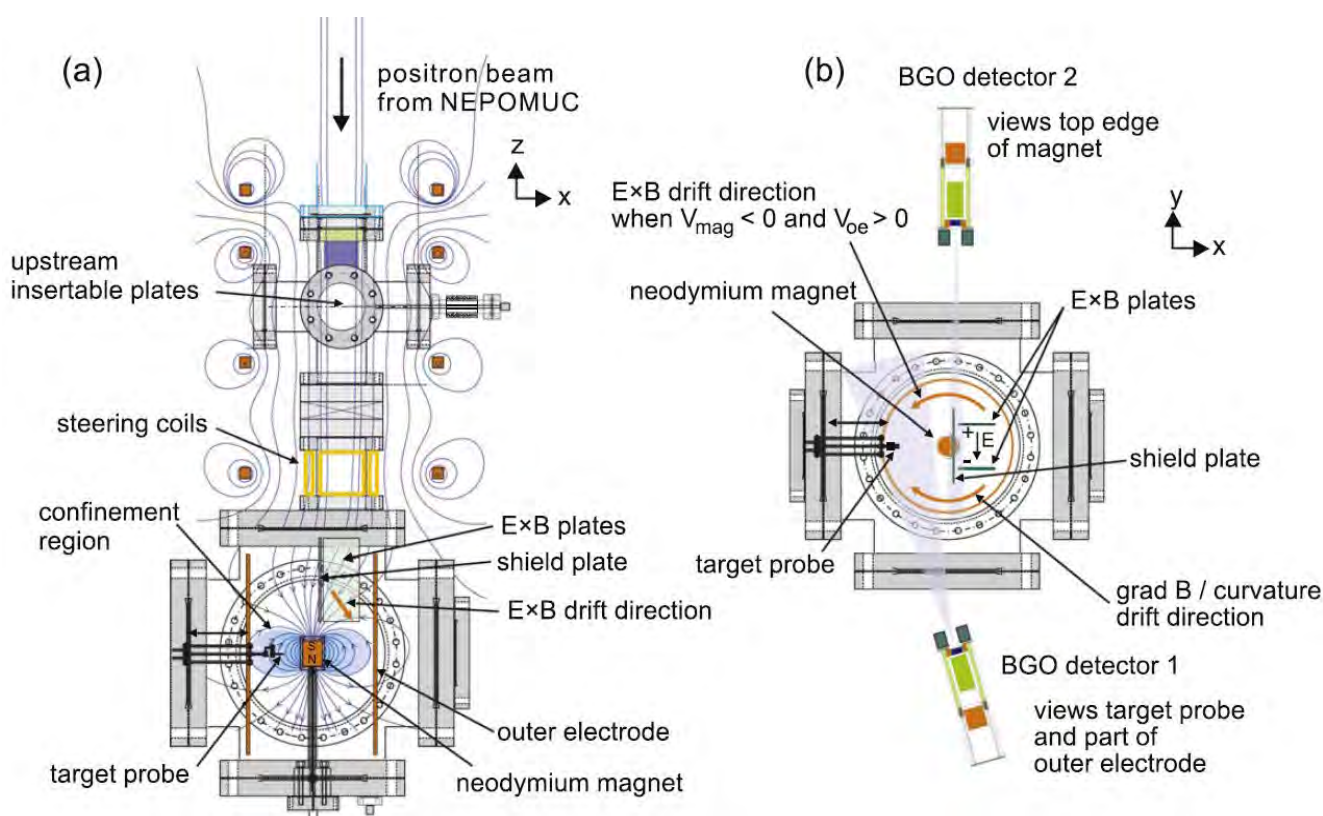


Figure 7: Dipole trap at the open beam-port (OP) at NEPOMUC: (a) A side view of the vacuum chamber and the interface to the NEPOMUC positron beam. Blue lines show magnetic field lines. (b) Top view of the main chamber, showing the viewing angles of the two scintillation detectors used to monitor the positron injection. Figure from Ref. [1].

ions diffusion inside all solid state thin-film batteries, using the NDP technique. At MARIA, the experimental time needed to explore the battery degradation during charging-discharging cycles is already remarkably short. Even in the classical one detector approach, the full charge-discharge process can be completed, for instance, in 2 minutes and there will be 720 cycles per 24 hours of a neutron beamtime. To boost the count rate even further and collect as many charged particles as possible, one can use a multi-detector arrangement where all of the spectra are summed up in a single spectrum. Such a new NDP setup, fitting perfectly to the sample position of MARIA, is under construction at the JCNS. It will be equipped with 8 charged particle detectors for simultaneous data collection. Such a boost to the counting rate paves the way for performing time-resolved in-situ or in-operando NDP measurements that are at present unthinkable. In particular, the investigation of Li transfer at a fast (subminute) rate becomes possible, opening up an exciting possibility to explore processes of fast battery charging and explain battery degradation in time. The first experiments with the new NDP setup at MARIA are planned for the second half of 2016.

Development of positron instrumentation at NEPOMUC

The positron source NEPOMUC delivers a high-intensity beam with a kinetic energy of 1 keV. However, for most of the experiments conducted at NEPOMUC, the brightness of the beam is enhanced by focusing the primary positron beam onto a tungsten single crystal, stochastic cooling in the crystal and subsequent reemission of thermalized positrons into the vacuum with discrete energy. By biasing the crystal and adjusting the extraction fields of the remoderation device, the energy of the remoderated positron beam can be set within a wide range between 5 and 300 eV. The remoderated beam has an enhanced phase space density, and due to the high efficiency of the device still contains 5 – 10 % of the original particle flux. Usually, the energy of the remoderated positron beam is set to 20 eV. In 2015, the primary and brightness enhanced beam was optimized for different kinetic energies and transported to a new installation at the multi-purpose open beam port (OP), which is used for transportable experimental set-ups.

Besides the beam monitors used in the NEPOMUC beam line, a separate analysis tool was installed at the OP which enables the determination of various beam parameters such as beam size, intensity, longitudinal and transverse energy as well as band width. The longitudinal energy component is measured with the retarding field technique, and the transverse energy component, is determined by measuring the beam diameter in an adiabatically varying magnetic guiding field. In a series of experiments, the energy-dependent intensities of the primary beam at 400 eV and 1 keV kinetic energy and of the remoderated beam at 5, 12 and 22 eV were determined. Significant losses for the primary beam are attributed to the non-adiabatic positron transport in the beamline.

As a result of collaborative research, (Max Planck Institute for Plasma Physics, Greifswald and Garching, University of Tokyo, Universität Greifswald, Lawrence University, Appleton, USA, and TUM, partially supported by JSPS Grant-in-Aid for Scientific Research 25707043) we envisage the creation of a positron-electron plasma for the first time. To this end, a new apparatus was installed at the OP in order to study the efficient injection of a positron beam into a dipole trap (see Fig. 7) [1]. A set of Helmholtz coils provides the magnetic guiding field up to the

entrance of the experimental chamber and additional correction coils allow for two-dimensional steering of the beam propagation direction. A permanent neodymium magnet with a field of 0.6 T at its surface is positioned in the center of the main vacuum chamber. The intense 5 eV positron beam was transported into the confinement region of the dipole field trap using the ExB drift of the positrons between a pair of tailored plates that created the electric field. An injection efficiency of 38 % was achieved. We determined the lifetime of the positron cloud in the dipole trap, showing that a small population persists for about 1 ms.

At the Coincidence Doppler Broadening Spectrometer (CDBS), a brightness enhancement system was designed and constructed in order to enable CDB spectroscopy with high spatial resolution (supported by the BMBF, project no. 05K13WO1). The new positron guiding system consists of various magnetic and electrostatic lenses for focusing the positron beam onto a 100 nm thin Ni(100) re-moderation foil. With this new set-up, a positron beam diameter in the micrometer range is anticipated at the sample position. In addition, new positionable mountings for high purity Germanium were constructed, which enable quick switching between two different spectroscopic modes: (i) In CDBS, germanium de-



Figure 8: Photo of the pulsing unit and the positron elevator in front of the Surface Spectrometer in the experimental hall of the FRM II. The positron beam traverses the beam line from left to right. Figure from Ref. [2].

tectors are read-out coincidentally in pairs, and (ii) background-free DBS is achieved by using germanium detectors in coincidence with BGO-scintillation detectors for lateral resolved and depth dependent defect imaging. In addition, the distance between the detectors and sample can be varied dependent on the maximum processible count rate. This new set-up is planned to be tested within the first reactor cycle in 2016.

At the surface spectrometer (SuSpect), the detection system for determining the positron intensity at the sample position has been replaced. The new BGO-detectors are well collimated with respect to the sample position and allow to monitor the beam intensity during the measurement of positron annihilation induced Auger-electrons. With the exception of SuSpect, at all spectrometers attached to the NEPOMUC beam facility the sample can be set to negative potentials in order to adjust the positron implantation energy. Due to experimental constraints, the application of acceleration potentials at the sample position inside SuSpect is limited to very low values. In order to enable depth resolved positron measurements by variation of the implantation energy, the total energy of the beam has to be increased before the additional potential energy is used to accelerate the pulse onto the sample (supported by the BMBF, project no. 05K13WO1). To this end, a so-called positron elevator was built and commissioned which enables the elevation of the total energy of a positron beam [2]. The whole device has been integrated into the NEPOMUC beam facility in front of SuSpect, as shown in Fig. 8. The total energy of a pulse created by a two stage pulsing system is increased during the passage of the center electrode of the elevator. An additional chopper can be used to cut out pulses, or to further reduce the background. The positrons are accelerated towards the sample, which is commonly near ground potential. During the first beam times, the device was successfully put into operation and the main characteristics were determined. The overall pulse width was 1.663(5) ns at a repetition rate of 5 MHz. The shape of the beam was assessed using a beam monitor. It could be demonstrated that an energy elevation to 1.6 keV leads to a beam diameter of 2.56 mm FWHM compared to 1.85 mm FWHM of the dc beam. The high amplitude sinusoidal, which is needed for the positron elevator, is generated in

a resonator circuit. After several optimizations, the Q-factor of this RLC-circuit could be raised to 371. Given these parameters, the total energy of the beam could be increased by 3.5 keV. After pulsing and energy elevation, the positron intensity was still at 87.7 % of the dc beam intensity, demonstrating the high efficiency of this new set-up.

At the interface for the Scanning-Positron-Microscope (SPM), which was developed at the Universität der Bundeswehr, major improvements were made in order to enable positron lifetime measurements with high spatial resolution. The SPM interface comprises a pulsing system, which is operated at 50 MHz, and a second tungsten single crystal remoderator for further brightness enhancement. In addition, a beam energy elevator was successfully put into operation. This device allows us to increase the total beam energy by about 1.2 keV. Within the next beamtime a further increase of the total beam energy is anticipated in order to match the requirements of the SPM. In contrast to the device at SuSpect, the elevator of the SPM interface is operated without magnetic fields. Several beam parameters could be determined within the first measurements. At the end-stage of the SPM interface, a pulse width of about 250 ps and a beam diameter of less than 200 μm were achieved. The efficiency of the pulsing system including the elevator was estimated to be about 65 %. The current set-up is shown in Fig. 9.

[1] H. Saitoh, et al.; *New J. Phys.*, 17(10), 103038 (2015).

[2] A novel pulsed positron beam with variable energy, Niklas Grill, Master Thesis, TUM, November 2015.

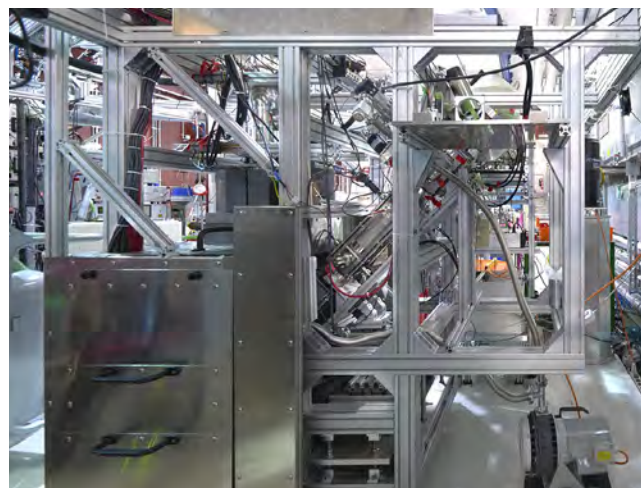


Figure 9: Photo of the SPM interface housing the pulsing system, the remoderation unit, and the positron beam elevator.

Improved uniaxial stress cell

The modular experimental setup for a pressure cell for neutron scattering on samples under uniaxial pressure, constructed by Alfonso Chacon in 2009, was recently modified. His pressure cell is driven hydraulically, and can be readily installed in the CCR-5 cryostat. The improvement by Alexander Schade from E21 consists of two parts. First, the pressure can now be controlled electronically, and all sensors are connected to NICOS at MIRA. To archive this, he added a proportioning valve from ASCO Nomatics to the experimental setup, and implemented new ENTANGLE-devices for gas pressure and the piezo-based force sensor. Fig. 10 shows a typical calibration curve of gas pressure vs. force, as measured with NICOS. For precise measurements of the pressure, the setup must be recalibrated for each sample, because the zero offset and the scaling are functions of the sample's height. The second improvement was to install two PT-1000 thermometers at close proximity to the sample. This enables precise measurements of the temperature gradient over the sample. The modified pressure cell is shown in Fig. 11. It demonstrated that it is possible to archive a gradient < 0.1 K at $T = 311$ K in the CCR-5 cryostat. The system has already been used in experiments at MIRA and is now available for all users at the MLZ.

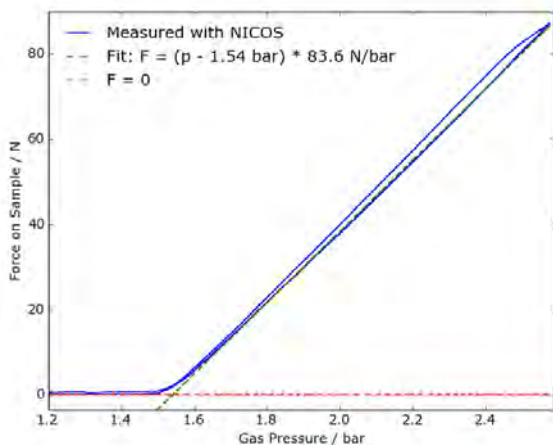


Figure 10: Gas pressure calibration curve, measured with NICOS and the new ENTANGLE-devices.



Figure 11: Photograph of the modified pressure cell.

X-ray hybrid-pixel detector for NREX

To gain complementary information about a sample at the same spot and at the same time, NREX provides an in-situ X-ray set-up. Unlike neutrons, the flux of conventional fixed Cu-K_α anode radiation sources allows one to detect diffuse scattering on small time scales (i.e. seconds). In a pioneering work, it was shown that the interfacial morphology has direct impact on the superconducting transition temperature [3]. To reduce the time for mapping the reciprocal space, we made use of a position sensitive X-ray detector. In collaboration with E17 (TUM), we equipped NREX with an EIGER 1M test system from Dectris Ltd. (Switzerland). The functional principle of this position sensitive detector (PSD) is

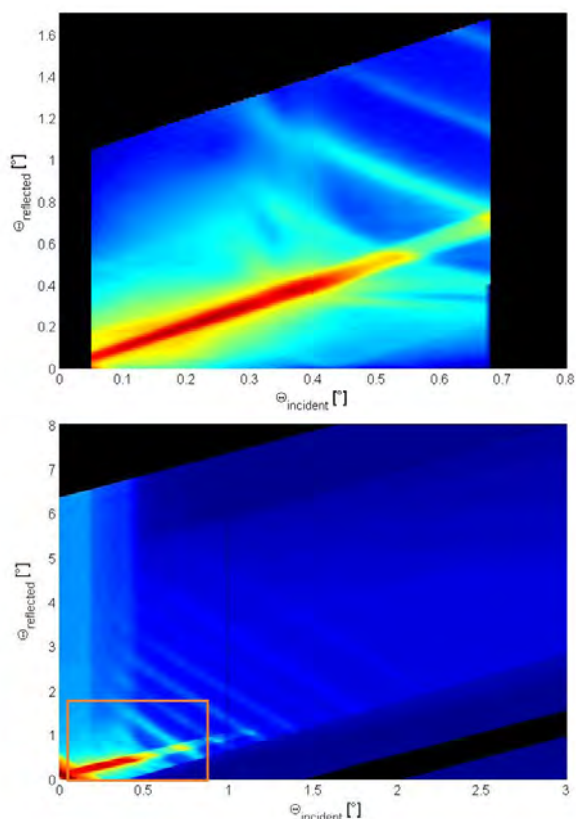


Figure 12: Scattering maps of a $(\text{Fe } 10\text{nm} / \text{Si } 10\text{nm})_{50}$ – sample measured with a 0-dimensional NaI detector and a PSD (bottom) (data acquisition: top: 72 h, bottom: 5 h). While keeping the same measurement conditions, the PSD allows measurement of the diffuse scattered intensity more than 100 times faster. The highlighted area in the bottom picture shows the resolved region of the top.

based on direct electron-hole pairs, created in depleted silicon by X-ray photoionization. The charge-ion-clouds are then read out pixel-wise with a spatial resolution of $75 \mu\text{m}$ and subsequent energy filtered to minimize electronic noise and dark current. Comparing both detectors, the PSD offers a drastically increased intrinsic energy resolution. During normal neutron-reactor operation, the PSD showed a slightly increased signal to noise ratio. At the same time, the improved statistics are due to the higher detection efficiency. Moreover, keeping the same angular resolution conditions constant, the data acquisition time for reciprocal space mapping can be accelerated by a factor of 100.

In contrast to the NaI-detector signals, which are discriminated in a narrow energy window, signals detected in the hybrid-pixel detector are actively suppressed only below an adjustable energy threshold. An upper pseudo-threshold is given by the energy dependence of the detector's quantum efficiency. This unfortunate characteristic spoils the signal to noise ratio compared to the NaI performance, in

the case when the neutron reactor is switched off. To overcome this issue, it is planned to continue the test with a more appropriate PSD (for example Medipix3 in fine pitch configuration) and thus provide in-situ X-ray reflectometry at NREX for routine experiments.

[3] Y. Khaydukov, et al., J. Appl. Phys. 118, 213905 (2015)

Upgrade of the phase space transform chopper at SPHERES

The Phase Space Transform (PST) chopper at SPHERES (**S**pectrometer for **H**igh Energy **RES**olution) has been upgraded. Besides its function as a duty-cycle chopper and primary beam deflector, the chopper achieves, by the motion of the mosaic graphite crystals on its circumference, a phase space transformation of the incoming wavelength spectrum, which enhances the usable flux at the monochromator. The original three-wing PST chopper could not be operated at the optimal speed due to mechanical restrictions. Therefore, a new more compact one-wing PST chopper has been designed, which is mechanically quite challenging. This innovative work was carried out by the Central Institute for Engineering, Electronics and Analytics (ZEA-1)

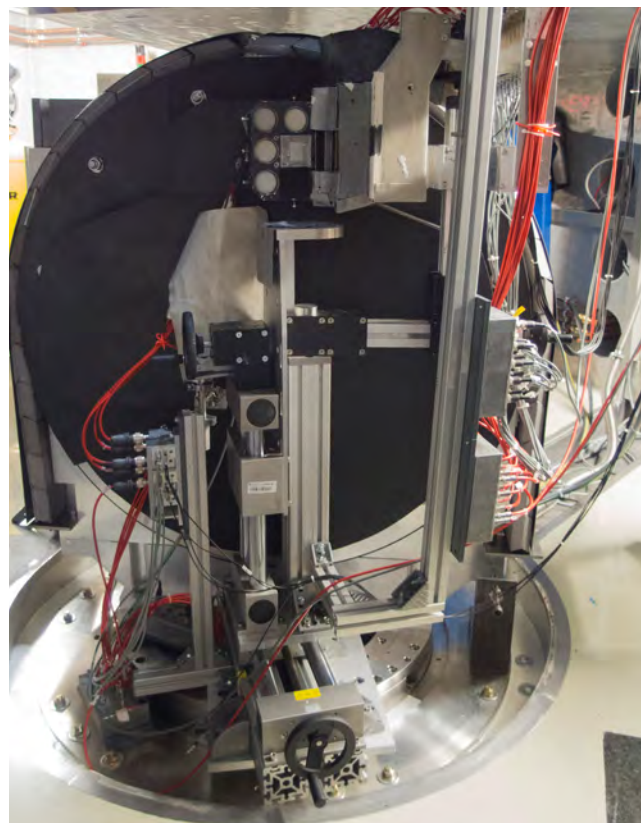


Figure 13: The new chopper enclosed in its shielding installed inside SPHERES.

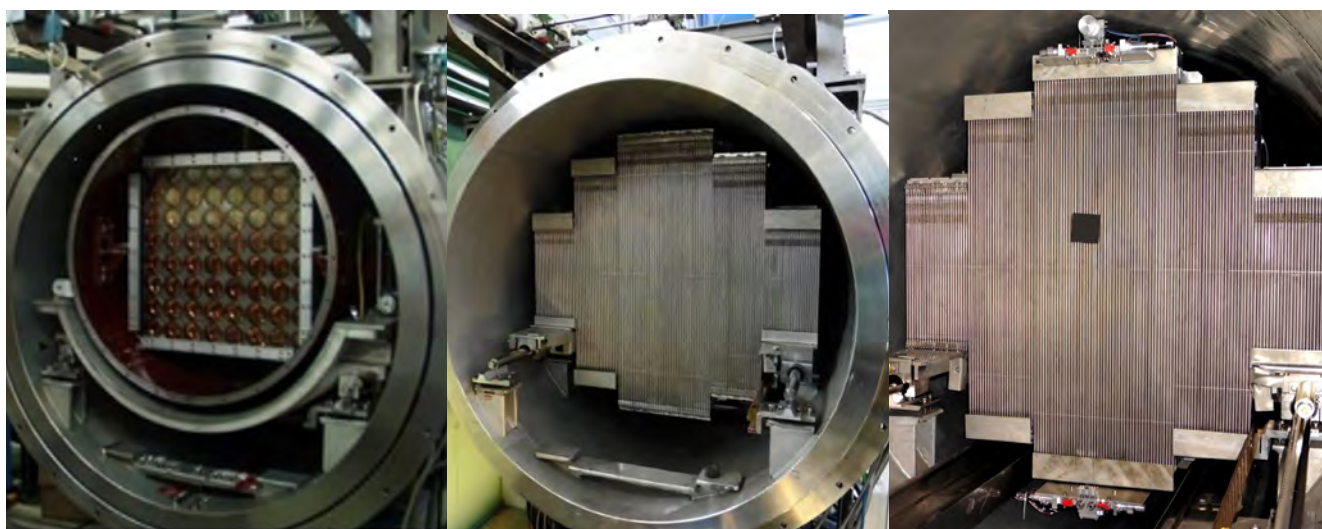


Figure 14: From left to right: the old KWS-2 detector, then during the installation phase and finally the new one with the mobile (XY) beamstop visible.

of the Research Centre Jülich. Together with the upgrade of the chopper, the graphite deflector crystals were also replaced with ones of a higher reflectivity and mosaicity to further increase the intensity.

This year the new PST chopper was installed at the instrument (see Fig. 13) and successfully put into operation. It now runs at the desired frequency with a crystal speed of 225 m/s, close to the optimum for the phase space transformation. Thanks to the increased velocity and the better deflector crystals, the intensity in most detectors has now been doubled! In addition to the intensity increase of a factor 2, the signal-to-noise ratio for the large angle detectors has been improved by about 10 %. A couple of low intensity scattering experiments have already benefited from the enhanced performance of SPHERES.

A new multi-MHz detection system for KWS-2

The small-angle neutron diffractometer KWS-2, operated by the Jülich Centre for Neutron Science (JCNS) at the Heinz Maier-Leibnitz Zentrum (MLZ), is dedicated to the investigation of mesoscopic multi-scale structures and structural changes due to rapid kinetic processes in soft condensed matter and biophysical systems. Following demands from the user community, it has recently been considerably upgraded, with the aim to boost its performance with respect to the intensity on the sample, the instrumental resolution, and the minimum scattering variable Q_{\min} . In the high-intensity mode, an intensity gain of up to twelve times compared to the conventional pinhole mode for the same resolution

can be achieved with lenses based on increasing the sample size. In the tunable resolution mode, with chopper and TOF data acquisition, improved characterization of the scattering features within different Q ranges is enabled due to the possibility of varying the wavelength spread $\Delta\lambda/\lambda$ between 2 % and 20 %. In the extended Q -range mode, by means of lenses and a secondary high-resolution detector (pixel size of 0.45 mm), a Q_{\min} down to $1 \cdot 10^{-4} \text{ \AA}^{-1}$ can be achieved, which in combination with the pinhole mode, permits the exploration of a continuous length scale from 1 nm to 1 μm .

A vast improvement in performance was achieved by the recent upgrade of the instrument's detection system. A new detector consisting of an array of ^3He tubes with an active detection area equivalent to 0.9 m^2 (Fig. 14) and innovative rapid readout electronics replaced the old (scintillation, 60 cm x 60 cm) system. The detector's masterpiece was supplied by GE Reuter Stokes Inc. and installed in close collaboration with the JCNS and ZEA-2 (Central Institute for Engineering, Electronics and Analytics – Electronic Systems) teams on-site. To improve the read-out characteristics and reduce the noise, the detection electronics is mounted in a closed case on the rear side of the ^3He tubes frame. The efficiency of the ^3He tubes is about 85 % for $\lambda = 5 \text{ \AA}$ and the resolution slightly better than 8 mm.

The new detection system is characterized by a dead-time constant of 25 ns and a count rate as high as 5 MHz at 10 % dead-time. Compared to the old detector, this is an improvement of a factor 25

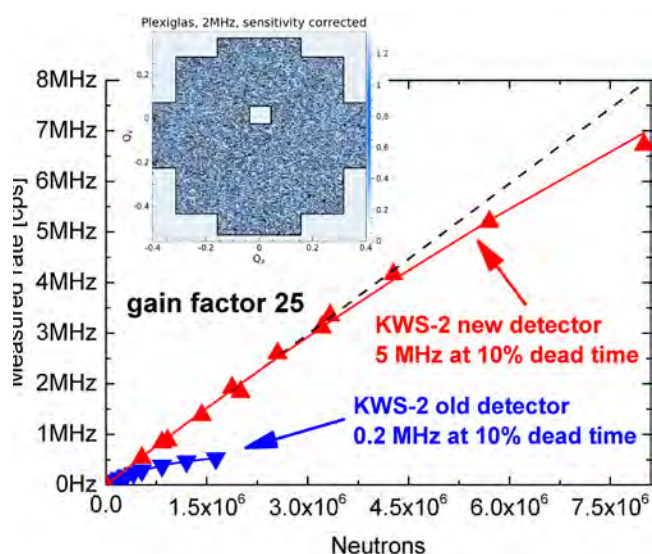


Figure 15: The dead time of the new KWS-2 detector extracted from the fit of the measured count rate (symbols) with the paralyzable dead time model (solid line); the inset shows the scattering pattern (flat) from the incoherent scattering standard sample (Plexiglas) measured with a count rate of 2 MHz, after the correction for detector sensitivity was applied.

(Fig. 15). The much higher count rate will shorten the measurement times and, thus, increase the number of experiments in the same time period by the optimal use of the high flux of up to 2×10^8 neutrons $\text{cm}^{-2} \text{s}^{-1}$ at the sample position. In addition, this

will enable new scientific opportunities in the field of the structural investigations of small soft-matter and biological systems. At high wave-vector transfers Q , these systems typically deliver only a very weak scattering signal above the buffer or solvent level, which can now be resolved due to the leap in performance enabled by the new detector.

Software upgrade and a new chopper for DNS

During 2015, the main upgrade activity at DNS was dedicated to the instrument control software. A major milestone towards a user-friendly instrument was achieved in the second reactor cycle of 2015 by the complete changeover to the new generation instrument control software TANGO and NICOS. Furthermore, a new option for data reduction and visualization in diffraction mode was developed and implemented, based on the Mantid project.

As far as hardware is concerned, a new chopper for time-of-flight mode was installed. Its mechanical stability, control system and radiation safety were tested successfully during the last reactor cycle in 2015.



Figure 16: The new look of the diffuse scattering spectrometer DNS.

Neutron Laue diffractometer started routine operation

In 2015, the new neutron Laue diffractometer went into full operation (Fig. 17). It was designed by T. Keller from the MPI for Solid State Research in collaboration with the MLZ. Using the white thermal beam on SR8b after the RESI monochromator, it allows fast alignment and orientation of crystals (typically a few seconds per image, about one hour for a complete alignment). Being controlled by the MLZ standard NICOS software, operation is easy and intuitive. More technical details can be found in the MLZ Newsletter December 2015. Fast access to the instrument with a typical preparation time of one week is possible. Please contact the person responsible for the instrument or the MLZ User Office for details.



Figure 17: The new Laue diffractometer at the beamline SR8b.

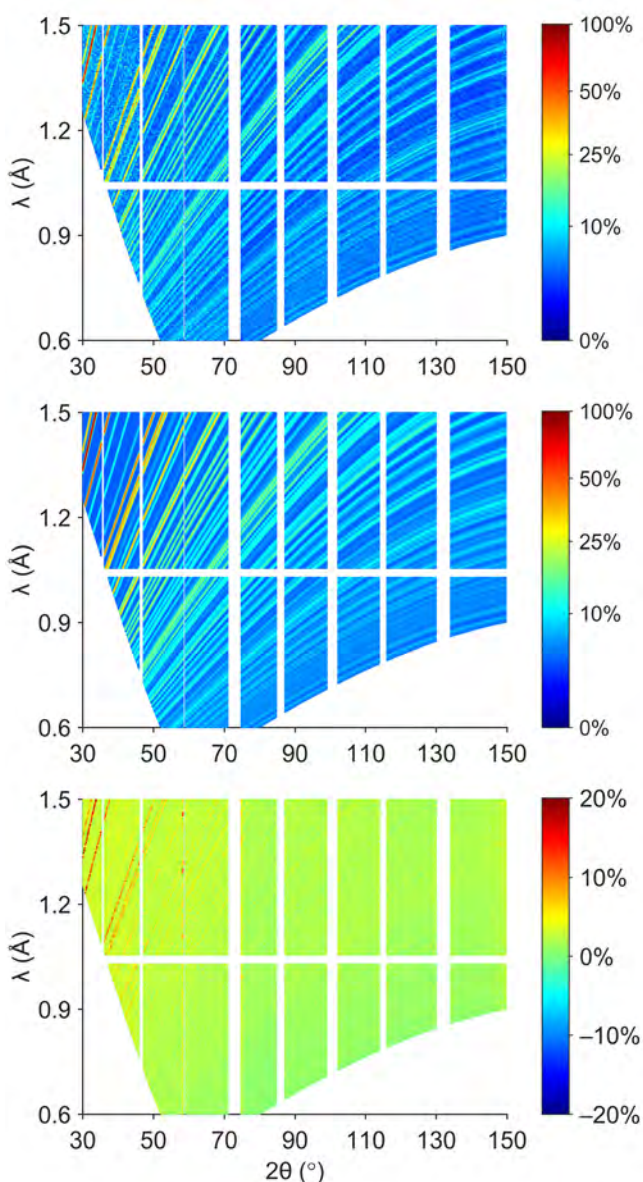


Figure 18: Measured (top), fitted (middle) and differential (bottom) diffraction pattern of CuNCN data from POWGEN. The color bar of each picture denotes the intensity as a percentage of the largest intensity peak in the simulated diffraction pattern.

POWTEX – ready for the neutron guide hall east

The main instrument components of POWTEX are still awaiting the desired on-site construction and commissioning phase in the reactor and neutron guide hall east of the FRM II. The double-elliptic neutron-guide system [4] was delivered in early 2014 by SwissNeutronics. It was complemented by the in-pile sections, which were recently delivered for all three of the SR5 instruments. All components of our chopper system, including the double-disk pulse chopper as well as the chopper for the instrument SAPHIR, are already running at the ZEA-1, Forschungszentrum Jülich. The serial production of the innovative large-area ^{10}B -detector manufactured

by CDT GmbH, Heidelberg, continues to proceed as planned, and the full read-out electronics has been finalized and tested. A significant part (30 %) of the modular central-detector has already been assembled. After having focused on the SR5 in-pile, the POWTEX engineering and construction team at ZEA-1 of the Forschungszentrum Jülich is finalizing the construction with subsequent manufacture of the very last major components for POWTEX, e.g., detector-housing parts and shielding. In conclusion, this will allow for mounting and testing of the first detector modules in the final detector-housing in preparation for the desired on-site construction and commissioning phase.

Meanwhile, we have further improved the novel method of multi-dimensional Rietveld refinement of angular- and wavelength-dispersive diffraction patterns as obtained at the POWTEX (MLZ) or DREAM (ESS) instrument. We have already successfully applied the refinement method for high-resolution data measured at POWGEN (ORNL), see Fig. 18. Therefore, the data-treatment procedure was also customized to yield the intensity as a function of the scattering angle and wavelength. These developments have recently been published [5].

[4] A. Houben, et al., Nucl. Instr. Meth. A 680, 124 (2012).

[5] P. Jacobs, et al., J Appl. Crystallogr. 48, 1627 (2015).

More of TOPAS for the neutron guide hall east

The TOPAS instrument continues to occupy its space in the new neutron guide hall east. The missing two portions of the spectrometer chamber were transported to the MLZ at the beginning of the year and assembled at the foreseen position of the instrument (Fig. 19). With the successful vacuum test, in which the 75 m³ volume of the chamber has been pumped down to a cryogenic vacuum of 10⁻⁵ mbar, we reached an important milestone in the construction of the new thermal chopper spectrometer at the MLZ.

In the meantime, the other ingredients of the chamber are “cooking” in the workshops at the Forschungszentrum Jülich. The mechanical support of the detector system (Fig. 20) has been finished and the transport system for mounting the detector boxes in the chamber is approaching completion and will be brought to Garching soon.

Also, the construction of the primary spectrometer is progressing. All components of the chopper system have been manufactured and will be assembled at the beginning of the year. The feature giving TOPAS its name is the Polarization Analysis. The polarization of the neutrons scattered at the sample will be analyzed across a large solid by the so-called ‘Magic PASTIS’ system (Fig. 21). It consists of a set of coils and μ metal sheets, in which a large neutron banana-shaped spin filter cell is introduced. The

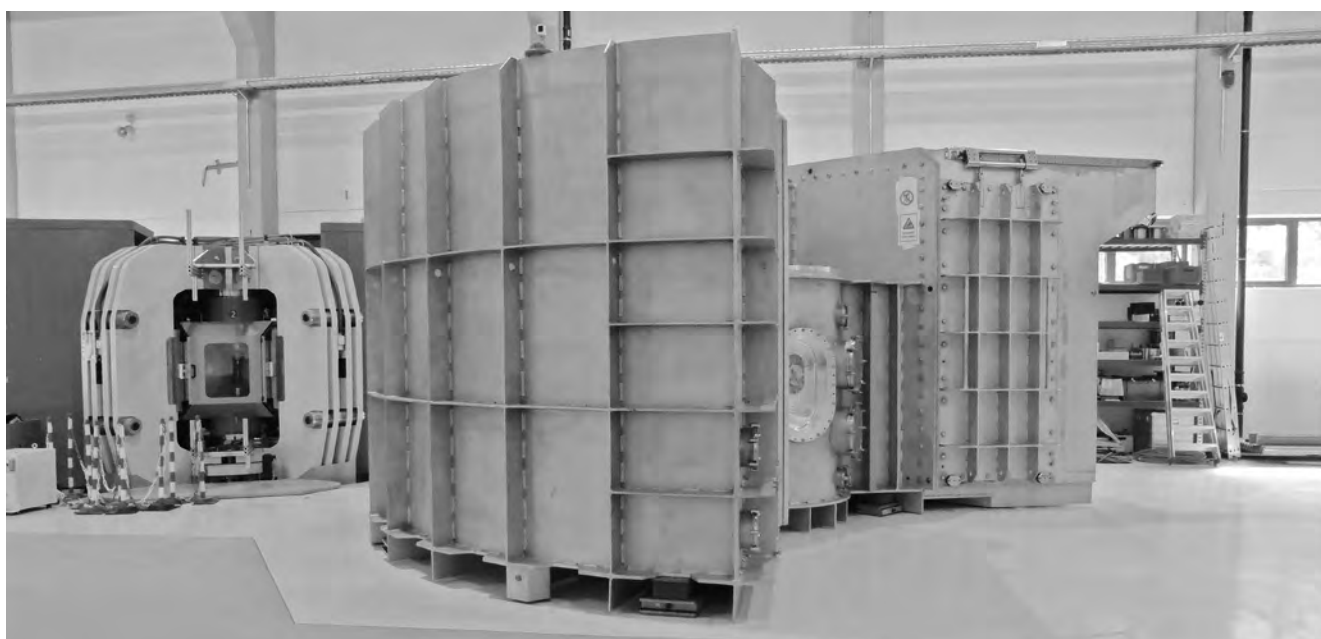


Figure 19: The assembled TOPAS spectrometer chamber in the neutron guide hall east.

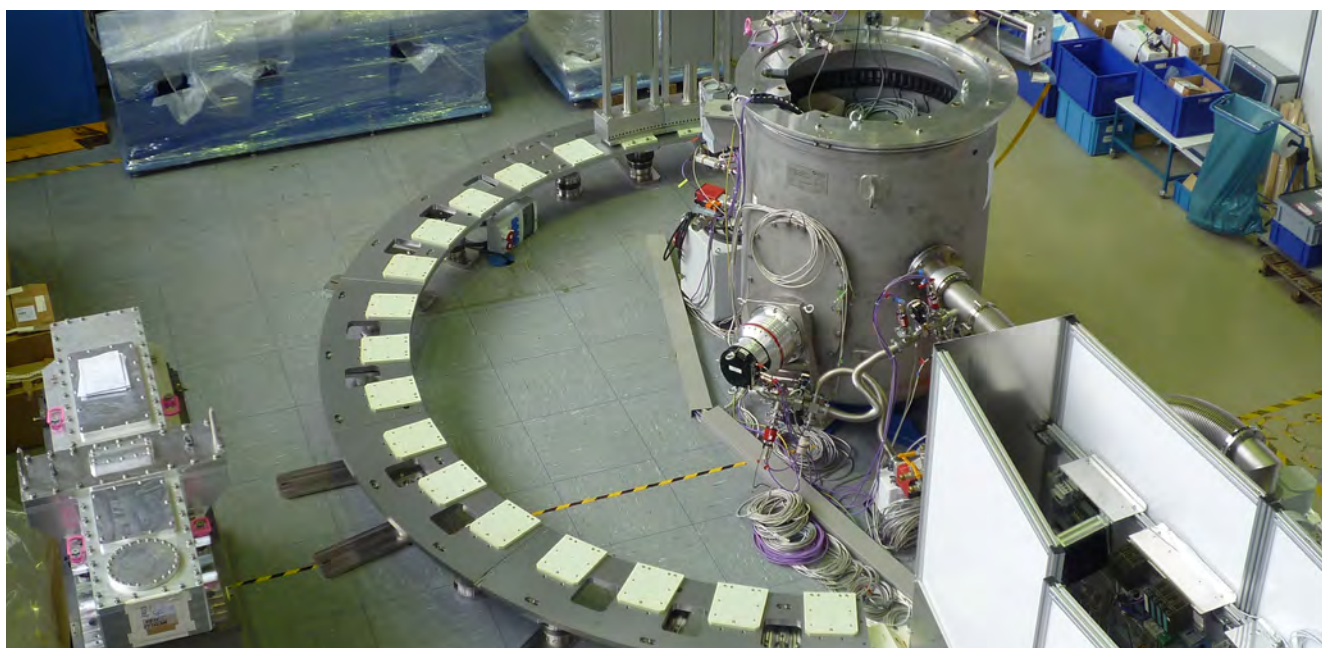


Figure 20: Detector bank and 3 detector boxes assembled in the workshop in Jülich.

complex magnetic system is necessary to provide PA in an arbitrary direction and to achieve an extremely homogeneous magnetic field at the position of the spin filter cell, which operates only if the magnetic field gradients are around 10^{-4} cm^{-1} or better.

As the 'Magic PASTIS' layout requires a magnetic field at the sample position in three orthogonal directions, we had to develop new means of preparing the initial neutron polarization to match. For that, we developed a combination of coils and permanent magnets. The high velocity of thermal neutrons poses a particular challenge, as the 'smoothness' of the change in direction of the magnetic field must be very good in order to rotate the neutron spin adiabatically. Therefore, the system was first modeled to confirm that the conditions for the rotation of the fastest neutron available at TOPAS ($v = 5700 \text{ m/s}$) are fulfilled. The setup was then manufactured and the 3-dimensional mapping of the field distribution and bench testing is ongoing.

The next big step for the realization of TOPAS is the exchange of the beamport SR5 during the reactor shutdown starting in October. This provides the prerequisites for bringing thermal neutrons into the neutron guide hall east, which is eagerly anticipated by the instrument teams.

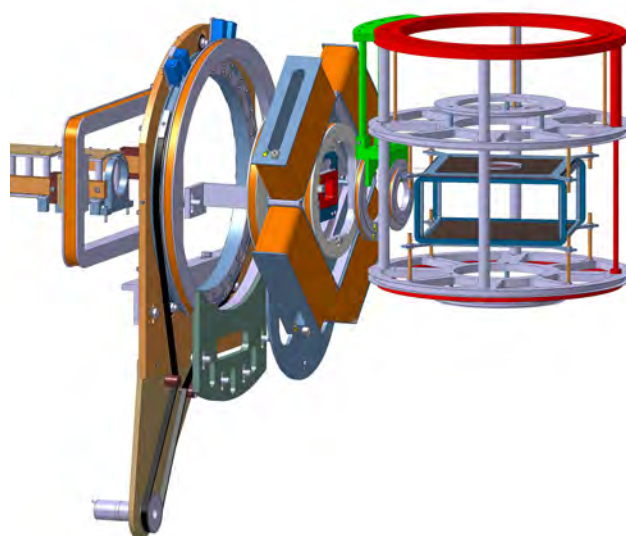


Figure 21: (Top) Schematic of the coil and magnet layout for the preparation and analysis of the neutron polarization. (Bottom) Image of the coil and magnet configuration for the preparation of the initial neutron polarization on the frame for the 3-d mapping of the field distribution.

Behind the Scenes – Service groups and Labs

E. Babcock¹, K. Bingöl¹, G. Brandl¹, A. Felder¹, A. Kriele³, J. Krüger², P. Link², S. Masalovich², J. Peters², S. Pütter¹, H. Reithmeier², Z. Salhi¹, A. Weber¹, H. Wenninger², J. Wuttke¹, K. Zeitelhack²

¹Jülich Centre for Neutron Science (JCNS) at MLZ, Forschungszentrum Jülich GmbH, Garching, Germany

²Heinz Maier-Leibnitz Zentrum (MLZ), Technische Universität München, Garching, Germany

³German Engineering Materials Science Centre (GEMS) at MLZ, Helmholtz-Zentrum Geesthacht GmbH, Garching, Germany

Just as a successful stage production relies heavily on the numerous workers behind the scenes, our instruments need the support of the MLZ central service groups. Here, we report on the advances in sample environments, neutron detection, software development and the increasing capabilities of the MLZ laboratories.

The ³He detector system for SAPHiR

The SAPHiR instrument for time-of-flight neutron diffraction and radiography under extreme pressure and temperature conditions will exploit two different position sensitive neutron detection technologies. Three detector banks comprising approximately 650 ³He-filled position sensitive proportional counters (PSD) will be positioned at 90° and 0°, while a bank of four scintillation detector modules with wavelength-shifting fibers will be placed at backward scattering angles. The latter was developed by the detector group at the Forschungszentrum Jülich.

The PSDs with a diameter of 8 mm and 400 mm active length are filled with ³He gas with a pressure of 20 bar. 48 horizontally mounted PSDs make up a segment and are arranged in a curve with a pitch of



Figure 1: Detector segment with 48 detector tubes in a curved assembly.

8.15 mm (Fig. 1), while five segments form a detector bank (Fig. 2). Eight detector tubes on either side of the bank, which are outside the field of view, are



Figure 2: Detector bank with five segments, each comprising 48 or 40 detector tubes respectively. The position sensitive mesytec electronic modules are placed behind the tubes.

not mounted. The focal point of the curved geometry is the sample position and the focal length amounts to 1.5 m.

The assembly of the first detector bank and all ten segments for both 90° banks was completed in 2015. The demanding mechanical precision required to mount the detectors was well achieved and proper detector performance of the ten segments was successfully proven with a ^{252}Cf -source in the detector laboratory. The full integration of one detector bank is ongoing. Once it has been completed, the two banks will be mounted in the neutron guide hall east in early 2016. The construction of the forward detector bank is under way.

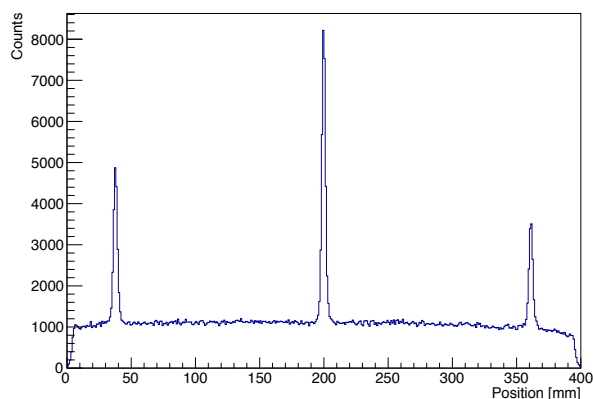


Figure 3: Histogram of a position resolution measurement for a single detector tube measured with a BN plate with three 2 mm wide slits (see text for details).

The required position resolution was measured using a Boron Nitride absorber plate with three 2 mm wide slits and a ^{252}Cf source moderated to approximately 1 Å. An example is shown in Fig. 3. Due to the small distance between the detector and the source, the left right peaks have a lower intensity than the central peak. The average position resolution (FWHM) amounts to 2.8 mm and is in agreement with the specification of 3 mm.

Plug'n Play NICOS

While it is obvious how to define excellence in science, it is not so easy to measure the success of the instrument control group. As a valid point of reference we take the number of days when the scientific instruments were “down” due to problems with the instrument control soft- and hardware. In 2015, we were able to keep this number very close to zero.

The basis of this achievement is the large number of improvements in the instrument control software. In 2015, within the NICOS development alone, almost 1500 changes were implemented. Most of these changes were not noticed by the users, but they lead to very stable instrument control software for executing the experiments.



Figure 4: Plug'n Play digital I/O box to be used easily with TACO and NICOS instrument control software.

The success of instrument control is based, in particular, on the concept of the TACO/TANGO boxes for the sample environment. This concept could easily be extended to other components of instrument control.

As part of their training, our apprentices developed a box to control 8 digital inputs and 8 digital outputs. The input interprets signals in a range from 3 up to 24 volts as a ‘1’ signal. The digital outputs would be set to 24 volts if they were set to ‘1’ by the software. The box was designed to connect the signals to the instrument setups easily, and vice versa. The connectors are standard banana-type plugs and sockets, as used in most labs. The actual input and output states are displayed via some LED's in the front of the box (see Fig. 4). A small display at the front of the box is also used to give information about the current status of the software. As well as the network address, it shows the current state of the box. The box could very easily be used inside NICOS via the Plug'nPlay mechanism integrated into NICOS.

Project Groups “Electronics” and “Engineering”

The project groups at the MLZ coordinate activities in the areas of instrument development, commissioning tasks and technical service. They act as the

interface between instrument scientists, technical support groups or companies and management. The project groups cooperate mainly with the service groups for instrument control at the MLZ and the Central Institutes for Engineering and Technology (ZEA-1) and Electronic Systems (ZEA-2) of the Forschungszentrum Jülich in the fields of electronics and automation, neutron detectors, control software and mechanical engineering.

The most notable projects in 2015 included:

- Installation and commissioning of the new ^3He detector at KWS-2
- The new chopper at the backscattering spectrometer SPEHRES
- Roll out of new Compact-PCI hardware to replace old unreliable systems
- Cooperation with Media TUM: Integrated user and data access
- New chopper for DNS
- Roll out of Tango control boxes to sample environment equipment
- Migration of three more JCNS-instruments to NICOS



Figure 5: Installing the new high-performance ^3He -detector for the small angle neutron diffractometer KWS-2.

A vast improvement in performance was achieved due to the new detector for KWS-2 (Fig. 5). The detector was supplied by General Electric Reuter Stokes Inc. and installed in close collaboration with JCNS and ZEA-2. An improvement by a factor of 25 compared to the old detector opens up new scientific opportunities within the field of the structural investigation of small soft matter and biological systems. As KWS-2 is already back in user operation, the scientists will immediately benefit from this improved KWS-2 for their research.

A key component of the third-generation neutron backscattering spectrometer SPHERES is the phase space transform (PST) chopper. After careful simulation work, a new disc design and an optimized speed held the promise of a considerable gain in performance. The new design of the one hole chopper turned out to be mechanically quite challenging. However, the team at ZEA-1 succeeded in producing the chopper and it is now in operation at the instrument. It was possible to increase the neutron intensity by a factor 2 and the signal-to-noise ratio was improved by 10 %. The first users have already been able to benefit from the considerable improvements in performance.

Replacing old hardware and implementing state-of-the-art operating systems and software is a continuous task in the effort to guarantee the reliable operation of the instruments. Another aspect is the MLZ-wide standardization to facilitate servicing of the complex systems. In 2014, new workstations were installed at all JCNS instruments in order to replace the instrument control and user computer systems. All newly commissioned systems run the CentOS 6 Linux-based operating system, which guarantees long-term support until 2020. A central software repository has been created that contains both public domain software unavailable in CentOS' repositories and in-house developed software for instrument control and data evaluation. A two-stage continuous integration process facilitates the automatic provision of test and production packages. Thus, the entire software at each instrument can be installed in a reliable and reproducible way. Due to the integrated logging capabilities of the operating system's package manager, the version of a specific component can easily be determined at any time. Malfunctioning software can be downgraded to the previous known stable version. In 2015, this successful approach began to be applied to the slow control and data acquisition systems. Device drivers and TACO/Tango server packages were prepared in close cooperation with the ZEA-2. New Compact-PCI systems equipped with CentOS 6 and their own packages were set up at the instruments BIODIFF, DNS, KWS-1, KWS-2, and J-NSE.

Although already partly reported in 2014, the DNS upgrade continued and came into full effect in 2015. The transition to the most modern generation of in-

strument control software at MLZ, Tango and NICOS, has now been completed and has gone into user operation. Another essential step was the installation and commissioning of the new JCNS-made chopper. The new DNS will clearly attract the users, providing higher intensity, better performance and new options.

Efforts to develop device drivers using Tango as a successor to TACO, with special focus on the simple and pluggable interfaces in use at the MLZ, have been incorporated into a new software package called Entangle, which already provides Tango support for over 50 hardware components in use at the instruments.

Three more JCNS instruments are being migrated to the new MLZ unified control software stack, Tango and NICOS. The implementation of custom components is underway for KWS-1, MARIA and SPHERES, each of which presents its own chal-

lenges, and will go live for users in the first reactor cycle in 2016.

As part of the ongoing effort to provide a high-quality, consistent service for users throughout the MLZ, existing JCNS sample environment equipment has also been fitted with Tango control boxes, which interface natively with NICOS as well as via a proxy with older systems using TACO. As a result, experiments can now be performed in a fully automated mode under remote control.

Another area where service for the users will improve considerably in 2016 is data access. A metadata catalog is being developed in collaboration with the mediaTUM team at the University Library and achieved several important milestones in 2015, such as integration with the upcoming user office software GhOST. The catalog will provide the same interface as ICAT, a similar system that is in use at other facilities. That will make inter-facility sharing of user login credentials and measurement data possible.

Hot and Cold – new sample environment available

In 2015, as well as many minor improvements, the MLZ sample environment acquired the major addition of a cryostat and a furnace.

First, the POLI single crystal diffractometer was equipped with a new close-cycle cryostat dedicated for use with the spherical neutron polarimetry experiments (Fig. 6). This was the result of cooperation between JCNS and RWTH Aachen. Due to the rather long tail of the cryostat, it can be mounted inside the polarimeter cryopad. Placing the bulky cold head above the Cryopad allows the user an additional degree of freedom in tilting the sample by $\pm 5^\circ$ about the scattering plane. This enhanced flexibility is extremely useful for the optimal orientation of a single crystal during the experiment. Additionally, the thin tail allows Helmholtz coils to be used together with the cryostat. Small magnetic fields at the sample position can be applied to the study of e.g. magnetic domains. Moreover, the sample can be positioned with a 0.04 mm precision, without the need to take the sample stick out of the cryostat. Temperatures below 4 K can be reached using a 1 W cold head type SRDK-408 from Sumitomo.



Figure 6: Long tail closed-cycle cryostat for use with the spherical polarimeter cryopad.

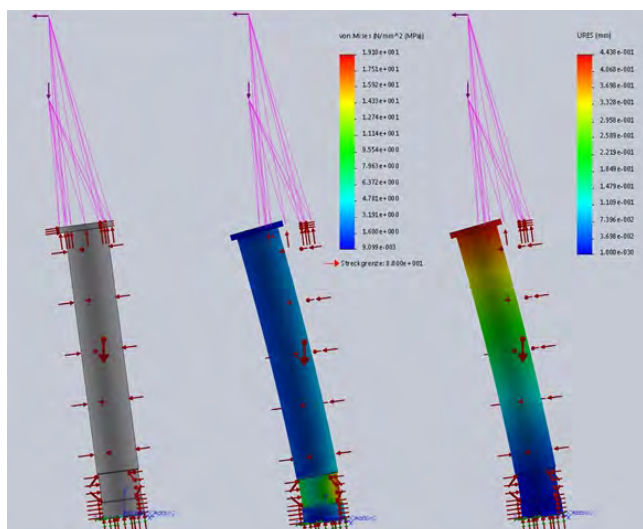


Figure 7: Stress simulations for the cryostat.

The highest sample temperature is limited to 420 K by the Cernox sensor, which is almost 100 K more than the standard MLZ cryostats currently used. This broadens the spectrum of application to new ferroic materials e.g. magnetocalorics, magnetic shape memories, etc. A further increase in the sample temperature up to 800 K will be possible using a dedicated sample stick with a thermocouple. The system integration of the cryostat is state-of-the-art, using the MLZ typical Taco middle layer for easy remote control, including remotely operated electromagnetic valves for evacuation/pressurizing of the sample space. The construction itself was rather difficult: the rather long and thin tail needs to be stable and able to withstand the forces from the cold head and the connected Helium tubes. The design was optimized by numeric calculations and examples are shown in Fig. 7. The first test experiment on POLI was performed in the autumn of 2015 and in the near future the cryostat will be introduced into routine operation and will be available to the users. On user request, further developments such as high electric fields, high temperatures, or magnetic fields will be considered.

Second, a new high temperature furnace was developed for SPHERES (Fig. 8). The MLZ standard High Temperature Furnaces (HTFs) are designed for temperatures up to approximately 2200 K, but are too bulky for the very restricted installation situation at SPHERES. For this reason, the sample environment group developed a furnace with small dimensions in the middle and lower section, with an overall external tail diameter of max. 130 mm



Figure 8: High temperature furnace for SPHERES.

(a factor 3 smaller than the standard), that can take in samples of 40 mm length and heat them up to more than 1673 K homogeneously. With the assistance of FEM simulation software, the effects of crucial design parameters were studied. This leads to a total of only three heat shields. In order to ensure good temperature distribution, a resistive heating element of 300 mm length and an inner diameter of 45 mm was chosen. As a result, the HTF can reach a temperature of up to 1873 K. The heating element of the furnace is powered by a DC power supply unit that provides a max. output current of 310 A. Temperature and temperature ramps can be set via an Eurotherm control unit. A thermocouple is used to measure the temperature of the sample. As the furnace is equipped with a water-cooling system, the water temperature as well as the water flow through the furnace are monitored and lead to automated shutdown of the furnace if the water temperature exceeds a certain value or when the water flow falls

below a particular rate. A sample of Cobalt was used for the first experiment at SPHERES where the hyperfine interaction in the ferromagnetic cobalt, which should set in at 1388K [1], was observed.

[1] Deka, S. et al. *Chemistry of materials* 16 (7), 1168-1169 (2004).

Bridging distances: the new UHV transport chamber

MARIA is a dedicated instrument for the neutron reflectometry of thin films. However, due to limited space, a UHV system for thin film growth and in-situ measurements cannot be installed on-site. Hence, up to now ultra-thin films, which are sensitive to ambient air, have been produced in the MBE system located in the thin film laboratory nearby and covered by protecting cap layers in-situ. However, these layers may change the physical properties of the sample, which is undesirable and prevents further manipulation of the sample, e.g. growth of additional layers.

Recently, we solved this problem by developing a handy mini UHV-chamber which is capable of both sample transfer and quasi in-situ measurements

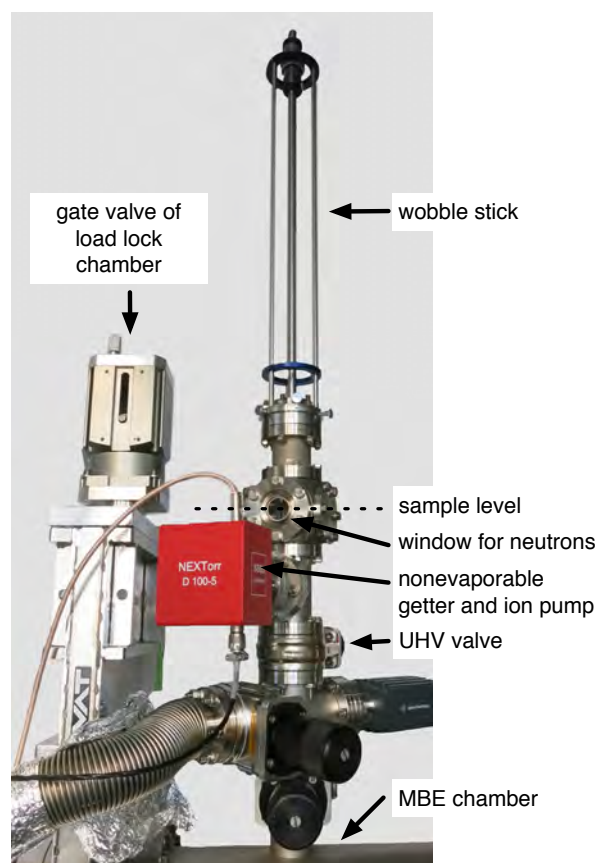


Figure 9: The mini transfer chamber attached to the MBE system.

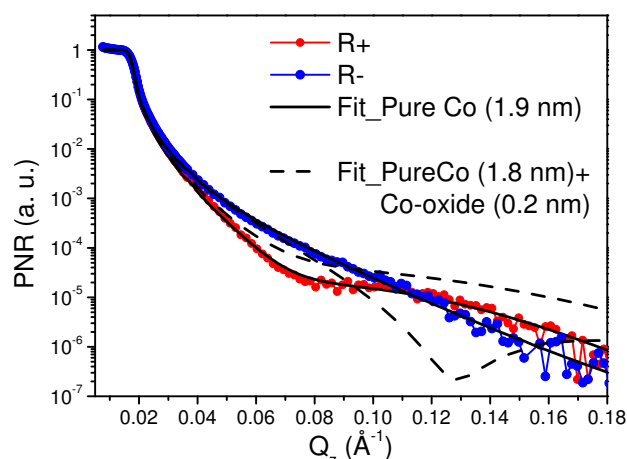


Figure 10: PNR data measured at MARIA reflectometer fitted for the nominal structure of Co(1.9 nm)/MgO(001) compared to a fit with Co oxide on top.

at the neutron reflectivity instrument, respectively. Quasi in-situ polarized neutron reflectivity (PNR) measurements can be performed at room temperature in magnetic fields of up to 600 mT at MARIA. Our solution consists of a DN CF-40 cube with two opposing sapphire windows for the neutron beam, a combined non-evaporable getter and ion pump to maintain the vacuum, a wobble stick, which is needed for in-situ sample transfer and also serves as a sample holder for samples of up to 1 cm², and a valve for sample exchange by mounting the chamber on the MBE system (Fig. 9).

The pressure in the transfer chamber is kept within the 10⁻¹⁰ mbar range during transport and PNR measurement. In Fig. 10 we present a first quasi in-situ PNR measurement on a Co thin film. Co thin films are sensitive to exposure to the atmosphere and change their magnetic behavior. A 21 Å thin film of Co was prepared in the MBE setup on MgO(001) and afterwards measured at MARIA at room temperature in a magnetic field of 300 mT in the Q-range up to 0.18 Å⁻¹. PNR has the advantage over bulk magnetization measurement techniques that it can measure magnetic moments very precisely and does not require correction of the substrate contribution as in the VSM or SQUID magnetometer. The magnetic field during the measurement was kept parallel to the polarization axis of the neutron beam. The separation of the spin up (R+) and spin down (R-) reflectivity near the critical edge allows one to calculate the magnetic moment per formula unit in the film. Fitting of the PNR data was performed by assuming a magnetically dead intermixed layer of

~0.5 nm at the interface of the Co film and MgO substrate. During the fitting, the nuclear scattering length density of the Co film was allowed to vary within 3 % of its theoretical value ($2.27 \cdot 10^{-6} \text{ \AA}^{-2}$). The fitting result indicates that the thickness of the Co film is ~1.9 nm with a reduced magnetic moment of ~1.2 $\mu\text{B}/\text{Co}$ atom. In order to confirm the reliability of the fit, we checked assuming an additional layer of Co oxide of different thicknesses (e.g. 0.2, 0.5, 1.0 nm etc.) on top of the Co film, but they did not fit the PNR data.

From the PNR data of the Co film and its fitting, we can categorically state that the Co film does not have Co oxide on top. So, samples which are delicate to handle in ambient conditions can be successfully measured using our handy mini UHV chamber. Booking access to the MBE system as well as the transport chamber is possible via the MLZ user office system, in combination with an application for beam time at neutron instruments such as MARIA.

Making GISAS simulations accessible

The Scientific Computing Group participates in workpackage 10 (data analysis software) of the EU INFRADEV project SINE2020, which began in October 2015. In an international division of tasks, MLZ assumed responsibility for evolving BornAgain into user-friendly reference software for simulating and fitting reflectometry, off-specular scattering and grazing-incidence small-angle scattering (GISAS). With this aim in mind, the following work was accomplished in 2015:

In January, we went public with BornAgain 1.0. As the release number indicates, this was the first version with a fully usable, stable simulation kernel. At the same time, the online documentation was mi-

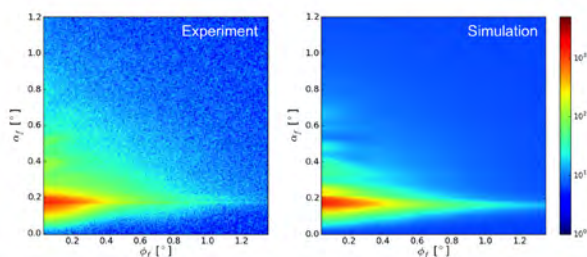


Figure 11: GISAXS experiment (GALAXI) and simulation (BornAgain) of Ag/PTFE/HMDSO nanocomposite. Samples have been produced by Dr. J. Kousal, Dr. O. Kylian and A. Kuzminova, Charles University of Prague, group of Prof. Biederman.

grated to the new web site www.bornagainproject.org. Since then, we have steadily expanded the tutorial, providing example scripts for all kinds of sample structures that can be modeled using BornAgain. The entire simulation layer is now accessible through application programming interfaces (API) for the programming languages C++ and Python, and through a graphical user interface (GUI). The Python API provides advanced users with full scripting capabilities. The GUI and the integrated collection of application examples provide an easier way to get started with BornAgain, especially for users who have little programming background. For each simulation set up in the GUI, it is possible to export a Python script. This helps users to move on from the GUI to the API utilization mode.

On top of the simulation layer, a fit layer provides ways to match the simulation to a measured detector image. So far, this layer is only accessible from C++ and Python. In 2016, the GUI will be enhanced to provide full coverage of one- and two-dimensional fitting.

For the experimental validation of BornAgain, a set of metal/polymer nanocomposite samples with increasing complexity was investigated using GISAXS at the high-brilliance diffractometer GALAXI (Jülich, courtesy of Emmanuel Kentzinger), and using X-ray reflectometry in the MLZ materials science lab (courtesy of Armin Kriele and Ralf Gilles). Fig. 11 shows the excellent agreement between measured and simulated GISAXS images.

Time-of-flight data reduction

As reported last year, after long deliberation we took the decision to base all data reduction for time-of-flight instruments on the software platform Mantid. Mantid, developed since 2007 by ISIS and SNS, has by now more than 2 million lines of code and contains over 700 algorithms for data reduction and analysis. This makes Mantid somewhat difficult to use, but also provides an unprecedented opportunity for code reuse.

In 2015, we continued the two projects begun in 2014: to bring Mantid to TOFTOF and DNS. The TOFTOF project has essentially been completed; the new workflow will become default in the next reactor cycle. The raw data reduction can be con-

trolled either through Python scripts or through a GUI. The underlying algorithms are in part generic, in part instrument-specific as contributed by us. All algorithms are covered by automatized tests that ensure stability even if the Mantid core evolves.

As far as DNS is concerned, Mantid support is ready for diffraction mode. We have developed special algorithms that reproduce the functionality of the legacy software *dnsplot*, and resolved some issues encountered in that program. The algorithms have been validated against *dnsplot*, and are now being tested by internal DNS users. In 2016, we will continue to work on the graphical representation of single crystal diffraction data, and implement Zorn's multiple scattering correction of polarized diffraction data. The data reduction workflow for time-of-flight data from DNS and TOPAS is now being developed in close collaboration with the instrument scientists.

Multiple-scattering simulation for neutron backscattering

Our software for simulating multiple scattering contamination in neutron backscattering spectra is basically complete. In applying it to exemplary data we realized, however, that simulations should not be trusted unless the input comprises reliable values of the temperature-dependent total transmission. In the future, SPHERES will be equipped with a transmission monitor that provides this input.

Update on Organizational Software

At the beginning of the year, a commercial absence management service portal was put into action. Every staff member of FRM II now has access to the portal, where one's own absences as well as the absences of group colleagues can be viewed.

The „ORG-SOFTWARE“, which originally became available in 2014, has been expanded with the new module „Änderungsanzeigen“ (notices of change). It allows users not only to perform data management and effective data monitoring as before, but also to create, save, modify and reuse their own database queries and personalized settings.

The „Kontenverwaltung“ (account management) is now equipped with new features. These include amongst others: monitoring the business trips of the FRM II staff as well as a comprehensive budget and

cost control for FRM II accounts. The web interface of the „Kontenverwaltung“ was updated accordingly. Those responsible for the budget can gain an overview of all expenses on their accounts, manage orders and view data on the business trips of their groups.

Sample preparation and analysis for Materials Science

The Materials Science Lab at MLZ serves as a laboratory for the preparation of samples (polishing, cutting, chemical treatment and annealing) for subsequent neutron scattering measurements and provides several analytic instruments, for instance X-ray Diffractometer (XRD), Differential Scanning Calorimeter (DSC), Micro-Hardness and Optical Microscopes to perform complementary analytics.

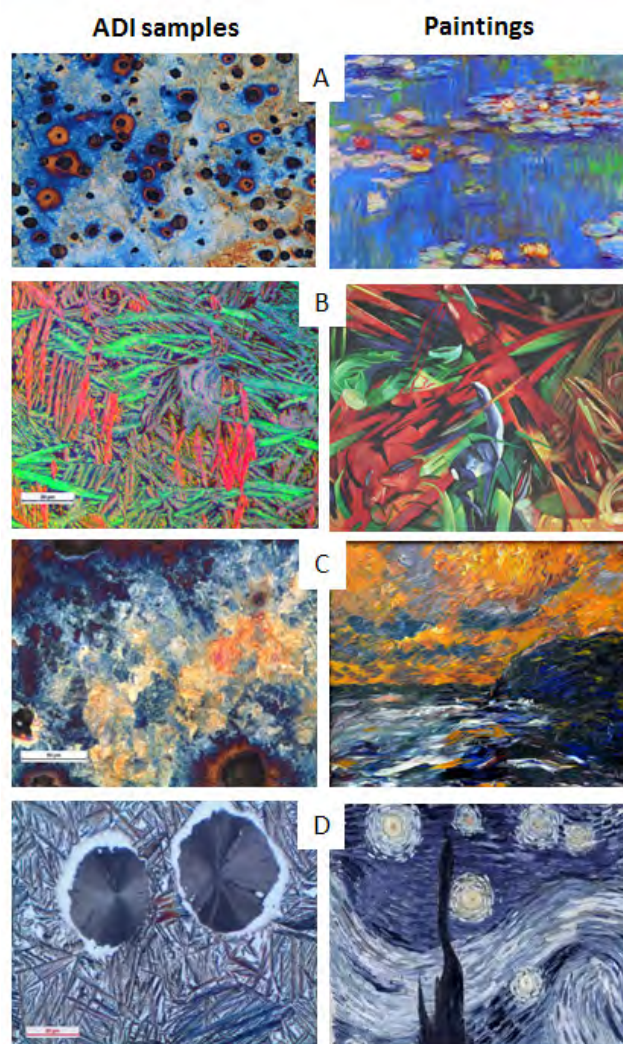


Figure 12: Micrographs of polished and etched ADI samples showing (A) martensitic texture vs Water Lilies from Claude Monet, (B) austempered ductile iron needles vs The fate of animals from Franz Marc, (C) perlitic texture vs Autumn sea from Emil Nolde and (D) ADI texture with spherical graphite vs Star night from Vincent v. Gogh.

The lab is open to all users of FRM II, including external guests. In 2015, the lab was used by guests more than 700 times, which is the result of the aim of the staff responsible to make access to the lab as easy as possible and to run all instruments efficiently 24 hours a day, 7 days a week.

As an example to illustrate the potential of the lab's capabilities, we present here the results of the Master's Thesis of Hyun-Suk Jung (Institute of Metal Forming and Casting, utg), an external user of the lab, who studied Martensite in Austempered Ductile Iron (ADI) using Optical Microscopy and X-Ray Diffraction (XRD).

ADI samples were heat treated with different temperature histories to obtain multiphase ausferritic texture with different volume fractions of acicular ferrite, spherical graphite and residual austenite. The metastable austenite can be transformed into martensite by plastic deformation which will change the rigidity, hardness and ductility of the material.

Various wet chemical etchants were applied on polished samples to obtain micrographs to visualize the formation of martensitic needles after mechanical compression. Some of these micrographs are amazing, akin to famous paintings by Monet, Marc, Nolde and v. Gogh. (Fig. 12) Subsequent Micro-hardness

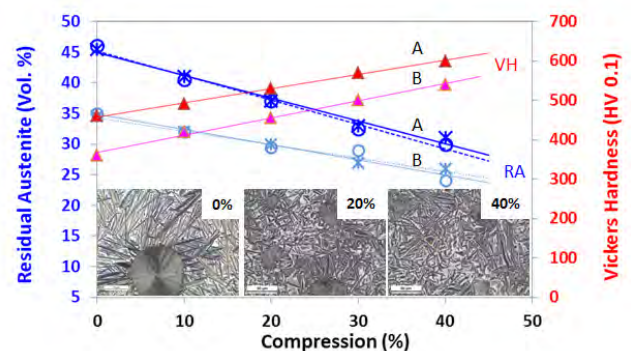


Figure 13: Residual Austenite volume content and micro-hardness of two ADI samples pre-treated at different temperature pathways after mechanical compression. The optical micrograph insets show the degradation of the acicular ferrite and spherical graphite due to plastic deformation.

and XRD measurements were performed to analyse the hardness and phase constitution. From the XRD results, the content of the residual austenite was calculated and compared to results obtained from magnetic saturation measurements using the Joch-Isthmus technique. It can be shown that the content of martensite increases linearly, whereas the volume fraction of residual austenite decreases linearly with the ratio of compression, respectively (Fig. 13). Results gained from XRD and Joch-Isthmus measurements are in a good agreement. Consequently, the hardness of the material increases under compression, which makes the material suitable for high performance applications.

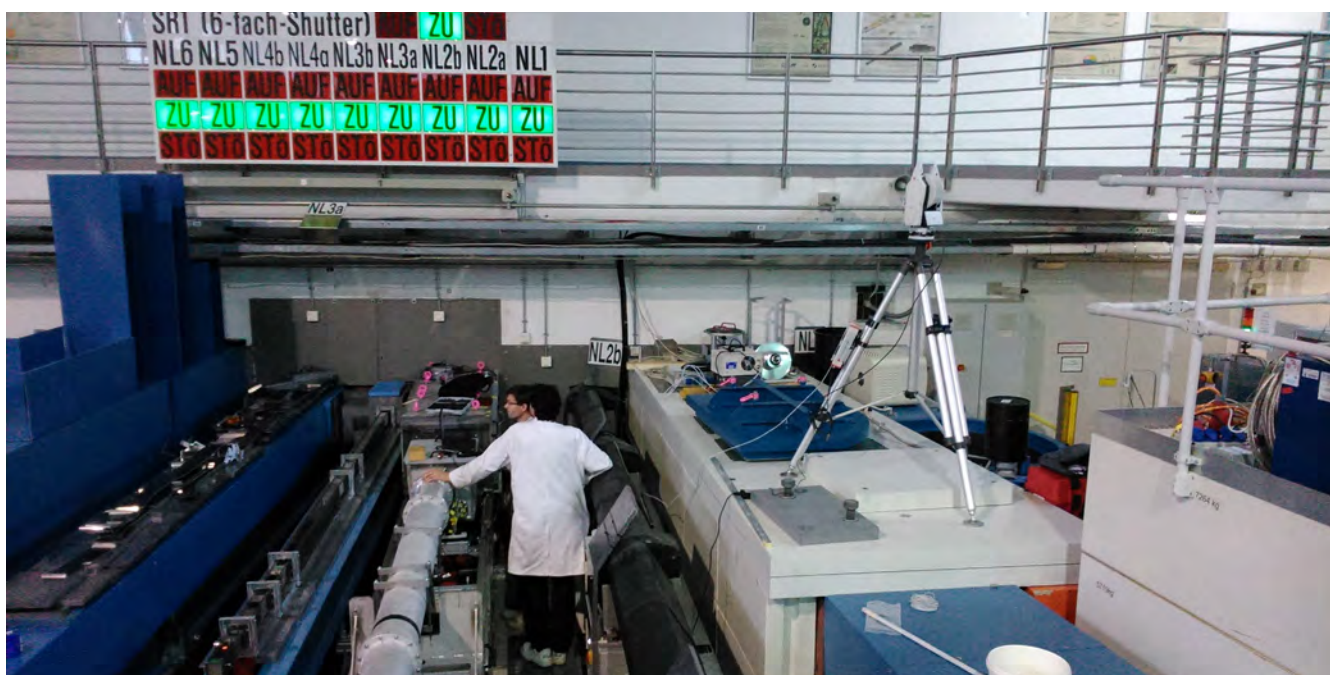
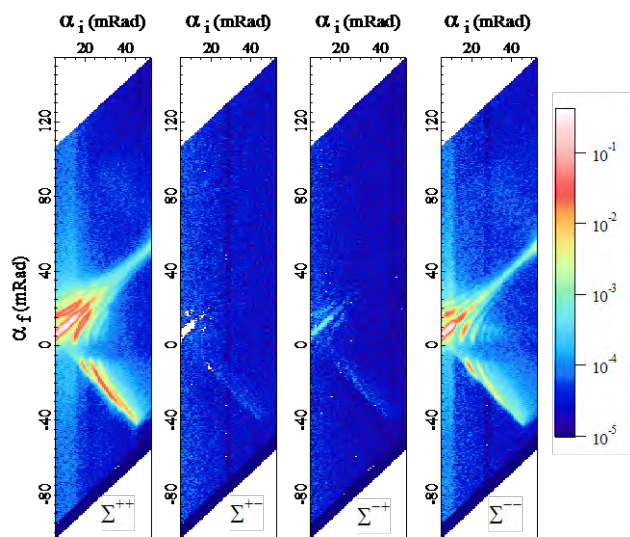
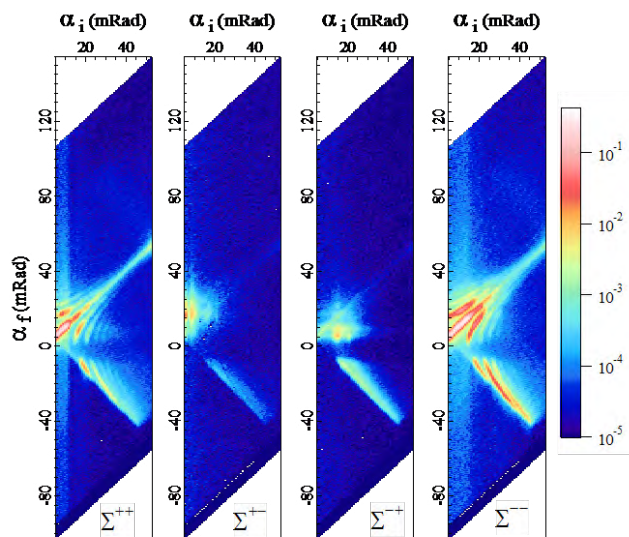


Figure 14: Repositioning of NL3-a guide elements during an instrument upgrade at KWS-2.



Polarization corrected, saturated sample at 0.7 T



Polarization corrected, remanent magnetization of sample

Figure 15: An example to show data corrections. Data was obtained on a Fe58Fe superlattice grating produced by K. Temst (KU Leuven) and loaned by A. Wildes (ILL). Data displayed are the cross sections Σ , corrected for the polarizing analyzing power of the instrument (a 10 Å incident wavelength was used).

Guides and Polarizers

Once more, the Neutron Optics group's in-house production capabilities have been crucial to successful instrument operation. A failure at the guide NL6-S between the instruments DNS and Spheres was repaired at very short notice. Furthermore, the ongoing project of guide refurbishment has been advancing. In summary, a total length of 35 m of neutron guide elements with state-of-the-art quality has been produced. The alignment and adjustment service is of ever-increasing importance. Fig. 14 shows the team at the neutron guide NL3-a, where the neutron guide had to be removed for an instrument upgrade. Very precise repositioning here was achieved by means of a Lasertracker system.

Another success story is the HELIOS facility. In 2015, more than 100 cells with highly polarized ^3He gas were provided for different instruments at the MLZ. During this period, the gas polarization at HELIOS was kept very stable at a level as high as 82 %, thus allowing researchers to perform a highly-efficient neutron polarization analysis both for cold (SANS-1, REFSANS and PUMA) and hot (POLI) neutrons. While at POLI the ^3He cells are routinely used in user experiments, the application of the cells at other instruments served as a basis for the testing, refinement and calibration of polarizing hardware. Precise calibration is possible because very high (nearly 100 %) neutron polarization and spin-flip efficiency can be achieved using such highly polarized ^3He gas.

Polarization Analysis on MARIA

The JCMS operates and develops neutron spin filters ^3He NSF for polarized neutron instrumentation based on the spin-exchange optical pumping SEOP technique. Notably, a completed in-situ SEOP polarizer was developed and put into continuous operation on MARIA for the 2015 reactor cycles, providing stable polarization efficiency over the experimental time. This device offers large angular coverage of around $\pm 5^\circ$ provided by a 12.5 cm inner diameter

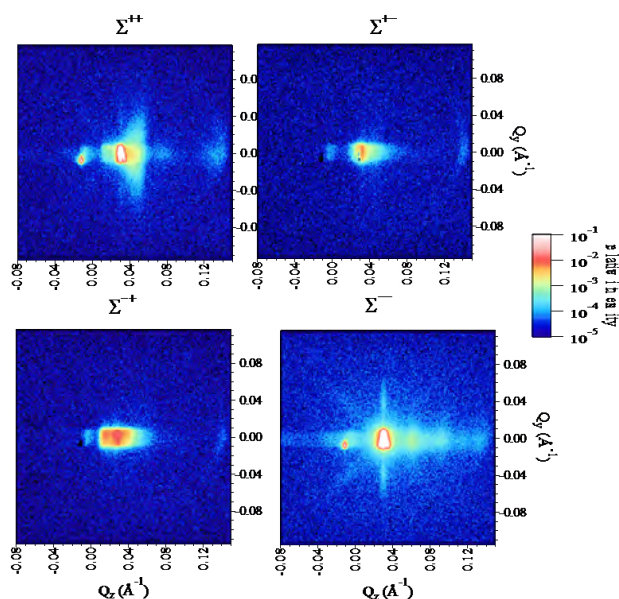


Figure 16: Polarized GISANS data from a FeCo super mirror at an angle of 1° . Polarized GISANS can give information on the nature of lateral correlations and grain structure of the layers, as well as on the roughness between the layers, separating the magnetic from non-magnetic portions. Data was taken during MLZ experiment 10100, from E. Kentzinger. This data is also corrected for analyzing and polarizing power of the instrument.



Figure 17: Left, a photo of a doughnut shaped cell “Homer” for PASTIS testing made of GE180 produced in FZ-Jülich by P. Pistel (glassworkshop ZEA-1 FZ Jülich) which has 0.5 bar ^3He gas and a 1074 hour relaxation time. Right, a C-shaped cell that has uniform path length for wide-angle neutron scattering experiments, the “Marge” cell has a 120° coverage and a 160 hour relaxation time with a fill pressure of 1.1 bar of ^3He gas.

spin filter cell that rests only 50 cm away from the sample position inside the MARIA sample magnet. During 2015, several polarization analysis experiments were performed with the system, which required very little maintenance. The analysis of data has been developed such that the data can be corrected for imperfections in the neutron polarization and analyzing power of the instrument. Thus, one obtains the cross sections separately for spin-flip and non-spin flip scattering. Access to use of the full polarization analysis is available through the MLZ proposal system for the MARIA instrument.

Similar polarization analysis systems using ^3He are under development for the KWS-1 and KWS-2 small angle scattering diffractometers, and as an incident beam polarizer for the TOPAS thermal time-of-flight neutron spectrometer to be constructed in the new east guide hall. More exciting news from these systems is expected as they are developed further and are tested and put into operation. TOPAS has the additional drive to use a ^3He NSF for analysis too:

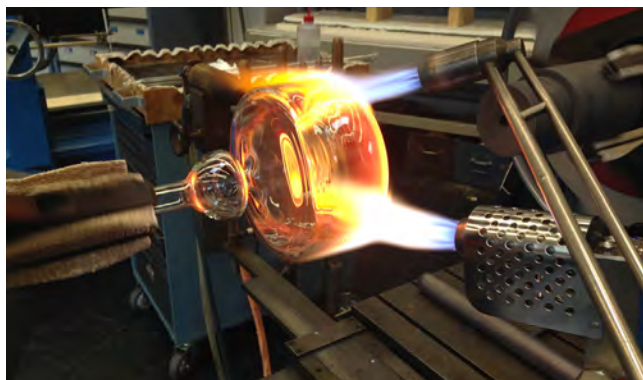


Figure 18: Here the glass blower is forming a large angle banana-shaped cell on the glass blower's lathe. Two hydrogen torches are used to reach the required temperatures and uniformity of the heating. At this stage the outer diameter of the cell is ~ 24 cm and the cylinder ~ 10 cm long.

details of TOPAS and this so called ‘magic-PASTIS’ system are detailed in the TOPAS section of this report.

Wide angle banana-shaped

^3He Neutron spin filter cell development

We have constructed all-blown GE180 wide-angle ^3He spin-filter cells (Fig. 17). Such cells are unique “firsts”, and result from the collaboration between NIST and JCNS. GE180 is chosen because of its suitability for good ^3He T1 relaxation times, neutron compatibility, and the fact that it is the best known material for use in SEOP polarization of the ^3He gas. However, this glass requires special attention from the glass-blower in order for it to be formed into large cells. We routinely produce large diameter cylinders, up to 13 cm O.D., and one such cell is used for analysis on MARIA. The banana shaped cells, however, are even bigger at the outset. C-shapes are formed by first blowing a large cylinder of up to 24 cm O.D. which then has a hole “pushed” through the ends to make a doughnut (Fig. 18). The C-shape is then completed by sealing off sections to make a cell with the desired angular coverage. Such analyzer cells are destined to be used for polarization analysis on neutron spectrometers with large angular-area detector arrays such as DNS or TOPAS, which is being constructed for the new neutron guide hall east of the MLZ.

Extending to the East (Infrastructure)

In order to supply the new neutron guide hall east (UYM) with neutrons, one very demanding task is the replacement of the existing plug JMA05 by a new one that complies with the latest requirements. After some years of planning, preparation and obtaining approval, this project is now scheduled to be realized in spring 2016.



Figure 19: Setup for cold tests of the replacement of plug JMA05.

For this - as one of several important subprojects - a setup for cold tests of the replacement of plug JMA05 was completed in spring 2015 within UYM (Fig. 19) where cold tests are now performed regularly.

In parallel, the hot phase within the experimental hall (UJA) began in December 2015 with the removal and partial disposal of the Instrument TRISP in order to gain the necessary working space (see Fig. 20). Subsequent to this, the setup for the replacement of plug JMA05 will be installed in UJA and - after final cold tests within UJA - it will be possible to embark on the plug exchange.

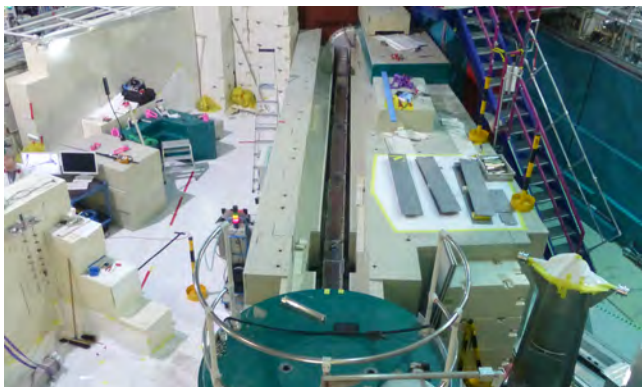


Figure 20: The instrument TRISP after removal of its neutron guides.

A further milestone, this time concerned with the operational readiness of the new instruments in UYM, will be the provision of the technical infrastructure (e.g. cooling water, pressurized air). For this, the existing systems (e.g. cooling water FAK-40), which up to now have only been used to supply the instruments in the neutron guide hall west, will be extended to UYM. Here, the technical and regula-

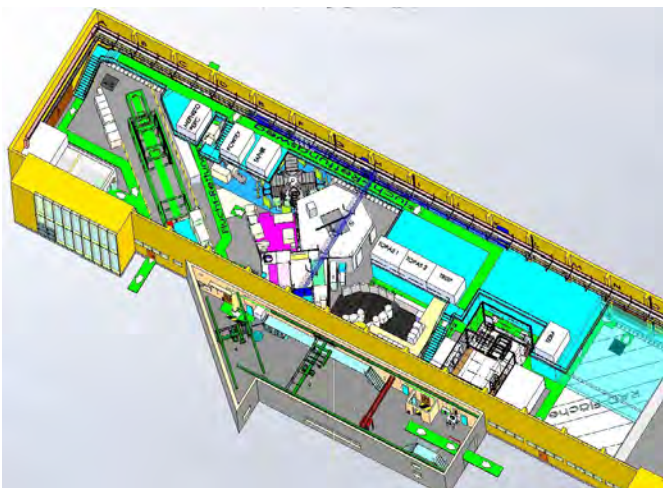


Figure 21: Artists view into the neutron guide hall east.

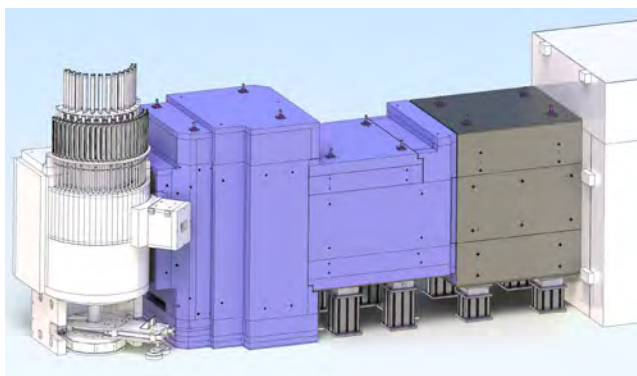


Figure 22: Shielding design for KOMPASS.

tory planning for these extensions is now in place, and the systems can be installed after application to and approval from the authorities. Fig. 21 shows the present 3D planning guide for the build-up of the instruments and technical infrastructure in UYM. This is our central base for coordinating with the planning and construction companies and with the new instruments and helps to identify and eliminate possible problems at an early stage.

In addition, to highlight briefly one of our instrument specific contribution, the support provided in building the new instrument KOMPASS through the development of pre-design and of detailed design for mechanical structures (e.g. lifting unit for the velocity selector) and for radiation shields (see Fig. 22) is worthy of mention. Since KOMPASS is located immediately after the instrument N-REX and also uses the same neutron line, one of the very demanding tasks within this project was to implement the instrument requirements taking into account the narrow space and the existing connection boundaries. Currently the manufacturing of most of the parts for the radiation shields has been completed and their assembly is work in progress (Fig. 23).



Figure 23: Assembly of the radiation shields for KOMPASS.

Support for the MLZ from Jülich: Engineering and Electronics

R. Hanslik¹, D. F. Förster¹, C. Tiemann¹, H. Kämmerling¹, S. Keuler², R. Bruchhaus³

¹Central Institute of Engineering, Electronics and Analytics, Engineering and Technology (ZEA-1), Forschungszentrum Jülich GmbH, Jülich

²Central Institute of Engineering, Electronics and Analytics, Electronic Systems (ZEA-2), Forschungszentrum Jülich GmbH, Jülich

³Jülich Centre for Neutron Science (JCNS) at MLZ, Forschungszentrum Jülich GmbH, Garching

Experts from the Central Institute of Engineering, Electronics and Analytics (ZEA) based at the Forschungszentrum Jülich provide considerable manpower and expertise to support and drive neutron scattering instrument improvement and operation at the MLZ. In 2015, key projects included the construction, manufacture and installation of the new chopper for the spectrometer SPHERES and the installation of the high-vacuum chamber of the time-of-flight spectrometer TOPAS. The new detector for the small-angle neutron spectrometer KWS-2 was commissioned, and for SAPHiR the detector group delivered highly advanced scintillation detector segments. A very challenging masterpiece of equipment manufactured in Jülich was the new three channel beam plug for the beamtube SR5, which is the key component in supplying the guide hall east with neutrons for four new instruments in the future.

A considerable workforce dedicated to supporting and driving neutron scattering instrument improvement and operation at the MLZ is located at the Forschungszentrum Jülich, in Jülich. The Central Institute of Engineering, Electronics and Analytics, Engineering and Technology (ZEA-1) includes groups of expert engineers for design and construction. In addition, it operates workshops in which everything, from tiny μm -sized parts up to heavy weights of several tons, can be precisely machined, handled and assembled. The Central Institute of Engineering, Electronics and Analytics, Electronic Systems (ZEA-2) specializes in preparing customized control electronics and software as well as detector solutions for the neutron scattering instrument suite at the MLZ. These groups of skilled experts and the large-scale infrastructure are key for enhancing the performance of the neutron scattering instruments

and to meet the requirements that arise from the challenges in the different scientific fields.

In terms of engineering, key projects in 2015 included the manufacturing, assembly, testing and on-site installation of the new chopper for the backscattering spectrometer SPHERES as well as the manufacturing of the new beam plug for the beam tube SR5 which will supply the new instruments in the guide hall east with three neutron beams. The installation of the vacuum chamber of the time-of-flight spectrometer TOPAS also made considerable progress in 2015. After a major upgrade of the key components and instrument control software, the diffuse neutron scattering spectrometer DNS was transferred back into user operation in 2015. ZEA expertise was a key enabler of this successful upgrade.

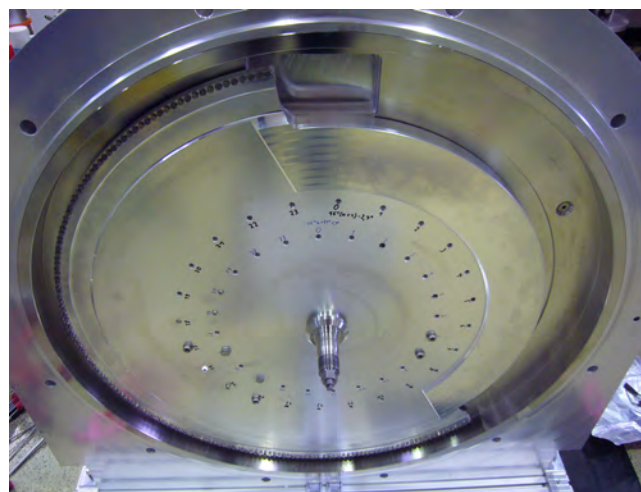


Figure 1: The new one-wing chopper disk with a radius of 43 cm.

Engineering

A sophisticated piece of equipment installed in 2015 is the new phase space transform chopper at the instrument SPHERES (Spectrometer for High Energy RESolution). It was mechanically a big challenge to bring an optimized one-hole geometry, as compared to the previously used three-hole geometry of



Figure 2: New plug for beam tube SR5, a highly engineered heavy weight of steel, concrete and advanced shielding.

the old chopper into operation. Careful simulations of the mechanical stability of the housing under the boundary conditions of the desired speed of 225m/s at the edge of the chopper disk were performed. Special care was taken to optimize the balancing of the disk to achieve an operation at very low vibration levels. Extensive testing over several weeks at the ZEA-1 chopper laboratory in Jülich has proven reliable operation for the experiments at the MLZ, Fig. 1. The last step of this project included the transport and installation of the chopper in the guide hall at the MLZ. The efforts of the teams involved at ZEA-1 were rewarded by a doubling of the neutron intensity at the sample and an improvement of the signal-to-noise ratio of 10 %, which is a considerable benefit for the experiments of the scientific users. Now, the instrument SPHERES with its brand new chopper has been transferred back into user operation.

The key project for the MLZ in terms of instrumentation is the installation and operation of, in total, six more instruments in the guide hall east. Four out of these six instruments need to be supplied by three beams of thermal neutrons from the beam tube SR5. For this, the existing plug with two channels

needs to be replaced by a new plug with three channels. The function of the plug is twofold. In the open position, the neutrons can pass through the guides to the instruments. In the closed position, the plug serves as a shutter which provides the necessary shielding effect to secure safety at the guides and the instrument site. The construction, manufacture and assembly are very demanding tasks since the position of the plug is very close to the core of the neutron source. Many steps require approval from the authorities and the Technischer Überwachungsverein (TÜV) as the consultant body. The plug was designed and manufactured by ZEA-1 in 2015. Essential for the success of this very sophisticated task was very close collaboration between the reactor operation team, more specifically with the quality control of the FRM II, and the FRM II infrastructure team in Garching. Meanwhile, the heavy weight plug totaling 12 tons of high-density concrete, steel and shielding materials was moved, dismantled into two parts, to the MLZ in Garching, Fig. 2. The infrastructure team will now take over and perform the plug replacement in 2016.



Figure 3: TOPAS high vacuum chamber in the guide hall east during leak testing.

Another heavy weight of 31 tons and a massive project was the transfer and installation of the high-vacuum chamber of the time-of-flight spectrometer TOPAS. The chamber was successfully assembled and carefully tested in the ZEA-1 workshop in Jülich before a heavy goods transport to the MLZ was organized at the beginning of 2015. The three main parts were then assembled in the guide hall east, Fig. 3. Special care was taken to position the center of the chamber at the point where the neutron beam was expected to leave the beam tube SR5. The final step of the work on-site at the MLZ in 2015 was the successful vacuum test of the chamber which reproduced excellent values from earlier tests in Jülich. The chamber has now been made ready for the assembly of the detector tube holders and detector tubes, which will be undertaken in 2016.

Electronics

For the upcoming instrument SAPHiR (Six Anvil Press for High Pressure Radiography and Diffraction), the ZEA-2 detector group developed and delivered four detector segments with an area of $\sim 0.5 \text{ m}^2$ each and a spatial resolution of $\sim 2.5 \text{ mm}^2$ in cooperation with the Bavarian Research Institute of Experimental Geochemistry and Geophysics, Fig. 4.

The detector segments are based on a LiF/ZnS Scintillator with Wavelength-Shifting-Fibers (WLSF) which guide the light from the scintillator to the readout PMT modules. A central readout electronics is connected to a computer based data acquisition system. Later, this DAQ will be integrated into the instrument control.

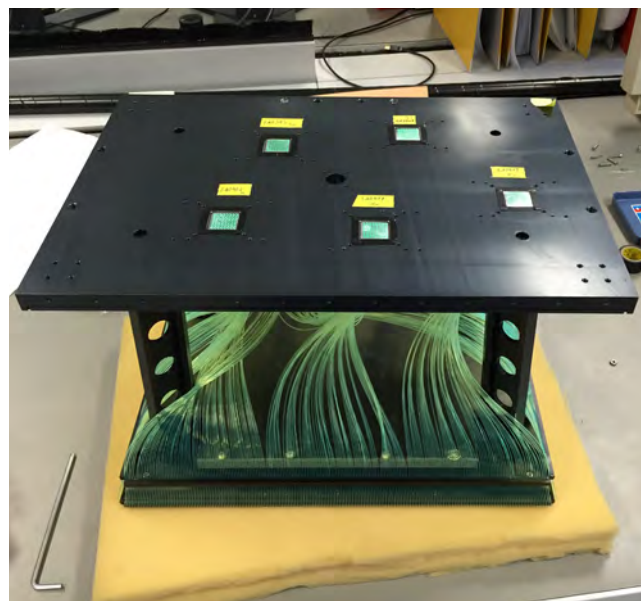


Figure 4: Wavelength-Shifting-Fiber (WLSF) based detector segment for SAPHiR connecting the WLSF and the five Multi-Anodes Photomultiplier Tube modules which are used for the readout.

Another main topic was the preparation for the successful commissioning of the new GE-Reuter Stokes ^3He detector at KWS-2. Working in close collaboration, the electronics group at the MLZ and the ZEA-2 software team supported the factory acceptance test as well as implementing the software control. First successful tests were performed in Jülich on a detector module supplied in advance by the manufacturer. The respective network data packages are histogrammed on the fly and the resulting histograms are forwarded by a Taco server to the C-PCI detector system using the existing software interface and instrument control software. The new Taco server supports standard, real-time and time-of-flight (ToF) DAQ modes. Furthermore, the interaction with the SPS was newly implemented in order to switch off the high-voltage supply before the detector drives in the tube, and use heart beat UDP packages for synchronisation.

The vacuum system connecting KWS-1, KWS-2 and SANS-1 was successfully commissioned. A manual and an automatic mode are implemented using a system consisting of two Pfeiffer pumps. Switching between the modes and the configuration of the vacuum thresholds can easily be done using the graphical touch panel as well, Fig. 5. Depending on the vacuum level, either one or both pumps are activated. In order to assure continuous operation at all three instruments, the software automatically identifies a poor vacuum level. Subsequently, it is able to interrupt the pumping of an instrument with a better level and, thus, improve the vacuum level of the other instrument.

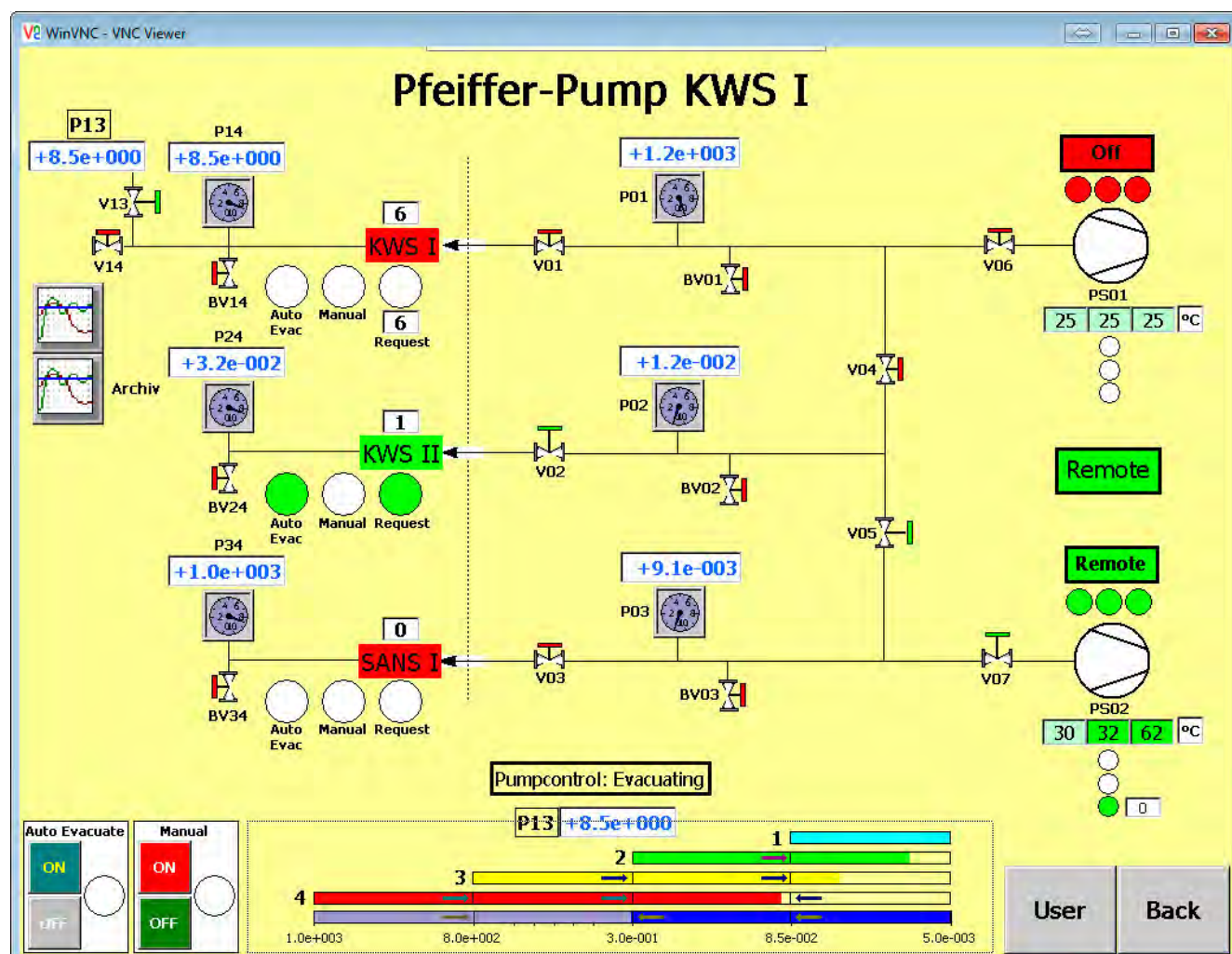
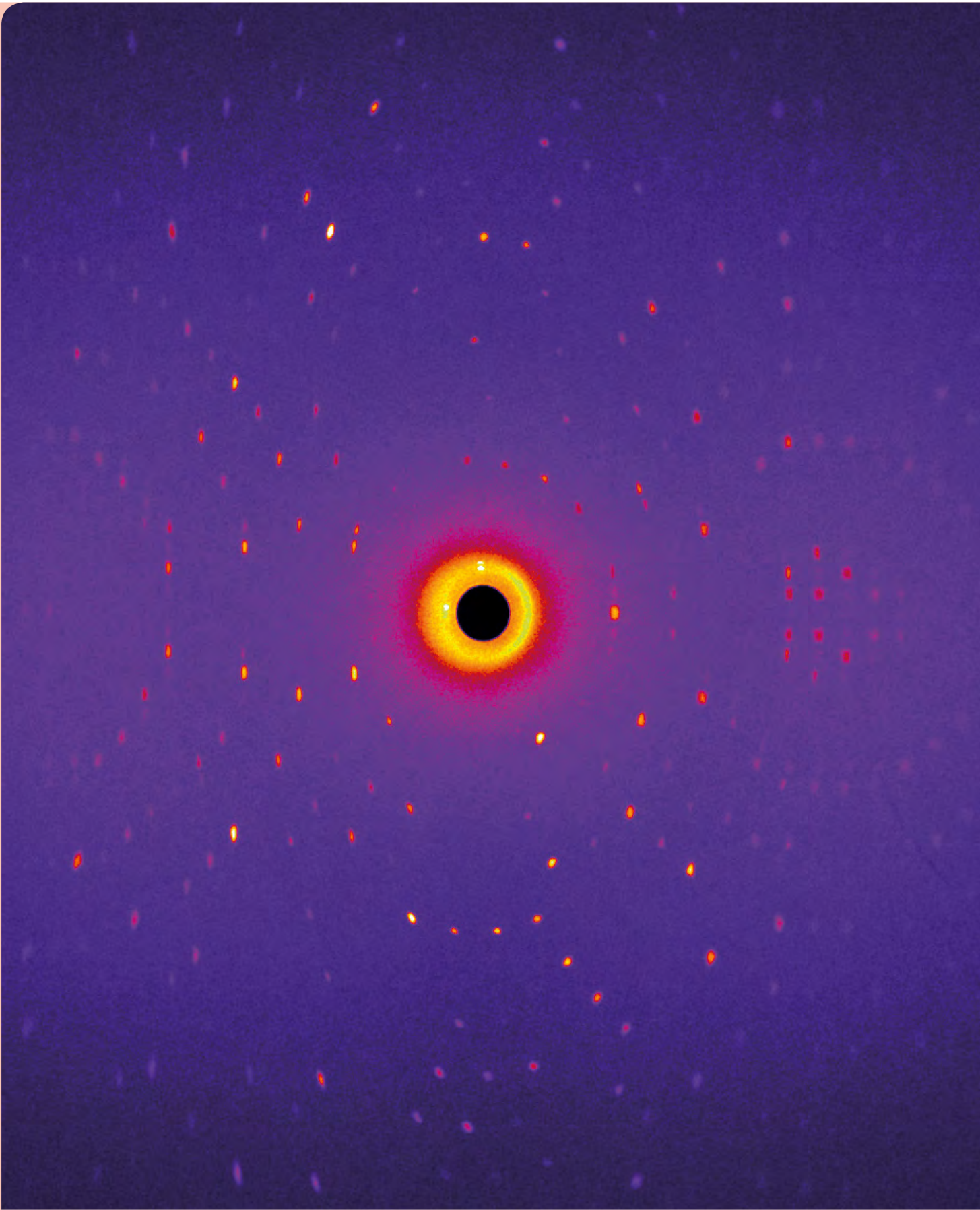


Figure 5: Overview of the vacuum system control touch panel for the three instruments KWS-1, KWS-2 and SANS-1.

Neutron diffraction pattern of an enzyme crystal measured at the instrument BIODIFF. The enzyme under investigation was a glycoside hydrolase which catalyses the decomposition of complex carbohydrates, an important step in the production of biofuels (for more information see pages 92 & 93).



Scientific Highlights

Static and quasi-elastic properties of the spiral magnet $\text{Ba}_2\text{CuGe}_2\text{O}_7$ studied by NRSE spectroscopy

S. Mühlbauer¹, J. Kindervater², W. Häußler^{1,2}

¹Heinz Maier-Leibnitz Zentrum (MLZ), Technische Universität München, Garching, Germany

²Physik-Department, Technische Universität München, Garching, Germany

We provide a novel route for using elastic and quasi-elastic neutron spin echo spectroscopy (Larmor labeling) for a unified approach to the study of both the static and dynamic properties of incommensurate magnetic structures with small propagation vectors. The archetypal non-centrosymmetric spiral magnet $\text{Ba}_2\text{CuGe}_2\text{O}_7$ serves as a model system for our study. We show how Larmor labeling can efficiently decouple instrumental wavelength-resolution and effective Q-resolution and give high precision access to the structural properties of the incommensurate domains of $\text{Ba}_2\text{CuGe}_2\text{O}_7$.

Properties of incommensurate spiral magnetic structures

Spiral magnetic structures have aroused great scientific interest over the last decade, not only due to their multiferroic [1] and topological properties [2]. The phase transition into spiral magnetic phases can be of special interest [3]: If critical magnetic fluctuations soften at finite momentum transfer, an otherwise 2nd order phase transition may be driven first order. This scenario, recently found to be substantiated in the helimagnet MnSi [4], is relevant for incommensurate magnetic structures in general. As the Brazovskii scenario is exclusively based on phase space considerations, it is an interesting open question as to whether it is also applicable to systems with lower dimension.

A possible candidate for such considerations is the non-centrosymmetric tetragonal antiferromagnet (AF) $\text{Ba}_2\text{CuGe}_2\text{O}_7$ ($P\bar{4}21m$), which shows an incommensurate spiral magnetic structure, provided by the Dzyaloshinskii-Moryia interaction. Below $T_N=3.2\text{K}$ and at zero magnetic field, neutron diffraction has established an incommensurate, almost AF cycloidal magnetic structure in the (a, b)-plane

with $\xi = 0.0273$ (see Fig. 1). Four magnetic satellite reflections indicative of two degenerate magnetic domains are observed at $(1\pm\xi, \pm\xi, 0)$, centered at the AF Neel point $(1,0,0)$ [5, 6]. The phase transition from paramagnetism to spiral long-range order is characterized by an interplay of 2D physics and Brazovskii correlations. In a magnetic field, $\text{Ba}_2\text{CuGe}_2\text{O}_7$ exhibits a multitude of different incommensurate magnetic structures, hints for weak FM behavior and weak ferroelectricity [5, 6, 7, 8].

Larmor labeling and NRSE spectroscopy on incommensurate magnetic structures

In a text-book experiment, we show how neutron Larmor labeling on the NRSE spectrometer RESEDA @ MLZ can be used for a close examination of the magneto-structural properties of the incommensurate spiral magnetic structures of $\text{Ba}_2\text{CuGe}_2\text{O}_7$ [9]. Moreover, we report on first quasi-elastic measure-

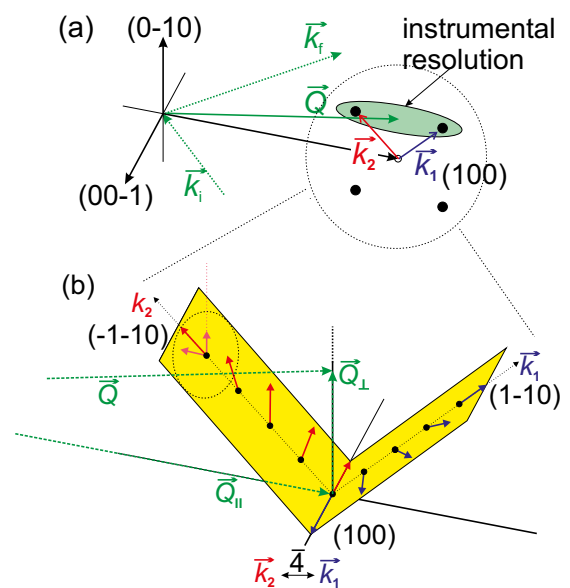


Figure 1: (a): Schematic depiction of the experimental setup: The momentum transfer Q is aligned almost parallel to $(1,0,0)$ along $(1\pm\xi, \pm\xi, 0)$. The instrumental resolution is given by the shaded green ellipsoid. (b): Illustration of both AF cycloidal magnetic domains of $\text{Ba}_2\text{CuGe}_2\text{O}_7$ with propagation vectors $(\pm 1, -1, 0)$. For clarity, only one sublattice is drawn. Both domains are related by the symmetry operation $\vec{4}$.

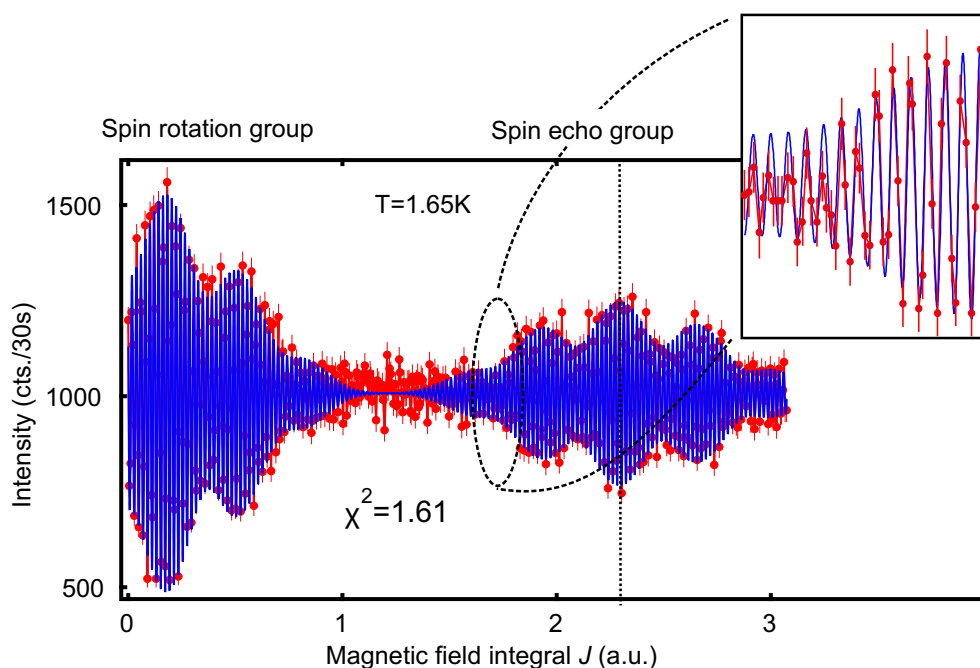


Figure 2: Elastic spin rotation signal and spin echo signal, recorded at a temperature of $T = 1.65$ K and for a spin echo time of $\tau = 0.08$ ns. Red data points correspond to the measured points. The fitted model is shown in blue. The inset depicts a zoomed version of the recorded data points and the corresponding fit function.

ments where we study the linewidth of the diffraction peaks associated with the decay of the cycloidal magnetic order upon crossing T_N .

To this end, we calculate the general case of elastic and quasi-elastic neutron spin echo measurements from incommensurate helical, cycloidal and elliptical magnetic structures with polarizing properties: As the resolution in Q space of a typical neutron spin echo spectrometer is limited by the velocity selector generally used on such instruments, the interference effects that arise due to the overlap of multiple incommensurate domains have to be considered. A characteristic beating of the spin echo signal as a function of the precession field is expected from theory.

When applied to the special case of $\text{Ba}_2\text{CuGe}_2\text{O}_7$, the characteristic beating of the spin echo signal as a function of the precession field is accurately confirmed by our experiment (see Fig. 2). This beating allows for efficient decoupling instrumental wavelength-resolution and effective Q -resolution and gives precise access to the structural properties of incommensurate domains. Looking at quasi-elastic measurements of the diffraction peaks associated with the cycloidal spin spiral of $\text{Ba}_2\text{CuGe}_2\text{O}_7$, we find hints for a broadening of the linewidth at T_N whereas below T_N , no dynamic processes are observed [9].

We have shown experimentally and theoretically that a characteristic beating of the spin rotation and spin echo signal, which is caused by the polarizing properties of the sample, allows for precise measurement of the incommensurate propagation vectors otherwise inaccessible by instrumental resolution. Our study introduces a way of using this Lamor labeling technique on neutron spin echo spectrometers as a general approach for the investigation of the structural and quasi-elastic properties of incommensurate magnetic structures of different kinds. It is worth noting that the limitation to samples with polarizing properties can be avoided by the installation of an additional neutron polarizer after the sample region. However, tight technical restrictions apply to the neutron polarizer used for this purpose, as the flight path of the neutrons must not be affected.

- [1] M. Mostovoy, *Phys. Rev. Lett.* 96, 067601 (2006).
- [2] S. Mühlbauer et al., *Science* 323, 5916, 915 (2009).
- [3] S. A. Brazovskii, *Sov. Phys. JETP* 41, 85 (1975).
- [4] M. Janoschek et al., *Phys. Rev. B* 87, 134407 (2013).
- [5] S. Mühlbauer et al., *Phys. Rev. B* 84, 180406 (2011).
- [6] S. Mühlbauer et al., *Phys. Rev. B* 86, 024417 (2012).
- [7] H. Murakawa et al., *Phys. Rev. Lett.* 103, 147201 (2009).
- [8] J. Chovan et al., *Phys. Rev. B* 88, 064421 (2013).
- [9] S. Mühlbauer et al., *Phys. Rev. B* 92, 224406 (2015).

Controlling the DMI to alter the chiral link between structure and magnetism for $\text{Fe}_{1-x}\text{Co}_x\text{Si}$

S.-A. Siegfried¹, E. V. Altynbaev^{2,3}, N. M. Chubova², V. Dyadkin^{2,4}, D. Chernyshov⁴, E. V. Moskvina^{2,3}, D. Menzel⁵, A. Heinemann¹, A. Schreyer¹, S. V. Grigoriev^{2,3}

¹German Engineering Materials Science Centre (GEMS), Helmholtz-Zentrum Geesthacht GmbH, Geesthacht, Germany

²Petersburg Nuclear Physics Institute, Gatchina, St. Petersburg, Russia

³Saint-Petersburg State University, St. Petersburg, Russia

⁴Swiss-Norwegian Beamlines at the European Synchrotron Radiation Facility, Grenoble, France

⁵Institut für Physik der Kondensierten Materie, TU Braunschweig, Braunschweig, Germany

Monosilicides of 3d transition metals frequently show a chiral magnetic ordering, the absolute configuration being defined by the chirality of the crystal structure and the sign of the Dzyaloshinskii-Moriya interaction (DMI). Structural and magnetic chiralities are probed here for the $\text{Fe}_{1-x}\text{Co}_x\text{Si}$ series and their mutual relationship is found to be dependent on the chemical composition. The chirality of crystal structure has previously been shown to be governed by crystal growth, and the value of the DMI is almost the same for all monosilicides of Fe, Co, and Mn. Our findings [1] indicate that the sign of the DMI in $\text{Fe}_{1-x}\text{Co}_x\text{Si}$ is controlled by the Co composition x . We have been able to directly measure the change in the link between structure and magnetism in this helimagnetic B20 alloy.

The cubic B20 compounds have a non-centrosymmetric crystallographic structure described by the $P2_13$ space group. The absence of the inversion symmetry center of the crystal structure produces the Dzyaloshinskii-Moriya (DM) interaction [2]. Below the ordering temperature T_c , the ferromagnetic exchange (FM) interaction, together with the DM

interaction, result in the appearance of a spin helix with a certain chirality γ_m [3,4]. For the powder samples of $\text{Mn}_{1-x}\text{Fe}_x\text{Ge}$ [5, 6] and $\text{Fe}_{1-x}\text{Co}_x\text{Ge}$ [7], it was shown that the spiral wavevector $k = 2\pi/d$, where d is the spiral period, goes to zero at a certain composition. The monotonic behavior of the wave vector indicates that the DMI goes to zero at the very same composition and, therefore, should change its sign as a function of x .

Controlled structural chirality and its proof by resonant X-ray scattering

We exploited the idea of gaining full control of the DMI sign in a series of single crystalline $\text{Fe}_{1-x}\text{Co}_x\text{Si}$. Unlike germanides, the silicides can be grown as single crystals with fully controlled structural chirality [8]. The $\text{Fe}_{1-x}\text{Co}_x\text{Si}$ single crystals were grown using the Czochralski technique with the following concentrations: $x = 0.5, 0.6, 0.65, 0.7$ and 0.8 . The same structural chirality of all grown crystals was assured by subsequent use of every grown crystal as the seed for the next one. All samples show the same right-handed structural chirality ($\Gamma_c = +1$) as confirmed by the absolute structure.

The determination of the absolute structure was achieved via the refinement of the Flack-parameter [9]. This analysis is based on the difference between the Friedel pairs: $[I(hkl) - I(-hkl)]$ due to a resonant contribution in the X-ray scattering amplitude. The single-crystal diffraction data were collected using the PILATUS@SNBL diffractometer at the BM01A end station of the Swiss-Norwegian Beamlines at the ESRF (Grenoble, France).

Polarized small angle neutron scattering and the flip of the chiral link

The large size of the single crystals makes it possible to determine the chirality of the magnetic structure by polarized neutron diffraction [10, 11]. The

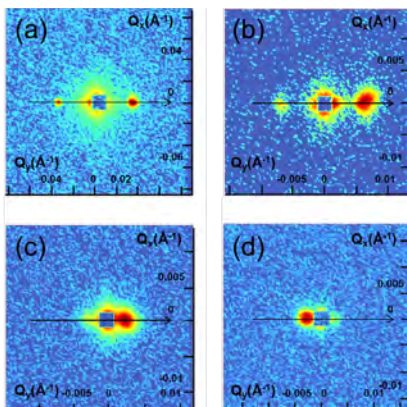


Figure 1: Maps of polarized SANS intensities of MnSi (a) and $\text{Fe}_{1-x}\text{Co}_x\text{Si}$ with $x = 0.5$ (b), 0.6 (c) and 0.7 (d) for polarization $+P_0$ along the field at $T \approx 3.5$ K.

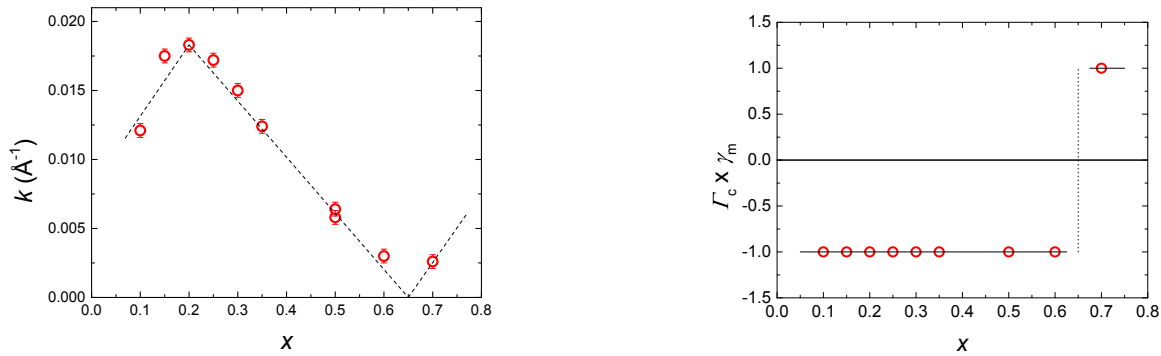


Figure 2: Dependence of (a) the helix wave vector k and (b) the product of structural and magnetic chirality $\gamma_m \times \Gamma_c$ on the concentration x .

helix chirality γ_m is quantified with the help of the polarization of the scattered neutron P_s at a fixed point in the momentum space $\mathbf{Q} = \mathbf{k}$ [5]:

$$P_s(\mathbf{k}) = \frac{I^+(\mathbf{k}) - I^-(\mathbf{k})}{I^+(\mathbf{k}) + I^-(\mathbf{k})} = \gamma_m P_0$$

where I^+ and I^- are the intensities of the scattered beam with initial polarization \mathbf{P}_0 parallel or antiparallel to the scattering vector \mathbf{Q} , respectively.

The polarized small-angle neutron scattering measurements were carried out at the SANS-1 instrument at the Heinz Maier-Leibniz Zentrum (MLZ). Fig. 1 shows the polarized SANS maps for the compounds MnSi and $\text{Fe}_{1-x}\text{Co}_x\text{Si}$ with $x = 0.5, 0.6$ and 0.7 at $T \approx 3.5$ K.

The MnSi reference sample shows a maximum of the scattering intensity at the right part of the detector [Fig. 1 (a)]. The samples with $x = 0.5$ [Fig. 1 (b)] and $x = 0.6$ [Fig. 1 (c)] show similar behavior. According to the previous given definition [5], the magnetic chirality is given as $\gamma_m = -1$. Clearly, the $\text{Fe}_{0.3}\text{Co}_{0.7}\text{Si}$ sample shows the opposite behavior [Fig. 1 (d)] with $\gamma_m = +1$.

Furthermore, the helix wavevector k has been extracted from the low temperature scattering maps and plotted in Fig. 2 (a). In Fig. 2 (b), the product from the structural and magnetic chirality is shown. $k \rightarrow 0$ at the critical concentration $x_c = 0.65$. The helix wave vector k and the DM constant D are linked via the equation [12]:

$$k = \frac{SD}{A},$$

where S is the average spin per unit cell and A is the spin wave stiffness. Expecting the spin wave stiff-

ness and the spin value to be monotonic functions of the Co content, $k \rightarrow 0$ implies $D \rightarrow 0$ at x_c . The critical concentration x_c separates two region with opposite values of the product $\gamma_m \times \Gamma_c$, which means that D not only goes to zero at x_c but also changes its sign.

Conclusion

In this work, the evolution of the structural and magnetic chirality in $\text{Fe}_{1-x}\text{Co}_x\text{Si}$ with varying Co concentration has been investigated by resonant X-ray diffraction and polarized neutron scattering, respectively. We were able to prove the flip of the chiral link with the concentration of the 3d element at the critical concentration x_c . This flip goes along with the transformation from the spiral to the ferromagnetic spin structure for $x \rightarrow x_c$.

To summarize, we show the possibility of applying the Dzyaloshinskii-Moriya interaction to control the magnetic chirality as required for future spintronic devices.

- [1] S.-A. Siegfried et al., Phys. Rev. B 91, 184406 (2015).
- [2] I. E. Dzyaloshinskii, Zh. Eksp. Teor. Fiz. 46, 1420 (1964) [Sov. Phys. J. Exp. Theor. Phys. 19, 960 (1964)].
- [3] P. Bak and M. H. Jensen, J. Phys. C 13, L881 (1980).
- [4] O. Nakanishi et al., Solid State Commun. 35, 995 (1980).
- [5] S. V. Grigoriev et al., Phys. Rev. Lett. 110, 207201 (2013).
- [6] K. Shibata et al., Nat. Nanotechnol. 8, 723 (2013).
- [7] S. V. Grigoriev et al., Phys. Rev. B. 90, 174414 (2014).
- [8] V. A. Dyadkin et al., Phys. Rev. B 84, 014435 (2011).
- [9] H. D. Flack and G. Bernardinelli, J. Appl. Crystallogr. 33, 1143 (2000).
- [10] S. V. Maleyev et al., Fiz. Tverd. Tela (S.-Peterburg) 4, 3461 (1962) [Sov. Phys. Solid State 4, 2533 (1962)].
- [11] M. Blume, Phys. Rev. 130, 1670 (1963).
- [12] S. V. Maleyev, Phys. Rev. B 73, 174402 (2006).

Band structure of helimagnons in MnSi resolved by inelastic neutron scattering

M. Kugler^{1,2}, G. Brandl^{1,2}, J. Waizner³, M. Janoschek⁴, R. Georgii^{1,2}, A. Bauer¹, K. Seemann^{1,2}, A. Rosch³, C. Pfleiderer¹, P. Böni¹, M. Garst³

¹Physik-Department, Technische Universität München, Garching, Germany

²Heinz Maier-Leibnitz Zentrum (MLZ), Technische Universität München, Garching, Germany

³Institute for Theoretical Physics, University of Cologne, Cologne, Germany

⁴Los Alamos National Laboratory, Los Alamos, USA

A magnetic helix realizes a one-dimensional magnetic crystal with a period given by the pitch length λ_h . Its spin-wave excitations – the helimagnons – experience Bragg scattering off this periodicity, leading to gaps in the spectrum that inhibit their propagation along the pitch direction. Using high-resolution inelastic neutron scattering, the resulting band structure of helimagnons was resolved by preparing a single crystal of MnSi in a single magnetic-helix domain. At least five helimagnon bands could be identified that cover the crossover from flat bands at low energies with helimagnons basically localized along the pitch direction to dispersing bands at higher energies. In the low-energy limit, we find the helimagnon spectrum to be determined by a universal, parameter-free theory. Taking into account corrections to this low-energy theory, quantitative agreement is obtained in the entire energy range studied with the help of a single fitting parameter.

Universal helimagnon theory

The B20 compound MnSi is of great interest as a magnetic model system. A small magnetic anisotropy stabilizes a helimagnetic spin spiral below $T_c = 29$ K due to the competition between the exchange interaction and the Dzyaloshinsky-Moriya interaction [1]. The small magnetic Brillouin zone $k_h = 0.036 \text{ \AA}^{-1}$ ensures, that the dispersion of the magnons is universal in the sense that it is captured by an effective continuum theory and is determined by only a few parameters.

In the low-energy limit, the Hamiltonian depends only on three parameters: (i) the critical field H_{c2} , (ii) the pitch vector k_h , and (iii) the numerical value $\chi_{con} = 0.34$ for MnSi that effectively measures the strength of the dipolar interaction. All these param-

eters are known from independent measurements, resulting in a universal prediction for the helimagnon spectrum [2].

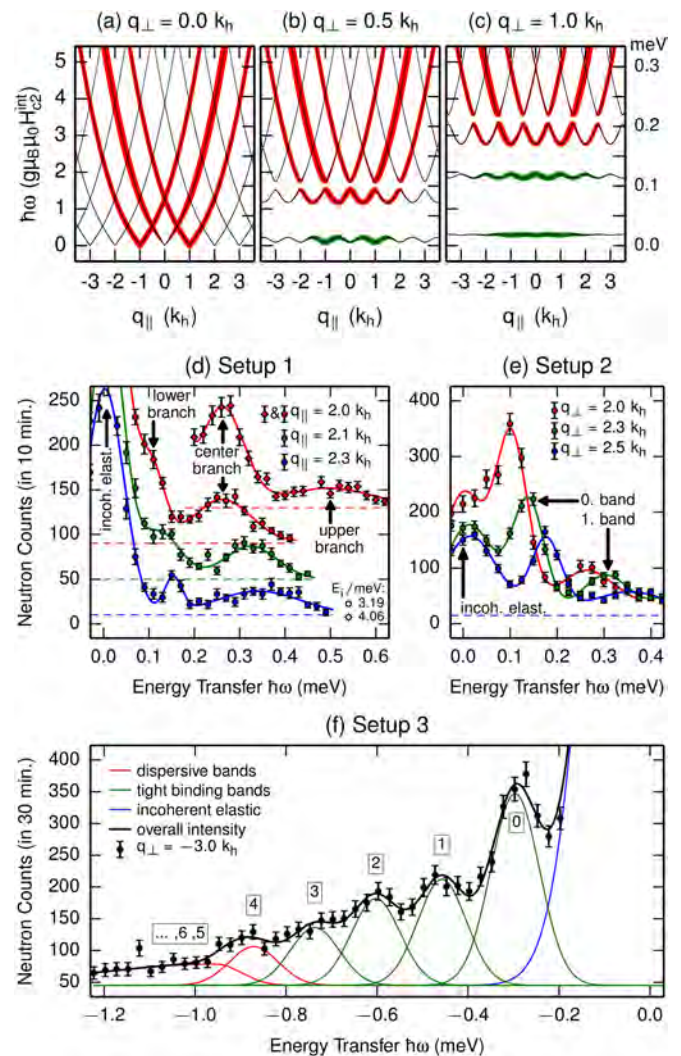


Figure 1: (a)–(c) Universal helimagnon spectrum for momenta q_{\parallel} along the pitch direction k_h in the repeated zone scheme (thin lines) for various values of perpendicular momentum q_{\perp} . The thickness of the colored lines indicates the theoretically expected intensity for inelastic neutron scattering. The colors red and green distinguish between dispersive and practically flat helimagnon bands, respectively. The energy units on the right axes correspond to MnSi at 20 K. (d)–(f) show corresponding example constant-Q scans performed at MIRA. Three helimagnon branches are measured with setup 1 (d), while setup 2 (e) and setup 3 (f) clearly resolve the first two and five bands, respectively. Note that the scans in (d) are shifted by 40 counts with respect to each other for clarity.

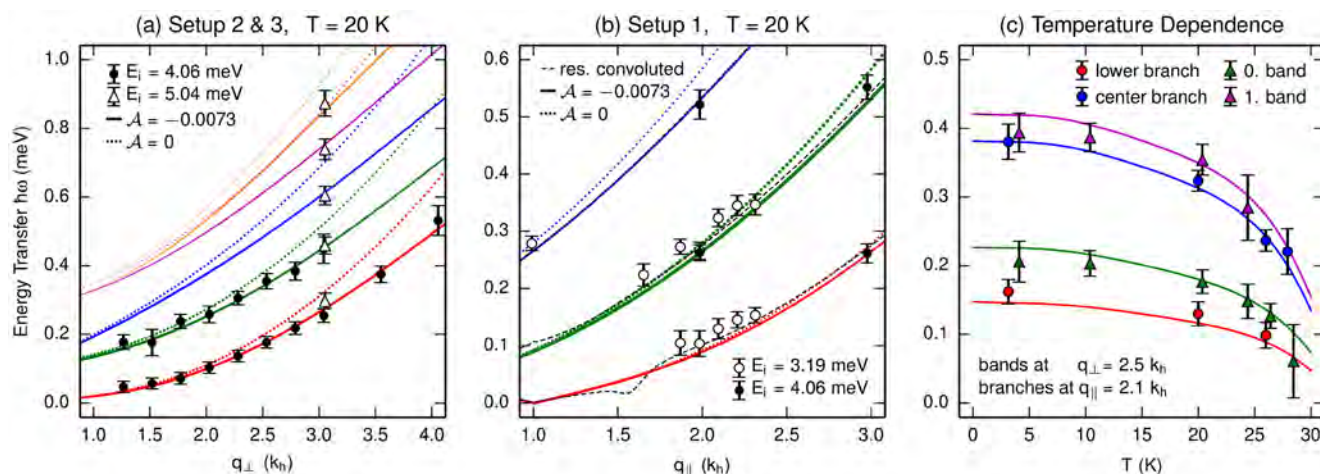


Figure 2: Comparison between theory and experiment. (a), (b) Helimagnon spectrum at 20 K as a function of q_{\perp} and q_{\parallel} with nominally $q_{\parallel} = 0$ and $q_{\perp} = 0$, respectively. The universal spectrum (dotted lines) agrees with the data at low energies; the higher order correction is necessary (solid lines) for quantitative agreement at higher energies. The instrumental resolution slightly shifts the lower and center branch upwards [black dashed line in (b)]. (c) T dependence of the two helimagnon modes lowest in energy measured at certain fixed momenta.

For momenta q_{\parallel} strictly longitudinal to the pitch vector, the helimagnons decouple from the periodic potential resulting in three dispersive branches, see Fig. 1(a). A finite q_{\perp} activates Bragg reflections that open gaps at the Bragg planes, see Fig. 1(b) & (c). The size of these band gaps, however, strongly decreases as a function of the band index $n = 0, 1, 2, \dots$. For large $q_{\perp} \geq nk_h$, the potential for a given band n eventually becomes strong and basically localizes the helimagnon along the pitch direction. In this tight-binding limit, the bands are practically flat, i.e., independent of q_{\parallel} .

TAS measurements at MIRA

In order to verify the helimagnon theory, we used the novel triple-axis option at the multi-purpose instrument MIRA. We performed constant- Q scans around the (110) peak with fixed incident energy E_i and 30' collimators before and after the sample.

A small magnetic field was applied to align the pitch vector and, more importantly, to prepare a single magnetic-helix domain. Otherwise, the magnon excitation branches of four domains $\langle 111 \rangle$ would have been simultaneously excited, resulting in broad total spectra rendering the identification of individual magnon modes impossible.

Three setups were realized, see [2] for details: (i) a horizontal field enables us to measure the three dispersive branches at $q_{\perp} = 0$ (ii) a vertical field resolves the band energies vs. q_{\perp} and (iii) an alternative sample orientation proves that the helimagnon

spectrum is indeed decoupled from the nuclear lattice. Most measurements were performed at 20 K and example scans for the three setups are shown in Fig. 1(d)–(f).

Higher order correction

Figures 2(a) & (b) compare the experimental data at 20 K to the prediction of the universal helimagnon spectrum (dotted lines) using $\mu_0 H_{c2} = 0.53$ T [3] that determines the energy scale $g\mu_B\mu_0 H_{c2} = 0.062$ meV at 20 K. While there is perfect agreement at low energies, deviations become substantial at higher energies with the data assuming systematically lower values than predicted. It turns out that these deviations can be attributed to corrections to the low-energy theory caused by higher-order contributions – expressed as a single fitting parameter (solid lines).

Softening

In order to investigate the softening, the helimagnons were measured at $q_{\parallel} = 2.1 k_h$ with setup 1 and at $q_{\perp} = 2.5 k_h$ with setup 2 at different temperatures, see Fig. 2(c). The theoretically expected peak positions resulting from the values of $H_{c2}(T)$ obtained from ac susceptibility measurements [3] are shown as solid lines, in good agreement with experiment.

[1] P. Bak and M. H. Jensen, *J. Phys. C: Solid State Phys.* **13**, L881 (1980).

[2] M. Kugler et al., *Phys. Rev. Lett.* **115**, 097203 (2015).

[3] A. Bauer et al., *Phys. Rev. B* **82**, 064404 (2010).

Structural and magnetic phase transitions near optimal superconductivity in $\text{BaFe}_2(\text{As}_{1-x}\text{P}_x)_2$

D. Hu¹, X. Lu¹, W. Zhang¹, H. Luo¹, S. Li^{1,2}, P. Wang¹, G. Chen¹, F. Han³, S. R. Banjara^{4,5}, A. Sapkota^{4,5}, A. Kreyssig^{4,5}, A. I. Goldman^{4,5}, Z. Yamani⁶, C. Niedermayer⁷, M. Skoulatos⁷, R. Georgii⁸, T. Keller^{9,10}, P. Wang¹¹, W. Yu¹¹, P. Dai^{12,1}

¹Institute of Physics, Chinese Academy of Sciences, Beijing, China

²Collaborative Innovation Center of Quantum Matter, Beijing, China

³Materials Science Division, Argonne National Laboratory, Argonne, Illinois, USA

⁴Ames Laboratory, U.S. DOE, Ames, Iowa, USA

⁵Department of Physics and Astronomy, Iowa State University, Ames, Iowa, USA

⁶Canadian Neutron Beam Centre, National Research Council, Chalk River, Ontario, Canada

⁷Laboratory for Neutron Scattering, Paul Scherrer Institut, Villigen, Switzerland

⁸Heinz Maier-Leibnitz Zentrum, Technische Universität München, Garching, Germany

⁹Max-Planck-Institut für Festkörperforschung, Stuttgart, Germany

¹⁰Max Planck Society, Outstation at the Heinz Maier-Leibnitz Zentrum (MLZ), Garching, Germany

¹¹Department of Physics, Renmin University of China, Beijing, China

¹²Department of Physics and Astronomy, Rice University, Houston, Texas, USA

We use nuclear magnetic resonance (NMR), high-resolution X-ray, and neutron scattering studies to study structural and magnetic phase transitions in phosphorus-doped $\text{BaFe}_2(\text{As}_{1-x}\text{P}_x)_2$. Previous transport, NMR, specific heat, and magnetic penetration depth measurements have provided compelling evidence for the presence of a quantum critical point (QCP) near optimal superconductivity at $x = 0.3$. However, we show that the tetragonal-to-orthorhombic structural (T_s) and paramagnetic to antiferromagnetic (AF, T_N) transitions in $\text{BaFe}_2(\text{As}_{1-x}\text{P}_x)_2$ are always coupled and approach $T_N \approx T_s \geq T_c$ (≈ 29 K) for $x = 0.29$ before vanishing abruptly for $x \geq 0.3$. These results suggest that AF order in $\text{BaFe}_2(\text{As}_{1-x}\text{P}_x)_2$ disappears in a weakly first-order fashion near optimal superconductivity, much like the electron-doped iron pnictides with an avoided QCP.

Phase diagram in iron pnictides

High-temperature superconductivity of iron-based superconductors emerges near the zone boundary of antiferromagnetic (AF) order by electronic and isoelectronic substitution. A determination of the structural and magnetic phase diagrams will not only provide convincing evidence to distinguish the existence of a QCP hiding inside the superconducting dome, but will also form the basis for a microscopic theory of superconductivity. For electron-doped $\text{Ba}(\text{Fe}_{1-x}\text{T}_x)\text{As}_2$ ($T = \text{Co}, \text{Ni}$), a short-range incommensurate magnetic phase has

been found near optimal superconductivity and a quantum critical point was avoided. Although a QCP may be circumvented in electron-doped $\text{Ba}(\text{Fe}_{1-x}\text{T}_x)\text{As}_2$ due to disorder and impurity scattering in the FeAs plane induced by Co and Ni substitution [1], phosphorus-doped $\text{BaFe}_2(\text{As}_{1-x}\text{P}_x)_2$ provides

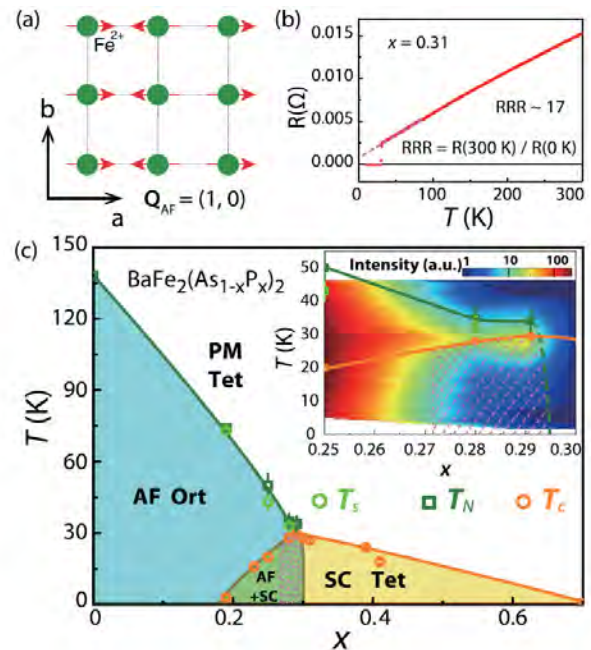


Figure 1: (a) The AF-ordered phase of $\text{BaFe}_2(\text{As}_{1-x}\text{P}_x)_2$, where the magnetic Bragg peaks occur at $Q_{AF} = (1; 0; L)$ ($L = 1; 3; \dots$) positions. (b) Temperature dependence of the resistance for the $x = 0.31$ sample, where $RRR / R(300 \text{ K})/R(0 \text{ K}) \sim 17$. (c) The phase diagram of $\text{BaFe}_2(\text{As}_{1-x}\text{P}_x)_2$, where the Ort, Tet, and SC are orthorhombic, tetragonal, and superconductivity phases, respectively. The inset shows the expanded view of the P-concentration dependence of T_s , T_N , and T_c near optimal superconductivity. The color bar represents the temperature and doping dependence of the normalized magnetic Bragg peak intensity. The dashed region indicates the mesoscopic coexisting AF and SC phases.

an alternative system for achieving a QCP since substitution of As by the isovalent P suppresses the static AF order and induces superconductivity without appreciable impurity scattering. Indeed, experimental evidence for the presence of a QCP at $x = 0.3$ in $\text{BaFe}_2(\text{As}_{1-x}\text{P}_x)_2$ has been mounting [2]. Due to the weak structural or magnetic order near optimal superconductivity, a conclusive determination of the nature of the structural and AF phase transitions in this region is absent.

Structural and magnetic phase transitions in $\text{BaFe}_2(\text{As}_{1-x}\text{P}_x)_2$

In the schematic picture of the existence of a magnetic QCP lying beneath the superconductivity dome, one would expect the antiferromagnetic phase transition temperature (T_N) to be gradually suppressed to zero. The superconducting dome will be separated into two different phases, one phase being a microscopic coexistence phase of magnetic order and superconductivity and another a pure superconducting phase [3]. Meanwhile, the magnetic correlation length diverges when approaching the QCP. To provide unambiguous evidence to check the existence of a QCP in a $\text{BaFe}_2(\text{As}_{1-x}\text{P}_x)_2$ system, we carried out systematic transport, NMR, X-ray and neutron scattering studies of single crystals, focused on determining the P-doping evolution of the structural and magnetic phase transition near $x = 0.30$.

Figure 2(a-f) shows constant energy scans and temperature for the $x = 0.19, 0.28, 0.29$ and 0.31 samples. The instrumental resolution limited peaks centered at $\text{QAF} = (1, 0, 3)$ found below T_N at $0.19, 0.28, 0.29$ compounds, which implies no incommensurate short-range magnetic order near optimal doping in a P-doped system. The temperature dependence of the scattering at $(1, 0, 3)$ reveals a continuously increasing magnetic order parameter near T_N and a dramatic suppression of the magnetic intensity below T_c . On increasing the doping levels to $x = 0.30$ and 0.31 , we find no evidence of magnetic order above 2K. Additionally, we have carried out further neutron scattering measurements on the $x = 0.29$ sample using TRISP, which reveal that the spins of the system freeze below 30.7 K on a time scale of $\tau \sim \hbar/\Delta E \approx 6.6 \times 10^{-10}$ s. This spin freezing temperature is almost identical to that of nearly optimally electron-doped $\text{Ba}(\text{Fe}_{1-x}\text{T}_x)_2\text{As}_2$. The high flux and excellent performance of MIRA and TRISP forms the basis for the success of this project. Cit-

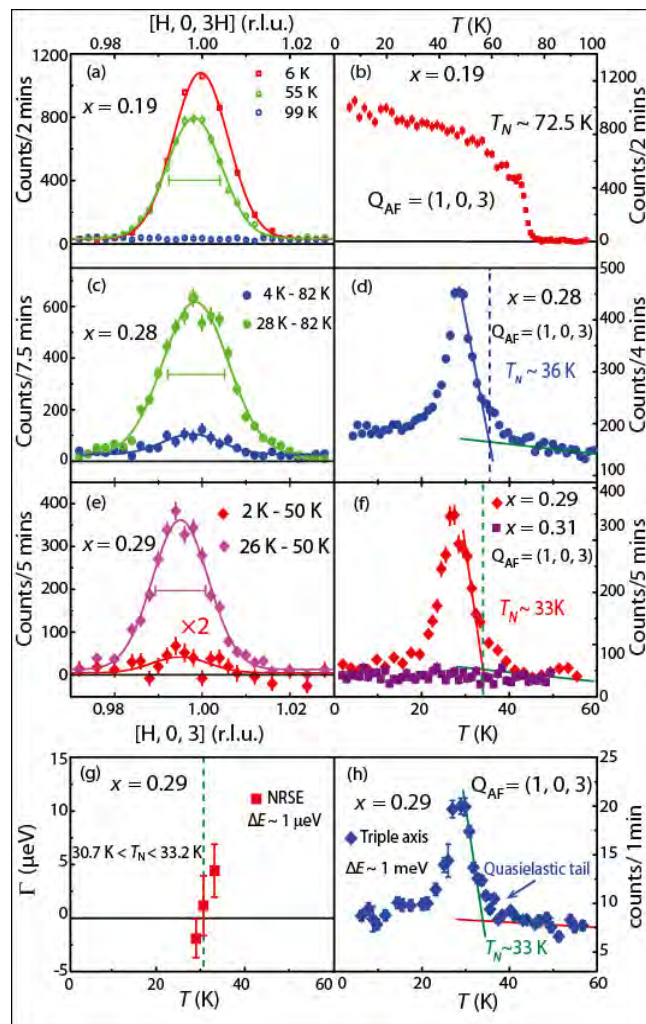


Figure 2: [(a),(c),(e)] Wave vector scans along the $[H, 0, 3]$ direction at different temperatures for $x = 0.19, 0.28, 0.29$, and 0.31 , respectively. Horizontal bars indicate instrumental resolution. [(b),(d),(f)] Temperature dependence of the magnetic scattering at $\text{QAF} = (1, 0, 3)$ for $x = 0.19, 0.28$, and 0.29 , respectively. (g) NRSE measurement of temperature dependence of the energy width (Γ is the full-width-at-half-maximum (FWHM) of scattering function and 0 indicates instrumental resolution limited) at $\text{QAF} = (1, 0, 3)$ for $x = 0.29$. (h) The magnetic order parameters from the normal triple-axis measurement on the same sample.

ing our additional X-ray and NMR results, we present the refined phase diagram of $\text{BaFe}_2(\text{As}_{1-x}\text{P}_x)_2$ in Fig 1 (c). We conclude that the static AF order in $\text{BaFe}_2(\text{As}_{1-x}\text{P}_x)_2$ disappears in the weakly first-order fashion and coexists and competes with superconductivity near optimal superconductivity, much as the electron-doped iron pnictides with an avoided QCP. For detailed discussions, see ref. [4].

[1] P. C. Dai, *Rev. Mod. Phys.* 87, 855 (2015).

[2] K. Hashimoto et al., *Science* 336, 1554 (2012).

[3] T. Shibauchi et al., *Annu. Rev. Condens. Matter Phys.* 5, 113 (2014).

[4] D. Hu et al., *Phys. Rev. Lett.* 114, 157002 (2015).

Magnetic and structural phase transitions in $\text{La}_{0.4}\text{Na}_{0.6}\text{Fe}_2\text{As}_2$ single crystals

S. Nandi^{1,2,3}, J.-Q. Yan^{4,5}, B. Saparov⁴, P. Čermák², Y. Xiao¹, Y. Su², W. T. Jin^{1,2}, A. Schneidewind², R. W. McCallum^{6,7}, T. A. Lograsso^{6,7}, B. C. Sales⁴, D. G. Mandrus^{4,5}, T. Brückel^{1,2}

¹Jülich Centre for Neutron Science JCNS, Peter Grünberg Institut PGI, JARA-FIT, Forschungszentrum Jülich GmbH, Jülich, Germany

²Jülich Centre for Neutron Science (JCNS) at MLZ, Forschungszentrum Jülich GmbH, Garching, Germany

³Department of Physics, Indian Institute of Technology, Kanpur, India

⁴Materials Science and Technology Division, Oak Ridge National Laboratory, Oak Ridge, Tennessee, USA

⁵Department of Materials Science and Engineering, University of Tennessee, Knoxville, Tennessee, USA

⁶Division of Materials Science and Engineering, Ames Laboratory, Ames, Iowa, USA

⁷Department of Materials Science and Engineering, Iowa State University, Ames, Iowa, USA

L $a_{0.4}\text{Na}_{0.6}\text{Fe}_2\text{As}_2$ single crystals have been grown out of a NaAs flux in an alumina crucible and characterized by measuring magnetic susceptibility, electrical resistivity and specific heat, as well as single-crystal X-ray and neutron diffraction. The single crystals show a structural phase transition from a high-temperature tetragonal phase to a low-temperature orthorhombic phase at $T_S = 125$ K. Concomitant with the structural phase transition, the Fe moments order along the a direction with an ordered moment of $0.7(1) \mu_B$ at $T = 5$ K. $\text{La}_{0.5-x}\text{Na}_{0.5+x}\text{Fe}_2\text{As}_2$ provides a material platform for the study of iron-based superconductors where the electron-hole asymmetry could be studied by simply varying the La/Na ratio.

Search for ideal material to study electron hole asymmetry in Fe-pnictides

Since the first report of superconductivity with a transition temperature (T_C) of 26 K in $\text{LaFeAsO}_{1-x}\text{F}_x$ in 2008 [1], tremendous efforts have been made to explore new iron-based superconductors. Superconductivity was observed in a wide variety of iron-based materials, such as “122” ThCr_2Si_2 -type AFe_2As_2 ($A =$ alkaline earth) [2]. As in cuprate superconductors, the electron-hole asymmetry was observed in the phase diagram of iron-based superconductors, which shows the doping dependence of magnetic, structural, and superconducting transitions. To study the electron hole asymmetry, it was necessary to dope the crystal at different crystallographic sites for the AFe_2As_2 . It has been suggested that this effect, coming from substitution at different crystallographic sites, con-

tributes to the electron-hole asymmetry in a phase diagram of iron-based superconductors [3]. In [4] we show from simple electron counting that the material $\text{La}_{0.5-x}\text{Na}_{0.5+x}\text{Fe}_2\text{As}_2$ could be tuned from electron-doped ($x < 0$) to hole-doped ($x > 0$) by varying the ratio between the alkali metal and rare-earth ions. In this way, the effect of substitution at different crystallographic sites could be minimized.

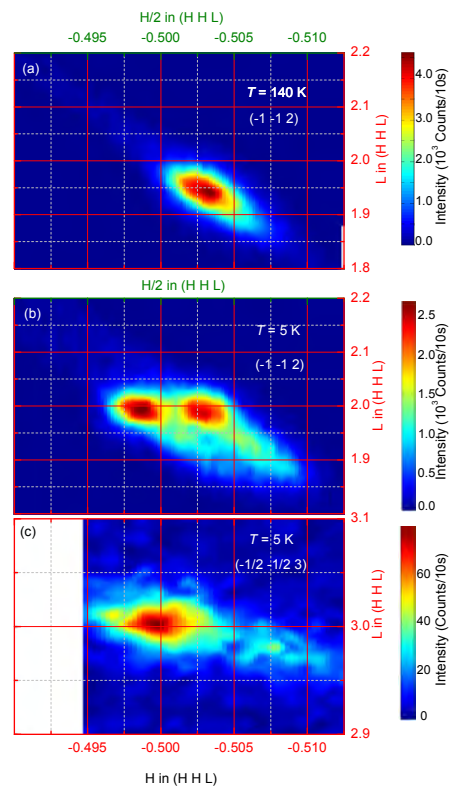


Figure 1: (a) 2D map for the tetragonal $(-1 -1 2)_T$ reflection at $T = 140$ K determined by $(\xi \xi 0)$ scans at different L values. Only a single peak consistent with the tetragonal symmetry of the lattice was observed. (b) At low temperature, the $(-1 -1 2)_T$ peak splits into two peaks characterizing the structural phase transition into the orthorhombic structure. (c) $(\xi \xi 0)$ scans at different L values for the magnetic $[-\frac{1}{2} -\frac{1}{2} 1]_T$ reflection. The magnetic peak is associated with only one structural twin domain (left) indicating the magnetic propagation vector to be $(1 0 1)_O$.

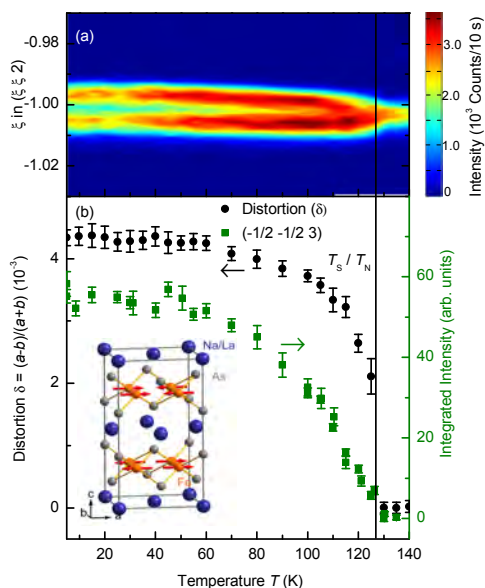


Figure 2: (a) Two-dimensional map of the Q scans as a function of temperature for the $(-1 -1 2)_T$ reflection. (b) Temperature dependence of the orthorhombic distortion measured by performing Q scans through the $(-1 -1 2)_T$ reflection and temperature dependence of the integrated intensity for the magnetic $[-\frac{1}{2} -\frac{1}{2} 3]_T$ reflection. Both temperature dependencies were measured during heating. The inset shows the determined magnetic structure of the compound.

Basic physical properties of $\text{La}_{0.4}\text{Na}_{0.6}\text{Fe}_2\text{As}_2$ single crystals

After successful growth of the $\text{La}_{0.4}\text{Na}_{0.6}\text{Fe}_2\text{As}_2$ single crystals, X-ray powder diffraction, electrical resistivity, magnetic susceptibility and heat capacity measurements were carried out to unravel the basic physical properties of the as-grown single crystals [4]. The physical properties show phase transitions at 125 K and below 30 K. Interestingly, the resistivity shows a drop below 30 K, which sharpens upon treating the sample with water, indicating that the sample is moisture sensitive. Further measurements confirmed filamentary superconductivity on the sample surface. It has been well established that other AFe_2As_2 members show a structural transition from a high-temperature tetragonal phase (space group $I4/mmm$) to a low-temperature orthorhombic phase (space group $Fmmm$). Therefore, in order to understand basic microscopic crystal and magnetic structure, we performed a single crystal neutron diffraction experiment at PANDA.

Neutron diffraction experiment at PANDA

For these neutron scattering measurements, a 3-mg as-grown square shaped single crystal of approximate dimensions $2.5 \text{ mm} \times 2.5 \text{ mm} \times 0.1 \text{ mm}$ was selected. The measurements were carried out with fixed incoming and final wave vectors of $k_i = k_f = 1.57$ and 2.57 \AA^{-1} . The measurements were performed in the $(1 1 0)_T - (0 0 1)_T$ scattering plane. We will use

tetragonal (T) and orthorhombic (O) subscripts for the reflections whenever necessary.

At $T = 300 \text{ K}$, the crystal structure is well described by a tetragonal lattice with lattice parameters $a = 3.875(5) \text{ \AA}$ and $c = 12.224(5) \text{ \AA}$. Figure 1(a) shows a two-dimensional (2D) map for the nuclear $(-1 -1 2)_T$ reflection at $T = 140 \text{ K}$. A single peak shape consistent with the tetragonal symmetry of the lattice was observed. As the sample is cooled below T_S , the $(-1 -1 2)_T$ peak splits into two, indicating orthorhombic crystal structure with $a \neq b$, as shown in Fig. 1(b). After an extensive search at $T = 5 \text{ K}$, a magnetic signal was found at the $[-\frac{1}{2} -\frac{1}{2} 3]_T$ position. Figure 1(c) shows a 2D map for the magnetic $[-\frac{1}{2} -\frac{1}{2} 3]_T$ reflection which is associated with the left nuclear twin in Fig. 1(b) and indicates that the magnetic propagation vector is $(1 0 1)_O$.

To determine the structural phase transition temperature, $(\xi \xi 0)$ scans were performed through the $(-1 -1 2)_T$ reflection as a function of temperature and are shown in Fig. 2(a). Broadening of the full width half maxima (FWHM) of the $(-1 -1 2)_T$ reflection below $T_S = (128.0 \pm 0.5) \text{ K}$ indicates a structural phase transition at this temperature. Fig. 1(b) shows the temperature dependence of the orthorhombic distortion, $\delta = (a-b)/(a+b)$, measured during heating of the sample. Orthorhombic distortion increases continuously to the lowest achievable temperature of 5 K. Fig. 1(b) shows the temperature dependence of the magnetic reflection $[-\frac{1}{2} -\frac{1}{2} 3]_T$, indicating the onset of the Fe magnetic order at $T_N = (128.0 \pm 0.5) \text{ K}$, the same temperature as the structural phase transition.

At low temperatures ($T = 5 \text{ K}$), a set of structural and magnetic peaks were collected to determine the Fe magnetic structure. The magnetic reflections can be well fitted by a stripe antiferromagnetic structure having moments along the “a” direction and with an ordered moment of $0.7(1) \mu_B$ at $T = 5 \text{ K}$. The inset to Fig. 2(b) shows the magnetic structure. According to this magnetic structure, the Fe moments are antiferromagnetically aligned along the “a” direction and ferromagnetically along the “b” direction, the same as the reported stripe antiferromagnetic structure of the AFe_2As_2 ($A = \text{Ca}, \text{Sr}, \text{Ba}$) compounds.

[1] Y. Kamihara et al., *J. Am. Chem. Soc.* 130, 3296 (2008).

[2] M. Rotter et al., *Phys. Rev. Lett.* 101, 107006 (2008).

[3] S. Avci et al., *Phys. Rev. B* 85, 184507 (2012).

[4] J.-Q. Yan et al., *Phys. Rev. B* 91, 024501 (2015).

Interplanar magnetic correlations in a high-temperature superconductor

A. T. Rømer¹, A. Schneidewind², K. Lefmann¹

¹Niels Bohr Institute, University of Copenhagen, Copenhagen, Denmark

²Jülich Centre for Neutron Science (JCNS) at MLZ, Forschungszentrum Jülich GmbH, Garching, Germany

A series of experiments carried out at the FRM II reactor as well as other neutron sources have revealed details of the magnetic order in the high-temperature superconductor $\text{La}_{1.88}\text{Sr}_{0.12}\text{CuO}_4$. In this system, stripe-like magnetic order within the CuO_2 planes coexists with superconductivity and displays a pronounced enhancement upon application of an external magnetic field perpendicular to the CuO_2 planes. Careful studies of the magnetic correlations between these planes have led to the revelation of the origin of the enhancement effect. The dominant source is an increase in the magnetic moments. A secondary source is due to the development of weak interplanar correlations. Surprisingly, fast cooling of the system also causes enhanced correlations between the CuO_2 planes. The results were published in *Physical Review B* 91, 174507 (2015) [6].

Magnetic stripe-like order

The high-temperature superconductor $\text{La}_{2-x}\text{Sr}_x\text{CuO}_4$ is a member of the cuprate family of Copper-based superconductors. It derives from the parent compound La_2CuO_4 which is a Mott insulator with three-dimensional antiferromagnetic order. The antiferromagnetic order of the Mott insulating phase disappears rapidly as a function of doping, but magnetic order survives in the form of an incommensurate spin-density-wave order even above the doping value where superconductivity sets in. A full understanding of this transition from a Mott insulator to a superconductor is one of the greatest challenges of condensed matter physics.

Part of the puzzle stems from the fact that magnetic order coexists with superconductivity. It turns out that magnetic and superconducting regions are not always spatially separated, but in some compounds

coexist microscopically. In $\text{La}_{2-x}\text{Sr}_x\text{CuO}_4$, magnetic order is quasi-two dimensional and is manifested as a quartet of peaks around the position of the antiferromagnetic ordering vector. This structure has been interpreted as a signature of a magnetic stripe-like pattern, where antiferromagnetic regions are intercepted by rivers of charge [1]. Muon spin resonance measurements on $\text{La}_{1.88}\text{Sr}_{0.12}\text{CuO}_4$ have revealed that magnetic order expands throughout the entire volume of the crystal [2]. Even so, application of a magnetic field leads to an enhancement of the magnetic order when measured by neutron scattering.

Magnetic field effect

In fact, a number of neutron scattering experiments on $\text{La}_{2-x}\text{Sr}_x\text{CuO}_4$ at different Strontium dopings have revealed that a boost in the magnetic order occurs upon application of an external magnetic field perpendicular to the Copper oxide planes. For dopings smaller than 13.5 %, an enhancement of preexisting magnetic order is observed [3], whereas in systems of larger doping which do not display zero-field magnetic order, the applied field can induce magnetic order [2,4].

The increase in magnetic ordering is connected to the presence of vortices surrounding the magnetic flux lines that penetrate the Copper oxide layers. Since the superconducting order is depressed in the vicinity of the vortex core, this region provides more favorable conditions for the development of magnetic order.

What has remained uncertain, however, is whether the increase in the magnetic signal measured by neutron scattering experiments is due to an actual increase in the magnetic volume fraction, or to an increase in the ordered magnetic moments. In fact, similar observations could stem from an enhancement of the spin-spin correlations out of the

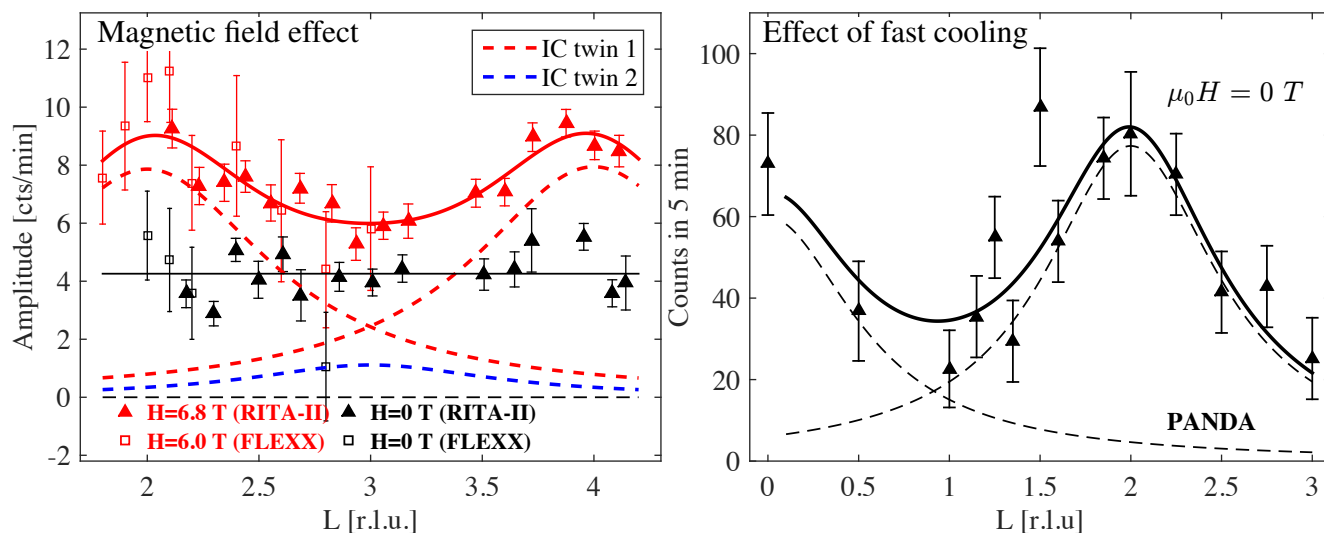


Figure 1: (Left) Background-subtracted elastic neutron response at the incommensurate magnetic ordering vector versus L in zero field, a 6.0 T field (FLEXX data), and a 6.8 T field (RITA-II data). The field was applied horizontally along the c axis, i.e. perpendicular to the CuO_2 planes. Weak interplanar correlations build up when the magnetic field is applied. (Right) L dependence of the incommensurate magnetic signal above background in zero field measured at PANDA after fast cooling of the sample. Note that fast cooling induces weak interplanar correlations in the sample. Adapted from Ref. [6].

CuO_2 planes, without any additional magnetic order induced in the system. Indications that magnetic ordering becomes more three-dimensional upon application of an external magnetic field was presented in Ref. [5]. Other than this report, very little has been done to investigate three-dimensionality of the magnetic order in the cuprates and the observation in Ref. [5] motivated us to pursue the question of whether the field-induced signal, observed in experiments using the more common CuO_2 plane crystal orientation, may be due to the induced interplanar correlations, and not to an increase in the magnetic volume fraction or ordered magnetic moments in the superconductor.

Interplanar magnetic correlations

To address this question, we performed scattering experiments where we specifically probed the magnetic intensity out of the CuO_2 plane. We used three different cold-neutron triple-axis spectrometers: PANDA at the FRM II research neutron source in Garching, RITA-II at the SINQ neutron source at PSI, Switzerland and FLEXX at the BER2 research reactor at HZB Berlin.

We found that spin-spin correlations between the CuO_2 planes do build up upon application of a field perpendicular to the planes, as shown on the left in Fig. 1. At the same time, the experiments revealed an increase in the magnetic moments, which in fact turned out to be the prevailing field effect.

To our surprise, we found from the experiments at PANDA that fast cooling of the sample can provoke a build-up of interplanar magnetic correlations and thereby cause an effect similar to the application of a magnetic field. The origin of cooling-induced interplanar correlations we ascribe to the presence of excess oxygen in the crystal. Excess oxygen is not easily avoided during crystal growth and fast cooling will freeze the oxygens at random positions. This could create pinning centers for magnetic correlations between neighbouring Copper oxide planes.

- [1] J. M. Tranquada et al., *Nature (London)* 375, 561 (1995).
- [2] J. Chang et al., *Phys. Rev. B* 78, 104525 (2008).
- [3] B. Lake et al., *Nature (London)* 415, 299 (2002).
- [4] B. Khaykovich et al., *Phys. Rev. B* 71, 220508(R) (2005).
- [5] B. Lake et al., *Nat. Mater.* 4, 658 (2005).
- [6] A. T. Rømer et al., *Phys. Rev. B* 91, 174507 (2015).

Morphology of the intermediate mixed state in a bulk niobium type-II superconductor

T. Reimann^{1,2}, S. Mühlbauer¹, M. Schulz^{1,2}, B. Betz³, A. Kaestner³, V. Pipich⁴, P. Böni², C. Grünzweig³

¹Heinz Maier-Leibnitz Zentrum (MLZ), Technische Universität München, Garching, Germany

²Physik-Department E21, Technische Universität München, Garching, Germany

³Paul Scherrer Institut, Neutron Imaging and Activation Group, Villigen, Switzerland

⁴Jülich Centre for Neutron Science (JCNS) at MLZ, Forschungszentrum Jülich GmbH, Garching, Germany

As with materials in the solid state, the phase diagrams of vortex matter in type-II superconductors exhibit crystalline, amorphous, liquid and spatially inhomogeneous phases. The multitude of different phases of vortex matter has therefore been shown to act as an almost ideal model system for the study of both the underlying properties of superconductivity and of general phenomena such as domain nucleation and morphology. We have recently demonstrated how neutron grating interferometry combined with small-angle neutron scattering yields detailed information on the vortex lattice and its domain structure in the intermediate mixed state of a type-II niobium superconductor.

Domain structures exhibiting striking similarities can be found in physical, biological and chemical systems with varying length scales, being abundant on the micrometer scale. While the interactions driving the domain formation are different, the resulting morphologies are surprisingly similar. In particular, generic structures such as bubble, stripe or dendritic domains are commonly observed. Represent-

ative of this multitude, the type-II superconductor niobium in its intermediate mixed state (IMS) has recently been identified as an ideal model system for studying the process of domain nucleation. The IMS structure composed of field free Meissner and Shubnikov domains which carry a vortex lattice can be conveniently tuned by a variation of temperature and external magnetic field. Hence, the IMS allows one to study the development of long range order paired with domain nucleation at a mesoscopic scale.

However, until now the morphology of the superconducting vortex lattice (VL) in real space has only been observable by means of surface sensitive techniques which suffer from the effects of surface pinning due to structural inhomogeneities, or from geometrical constraints. We have recently shown that neutron grating interferometry (nGI) (Fig. 1) combined with small angle neutron scattering (SANS) yields detailed information on the morphology of the VL and its domain structure in bulk superconductors covering length scales from 20 nm up to 10 μm [1].

Probing the domain structure: neutron grating interferometry

nGI is an advanced technique in neutron radiography where regions involving the scattering of neutrons under ultra-small angles (USANS) are identified [2]. Hence, signatures in reciprocal space leading to the scattering of neutrons are used to generate contrast in direct space. By applying the nGI-method to the archetypical type-II superconductor niobium, we examined the structure of the intermediate mixed state. Using nGI, we were able to identify in particular that: i) the IMS nucleation takes place in the center of the sample ii) it expands to the edge of the sample in increasing field and iii) as the IMS finally evolves into the Shubnikov phase, the transition is delayed at the sample edges (compare Fig. 2).

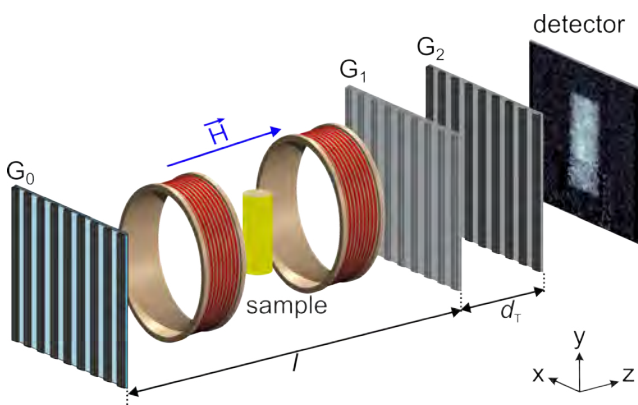


Figure 1: Illustration of the nGI setup for the IMS investigation. nGI is based on two neutron absorption gratings (G_0 and G_2) and one phase grating (G_1) implemented into a neutron imaging beamline.

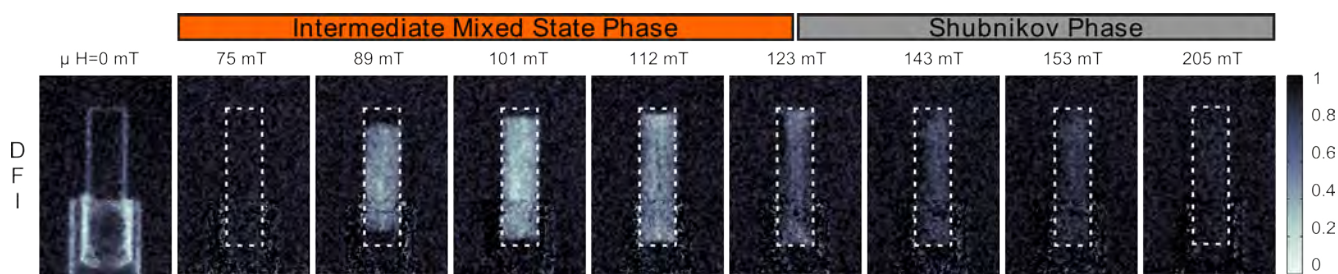


Figure 2: Dark-field images (DFI) results of an ultra-pure niobium rod as a function of increasing magnetic field after ZFC to $T = 4$ K. The contour of the sample is indicated by the dashed boxes. The results for $B > 0$ are normalized with those for $\mu_0 H = 0$ mT, hence only the pure magnetic contribution from the VL is visualized. White contrast marks the IMS regions, hence the DFI provides information about the VL domain formation in the IMS phase.

Probing the vortex lattice: small-angle neutron scattering

We complemented the nGI results obtained using SANS. This method is well suited for the investigation of vortex matter as it probes the typical vortex lattice parameter of a few 100 nm. Furthermore, the IMS phase can easily be identified by the field independent vortex spacing. The experiments confirmed the spatially resolved morphology found in the IMS phase and provided information on the structure of the vortices within the domains (Fig. 3). In agreement with the nGI results, SANS shows that the onset of the VL, as well as its transition from the IMS to the Shubnikov phase, is delayed at the sample edge. Moreover, by means of SANS it was possible to quantify the effect of field degradation at the sample edges at 14 mT.

Besides providing detailed information on the IMS domain nucleation in bulk niobium, our study, by combining neutron techniques in direct and reciprocal space, serves as a show case for a powerful procedure to investigate the domain formation in a multitude of systems in hard and soft condensed matter over a huge range of length-scales extending from the Å to the tens of micrometer scale.

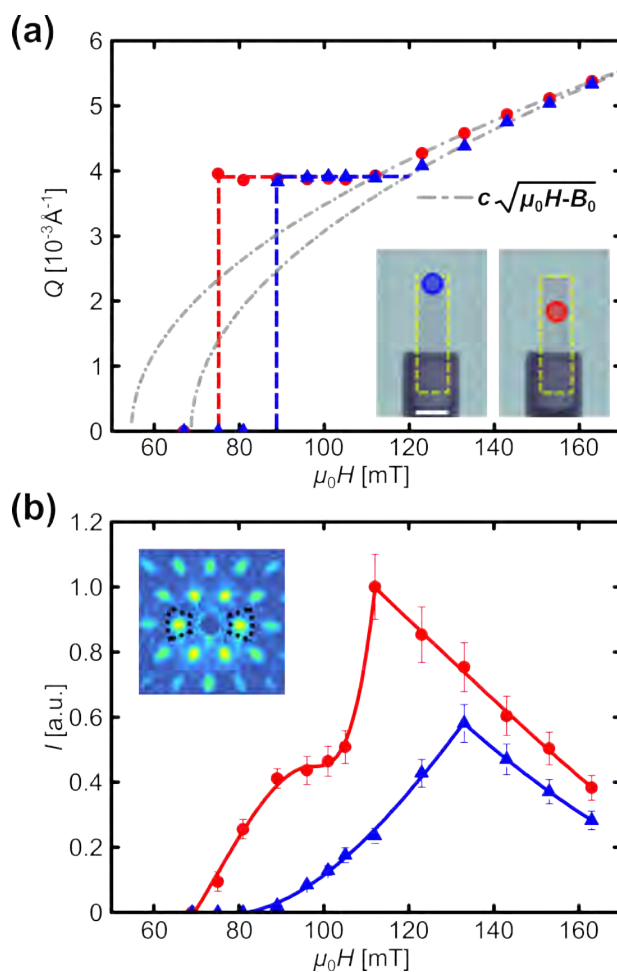


Figure 3: Quantitative analysis of the SANS data from the Nb rod for the two measurement positions indicated in the inset of (a). (a) Q-position of the first order Bragg peak of the VL as a function of the applied magnetic field. The measured positions of the peaks are shown in the inset of (b). (b) Integrated intensity of the first order Bragg peak versus magnetic field. Clearly, the appearance of VL is delayed on the sample edge.

[1] T. Reimann et al., Nat. Commun. 6, 8813 (2015).

[2] M. Strobl et al., Phys. Rev. Lett. 101, 123902 (2008).

Contrast matching SANS reveals structural properties in protein-gold hybrid materials

G. Nyström¹, M. P. Fernández-Ronco^{2,3}, S. Bolisetty¹, A. Radulescu⁴, M. Mazzotti², R. Mezzenga¹

¹Laboratory of Food & Soft Materials, ETH Zürich, Zürich, Switzerland

²Institute of Process Engineering, ETH Zürich, Zürich, Switzerland

³Laboratory for Advanced Fibers, EMPA, St. Gallen, Switzerland

⁴Jülich Centre for Neutron Science (JCNS) at MLZ, Forschungszentrum Jülich GmbH, Garching, Germany

Gold, with more than 5000 years of history, has been of enormous historical and cultural importance across civilizations. Its beauty and malleability made it highly desirable for ornamentation, jewelry and for use as a currency. The high value and price of gold has lasted to this day and creates a demand for the efficient utilization of gold in new lightweight materials. We used gold in the form of microcrystals and nanoparticles combined with protein fibrils to develop gold aerogels – a new class of ultra-light gold materials. By changing the colloidal gold shape, size and concentration we were able to tune the optical properties and final gold composition to reach contents above 20 karat equivalent, yet at densities $\sim 10^3$ lighter than any equivalent gold alloys. In this study, we show how contrast matching small-angle neutron scattering (SANS) has provided important structural information about these materials.

Amyloid fibrils as templates for protein-gold aerogels

Traditional silica or metal oxide aerogels are inherently brittle. One approach to improving the mechanical flexibility and, thereby, expanding the aerogel application range is to use organic colloidal precursors such as carbon nanotubes [1], graphene [2] or nanocellulose [3]. While the results reported previously are promising, each system has limitations. These limitations are related in particular to the colloidal stability of the precursor solutions and the flexibility in terms of the nature and maximum loading of additional inorganic particles in the final aerogels.

We recently proposed a new class of aerogel materials based on protein colloids, so called amyloid fibrils [4]. These fibrils, formed by the self-assembly of β -lactoglobulin in water, carry functional groups, [5] that can act as natural reduction sites for inorgan-



Figure 1: Photograph of protein gold microcrystal aerogel.

ic particles. The fibrils also serve the dual purpose of keeping the organic-inorganic hybrid dispersion stable even at high inorganic particle concentrations. To produce gold protein hybrid aerogels, gold was added in salt form (HAuCl_4) to the amyloid fibrils. Following either incubation at pH 2 and 70 °C or chemical reduction using NaBH_4 , gold microcrystals or gold nanoparticles stabilized with amyloid fibrils were formed. The addition of 150 mM NaCl transferred the dispersions to free standing hydrogels that were subsequently solvent-exchanged to ethanol and non-destructively dried to aerogels using supercritical CO_2 .

The aerogels obtained had very low densities (2.9 – 30.8 mg/cm^3) and high specific N₂ surface areas (325 m^2/g). By changing the size, shape and mass fraction of the gold particles, the optical properties of hybrid aerogels could be tuned (Fig. 2). Aerogels containing plate-like gold microcrystals (Fig. 2B) showed a traditional golden color, whereas the spherical gold nanoparticles (Fig. 2C) gave the aerogels a characteristic ruby red appearance that was tunable by particle size (Fig. 2D). The visual appearance of the gold microcrystal aerogels is almost identical to the appearance of traditional solid gold metal (Fig. 1). This is remarkable for a material that consists of more than 98 vol% of air.

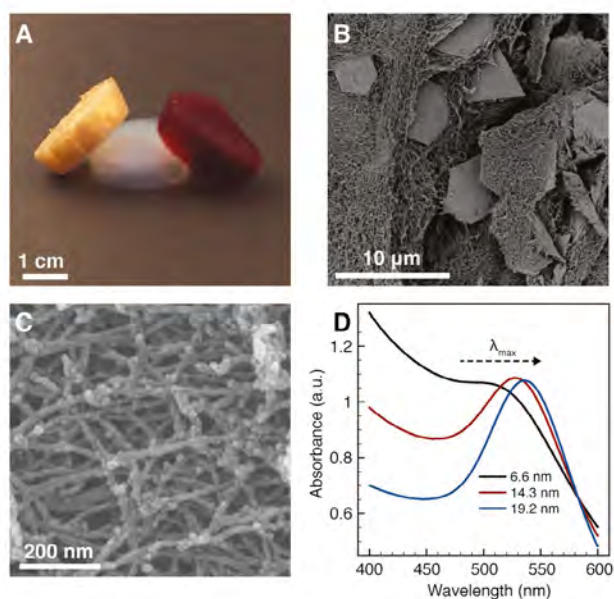


Figure 2: Photograph (A), electron micrographs (B-C) and UV/Vis characterization (D) of the protein and protein-gold hybrid aerogels.

The aerogel material presented may be used in bio-sensing, radiation protection, food decoration, as a replacement for traditional gold in jewelry or as components of artworks. We have explored the gold microcrystal aerogel as a pressure sensor and the gold nanoparticle aerogel as a substrate for heterogeneous catalysis [4]. The aerogels can also be crosslinked with glutaraldehyde vapor to render them wet-stable. This further broadens their application range and allows for a structural characterization of the samples under wet conditions, specifically using contrast matching SANS.

Contrast matching SANS on cross-linked protein-gold aerogels

Contrast matching SANS was used to selectively investigate the distribution of amyloid fibrils and gold particles within the aerogels (Fig. 3). At the contrast matching conditions for gold ($D_2O:H_2O = 74:26$ vol%), we found that the scattered intensities decay with a slope of $5/3$ for both types of gold particles (Fig. 3 blue circles). This slope is characteristic of the fractal exponent of a self-avoiding random walk and highlights the semi-flexible nature of the amyloid fibrils. When the solvent is matched to the amyloid fibrils ($D_2O:H_2O = 50:50$ vol%), different shapes of the scattering curves are recovered, reflecting the different form factors of the gold particles (Fig. 3 red squares). For the gold nanoparticle aerogels, (Fig. 3B) the scattering closely resembles

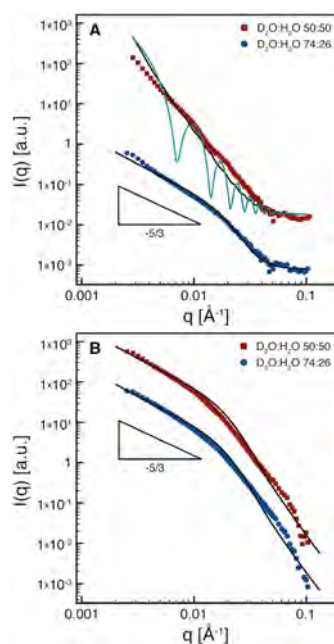


Figure 3: SANS measurements of the protein gold crystal (A) and protein gold nanoparticle (B) aerogels at solvent matching conditions for protein fibrils (red squares) and solvent matching conditions for gold (blue circles). The scattering data have been offset for clarity.

the scattering from the amyloid fibrils. This indicates that the gold nanoparticles are uniformly coated on the amyloid fibrils, in agreement with electron microscopy (Fig. 2C). For the gold microcrystals, a distinctly different scattering profile is found with a higher slope (~ 3). This reveals the bulk characteristic of the gold microcrystals (lateral dimension in the micrometer scale, Fig. 2B) for q corresponding to length scales of 15 – 200 nm. The continuous lines in Fig. 3 are fitted curves using the form factors for polymers with excluded volume [6] (fibrils) and infinitely large disks with polydisperse (black line) or monodisperse (green line) thickness (gold microcrystals), respectively, showing good agreement between scattering profiles and the expected shapes of the organic and inorganic components. The slight upturn in the form factors of the large disks at low q in Fig. 3A is attributed to extra edges present in the gold single crystals (of fractal dimensionality 1), a feature missing in the form factor of disks.

In conclusion, these results provide the structure and conformation of the protein and gold particles within the aerogel and show the power of contrast matching SANS to reveal decoupled structural information from organic-inorganic hybrid materials.

- [1] M. B. Bryning et al., *Adv. Mater.* 19, 661 (2007).
- [2] H. Hu et al., *Adv. Mater.* 25, 2219 (2013).
- [3] Y. Kobayashi et al., *Angew. Chem. Int. Ed.* 53, 10394 (2014).
- [4] G. Nyström et al., *Adv. Mater.* 28, 472 (2016).
- [5] S. Brownlow et al., *Structure* 5, 481 (1997).
- [6] J. S. Pedersen et al., *Macromolecules* 29, 7602 (1996).

Biomimetic multifunctional magnetite/gel composites

B.-H. Wu^{1,2}, M. Sigleitmeier², H. Cölfen², D. Schwahn³, V. Pipich¹

¹Jülich Centre for Neutron Science (JCNS) at MLZ, Forschungszentrum Jülich GmbH, Garching, Germany

²Department of Chemistry, Physical Chemistry, University of Konstanz, Konstanz, Germany

³Heinz Maier-Leibnitz Zentrum (MLZ), Technische Universität München, Garching, Germany

Nature provides many archetypes of highly ordered systems, and some of these biomaterials are known for their remarkable properties. An amazing example is the teeth of chitons (Fig. 1A-D) consisting of a magnetite/protein-polysaccharide hybrid shell. The fully mineralized teeth display remarkable properties such as outstanding fracture toughness, wear resistance and the highest reported hardness in biominerals [1]. Another intriguing biomaterial is Nacre (Fig. 1E-H), which consists of highly oriented aragonitic crystals and an organic matrix showing striking mechanical properties. Inspired by nature's fabrication strategies, we attempted to explore the use of biomolecules in the study of the mineralization of materials by combining the properties of Chiton teeth and Nacre. The mechanism of bio-inspired magnetite mineralization and the organic-inorganic hybrid structures were studied using SANS.

In the present work, we investigated an in situ mineralization process of magnetic nanoparticles inside the gelatin-chitin (the nacre organic matrix) composite with controllable mineral content varying from 20 wt % up to 70 wt % [2,3]. We were able to show that, with increasing mineral content, the gelatin hydrogel structure as well mechanical and magnetic properties are changed. We explored the role of gelatin hydrogels during bio-inspired magnetite mineralization by using small (SANS) and very small (VSANS) angle neutron scattering at the KWS-1 and KWS-3 diffractometers. The scattering contrast of the aqueous solution was adjusted through the D₂O content in order to determine the structure of the organic and inorganic components separately.

Magnetite/gelatin composites

Fig. 2 displays three SANS-VSANS scattering patterns of composites dissolved in pure and in 28 vol% D₂O, matching the scattering of magnetite and gelatin, respectively. Gelatin hydrogel shows a spatially

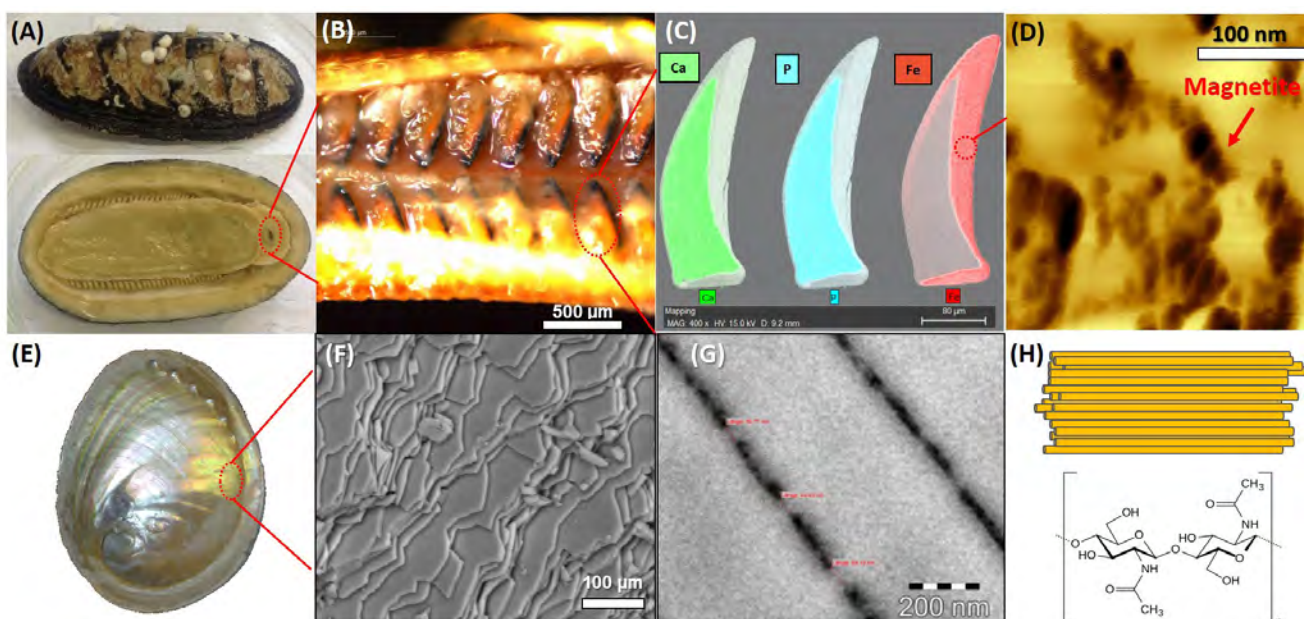


Figure 1: Hierarchical structures of Chiton teeth and Nacre: (A) Chiton; (B) the Chiton radula teeth; (C) SEM EDX results of the teeth; (D) AFM result on the tooth mineral shell; (E) Nacre; (F) Nacre tablet structure (SEM); (G) TEM result on the Nacre mineral bridges structure; (H) the α -chitin texture and the chemical structure.

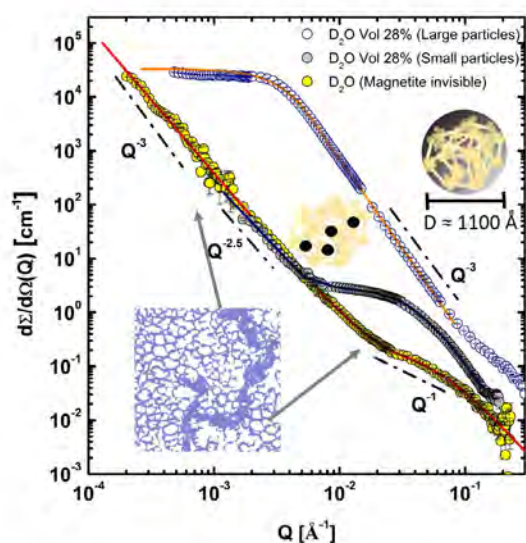


Figure 2: SANS-VSANS scattering profiles present small magnetite particles in the gelatin matrix (obtained by the coprecipitation method) in two contrasts correspondingly: in pure D_2O (magnetite is matched, circles with yellow filling) and 28 vol% D_2O (matrix is matched, circles with grey filling). The scattering profile of the gelatin-magnetite composite obtained by the partial-oxidation method in gelatin-matching contrast is plotted by symbols with white filling.

confined cavity structure appearing as homogeneously distributed cages throughout the gel matrix, which allows small magnetite particles to be formed. The interaction between ions and the network is another key parameter in controlling the mineralization mechanism. Strong interaction between ferric ions and gelatin molecules leads to an inhomogeneous mineralization and a ‘particle in matrix’ structure, while weak interaction between ferrous ions and the gelatin matrix causes a homogenous-like mineralization and a ‘matrix in particle’ structure.

Multifunctional layered magnetic composites

The introduction of a nacre organic matrix with chitin fibrous texture as a second organic matrix allows one to influence the mineral organization due to structure spatial constraints. Fig. 3 displays two SANS-VSANS scattering patterns of magnetite in a chitin-gelatin composite (top) and in a gelatin matrix (bottom) dissolved in 28 vol% D_2O (magnetite visible). The magnetite-gelatin-chitin sample shows a power law of Q^{-1} in the low Q -regime, approximately valid for linear structures, thereby indicating rod-like particles or stretched chains of particles. The scattering of magnetite in the gelatin matrix (ferrogel) in the low Q -range shows characteristic behavior of chain-like clusters having a Q^{-2} power law. Thus, the

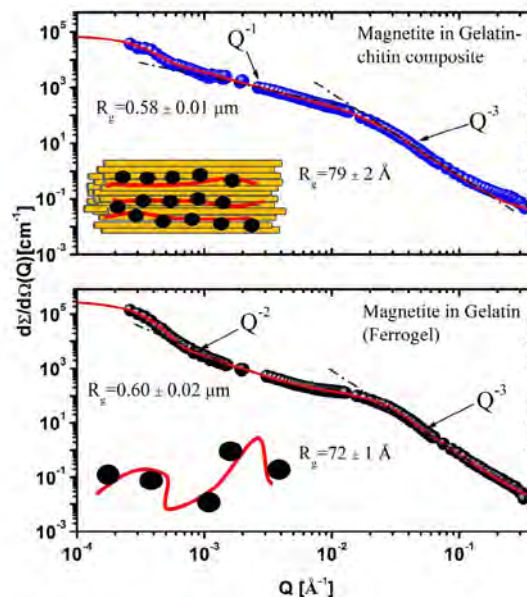


Figure 3: SANS-VSANS scattering patterns of samples measured in the matrix-matching contrast and mineralized by the coprecipitation method: (top graph) corresponds to a hybrid matrix when a demineralized Nacre layer was filled by gelatin, (bottom graph) corresponds to a ‘pure’ gelatin matrix.

chitin fiber-like structure of nacre organic matrices supports the formation of linear aligned magnetite nanoparticles (pearl necklace-like, with power law of Q^{-1}), whereas branch-like arrangement of nanoparticles (power law of Q^{-2}) are formed in gelatin gel matrices.

These structural and mineralization mechanisms are compared with the morphology of biological samples such as Chiton teeth, a comparison which will help to optimize the material for improved mechanical performance.

[1] L. M. Gordon, *Nature* 469, 194 (2011).

[2] M. Helminger et al., *Adv. Funct. Mater.* 24, 3187 (2014).

[3] M. Sigleitmeier et al., *Beilstein J. Nanotechnol.* 6, 134 (2015).

Chain exchange in polymeric micelles: Effect of core crystallization and conformational entropy

T. Zinn¹, L. Willner², V. Pipich³, D. Richter², R. Lund¹

¹Department of Chemistry, University of Oslo, Oslo, Norway

²Jülich Centre for Neutron Science (JCNS) & Institute of Complex Systems (ICS), Forschungszentrum Jülich GmbH, Jülich, Germany

³Jülich Centre for Neutron Science (JCNS) at MLZ, Forschungszentrum Jülich GmbH, Garching, Germany

The molecular exchange kinetics of a block copolymer micellar model system with partially crystallized cores was studied by TR-SANS using the kinetic zero average contrast technique (KZAC). We found that crystallinity leads to significant enthalpic and entropic contributions to the activation barrier for molecular exchange. While the former leads to enhanced stability, the entropic gain favors the process. A considerable part of the entropy change could be related to the gain in the conformational degree of freedom when the n-alkyl block is transferred from the confined state in the core to the solvent. The study provides deep insight into the fundamental processes of micellar kinetics and their microscopic mechanism, which is relevant to all self-assembled, semi-crystalline soft matter and biological materials.

Block copolymer micelles reach and maintain their thermodynamic equilibrium via molecular exchange processes. Through the TR-SANS/KZAC technique, molecular exchange was found to proceed primarily via the exchange of single chains (unimers), as suggested by theory. In the theoretical picture, the exchange is considered as an Arrhenius type process characterized by a single relaxation time $\tau = \tau_0 \exp(E_a / RT)$. The activation energy E_a is provoked by the expulsion of the core block into the solvent swollen corona, thereby forming an unfavorable extra polymer/solvent interface. A summary of previous experiments, theoretical background and experimental techniques has recently been published in an extensive review article. [1] Common to all kinetic studies performed so far has been the use of block copolymers where the insoluble block forms an amorphous melt-like core with properties similar to those in the bulk state. In this work we have thoroughly scrutinised the effects of core block crystal-

lisation on the kinetics by TR-SANS/KZAC using a micellar model system, as illustrated in Fig. 1.

Structure and thermodynamic properties

For the kinetic study, we used well-defined amphiphilic poly(ethylene oxide)-mono-n-alkyl ether (C_n -PEO5, $n = 21 - 30$) block copolymers. Small angle neutron scattering revealed that spherical star-like micelles are formed in an aqueous solution consisting of small collapsed n-alkane cores ($R_c = 2 - 3$ nm) surrounded by a water swollen PEO corona. [2] A key feature for the present study is the crystallisation of the n-alkanes inside the micellar cores. This was detected on dilute micellar solutions by the complementary techniques nano-DSC and densitometry. The melting points T_m and enthalpies of fusion ΔH_{fus} were extracted and indicated a clear melting point depression ΔT_m and partial crystallinity in comparison with pure n-alkanes. A detailed analysis revealed that ΔT_m is inversely proportional to the core size R_c (Gibbs-Thomson behaviour), showing that the n-alkanes are self-confined inside the micellar cores. [3]

TR-SANS and equilibrium kinetics

Chain exchange in dilute micellar solutions were monitored by TR-SANS using the KZAC technique. Fig. 2 shows the relaxation curves of C_{28} -PEO5 micelles at different temperatures. For all temperatures, the decay is a single exponential yielding

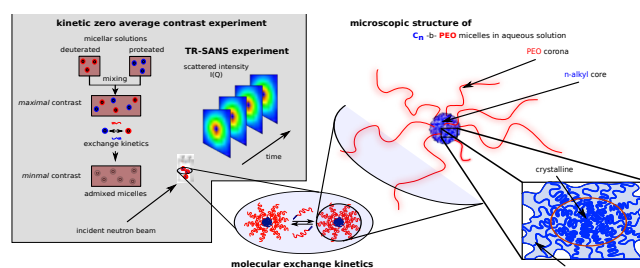


Figure 1: Schematic illustration of TR-SANS/KZAC experiments of molecular exchange kinetics in a micellar model system with crystallized cores.

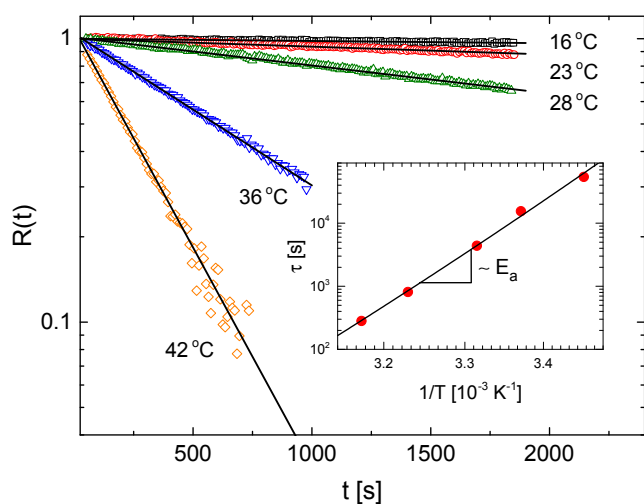


Figure 2: Relaxation curves of C_{26} -PEO5 micelles at different temperatures. Inset shows a corresponding Arrhenius plot to extract E_a and τ_0 .

characteristic times which were used to deduce the activation energies E_a and the fundamental time constants τ_0 by classical Arrhenius plots, an example being shown in the inset of Fig. 2.

It is important to note that the values extracted for the activation energy assume rather high numbers, which can be understood from the fact that E_a contains a significant contribution from the enthalpy of fusion, indicating that the residence time of the n-alkanes within the crystallized cores is significantly increased. A confusing result of the Arrhenius analysis is, however, the discovery of unphysically low τ_0 -values ranging from $10^{-27} - 10^{-16}$ s. In order to explain the extremely small times, we took into account a strong entropic contribution by replacing E_a with the total activation free energy analogous to the classical theory of Eyring for chemical reactions [4]. Accordingly, the Arrhenius equation was rewritten as $\tau = \tau_0^\dagger \exp(-\Delta S^\ddagger/R) \exp(\Delta H^\ddagger/RT)$ with ΔH^\ddagger and ΔS^\ddagger as the enthalpy and entropy change, respectively, for the transfer of an n-alkane chain from the interior of the core to the water-rich micellar surface.

Entropic contributions to molecular exchange

Within the above formalism, the fundamental time constants are given by $\tau_0 = \tau_0^\dagger \exp(-\Delta S^\ddagger/R)$. τ_0^\dagger was estimated as a characteristic diffusion time in the order of 3 – 14 ns leading to an entropic part of $\Delta S^\ddagger = 130 - 360$ J/K/mol to account for the extremely small numbers for τ_0 . This entropic contribution is due in part to ΔS_{fus} . However, there remains an excess entropy ΔS_{ex} which we assigned to a gain in

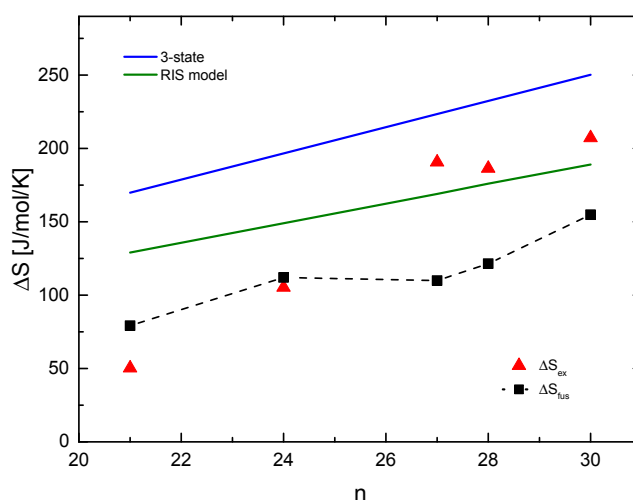


Figure 3: Entropic contributions to molecular exchange ΔS_{fus} and ΔS_{ex} vs n-alkane chain length. Solid lines represent a comparison to theoretical considerations: a simple 3-state model (blue line) and a full calculation based on Florys' RIS model (green line).

the conformational degree of freedom experienced by the n-alkane chain upon release from the confined core. In order to estimate the accompanying entropic gain during expulsion, we calculated first an upper value on the basis of a simple equally weighted three state approach and finally, by a full rotational isomeric state (RIS) calculation. The individual contributions ΔS_{fus} and ΔS_{ex} are plotted in Fig. 3 and compared to the theoretical calculations.

The plot demonstrates that, allowing for experimental uncertainties, the calculations are in good correspondence with the experimental values. The extracted entropy, ΔS^\ddagger , is slightly higher than the values calculated from RIS, which suggests an additional translational component to the entropy. In contrast to the enthalpic part, entropy causes the n-alkanes to be expelled faster as the chain can adopt more possible orientations in a dissolved state.

In conclusion, by combining kinetic and structural data measured by TR-SANS/SANS and by considering thermodynamic information obtained from DSC, the effect of core chain crystallization on the equilibrium kinetics could be elucidated.

- [1] R. Lund et al., *Adv. Polym. Sci.* 259, 51 (2013).
- [2] T. Zinn et al., *Soft matter* 10, 5212 (2014).
- [3] T. Zinn et al., *Phys. Rev. Lett.* 113, 238305 (2014).
- [4] T. Zinn et al., *ACS Macro Lett.* 4, 651 (2015).

Effect of proteins on calcium mineralization in solutions associated with wastewater desalination

Y. Dahdal¹, V. Pipich², R. Kasher¹, Y. Oren¹, D. Schwahn³

¹Zuckerberg Institute for Water Research, Jacob Blaustein Institutes for Desert Research, Ben-Gurion University of the Negev, Israel

²Jülich Centre for Neutron Science (JCNS) at MLZ, Forschungszentrum Jülich GmbH, Garching, Germany

³Heinz Maier-Leibnitz Zentrum (MLZ), Technische Universität München, Garching, Germany

A serious issue that arises in the reclamation of potable water using membrane technology such as reverse osmosis is that of biofouling and scaling. In particular, the formation of calcium phosphate at the surface of membranes poses a serious problem. In this report, we present SANS studies on the effect of the protein BSA on mineralization in a model salt solution (SSE), simulating the secondary effluent of a wastewater reclamation plant. These studies are important as the microorganisms that exist in wastewater excrete organic molecules such as proteins and polysaccharides. Individual and grafted BSA on gold nanoparticles was exposed to SSE. It is shown that BSA immediately induces stable composite particles in the micrometer scale. The dissolved BSA monomer is much more effective with respect to mineralization as compared to BSA grafted on gold nanoparticles. This is an interesting result as the grafted BSA simulates in some respects a biofilm at the surface of the membranes.

Reverse-osmosis (RO) desalination is an attractive technology nowadays for achieving high quality potable water from pretreated domestic wastewaters. One of the main limitations on cost-effective RO de-

salination is fouling of the membranes, mainly biofouling and scaling by calcium phosphate. The feed for RO treatment, i.e. the solution to be reclaimed as potable water, contains salt molecules as well as biomolecules such as proteins and polysaccharides excreted from microorganisms. These molecules strongly influence the mineralization of calcium phosphate and carbonate, as they emerge from specific interactions between organic and inorganic components widespread in nature and extensively studied under the concept of biomineralization [1,2].

We explored these phenomena using the technique of small-angle neutron scattering (SANS) at KWS-1 and 2 at MLZ [3-5]. The organic molecule bovine serum albumin (BSA) was exposed to a simulated secondary effluent (SSE) in order to study its effect on mineralization. The SSE solution represents a model salt solution simulating a RO desalination concentrate of the Shafdan secondary wastewater reclamation plant in Israel [6]. In these experiments, processes were simulated which occur in the feed at the high pressure side of the RO device during desalination.

Grafted protein BSA dissolved in salt-free water

We studied BSA as a free molecule and as grafted on gold nanoparticles (BSA-GNP) in order to simulate BSA attached as a biofilm at the membrane surface. The molecules were first characterized in salt-free water. Fig. 1 shows scattering from the BSA coated gold nanoparticles (BSA-GNP), which could be analyzed with the form factor of dimers, depicted as a solid line. The dimers are composed of two BSA monomers of 64.5 Å diameter at a distance of around 72 Å and attached by about three GNPs.

Proteins in SSE

Dissolving BSA in SSE leads to the fast formation of stable colloids in the micrometer scale within a few seconds. Fig. 2a shows a scattering pattern deter-

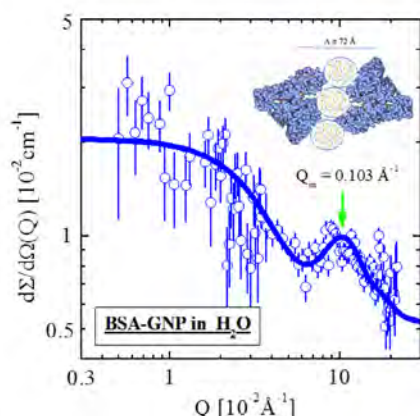


Figure 1: Scattering from BSA-GNP colloids in salt-free H₂O.

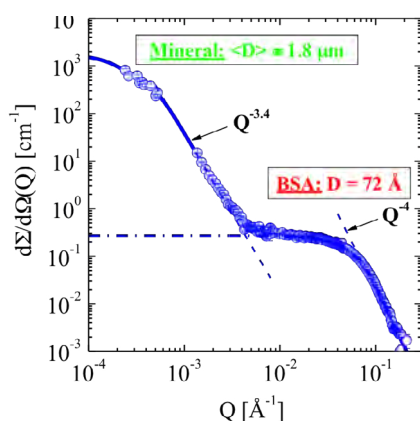


Figure 2a: Scattering immediately after dissolving BSA in SSE. At small and large Q values μm large protein-mineral composite particles and BSA monomers are observed, respectively.

mined immediately after mixing BSA in SSE. Strong scattering due to the formation of micron-sized particles is observed at small Q values, whereas at large Q 's scattering from BSA monomers is visible. Quantitative analysis shows that only $\sim 20\%$ of BSA is involved in the mineralization of composites of volume fraction $\sim 2.3 \times 10^{-4}$ which are composed of BSA and mineral of $\sim 34\%$ and $\sim 66\%$, respectively. Fig. 2b shows BSA-GNPs in salt-free water as well as its effect of initiating a large increase in scattering when exposed to the salts of SSE. Analysis shows that colloidal particles of $\sim 0.3 \mu\text{m}$ diameter and volume fraction $\sim 3 \times 10^{-5}$ are formed and are composed of $\sim 18\%$ protein and $\sim 81\%$ mineral. The latter information regarding the composite particles was derived from contrast variation of the SSE- H_2O /SSE- D_2O mixture.

Relevance of proteins for the process of RO Desalination

Modification of BSA is at the root of the main difference in the SANS scattering patterns presented in Fig. 2a and 2b. The apparent similarity of both studies is the fast process of the formation of stable organic-inorganic composites after adding both types of BSA entities to SSE. On the other hand, the BSA dimers with the order of 10^{-5} volume fraction induced a much smaller amount of mineral than BSA monomers which induced a mineral volume fraction of the order of 10^{-4} . A reasonable explanation might be that mineralization by BSA monomers occurs at any point on the protein monomer's surface, whereas BSA coated at GNPs adopts a constrained structure so that only part of the interface was exposed to the SSE solution.

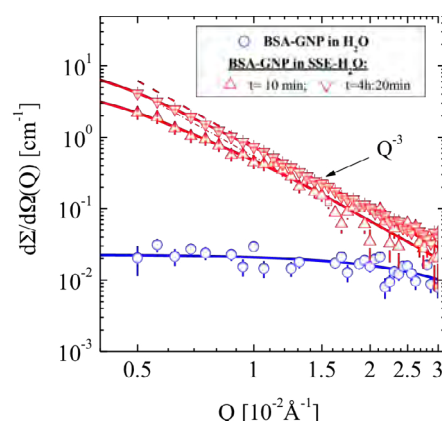


Figure 2b: BSA-GNPs in salt-free water (H_2O) and SSE- H_2O . Mineralization shows strong enhanced scattering.

Summary

This study unveils a strong interrelation between bio-molecules, represented in the present case by the protein BSA and the formation of calcium minerals, and of calcium phosphate in particular. It has been shown that GNP bound BSA dimers (Fig. 1) are less prone to calcium mineralization in comparison with dissolved BSA monomers. The results obtained from the present model system SSE suggest that removing both the organic macro-molecules and calcium phosphate nanoparticle in tertiary wastewater effluents prior to RO desalination may be highly beneficial. On the other hand, bio-molecules such as BSA are effective coagulants of calcium minerals. This observation might stimulate further research with the aim of finding chemical substances with similar organic functional groups which are sufficiently cheap and effective to be applied as coagulants prior to a RO or nanofiltration (NF) processes.

Acknowledgements

Funding by the Ministry of Science, Culture and Sport (MOST), Israel and the Bundesministerium für Bildung und Forschung (BMBF), Germany (grant no. WT0902), and by the German-Israeli Foundation for Scientific Research and Development (GIF) (grant no. I-101-307.4-2013) is gratefully acknowledged.

- [1] S. Mann, *Biom mineralization: Principles and Concepts in Bioinorganic Materials Chemistry*, Oxford University Press, Oxford (2001).
- [2] V. Pipich et al., *J. Am. Chem. Soc.* 130, 216879 (2008); A. Heiss et al., *Biophys. J.* 99, 3986 (2010).
- [3] V. Pipich et al., *Langmuir* 29, 7607 (2013).
- [4] Y. N. Dahdal et al., *Langmuir* 30, 15072 (2014).
- [5] Y. N. Dahdal et al., *Polymer* 85, 77 (2016).
- [6] Z. Steiner et al., *Environ. Sci. Technol.* 44, 7937 (2010).

Dynamic phase diagram of soft nanocolloids – A recipe book

S. Gupta¹, M. Camargo², J. Stellbrink³, J. Allgaier³, A. Radulescu⁴, P. Lindner⁵, E. Zaccarelli⁶, C. N. Likos⁷, D. Richter³

¹JCNS-SNS, Oak Ridge National Laboratory (ORNL), Bethel Valley Road, Oak Ridge, USA

²Centro de Investigaciones en Ciencias Básicas y Aplicadas, Universidad Antonio Nariño, Santiago de Cali, Colombia

³JCNS-1 and ICS-1, Forschungszentrum Jülich GmbH, Jülich, Germany

⁴Jülich Centre for Neutron Science (JCNS) at MLZ, Forschungszentrum Jülich GmbH, Garching, Germany

⁵Institute Laue-Langevin, Grenoble, France

⁶CNR-ISC and Dipartimento di Fisica, Università di Roma, Roma, Italy

⁷Faculty of Physics, University of Vienna, Vienna, Austria

We introduced new block copolymer micelles, which allows us to investigate a broad range of micellar aggregation numbers $10 \leq N_{\text{agg}} \leq 1000$ and concentrations $0.1 \leq \phi/\phi^* \leq 10$ of soft colloids using the same well-defined model system. We interpret rheological and dynamic light scattering (DLS) data in terms of recently developed experimental and theoretical approaches that quantitatively describe microscopic structures as observed by complementary small angle neutron scattering (SANS) experiments. This finally enabled us to derive the dynamic phase diagram of soft colloids, showing convincing agreement between experiment and theory without any adjustable parameter.

Neither Gaussian chains nor hard spheres

Recent studies on soft matter include a large variety of complex fluids such as synthetic polymers, biological macromolecules, colloids, amphiphilic systems and membranes, as well as liquid crystals. A currently active field of research is focused on the special class of soft colloids, i.e. elastic and deformable colloidal particles, which display a dual character between polymers and hard spheres [1]. Examples of such soft colloids are vesicles, dendrimers, microgels, polymer-grafted nanoparticles, block copolymer micelles and star polymers. Due to their hybrid nature, soft colloids macroscopically show interesting structural and dynamic properties resulting from their unique microscopic structure.

Multi-scale approach combining experiment, theory and simulation

We present a comprehensive experimental and theoretical study covering micro-, meso- and macroscopic length and time scales, which enables us to establish a generalized view in terms of the structure–property relationship and equilibrium dynamics of soft colloids. We introduce a new, tunable block copolymer model system, which allows us to vary the aggregation number, and consequently its softness, by changing the solvophobic-to-solvophilic block ratio ($m:n$) over two orders of magnitude. Based on a simple and general coarse-grained model of the colloidal interaction potential, we verify the significance of the interaction length σ_{int} governing both structural and dynamic properties. We put forward a quantitative comparison between theory and experiment without adjustable parameters, covering a broad range of experimental polymer volume fractions and regimes from ultra-soft star-like

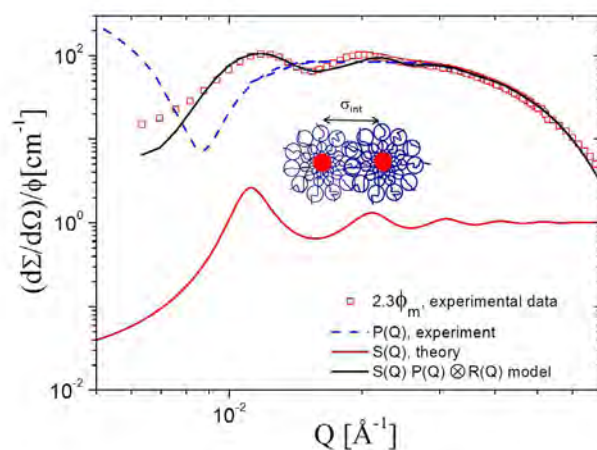


Figure 1: Normalized intensity $(d\Sigma/d\Omega)/\phi$ for $N_{\text{agg}} = 176$, $\phi/\phi^* = 2.3$ and $m:n = 1 : 37$, compared to theoretical results, together with contributions from form factor, $P(Q)$, and structure factor $S(Q)$. Inset schematic illustration of overlapping micelles and their interaction length.

to hard sphere-like particles, that finally results in the dynamic phase diagram of soft colloids. In particular, we find throughout the concentration domain a strong correlation between mesoscopic diffusion and macroscopic viscosity, irrespective of softness, manifested in data collapse on master curves using the interaction length σ_{int} as the only relevant parameter. A clear re-entrance in the glass transition at high aggregation numbers is found, recovering the predicted hard-sphere (HS) value in the hard-sphere-like limit. From the dynamical point of view, it has been verified that both the shear viscosity η_0 and the inverse of the self diffusion coefficient D_s behave in the same way around the overlap volume fraction ϕ^* of the micelles, apparently showing a strong correlation between mesoscopic diffusion and macroscopic viscosity, irrespective of the softness of the colloids.

Neutrons provide basis for rational design of materials

Small angle neutron scattering (SANS) reveals experimental structure factors $S(Q)$ which, in combination with liquid state theory and simulations, lay the basis for understanding soft colloids. As a representative example, in Fig. 1 the partial core contrast SANS $I(Q)$ for $m:n = 1:37$ and $\phi/\phi^* = 2.3$ is illustrated in the open symbols for the forward scattering. The curves for $S(Q)$ calculated for $N_{\text{agg}} = 176$ and the corresponding $\phi_{\text{TH}} = 0.162$, form factor $P(Q)$ from SANS and $P(Q)S(Q) \otimes R(Q)$ (resolution) are also displayed.

Dynamic phase diagram as recipe book

All information related to both statics and dynamics has been brought together in an experimental dynamic phase diagram which was compared with the theoretical one, as shown in Fig. 2. Again, packing fraction ϕ based on σ_{int} as the only relevant length scale was shown to be the appropriate reduction parameter, allowing a generic description of the macroscopic viscosity $\eta_0(\phi)$, the mesoscopic diffusivity dynamics $D(\phi)$ and microscopic structure $S(Q)$, and comparison of these properties for particles with varying softness. The excellent agreement between our new experimental systems with different but already established model systems shows the relevance of block copolymer micelles as a clever realization of soft colloids and the general validity of the coarse-graining approximation for describing

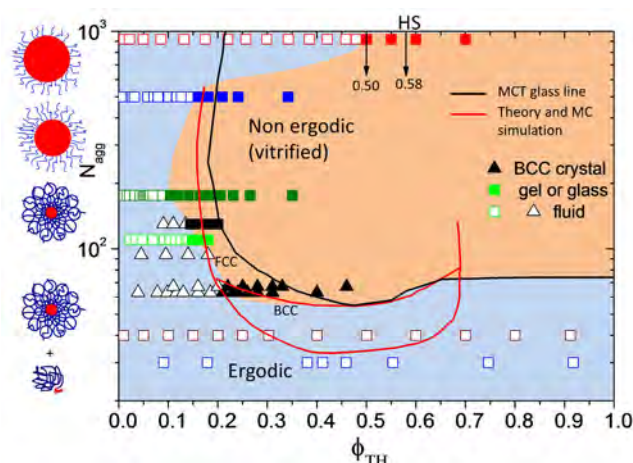


Figure 2: Dynamic phase diagram for soft colloids as a function of N_{agg} and the ϕ . Open symbols: fluid or ergodic phase; solid squares and stars: gel/glass phase (nonergodic); solid triangles: BCC; solid lines: theoretical equilibrium phase diagram, and the MCT ideal glass line; stars: star-polymers from Vlassopoulos et al. Side sketches: schematic representation of micelles and unimers with change in N_{agg} .

structural, dynamical and phase features of dense, soft colloid suspensions, which understanding could provide guidance in the rational design of materials for targeted applications. Finally, this recipe book for soft colloids enabled us to prove the validity of the Stokes-Einstein Relation in soft colloids up to the Glass Transition [3]. Our findings impressively confirm the microscopic origin of colloidal “softness” and its effects on the validity of the Stokes-Einstein relation for degrees of metastability, where it normally breaks down in the case of hard colloidal and molecular systems. In this way, they open up new realms for understanding and tailoring complex fluids, not only with respect to structure and phase behaviour, but also for colloidal dynamics.

[1] D. Vlassopoulos et al., *Soft Matter* 8, 4010 (2012).

[2] S. Gupta et al., *Nanoscale* 7, 13924 (2015).

[3] S. Gupta et al., *Phys. Rev. Lett.* 115, 128302 (2015).

Influence of Ibuprofen on phospholipid layers

S. Jaksch¹, F. Lipfert¹, A. Koutsioubas¹, S. Mattauch¹, O. Holderer¹, O. Ivanova¹, S. Hertrich², S. F. Fischer², B. Nickel², H. Frielinghaus¹

¹Jülich Centre for Neutron Science (JCNS) at MLZ, Forschungszentrum Jülich GmbH, Garching, Germany

²Physik-Department, Technische Universität München, and CeNS, Ludwig-Maximilians-Universität München, München, Germany

A basic understanding of biological membranes is of paramount importance as they comprise the very building blocks of life itself. Cells depend on a range of properties of the membrane in order to function. We investigated the influence of ibuprofen on the structure and dynamics of L- α -phosphatidylcholine (SoyPC) membranes using grazing incidence small-angle neutron scattering (GISANS) and neutron reflectometry at the Heinz Maier-Leibnitz Zentrum (MLZ) [1]. We were able to determine that ibuprofen induces a two-step structuring behavior in the SoyPC films, where the structure evolves from a lamellar phase for pure SoyPC, through a superposition of two hexagonal phases to a hexagonal phase at high concentrations. This behavior may be instrumental in explaining the toxic behavior of ibuprofen in long-term application.

Phospholipid membranes as model systems

Phospholipid membranes are used as model systems for the study of biological cell membranes. Aefner et al. reported stalk formation in such systems [2], [3]. While the relative humidity was used as a stimulus in those studies, we have used ibuprofen. Ibuprofen is a common drug used as a painkiller and for the treatment of cancer [4] and Alzheimer's [5]. SoyPC is a phospholipid known to form multilayers. Previous studies have reported ibuprofen to be toxic in long-term application, which has been linked to an increased permeability of the cell membrane [6], [7]. We investigated fully hydrated SoyPC membranes deposited on hydrophilic silicon surfaces at 35 °C.

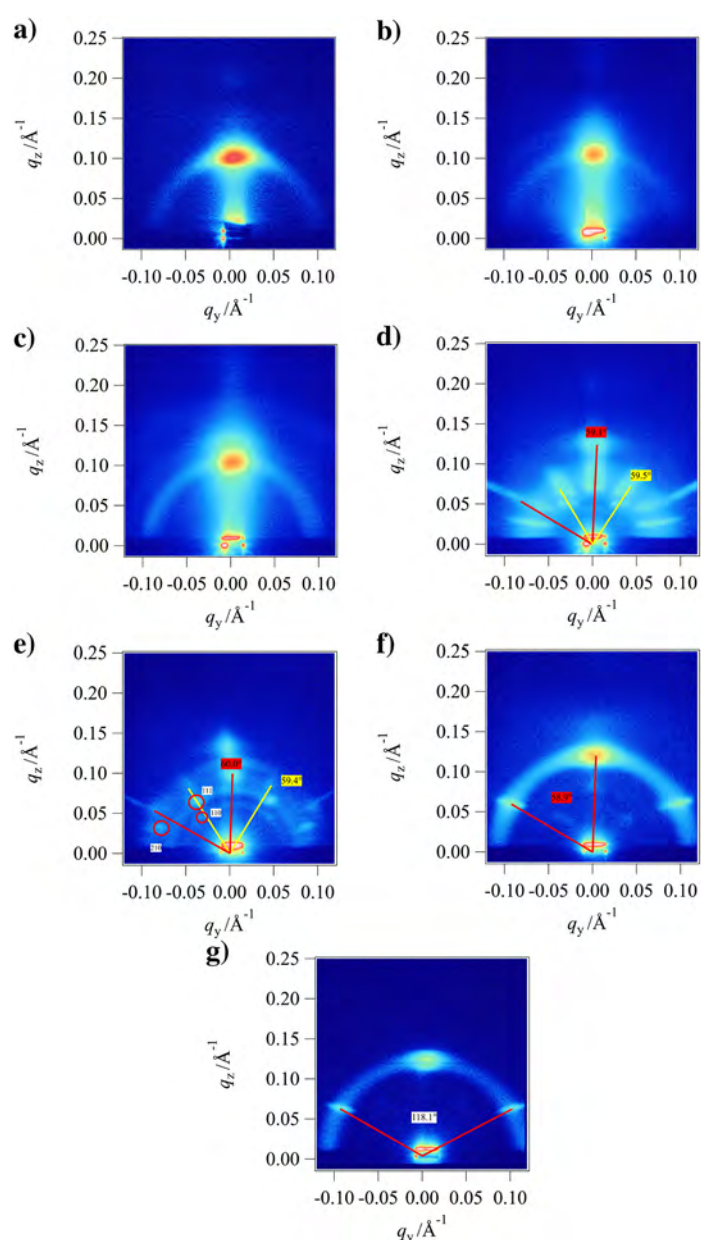


Figure 1: GISANS images at an incident angle of 0.2°. Concentrations of ibuprofen are (a) 0 mol %, (b) 13.6 mol %, (c) 25.0 mol %, (d) 34.5 mol %, (e) 43.1 mol %, (f) 50.2 mol %, and (g) 53.3 mol %. Scattering with a hexagonal symmetry is shown by yellow and red lines; colored labels show the angles between the respective lines. Indexed peaks are shown by red (hexagonal lattice with parallel axis to the surface), yellow (hexagonal lattice with perpendicular axis to the surface), and black (primitive tetragonal lattice) circles, where labels show the indexes.

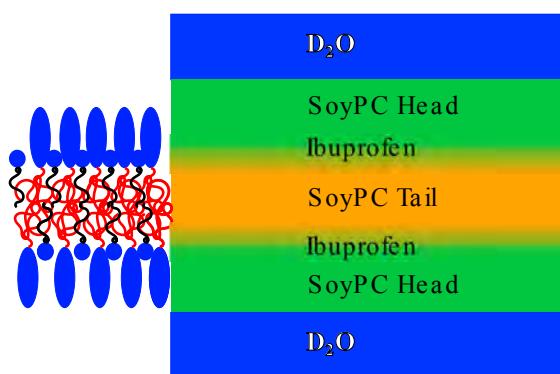


Figure 2: Depiction of the layer model used by the Parratt algorithm. For better visibility, the hydrophobic parts of SoyPC are in red, and those of ibuprofen are in black.

GISANS – Evolution of the structure

GISANS images of all samples can be seen in Fig. 1. These images show a clear evolution from a lamellar-based scattering to a scattering where several different structures contribute to a hexagonal structure with additional disordered lamellae, as can be seen from the persisting Debye-Scherrer ring.

At low concentrations, one single main maximum from lamellar scattering is visible. While hardly visible at 0 mol %, a Debye-Scherrer ring starts to appear at 13.6 and 25.0 mol %. This can be described as a powder of lamellar regions in the scattering volume.

Hexagonal structures emerge at 34.5 mol %. We find two hexagonal structures. In the 43.1 mol % GISANS image, the non-hexagonal peaks were indexed as the peaks of a primitive tetragonal lattice. Only a single hexagonal lattice is retained at 50.2 mol % and above.

Neutron reflectometry – Intra membrane composition

Reflectometry revealed the layer structure of the system as depicted in Fig. 2. In all systems, about 35 – 40 repetitions of these layers were found.

Another observation from these data is that the modeled roughness of the layers is maximal at 25.0 mol % ibuprofen. We attribute this roughness to a high strain of the membrane that occurs at the onset of ordering.

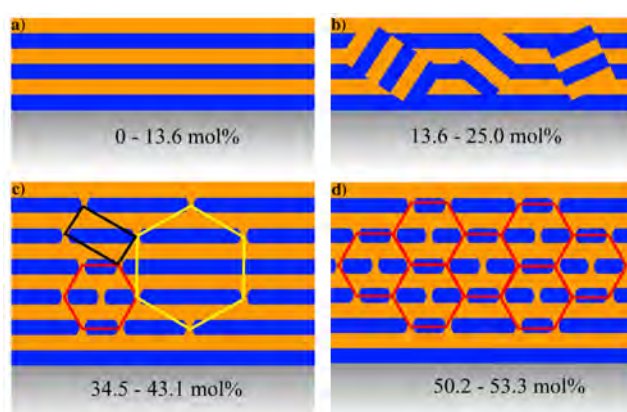


Figure 3: Sketch of the structural evolution of the sample. (a) For low concentrations of ibuprofen, the system is dominated by a lamellar structure while the introduction of more ibuprofen (b) induces disordering of lamellar areas and thus powder scattering of lamellar areas. In an intermediate concentration area (c), there are two different hexagonal lattices that are stabilized against each other by a primitive tetragonal lattice. At very high concentrations (d) only the hexagonal structure with an axis parallel to the substrate is retained. Color coding of the hexagonal structure corresponds to the color coding used in Fig. 1.

Overview and impact on toxicity

An overview of the structures observed is shown in Fig. 3. The introduction of ibuprofen into SoyPC phospholipid films has several effects. First, we observed the emergence of several coexisting lattices, and finally a single hexagonal lattice at 53.3 mol % ibuprofen in the film.

Regarding the toxicity, we have to bear in mind that the ibuprofen concentrations investigated here are beyond any medical applicability. However, it is conceivable that in the case of long-term treatment, where these complications occur, once a nucleation point for this damage is created, the damage starts to grow.

- [1] S. Jaksch et al., *Phys. Rev. E* 91, 022716 (2015).
- [2] S. Aeffner et al., *Eur. Phys. J. E* 30, 205 (2009).
- [3] S. Aeffner et al., *Proc. Natl. Acad. Sci. U. S. A.* 109, E1609 (2012).
- [4] M. J. Thun et al.; *J. Natl. Cancer Inst.* 94, 252 (2002).
- [5] S. Weggen et al., *Nature* 414, 212 (2001).
- [6] L. M. Lichtenberger et al., *Nat. Med.* 1, 154 (1995).
- [7] M. B. Boggara et al., *J. Phys. Chem. B* 114, 8061 (2010).

Photoactivation reduces side-chain dynamics of a LOV photoreceptor

A. Stadler¹, E. Knieps-Grünhagen², M. Bocola³, W. Lohstroh⁴, M. Zamponi⁵, U. Krauss²

¹Jülich Centre for Neutron Science (JCNS) and Institute for Complex Systems (ICS), Forschungszentrum Jülich GmbH, Jülich, Germany

²Institute of Molecular Enzymtechnology, Heinrich-Heine-Universität Düsseldorf, and Forschungszentrum Jülich GmbH, Jülich, Germany

³Lehrstuhl für Biotechnologie, RWTH Aachen, Aachen, Germany

⁴Heinz Maier-Leibnitz Zentrum (MLZ), Technische Universität München, Garching, Germany

⁵Jülich Centre for Neutron Science (JCNS) at MLZ, Forschungszentrum Jülich GmbH, Garching, Germany

We used neutron spectroscopy to study the molecular dynamics of a LOV photoreceptor protein in dark- and light-states [1]. The neutron scattering data revealed systematic and significant differences in the internal dynamics between the dark- and light-states of the photoreceptor. For a residue resolved interpretation of the neutron scattering data, we analysed molecular dynamics simulations of the LOV photoreceptor X-ray structure [1,2]. Light-induced changes in the protein result in altered side-chain mobility, primarily for residues on the protruding α -helix and LOV-LOV dimer interface. Our results stress the importance of molecular dynamics on the picosecond to nanosecond time scale for photoactivation and signaling in the LOV photoreceptor family.

LOV Photoreceptors

Flavin-binding light, oxygen and voltage (LOV) photoreceptors are ubiquitously distributed throughout all areas of life. The light-sensing function of all LOV proteins is intricately linked to the photochemistry of a flavin chromophore which, in the dark, is non-covalently bound within the LOV domain. Upon photon capture, a photocycle is initiated, which results in the formation of a covalent bond between a totally conserved cysteine residue and the 4a carbon atom of the flavin chromophore. As the longest living intermediate of the LOV photocycle, the adduct state represents the active and signaling state of the photoreceptor. We used neutron spectroscopy to probe the dynamics of the LOV photoreceptor PpSB1-LOV from *Pseudomonas putida* in the dark- and light-states. Our results stress the importance of molecular dynamics to the signaling mechanism of the PpSB1-LOV photoreceptor.

Neutron scattering experiments

We performed a comparative experimental study on the picosecond to nanosecond dynamics of the photoreceptor PpSB1-LOV in the dark- and light-state using neutron time-of-flight spectroscopy and neutron backscattering spectroscopy [1]. Neutron scattering experiments of protein solutions in a D_2O buffer were performed on the instruments TOFTOF and SPHERES at the Heinz Maier-Leibnitz Zentrum.

From the neutron scattering spectra, it was possible to distinguish between global protein diffusion and

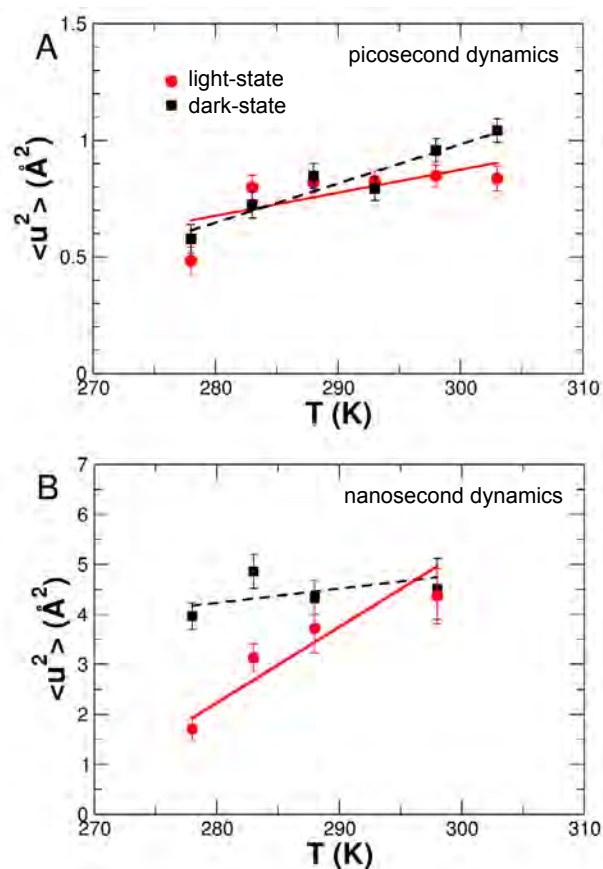


Figure 1: Mean square displacements $\langle u^2 \rangle$ of internal dynamics of the photoreceptor PpSB1-LOV in the light- and dark-adapted states. (A) Fast picosecond dynamics measured using TOFTOF, (B) slow nanosecond dynamics probed by SPHERES.

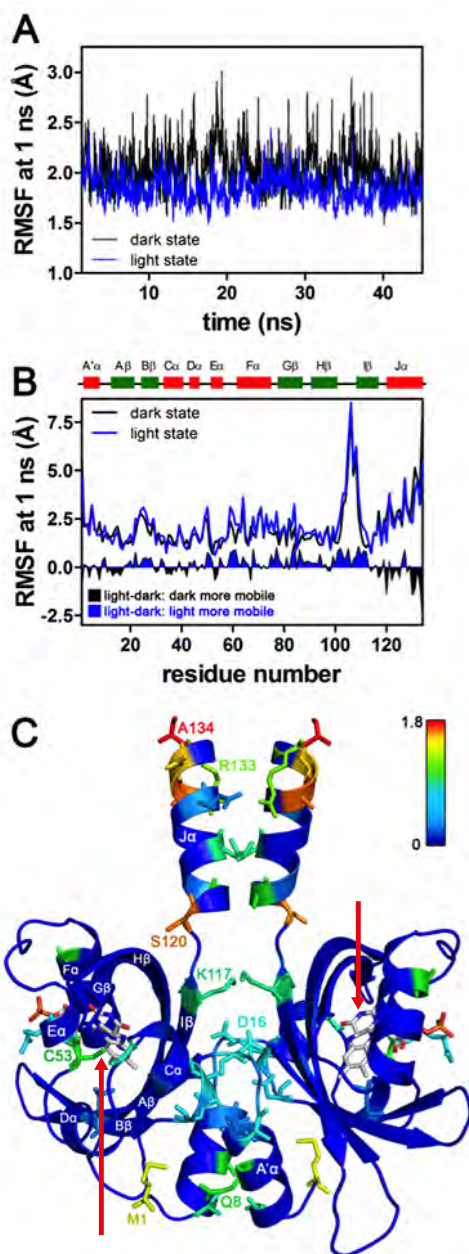


Figure 2: Analysis of molecular dynamics simulations. (A) By averaging over a time window of 1 ns. (B) Residue resolved RMSF plot obtained for the dark- (black line) and light-state simulations (blue-line). The corresponding light-dark RMSF plot highlights structural regions/residues showing increased fluctuations in the dark state (black filled peaks below the $Y=0$ line), compared to regions that are more mobile in the light state (blue-filled peaks above the $Y=0$ line). (C) Color coded structure model. For clarity only residues that show increased side-chain RMSF values in the dark state are shown in stick representation. The flavin chromophore is marked by an arrow.

internal macromolecular dynamics. The amplitudes of internal protein motions were quantified with mean square displacements $\langle u^2 \rangle$, see Fig. 1. Effective force constants $\langle k \rangle$ describing the resilience or ‘stiffness’ of the protein were derived from the temperature dependence of the $\langle u^2 \rangle$. Photoactivation results in a larger resilience of the photoreceptor on the fast picosecond time scale accompanied by a

slightly reduced flexibility at higher temperatures. On the slower nanosecond time scale, however, a significant softening of the light-state protein is observed accompanied by reduced flexibility of the photoreceptor over the temperature range.

Molecular dynamics simulations

To evaluate differences in side-chain mobility, we reanalyzed the molecular dynamics simulation data presented previously [1, 2] by calculating side-chain root mean square fluctuations (RMSFs) as a descriptor for side-chain flexibility. Here, the photoreceptor shows globally increased side-chain RMSF values in the dark-state simulation, compared to the respective light-state trajectory (Fig. 2A), which is in line with the experimentally observed increased $\langle u^2 \rangle$ values derived by SPHERES (Fig. 1). A residue-resolved RMSF plot identifies regions showing increased side-chain fluctuations in the dark-state simulations (Fig. 2B). To highlight structural regions that show increased side-chain fluctuations, the X-ray structure of the photoreceptor dimer is color coded according to the calculated light-dark RMSF absolute values, showing an increased flexibility for residues located in the dimer interface region and near the flavin chromophore (Fig. 2C).

Conclusions

We performed the first neutron scattering study of a LOV photoreceptor, revealing systematic and significant differences in fast picosecond to nanosecond side-chain dynamics between the dark- and light-state of the PpSB1-LOV photoreceptor. Our observation is in agreement with the assumption that side-chains located mostly on the protruding $J\alpha$ -helix and the LOV-LOV dimer interface become dynamically more stabilized upon photoactivation. Our results stress the importance of side-chain dynamics on the picosecond to nanosecond time scale for photoactivation and signaling in the LOV photoreceptor family. Based on our data, we can suggest that the reduction of side-chain dynamics of the $J\alpha$ -helix in the light-state transfers the light signal to other binding partners. Our work demonstrates the potential of neutron spectroscopy for the investigation of the role of molecular dynamics in the signal transduction of photoreceptor proteins.

[1] A. Stadler et al., *Biophys. J.* 110, 1064 (2016).

[2] M. Bocola et al., *Front. Mol. Biosci.* 2, 55 (2015).

Near surface dynamics in thin adsorbed layers of thermoresponsive microgel particles

S. Wellert¹, O. Ivanova², O. Holderer², R. v. Klitzing¹, K. Gawlitza^{1,3}

¹Stranski-Laboratory for Physical and Theoretical Chemistry, Technische Universität Berlin, Berlin, Germany

²Jülich Centre for Neutron Science (JCNS) at MLZ, Forschungszentrum Jülich GmbH, Garching, Germany

³Division 1.9 Chemical and Optical Sensing, BAM Federal Institute for Materials Research and Testing, Berlin, Germany

Scanning the dynamic profile across thin polymer coatings opens a new field for a better understanding and design of functionalized surfaces. Surface functionalization based on stimuli-responsive colloids is an active area of research. Here, the adsorption of thermoresponsive microgel particles at silicon surfaces was investigated. The cooperative and inner dynamics of the dispersed particles were characterized by neutron spin echo spectroscopy in transmission geometry (NSE). To access the inner properties of the adsorbed microgel particles, the newly established method of neutron spin echo spectroscopy under grazing incidence (GINSES) was used. A slowing down of the inner dynamics in the vicinity of the substrate and a relaxation comparable to the bulk at increasing distance was observed.

Surface functionalization by adsorbed microgel particles

Microgels are colloidal particles with an inner polymer network structure based on chemical cross-linking. In water, thermoresponsive microgels show a temperature dependent swelling/deswelling behavior. The formation of stimuli-responsive surface structures using microgel particles as colloidal building blocks is an active field of research. In this respect, it is essential to obtain detailed knowledge regarding the properties of single adsorbed microgel particles and particle layers, and to control the layer formation. Among other potential applications, microgel layers at solid interfaces are discussed as new biomaterials and coatings.

We investigated microgels made of the monomer 2-(2-Methoxy-ethoxy)ethyl methacrylate and the comonomer Poly(ethylene glycol)methyl ether

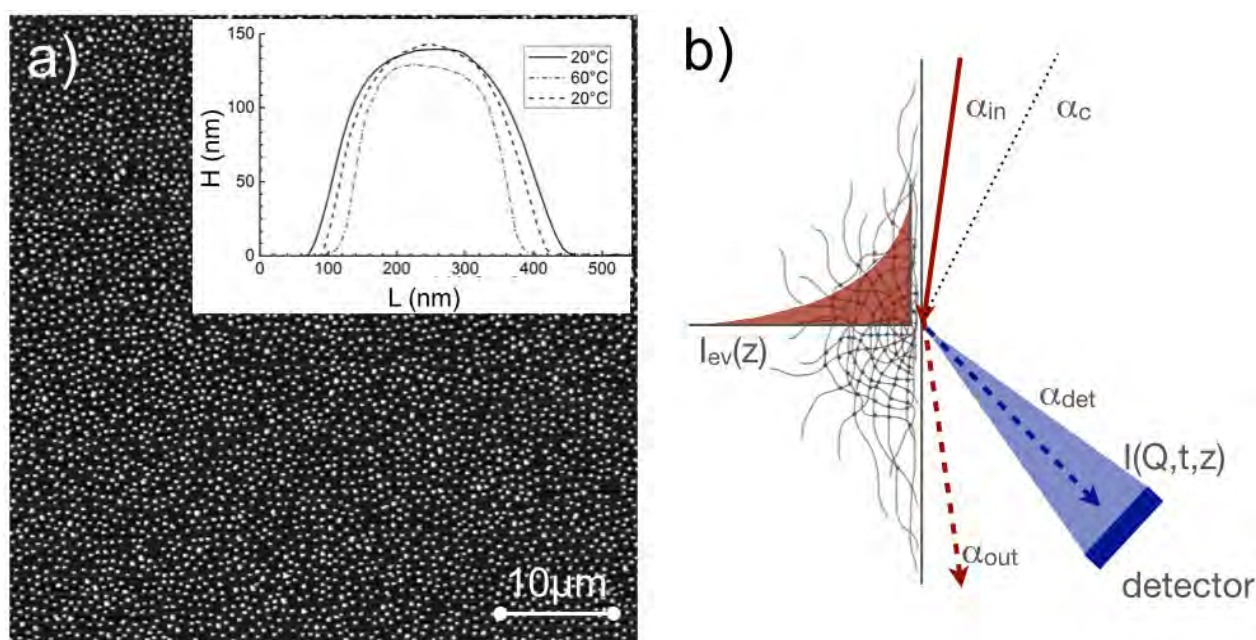


Figure 1: a) AFM image of microgels adsorbed on the surface of a silicon block (26 mol-% comonomer). The samples were prepared as loosely packed particle layers to minimize particle-particle interactions. The inset compares the averaged cross sections of individual particles in aqueous environment at 20 °C, 60 °C and again, at 20 °C. b) Scheme of the GINSES experiment. A neutron beam impinges onto a silicon substrate covered with a sample layer under an angle of incidence α_{in} . Below the critical angle of total reflection α_c an evanescent wave $I_{ev}(z)$ is generated, penetrates the sample to a depth z and is scattered from the sample layer. The scattered intensity $I(Q, T_{NSE}, z)$ is detected at α_{det} .

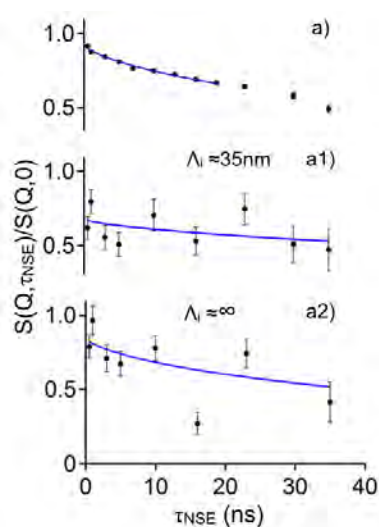


Figure 2: Intermediate scattering functions $S(Q, t_{\text{NSE}})/S(Q, 0)$ from samples of 5 mol-% comonomer measured at $Q = 0.08 \text{ \AA}^{-1}$. Plot a) results from bulk measurements in transmission geometry. Plots a1) and a2) were measured under grazing incidence in GINSES mode. a1): The angle of incidence was $\alpha_{\text{in}} = 0.35^\circ$ ($\alpha_{\text{c}} = 0.5^\circ$) at a penetration depth of about 35 nm. a2): At $\alpha_{\text{in}} = 1.0^\circ$ ($\alpha_{\text{in}} > \alpha_{\text{c}}$) scattering occurs over the whole particle height. Solid lines are fits to the Zimm-dynamics.

methacrylate in suspension [1,2] and adsorbed at silicon substrates [3]. These microgels have a volume phase transition temperature close to body temperature (37 °C, Figure 1a). Adsorbed at solid substrates, such coatings could support implant integration into its physiological environment by minimization of infections and inflammation.

Investigation of near surface dynamics of thin polymer surface structures

Many experimental techniques provide only indirect access to the dynamics in the vicinity of a solid interface. Neutron scattering methods are suitable for studying the inner structure and dynamics of adsorbed polymer structures. The combination of grazing incidence geometry and neutron spin echo spectroscopy (GINSES) opens up new experimental routes for the investigation of the dynamics with depths resolution in the time range between a few ns up to 100 ns. The experimental challenge is to scan the dynamics profile within the microgels perpendicular to the substrate (Figure 1b). Understanding the changes in the swelling/deswelling behavior of microgels after adsorption at a surface is of general interest.

Microgel dynamics in suspension and adsorbed state

Neutron spin echo spectroscopy in transmission mode was used to characterize the translational and inner dynamics in the bulk. Using GINSES, the inner dynamics of adsorbed microgel particles was explored [4]. As an example, Figure 2 summarizes the normalized intermediate scattering functions for a microgel system of 5 mol-% comonomer. As a refer-

ence, graph a) shows the data measured in the bulk. GINSES was carried out at a constant $Q = 0.08 \text{ \AA}^{-1}$. Data analysis showed Zimm-type dynamics. Apparent inner viscosities of 9.2 mPas have been estimated. Compared to D_2O , an increase in viscosity by a factor of 6.6 occurs.

Graphs a1) and a2) show the intermediate scattering functions recorded at two angles of incidence below ($\alpha_{\text{in}} = 0.35^\circ$) and above the critical angle of total reflection $\alpha_{\text{c}} = 0.5^\circ$ ($\alpha_{\text{in}} = 1.0^\circ$). This corresponds to the neutron penetration depths of 35 nm and virtually infinity. The solid lines are fits to Zimm-type dynamics only. A relaxation rate of $\Gamma = 0.010 \text{ ns}^{-1}$ (a) is found in the bulk. At a penetration depth of 35 nm, the neutrons are scattered from a region in the sample very close to the substrate. Here, for a1) $\Gamma = 0.0036 \text{ ns}^{-1}$ is obtained. At infinite penetration depth, the full height of the adsorbed particles is explored, leading to a relaxation rate of $\Gamma = 0.010 \text{ ns}^{-1}$.

Compared to the bulk, the relaxation rate in a1) is slowed down by a factor of 3 to 4. In the framework of Zimm dynamics, this corresponds to an apparent increase in the intrinsic solvent viscosity. The strong interaction of the microgels with silicon substrates and the compression of the network could be responsible for a region with inner dynamics different from the bulk behavior. Thermal fluctuations seem to be damped or suppressed.

At larger distances from the substrate, its influence seems to vanish and network fluctuations are again the dominant contribution to the dynamics. The relaxation rates are approximately the same as in the bulk measurement. This suggests that the confinement effect on the inner dynamics diminishes with increasing distance from the substrate, restoring a freely fluctuating network as observed in the bulk.

These experiments demonstrate the feasibility of the GINSES technique for thin polymer substrates. They indicate a slowing down of the inner dynamics of the adsorbed microgels in the vicinity of the substrate.

[1] K. Gawlitza et al., *Polymer* 55 (26), 6717 (2014).

[2] S. Wellert et al., *Macromolecules* 48 (14), 4901 (2015).

[3] S. Wellert et al., *Langmuir* 31 (7), 2202 (2015).

[4] K. Gawlitza et al., *Macromolecules* 48 (16), 5807 (2015).

SrC(NH)₃: Structure and properties of a nitrogen-based carbonate analogue

R. Missong¹, J. George¹, A. Houben¹, M. Hoelzel², R. Dronskowski¹

¹Institut für Anorganische Chemie, RWTH Aachen University, Aachen, Germany

²Heinz Maier-Leibnitz Zentrum (MLZ), Technische Universität München, Garching, Germany

Strontium guanidinate, SrC(NH)₃, the “nitrogen cousin” of the ubiquitous carbonate SrCO₃, is the very first compound including the doubly deprotonated anion of the guanidine molecule. SrC(NH)₃ was characterized via XRD, IR spectroscopy as well as density-functional theory, while neutron diffraction turned out as essential for clarifying the H-atom positions. The novel phase crystallizes in the hexagonal space group *P*6₃/*m* with a layer-like structural motif built from Sr²⁺ ions and complex anions of the type C(NH)₃²⁻; the latter adopt the unusual trinacria shape. While the anion’s CN₃ core is planar, the H atoms are slightly dislocated above and below the CN₃ plane. This study reveals the first insights into the bonding and crystal packing of the formerly unknown anion.

A short glimpse into guanidine chemistry

When Strecker first synthesized guanidine in 1860, some of its properties (such as the molecule’s enormous basicity) came to light [1]. This very basicity may be the reason why only trivial species such as substituted guanidines or guanidinium cations were

studied in terms of structure and properties thereafter. In 2009, the crystal structure of pure guanidine was eventually clarified using X-ray diffraction [2], and verified four years later by a single-crystal neutron-diffraction experiment to corroborate the somewhat crude H positions [3]. Furthermore, no anionic guanidates were identified until 2011 when RbCN₃H₄ was finally synthesized from guanidine and RbH [4], soon followed by other alkali-metal guanidates. We note that in 1922, Franklin already claimed the synthesis of a doubly deprotonated guanidinate anion, but without convincing evidence [5]. This anion has now been synthesized and structurally characterized in the alkaline-earth metal guanidinate SrC(NH)₃ [6].

A look into the crystal structure

A rough structural model of guanidinate was derived from X-ray powder data, extended in terms of H positions by DFT calculations, and eventually validated by means of high-resolution neutron diffraction (instrument SPODI, Fig. 1, left). SrC(NH)₃ crystallizes in the hexagonal space group *P*6₃/*m* (no. 176) with two formula units per unit cell (Fig. 2). The Sr ions line up along *c* with *z* = 0 and ½ while the gua-

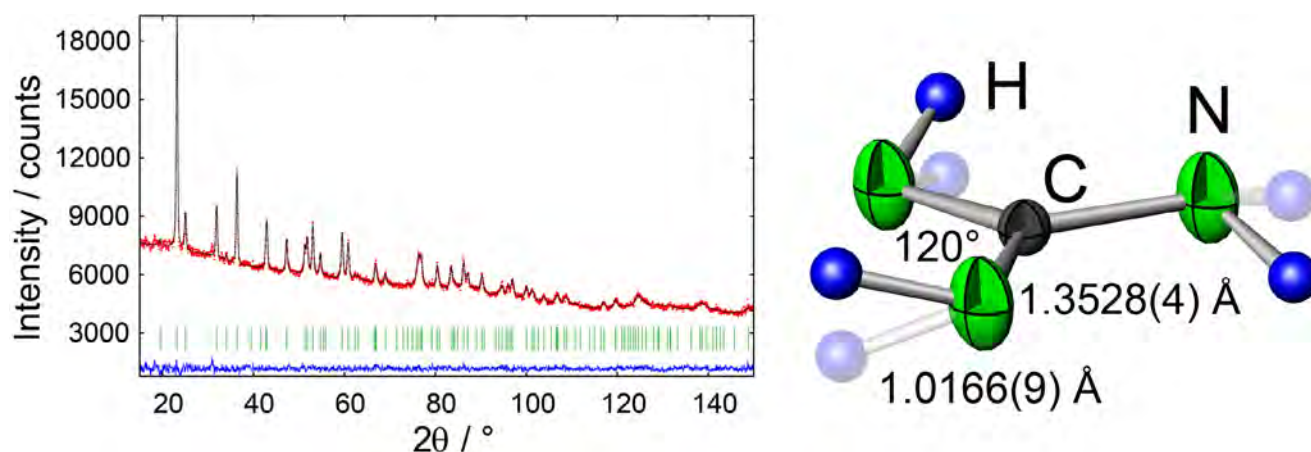


Figure 1 left: Observed (red), calculated (black) and difference intensities (blue) of the neutron Rietveld refinement of SrC(NH)₃ ($\lambda = 1.5484 \text{ \AA}$) with the Bragg reflections in green, right: ORTEP representation of the guanidine trinacria based on neutron data with 50 % probability. H lies equally above and below the mirror plane. (Adapted from [6]. © 2015 Wiley-VCH Verlag GmbH & Co. KGaA, Weinheim).

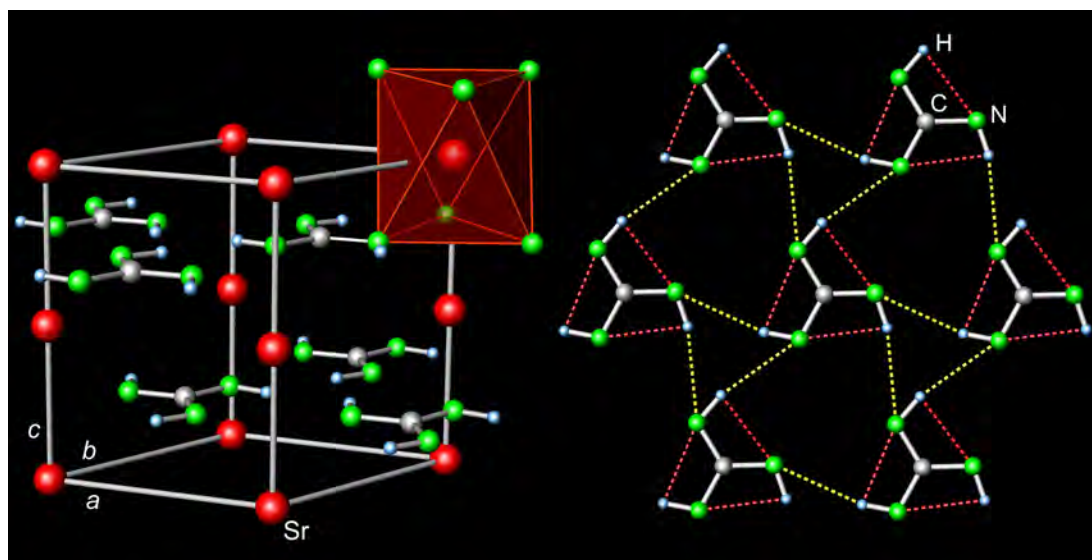


Figure 2 left: Perspective view into the crystal structure of $\text{SrC}(\text{NH}_3)_2$ with distorted octahedral coordination around Sr^{2+} ; right: layer of guanidinate anions with the trinacria motif and H contacts of intermolecular (yellow) and intramolecular (red) nature. (Adapted from [6]. © 2015 Wiley-VCH Verlag GmbH & Co. KGaA, Weinheim).

guanidinate anions are found at $z = \frac{1}{4}$ and $\frac{3}{4}$ such as to arrive at an alternating layer-like motif. Six N atoms coordinate one Sr^{2+} ion at 2.67 Å to form trans-aligned face-sharing SrN_6 octahedra along c . The CN_3 core is fully planar and the anion closely follows the predicted C_{3h} symmetry with a trinacria shape (Fig. 1, right). Despite significant incoherent scattering by the hydrogen atoms, refinement of the moderately anisotropic (C, N) and isotropic (H) displacement parameters was perfectly performed using the Rietveld method on neutron powder diffraction data (Fig. 1, left).

Where are the H atoms?

In order to obtain physically plausible N–H bond distances and displacement parameters, the H atom must shift slightly (0.3 Å) away from the mirror plane of the CN_3 core (Fig. 1, right). Within a centrosymmetric description, H lies either above or below (50% each) the CN_3 plane. This leads to two different conformational isomers of $\text{C}(\text{NH}_3)_2^{2-}$ for which either two or three H atoms remain on one side. While one may well imagine a long-range order of the dislocated H atoms, theory does not support such ordered conformational isomers as a positional transition from one side of the CN_3 plane to the other invokes only marginal energy differences below 2 kJ mol⁻¹. Apparently, the two conformational isomers are fully disordered in the crystal.

Chemical bonds and their strengths

The anion contains only one short C–N and one short N–H bond. The C–N distance of 1.35 Å lies between the values found in rubidium guanidinate

(1.33 and 1.39 Å) [4] and in pure guanidine (1.30 and 1.37 Å) [3]; indeed, the 1.35 Å corresponds to a bond order of $\frac{1}{3}$. The N–H distance of 1.02 Å compares well with the typical values. And yet, there is an unknown N–H⋯N motif within the layer of the guanidinate units (Fig. 2, right). One finds a comparatively long H⋯N = 2.59 Å of intermolecular type (yellow dashes), significantly wider than the proton-acceptor distances in pure guanidine (1.96–2.35 Å) [3] or in RbCN_3H_4 (2.01 Å) [4]. In addition, there is a shorter intramolecular H⋯N = 2.36 Å because the H atom “binds back” (red dashes) to another N atom of the same complex anion. To quantify the suspected H bonds, Crystal Orbital Hamilton Population (COHP) analysis [7] was performed. There, only tiny covalent contributions (less than 5 kJ mol⁻¹) for the H⋯N = 2.59 Å intermolecular distance are found, while the interaction of the H⋯N = 2.36 Å intramolecular one is slightly repulsive. Thus, this bond does not exist at all. We conclude that the crystal structure of $\text{SrC}(\text{NH}_3)_2$ is not held together by significant H bonds, but from ionic forces. At the same time, the crystal structure permits efficient packing of the bulky $\text{C}(\text{NH}_3)_2^{2-}$ anion. Further details on synthesis and structural investigations can be found in [6].

[1] A. Strecker, *Liebigs Ann. Chem.* 118, 151 (1861).

[2] T. Yamada et al., *Chem. Eur. J.* 15, 5651 (2009).

[3] P. K. Sawinski et al., *Cryst. Growth Des.* 13, 1730 (2013).

[4] V. Hoepfner et al., *Inorg. Chem.* 50, 3799 (2011).

[5] E. C. Franklin, *J. Am. Chem. Soc.* 44, 486 (1922).

[6] R. Missong et al., *Angew. Chem. Int. Ed.* 54, 12171 (2015).

[7] R. Dronskowski et al., *J. Phys. Chem.* 97, 8617 (1993).

Low temperature oxygen diffusion in $(\text{Nd/Pr})_2\text{NiO}_{4+\delta}$ explored using single crystal neutron diffraction

M. Ceretti¹, O. Wahyudi², A. Cousson³, A. Villesuzanne², M. Meven⁵, B. Pedersen⁴, W. Paulus¹

¹Institut Charles Gerhardt, Université de Montpellier, Montpellier, France

²ICMCB, CNRS-Université de Bordeaux, Pessac, France

³Laboratoire Léon Brillouin, Gif sur Yvette, France

⁴Heinz Maier-Leibnitz Zentrum (MLZ), Technische Universität München, Garching, Germany

⁵Institute of Crystallography, RWTH Aachen at MLZ and Jülich Centre for Neutron Science (JCNS) at MLZ, Garching, Germany

N $d_2\text{NiO}_{4+\delta}$ and $\text{Pr}_2\text{NiO}_{4+\delta}$ are today considered the most promising candidates for mixed electron/ion oxygen conductors at moderate temperatures. In order to investigate their oxygen diffusion pathways, we explored their structure via single crystal neutron diffraction. Large size and high quality single crystals were grown by using an image furnace. While the real structure for both compounds is incommensurate, the scattering density of the respective average structures was reconstructed using the Maximum Entropy Method. Unusually high displacement factors were found for the equatorial and apical oxygen atoms, showing large amplitudes. At 400 °C the anharmonic apical oxygen displacements are strongly enhanced, showing a double well potential and pointing towards the interstitial vacancy sites, creating a quasi continuous shallow energy diffusion pathway between apical and interstitial oxygen sites.

floating zone method [1]. The optimized growth parameters allowed large and homogeneous crystals without significant mosaic spread and stacking faults to be obtained. Both compounds crystallize in the K_2NiF_4 structure type and can accommodate extra oxygen atoms on interstitial sites, the non-stoichiometric region being $0 < \delta < 0.25$. This makes it possible to study the interplay of interstitial and apical oxygen atoms together with structural and lattice dynamic modifications, which are important factors with respect to diffusion mechanisms. In particular, we analysed more accurately oxygen displacement factors in PNO and NNO related to oxygen doping on interstitial sites, which is supposed to induce phonon assisted oxygen diffusion at moderate temperatures. To achieve this, we explored temperature dependent high resolution single crystal neutron diffraction studies combined with data analysis using the Maximum Entropy algorithm (MEM).

Oxygen diffusion pathway

The nuclear structures of the as-grown single crystals were investigated using single crystal neutron diffraction on different neutron 4-circle diffractometers (5C2@LLB at the ORPHEE reactor in Saclay,

High quality, large size single-crystals of $\text{Nd}_2\text{NiO}_{4+\delta}$ (NNO) and $\text{Pr}_2\text{NiO}_{4+\delta}$ (PNO) were successfully grown with the help of a mirror furnace, using the

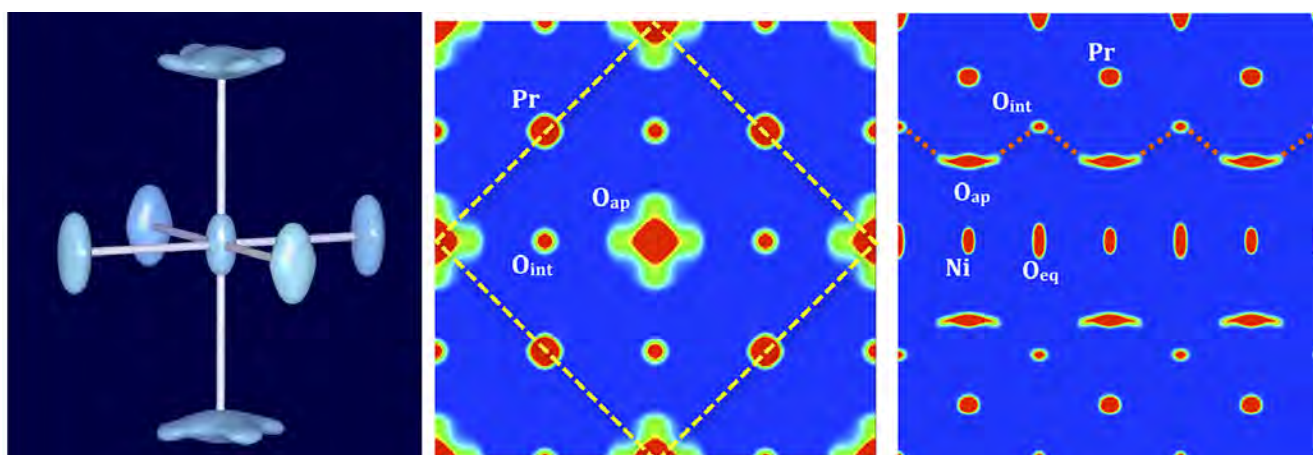


Figure 1: Representation of the nuclear densities of $\text{Pr}_2\text{NiO}_{4.25}$ obtained from MEM reconstruction of single crystal neutron diffraction data at room temperature. On the left: isosurfaces (density: $2 \text{ fm}^3/\text{Å}^3$) of the NiO_6 octahedron; in the middle: $2a \times 2a$ projection of the $14/mmm$ unit cell (the F-centred cell is outlined by yellow dashed bars) and on the right $3a \times c$ projection of the I-cell. A dashed red line indicates the oxygen diffusion pathways along the $[110]$ -direction in the F-cell (equivalent to $[100]$ of the I-cell), between apical and interstitial sites.

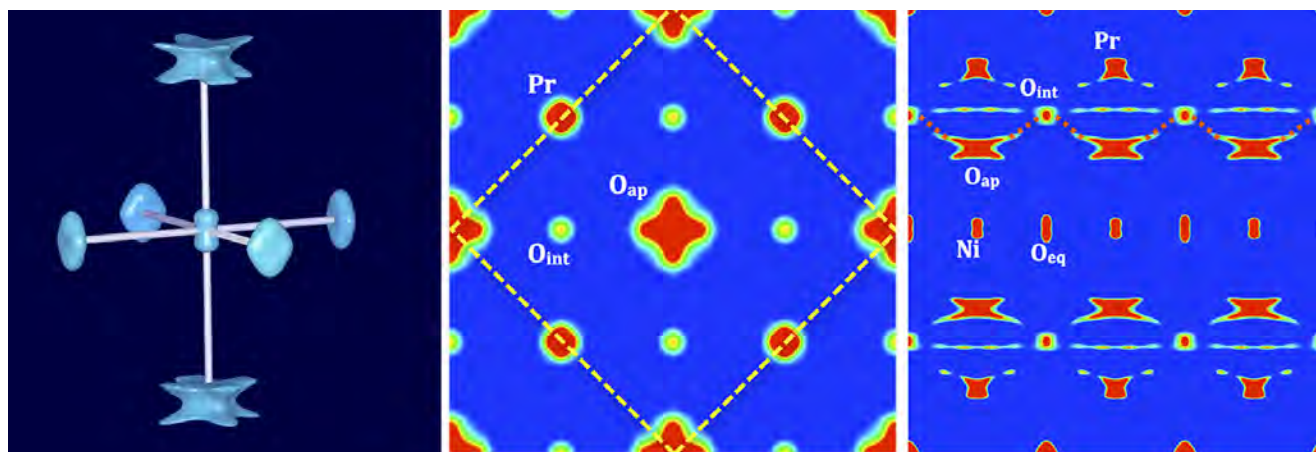


Figure 2: Representation of the nuclear densities of $\text{Pr}_2\text{NiO}_{4.25}$ obtained from MEM reconstruction of single crystal neutron diffraction data at 400 °C. Left: isosurfaces of the NiO_6 octahedron (density: $2 \text{ fm}/\text{\AA}^3$); middle: $2a \times 2a$ projection of the $I4/mmm$ unit cell (the F-centred cell is outlined by yellow dashed bars) and on the right $3a \times c$ of the I-cell. A dashed red line indicates the oxygen diffusion pathways along the $[110]$ -direction in the F-cell (equivalent to $[100]$ of the I-cell), between apical and interstitial sites.

HEiDi@MLZ and RESI@MLZ at the FRM II reactor in Garching).

Even though the real structure is quite complex, showing an incommensurate modulation, the refinements were done in the average space group $F4/mmm$ (equivalent to the standard space group $I4/mmm$). The resulting phased F_{obs} were subsequently used for MEM reconstruction. This approach has the advantage of according equal importance to strong and weak reflections, resulting in a much better defined background, when compared to the classical Fourier-methods. In addition, it yields an anharmonic description of the scattering densities, the only constraint on describing scattering densities being imposed by the symmetry of the used space group.

Neutron single crystal diffraction measurements have been performed in air at RT and at 400 °C [2], just above the incommensurate-commensurate phase transition, occurring at 360 °C.

At RT, the apical oxygen scattering densities correspond to an anisotropic libration mode in the (a,b)-plane and specifically along $[110]$, on an outer perimeter of about 2 Å, with a tilt angle of the NiO_6 octahedron of about 25°. It becomes evident that the large amplitudes of the apical oxygen atoms, pointing towards the adjacent interstitial sites, generate a low energy diffusion pathway between these two sites (right part of Fig. 1). The $[110]$ displacements of the apical oxygen atoms correspond to almost half of the diffusion pathway towards the interstitial sites. One may presume these displacements to be in part dynamically activated, leading to significant

oxygen mobility already at ambient temperature. The disorder scenario of the apical oxygen atoms is completely modified at 400 °C compared to the room temperature structure, showing a double well potential and strongly increasing the anharmonic displacements of the apical oxygen atoms. As evidenced in Figure 2 (right part), the outer parts of the O_{ap} displacements towards $[110]$ become much more pronounced, pointing to a significant extent towards the interstitial sites, compared to what is found at ambient temperature

Towards a phonon assisted diffusion mechanism

The anharmonic behaviour concerns the whole Pr_2O_2 rock salt layer, which can be regarded as dynamically decoupled from an embedding matrix of NiO_2 layers. This highlights the important role of lattice dynamics in contributing to the 2D oxygen diffusion mechanism at already moderate temperatures. These studies clearly underline the limitations of the classical approaches to describe these anomalously anharmonic lattice dynamics, when using harmonic potentials. Our results confirm the origin of the low temperature oxygen diffusion mechanism in K_2NiF_4 -type oxides to be related to structural instabilities of the apical oxygen atoms and associated phonon softening, allowing large apical oxygen displacements to dynamically promote oxygen diffusion [3,4].

[1] O. Wahyudi et al., *Crystengcomm* 17, 6278 (2015).

[2] M. Ceretti et al., *J. Mater. Chem. A* 3, 21140 (2015).

[3] W. Paulus et al., *J. Am. Chem. Soc.* 130, 16080 (2008).

[4] A. Villesuzanne et al., *J. Solid State Electrochem.* 15, 357 (2011).

Magnetic ground state of superconducting

$\text{Eu}(\text{Fe}_{0.88}\text{Ir}_{0.12})_2\text{As}_2$

W. T. Jin^{1,2}, Wei Li³, Y. Su², S. Nandi^{1,2}, Y. Xiao¹, W. H. Jiao⁴, M. Meven⁵, A. P. Sazonov⁵, E. Feng², Yan Chen⁶, C. S. Ting⁷, G. H. Cao⁸, T. Brückel^{1,2}

¹Jülich Centre for Neutron Science (JCNS-2) and Peter Grünberg Institut (PGI-4), Forschungszentrum Jülich GmbH, Jülich, Germany

²Jülich Centre for Neutron Science (JCNS) at MLZ, Forschungszentrum Jülich GmbH, Garching, Germany

³Shanghai Institute of Microsystem and Information Technology, Chinese Academy of Sciences, Shanghai, China

⁴School of Science, Zhejiang University of Science and Technology, Hangzhou, China

⁵Institute of Crystallography, RWTH Aachen at MLZ and Jülich Centre for Neutron Science (JCNS) at MLZ, Garching, Germany

⁶Department of Physics, State Key Laboratory of Surface Physics and Laboratory of Advanced Materials, Fudan University, Shanghai, China

⁷Texas Center for Superconductivity and Department of Physics, University of Houston, Houston, Texas, USA

⁸Department of Physics, Zhejiang University, Hangzhou, China

Recently, superconductivity with transition temperatures T_{SC} up to 22 K was observed in iron pnictide $\text{Eu}(\text{Fe}_{1-x}\text{Ir}_x)_2\text{As}_2$ with 5d transition-metal element doping. However, the magnetic ground state of the Eu^{2+} moments near the optimal Ir-doping level remains controversial. Due to large neutron-absorption cross sections of both Eu and Ir, the neutron diffraction measurements on such materials are quite challenging. Here, we have successfully determined the magnetic structure of the localized Eu^{2+} spins in optimally doped $\text{Eu}(\text{Fe}_{0.88}\text{Ir}_{0.12})_2\text{As}_2$ ($T_{\text{SC}} = 22$ K) by single crystal neutron diffraction measurement at 2.5 K at the hot-neutron diffractometer HEIDI. The Eu^{2+} moments were found to be ferromagnetically aligned along the c direction with an ordered moment of $7.0(1) \mu_{\text{B}}$ well below the Curie temperature $T_{\text{C}} = 17$ K, coexisting with the bulk superconductivity.

Motivation: Unclear magnetic ground state of superconducting $\text{Eu}(\text{Fe}_{1-x}\text{Ir}_x)_2\text{As}_2$

The discovery of unconventional superconductivity in the iron pnictides in 2008 has provided an opportunity to study the intriguing interplay between superconductivity and magnetism. EuFe_2As_2 is a unique parent compound within the iron pnictides as it contains two magnetic sublattices. This compound undergoes a spin-density-wave (SDW) transition in the Fe sublattice concomitant with a tetragonal-to-orthorhombic structural phase transition (SPT) below 190 K. In addition, the localized Eu^{2+} spins order in an A-type antiferromagnetic (A-AFM) structure below 19 K [1]. Recently, superconductivity was observed in 5d transition-metal element doped $\text{Eu}(\text{Fe}_{1-x}\text{Ir}_x)_2\text{As}_2$ with T_{SC} up to ~ 22 K [2]. However,

the magnetic structure of the Eu^{2+} moments near the optimal Ir-doping level ($x = 0.12$) remains unclear. Thus, it is important to unambiguously determine the magnetic ground state of the Eu^{2+} spins in optimally doped $\text{Eu}(\text{Fe}_{0.88}\text{Ir}_{0.12})_2\text{As}_2$ by neutron diffraction, the preferred experimental method for the bulk probe of the magnetic order.

Single crystal neutron diffraction

A 24 mg plate-like single crystal with dimensions $\sim 4 \times 4 \times 0.5 \text{ mm}^3$ was selected for the neutron diffraction measurements at HEIDI [3] with the neutron wavelength of 0.793 \AA , to reduce the neutron absorption of Eu and Ir. In contrast to the parent compound EuFe_2As_2 , in which both the SPT and the Fe-SDW transition were observed, both transitions were found to be completely suppressed for $\text{Eu}(\text{Fe}_{0.88}\text{Ir}_{0.12})_2\text{As}_2$ with bulk superconductivity.

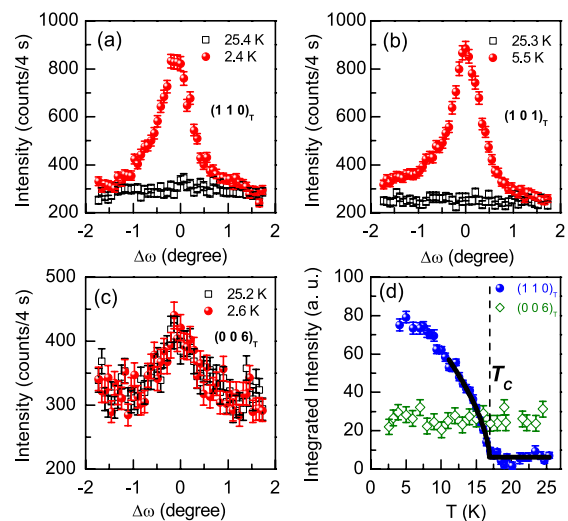


Figure 1: Rocking-curve scans (ω scans) of (a) $(1,1,0)_{\text{T}}$, (b) $(1,0,1)_{\text{T}}$, and (c) $(0,0,6)_{\text{T}}$ reflections at 25 K and at base temperature, respectively. (d) The temperature dependencies of the integrated intensities of the $(1,1,0)_{\text{T}}$ and $(0,0,6)_{\text{T}}$. The solid line represents a fit of the ferromagnetic order parameter close to the transition using a power law. The vertical dashed line denotes the ferromagnetic transition temperature T_{C} .

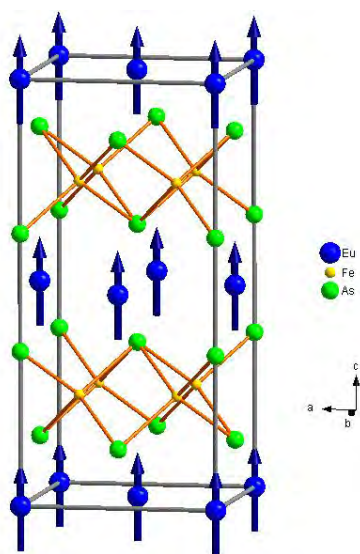


Figure 2: The ground-state magnetic structure of $\text{Eu}(\text{Fe}_{0.88}\text{Ir}_{0.12})_2\text{As}_2$ at 2.5 K.

As shown in Figs. 1(a) and 1(b), the weak nuclear reflections at 25 K, $(1,1,0)_T$ and $(1,0,1)_T$ are remarkably enhanced at the base temperature, indicating a huge ferromagnetic contribution from the Eu^{2+} spins. On the other hand, the $(0,0,6)_T$ reflection shows no discernible change upon cooling [Fig. 1(c)], suggesting that the ferromagnetic component of the Eu^{2+} spins in the ab plane is almost zero or cannot be resolved within the experimental uncertainty. In other words, within our experimental uncertainty, the Eu^{2+} spins are ferromagnetically aligned along the c direction in the ground state. As shown in Fig. 1(d), fitting of the order parameter using the power law close to the transition yields the ferromagnetic transition temperature $T_c = 16.89(7)$ K.

To determine the nuclear and magnetic structures of $\text{Eu}(\text{Fe}_{0.88}\text{Ir}_{0.12})_2\text{As}_2$, the integrated intensities of 508 (154 independent) reflections at 25 K and 478 (145 independent) reflections at 2.5 K were collected and refined. The nuclear structure of $\text{Eu}(\text{Fe}_{0.88}\text{Ir}_{0.12})_2\text{As}_2$ shows no evident difference between 2.5 and 25 K, and the reflections at 2.5 K could be well refined by the addition of a ferromagnetic Eu^{2+} moment of $7.0(1)$ μB purely along the c direction. The ground-state magnetic structure of $\text{Eu}(\text{Fe}_{0.88}\text{Ir}_{0.12})_2\text{As}_2$ at 2.5 K is shown in Fig. 2.

First-principles calculations

To better understand the role of 5d Ir doping, the first-principle electronic structure calculation was performed for $\text{Eu}(\text{Fe}_{0.875}\text{Ir}_{0.125})_2\text{As}_2$ using the projected augmented-wave method. The density of states (DOS) of $\text{Eu}(\text{Fe}_{0.875}\text{Ir}_{0.125})_2\text{As}_2$ is shown in Fig. 3(b) and compared with that of EuFe_2As_2 [Fig. 3(a)].

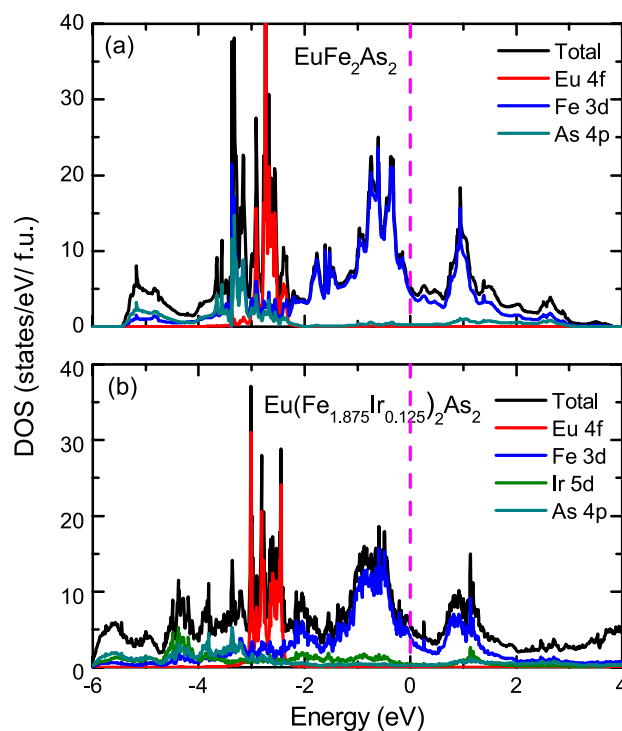


Figure 3: The total and partial electronic density of states (DOS) per unit cell of (a) EuFe_2As_2 and (b) $\text{Eu}(\text{Fe}_{0.875}\text{Ir}_{0.125})_2\text{As}_2$ in the quenched paramagnetic state in the Fe layer and the ferromagnetic interaction between the intralayer Eu spins in the Eu layer. The Fermi energy is set to zero (dashed line).

Similar to the parent compound, the Eu 4f states in $\text{Eu}(\text{Fe}_{0.875}\text{Ir}_{0.125})_2\text{As}_2$ are also quite localized. Apart from the Eu 4f states, the remaining DOS changes significantly with Ir doping. The total DOS at the Fermi level is slightly reduced by the Ir doping, accompanied by the broadening of the d bandwidth. Meanwhile, the width of the As 4p band also increases, reflecting stronger d-p hybridization due to Ir doping. The stronger hybridization and expanded bandwidth is not favorable for Fermi surface nesting, and thus suppresses the structural distortion and the Fe-SDW transition leading to the emergence of superconductivity. Energies of different possible magnetic structures of the Eu^{2+} moments in $\text{Eu}(\text{Fe}_{0.875}\text{Ir}_{0.125})_2\text{As}_2$ were also calculated. Theoretically, the ferromagnetic alignment of the Eu^{2+} spins along the c direction is indeed the most favored configuration, in good agreement with the result of the neutron measurements. For more detailed discussions, see ref. [4].

- [1] Y. Xiao et al., *Phys. Rev. B* 80, 174424 (2009).
- [2] W. H. Jiao et al., *New J. Phys.* 15, 113002 (2013).
- [3] M. Meven et al., *Neutron News* 18, 19 (2007).
- [4] W. T. Jin et al., *Phys. Rev. B* 91, 064506 (2015).

Anisotropy in the magnetocaloric effect of MnFe_4Si_3

P. Hering¹, K. Friese¹, J. Voigt¹, A. Grzechnik², A. Senyshyn³, M. Meven^{1,2}, T. Brückel^{1,4}

¹Jülich Centre for Neutron Science and Peter Grünberg Institut, Forschungszentrum Jülich GmbH, Jülich, Germany

²Institute for Crystallography, RWTH Aachen University at MLZ, Aachen, Germany

³Heinz Maier-Leibnitz Zentrum (MLZ), Technische Universität München, Garching, Germany

⁴Jülich Centre for Neutron Science (JCNS) at MLZ, Forschungszentrum Jülich GmbH, Garching, Germany

The magnetocaloric effect describes the change in temperature of a material when exposed to a magnetic field and forms the basis of magnetocaloric refrigeration technologies. We studied the anisotropic lattice expansion of the magnetocaloric compound MnFe_4Si_3 , which exhibits a distinct anomaly at the ferromagnetic ordering temperature as revealed by neutron powder diffraction at SPODI. The close relation between the lattice and spin degrees of freedom might be responsible for the large magnetocaloric effect (MCE) in this compound. In addition, a combined neutron and X-ray single crystal diffraction study revealed new details of the nuclear and magnetic structure. A new structural model in the space group P-6 was introduced and the magnetic structure was determined in the magnetic space group Pm' , with an easy axis of magnetization in the a,b-plane.

MnFe_4Si_3 and the magnetocaloric effect

Magnetic refrigeration technologies hold the potential for 20-30 % lower energy consumption when compared to conventional vapor compression cool-

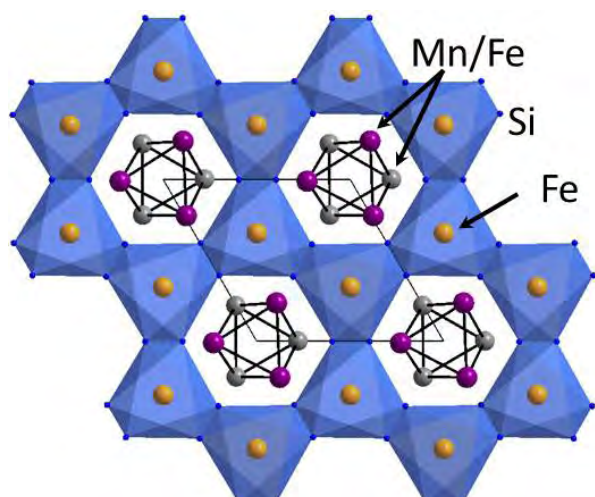


Figure 1: Projection of the crystal structure of MnFe_4Si_3 along [001]. FeSi_6 -Octahedra are indicated.

ing [1]. Within the system $\text{Mn}_{5-x}\text{Fe}_x\text{Si}_3$, the hexagonal compound MnFe_4Si_3 is a promising candidate for magnetic cooling in ambient temperature devices. Compared to other candidate materials, it has the advantage that it does not contain expensive rare earth elements such as Gd, nor toxic elements such as As. In addition, this compound is a good candidate for developing a better understanding of the underlying mechanism of the MCE in multiple site driven magnetocaloric materials [2].

Magnetic structure

Earlier studies based on polycrystalline samples report a crystal structure in the space group $\text{P6}_3/\text{mcm}$ with three symmetrically independent atomic positions: the first site has mixed occupancy of manganese and iron, a second site is exclusively occupied by Fe while the third is occupied by silicon (Fig. 1). We were able to synthesize single crystals of the compound using the Czochralski method, which opened up the possibility of studying the anisotropy of the magnetic properties along with single crystal X-ray and neutron diffraction experiments. A refinement of the crystal structure using neutron and X-ray data simultaneously led to a structural model in the space group P-6. The main difference in our new structural model, when compared to the previous model, is a partial ordering of the manganese and iron in the mixed occupied sites, revealed only

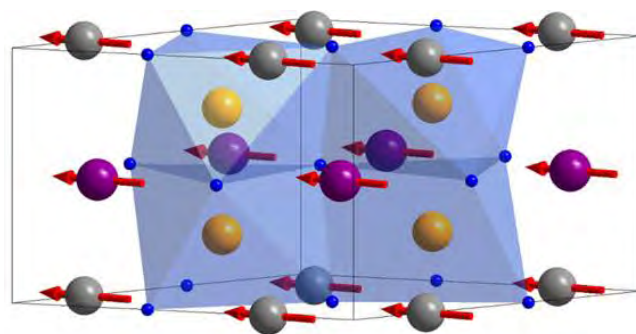


Figure 2: Ferromagnetic structure of MnFe_4Si_3 . The spins in the mixed occupancy site are indicated.

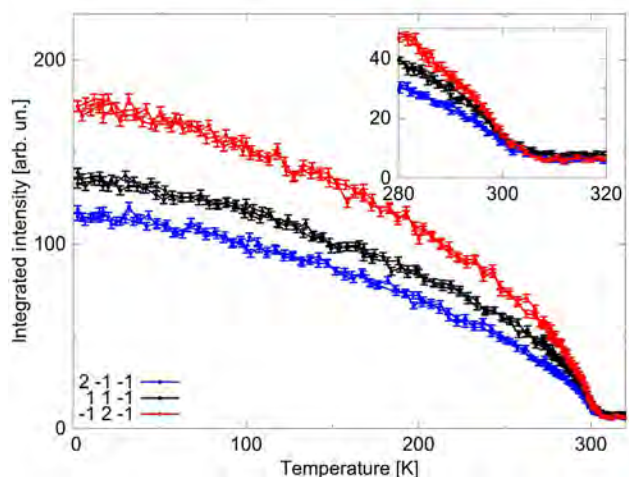


Figure 3: Temperature dependence of several reflections dominated by the contribution from magnetic scattering as measured on HEIDI (MLZ).

because of the enhanced contrast between Fe and Mn in neutron scattering.

MnFe_4Si_3 undergoes a magnetic transition to a ferromagnetic phase around 300 K [3, 4]. A refinement of the magnetic structure with the single crystal neutron data measured on TRICS (PSI) showed that the magnetic moments are coupled ferromagnetically and that the spins in the mixed occupancy sites are aligned in the a,b-plane (Fig. 2). Magnetic susceptibility measurements confirm this easy plane of magnetization [5]. No significant magnetic moment could be refined for the sites which are exclusively occupied by Fe. In addition, the intensities of symmetry equivalent reflections which are dominated by the magnetic scattering contribution were monitored on HEIDI (MLZ) over a broad temperature range and allowed to determine a T_c of 305(2) K (Fig. 3).

Anisotropy of thermal expansion

A large MCE is often related to a pronounced interplay between spin and lattice degrees of freedom [6]. In order to study this interplay and to characterize the effect of the magnetic ordering on the crystal lattice and structure, we also measured powder diffraction diagrams of MnFe_4Si_3 on the high resolution powder diffractometer SPODI at MLZ in the temperature range from 4 K up to 470 K. SPODI provides the possibility of measuring the whole temperature range without changing the experimental setup and, thus, enables an internally consistent data treatment to be applied for all measurements. Thermal dependence of the refined lattice parameters (Fig. 4) reveals a strong anisotropic thermal expansion of MnFe_4Si_3 . The hexagonal unit cell expands mainly

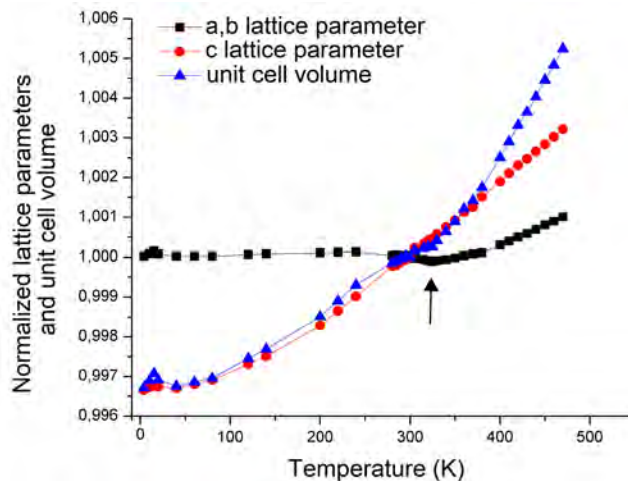


Figure 4: Normalized lattice parameter and unit cell volume of MnFe_4Si_3 as a function of temperature using the values at 300 K for normalization.

along the c-direction while the a-lattice parameter undergoes changes which are smaller by one order of magnitude. However, the a-lattice parameter exhibits a distinct minimum in the temperature range of the magnetic transition temperature (see arrow in Fig. 4) and nicely reflects a close relation between the lattice and spin degrees of freedom [5].

Conclusion

Neutron scattering experiments reveal two different – probably to a large degree independent – magnetic systems in the compound MnFe_4Si_3 . This observation, together with the strong anisotropy in the thermal expansion of the crystal lattice and the pronounced structural response to the magnetic transition, might be the key to the occurrence of a large magnetocaloric effect in other magnetocaloric materials too.

- [1] K. A. Gscheidner Jr. et al., *Int. J. Refrig.* 31, 945 (2008).
- [2] L. Caron et al., *Phys. Rev. B* 88, 094440 (2013).
- [3] H. Binczycka et al., *Phys. Status Solidi A-Apl. Mat.* 19, K13 (1973).
- [4] Songlin et al., *J. Alloy. Compd.* 334, 249 (2002).
- [5] P. Hering et al., *Chem. Mat.* 27 (20), 7128 (2015).
- [6] V. K. Pecharsky et al., *Int. J. Refrig.* 29, 1239 (2006).

Illuminating the function of a biofuels enzyme with neutrons

Q. Wan¹, J. M. Parks², B. L. Hanson³, S. Z. Fisher⁴, A. Ostermann⁵, T. E. Schrader⁶, D. E. Graham⁷, L. Coates⁸, P. Langan⁸, A. Kovalevsky⁸

¹Department of Physics, College of Science, Nanjing Agricultural University, Nanjing, China

²UT/ORNL Center for Molecular Biophysics, Biosciences Division, Oak Ridge National Laboratory, Oak Ridge, Tennessee, USA

³Chemistry Department, University of Toledo, Toledo, Ohio, USA

⁴Scientific Activities Division, European Spallation Source, Lund, Sweden

⁵Heinz Maier-Leibnitz Zentrum (MLZ), Technische Universität München, Garching, Germany

⁶Jülich Centre for Neutron Science (JCNS) at MLZ, Forschungszentrum Jülich GmbH, Garching, Germany

⁷Biosciences Division, Oak Ridge National Laboratory, Oak Ridge, Tennessee, USA

⁸Biology and Soft Matter Division, Oak Ridge National Laboratory, Oak Ridge, Tennessee, USA

Plants can be converted into a variety of renewable products such as fuels. To efficiently deconstruct biomass material, efficient enzymes such as glycoside hydrolases are being investigated. Glycoside hydrolases apply acid/base chemistry to catalyze the decomposition of complex carbohydrates by accepting protons from the solvent and donating them to substrates, cellulose and hemicellulose. However, it is not known how the catalytic acid residue acquires a proton and efficiently transfers it to the substrate. We used macromolecular neutron crystallography to directly determine protonation states of the active site residues of the enzyme xylanase at multiple pH values. We characterized the initial stage of the glycoside hydrolysis, in which the catalytic glutamate residue obtains a proton from water, and then delivers it to the glycosidic oxygen. The catalytic glutamate cycles between two conformations, “upward” and “downward”, with the energy barrier of ~4 kcal/mol, but is protonated only in the “downward” orientation with higher pK_a . These findings shed light on xylanase function and will aid in protein engineering efforts.

Protons are key players in glycoside hydrolysis

Catalysis by biomacromolecules called enzymes frequently involves proton transfer. To fully understand enzyme chemistry, accurate hydrogen atom positions must be mapped. One class of enzymes are glycoside hydrolases (GHs) that cleave, or hydrolyze, the glycosidic bond connecting two sugar units in a polysaccharide. The glycosidic bond hydrolysis by GHs is accomplished with rate enhancements of about 10^{18} , placing them among the most

efficient biocatalysts in Nature. GHs are utilized in the production of biofuels from plant biomass that requires decomposition of natural polysaccharides into fermentable sugars [1]. Understanding their catalytic mechanisms and ligand binding is of paramount importance for enzyme design to improve biofuel production.

GH enzymes enhance the rate of glycoside hydrolysis by using a general acid, usually the carboxylic acid of a glutamate (Glu) residue, which donates a proton to the leaving group oxygen. A second Glu residue located nearby acts as a nucleophile to attack the carbon atom of the glycosidic bond and generate a covalent intermediate. The next reaction step involves the general acid Glu switching its role to act as a general base, assisting an incoming water molecule to break the covalent intermediate. In the reactant state, the general acid must be weaker than the nucleophilic Glu, implying that the former has to be protonated, with a pK_a greater than 6, and the nucleophile must be deprotonated, with a pK_a less than 5. However, the protonation states of amino acid residues, as well as the distribution of hydrogen bonds, have not been directly observed in GH enzymes, and the changes in protonation predicted by the reaction mechanism have only been inferred from indirect measurements.

Atomic-level picture of a GH enzyme by neutron crystallography

Hydrogen atoms are crucial players in the mechanism of glycoside hydrolysis, participating in directional hydrogen bonding and proton transfer events. However, hydrogen atoms are virtually invisible to X-rays due to their poor scattering power. Neutrons represent a superb probe to locate hydrogen atoms

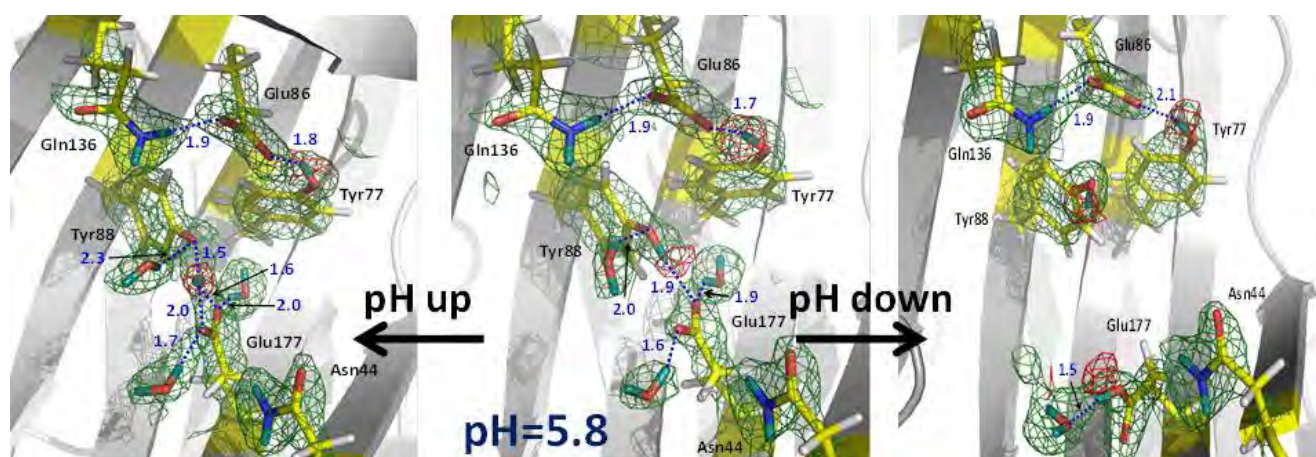


Figure 1: Nuclear scattering length density maps (green mesh) of the enzyme active site. The red mesh indicates the location of deuterium atoms, showing protonation (deuteration) of the catalytic glutamate Glu177 only in the downward conformation. Atomic distances are given in Å (blue).

and obtain atomic details of their movements in bi-macromolecules. Locating hydrogen (deuterium (D)) atoms in macromolecular neutron structures is straightforward even at medium resolutions with a d_{\min} of 2.0 - 2.5 Å. Thus, macromolecular neutron crystallography has been used to better understand the catalytic mechanism of glycoside hydrolysis. The research team obtained five neutron structures of a family 11 GH, xylanase, in the ligand-free and ligand-bound states to find out how the general acid Glu (Glu177) receives a proton from water and then delivers it to the substrate [2]. Surprisingly, the neutron structure at pD 6.2 (pD = pH + 0.4), in which the Glu177 side chain is in the “upward” conformation facing the nucleophilic Glu86, indicates that it is not protonated, even though its pK_a is 7 (Fig. 1, middle). Remarkably, no protonation of Glu177 is observed in Asn44Asp mutant, although a general acid pK_a of 8 is expected. Interestingly, at higher pD of 8.9, Glu177 is engaged in a strong hydrogen bond with a nearby tyrosine residue Tyr88 so that the phenolic D atom is found midway between oxygen atoms (Fig. 1, left side), indicating the hydrogen bond would also be strong at pD 6 and making Glu177 a stronger rather than a weaker acid. As it turns out, Glu177 side chain can have another conformation, rotated “downward” into a hydrophobic pocket. pK_a calculations estimate that Glu177 becomes a weaker acid, with higher pK_a , when it rotates “downward”. The energy barrier required (4.3 kcal/mol) is low so that the “downward” and “upward” conformations are in dynamic equilibrium. To locate the hydrogen on Glu177 in the “downward” conformation, a neutron structure at pD of 4.8 was obtained. Indeed, Glu177 was observed in the neutral, protonated (deuterated) form (Fig. 1, right side).

Glutamic acid conformational dynamics is essential for GH function

Based on the neutron structures, pK_a calculations and molecular dynamics simulations it is proposed that Glu177 obtains a proton from water when in the “downward” conformation. The general acid Glu177 side chain dynamically moves between the “downward” conformation, with high pK_a facilitating its protonation, and the “upward” conformation, with low pK_a facilitating the delivery of a proton to the glycosidic oxygen. These findings possibly resolve decades of confusion surrounding the question of why the general acid and nucleophilic glutamates in family 11 GH enzymes, while having similar hydrogen bonding interactions and solvent accessibilities, exhibit very different pK_a values and assume their corresponding catalytic roles. A better understanding of the GH catalytic mechanism provided by this neutron crystallographic study in combination with theoretical calculations will improve protein engineering efforts to design more efficient GH enzymes.

[1] D. B. Wilson, *Curr. Opin. Biotechnol.* 20, 295 (2009).

[2] Q. Wan et al., *Proc. Natl. Acad. Sci. U.S.A.* 112, 12384 (2015).

Depth sensitive morphology of model battery anodes – using the TOF-GISANS method

N. Paul¹, J. Brumbarov², A. Paul³, Y. Chen², J.-F. Moulin⁴, P. Müller-Buschbaum⁵, J. Kunze-Liebhäuser², R. Gilles¹

¹Heinz Maier-Leibnitz Zentrum (MLZ), Technische Universität München, Garching, Germany

²Institute of Physical Chemistry, University of Innsbruck, Innsbruck, Austria

³Lehrstuhl für Neutronenstreuung, Physik-Department, Technische Universität München, Garching, Germany

⁴German Engineering Materials Science Centre (GEMS) at MLZ, Helmholtz-Zentrum Geesthacht GmbH, Garching, Germany

⁵Lehrstuhl für Funktionelle Materialien, Physik-Department, Technische Universität München, Garching, Germany

Titania (TiO₂) nanotube arrays are an interesting model anode material due to their excellent rate capability, cycling stability and enhanced safety as compared to graphite. Combining titania arrays with a silicon thin film has the additional advantage of providing an even higher lithium storage capacity. We investigate the morphology of self-organised conductive TiO₂ nanotube arrays, with and without silicon coating, using time-of-flight grazing incidence small-angle neutron scattering (TOF-GISANS). We obtain values for their inner nanotube radii and intertubular distances with high statistical relevance due to the large probed volume. We find distinct signatures of a prominent lateral correlation of the TiO₂ nanotubes of 94 nm and a nanotube radius of 46 nm. The porosity averaged over the entire film using TOF-GISANS is 46 %. The inner nanotube radius is reduced to half (23 nm) through the silicon coating, but the prominent lateral structure is preserved [1].

Anode materials for Li-ion batteries

Silicon is a high capacity anode candidate for Li-ion batteries with a theoretical specific capacity of up to 4200 mAhg⁻¹ (Li₂₂Si₅). However, the large volume expansion of silicon during lithiation is its main disadvantage as this leads to mechanical degradation and massive solid electrolyte interface formation which, in turn, cause severe capacity loss over time. A thin silicon film deposited on a nanostructured conductive titania support could combine the advantages of both silicon and titania and offer higher lithium storage capacities and stability against volume expansion effects due to its nanomorphology [2]. Control of the morphology of nanostructures and a knowledge of statistically relevant morphological parameters, including porosity, is crucial for predicting the performance of any device.

Depth dependent nanotubular morphology

Selected 2D GISANS images of the TiO₂ nanotubes measured at the RefSANS instrument with different wavelengths, before and after Si coating (denoted as TNT-bare and TNT-Si), are shown in Fig. 1. Shorter wavelengths probe the inner film volume, where information on the morphology is averaged over the complete depth of the nanotubular film, as a comparatively greater scattering vector range (depth) is investigated, while longer wavelengths exclusively probe the film surface.

For the 2D GISANS data detected at shorter wavelengths, the wavelength dependent Yoneda peak is visible, along with the specular peak. As the wavelength increases, the Yoneda peak moves upwards towards the specular peak. The specular peak posi-

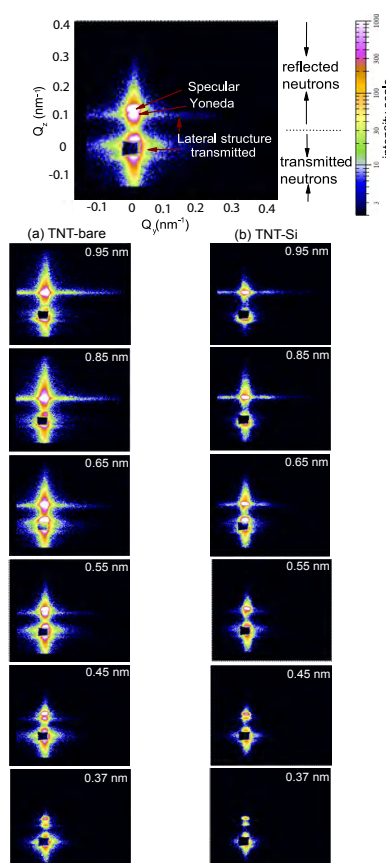


Figure 1: Top: Typical features of a 2D GISANS image. Bottom: Selected 2D GISANS images for (a) TNT-bare and (b) TNT-Si plotted for different mean neutron wavelengths (increasing from bottom to top, as indicated).

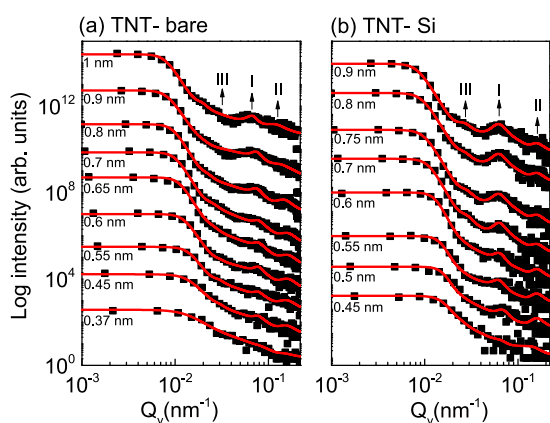


Figure 2: Horizontal line cuts from 2D TOF-GISANS images shown in Fig. 1 plotted along with their fits for (a) TNT-bare and (b) TNT-Si. Line cuts are taken at Q_y positions corresponding to the Yoneda peak positions. The curves are shifted upwards on the y-axis for clarity.

tion does not change, as it depends only on the incident angle, which is fixed for all measurements. For TNT-bare, the diffuse scattering increases at wavelengths larger than 0.45 nm, indicating the presence of a well-defined lateral structure which is due to the long range order of the nanotube pores. This lateral ordering becomes even more pronounced at higher wavelengths, or in other words, when only the surface of the nanotube array is probed, as the scattering depth is then limited to the top part (approx. 100 nm) of the nanotubular layer. In the case of TNT-Si, the well-defined lateral structure only starts to appear at wavelengths above 0.55 nm, which indicates that the silicon deposition introduces some inhomogeneities in the lateral structures in the film layer below the silicon coated upper portion. Observations at shorter neutron wavelengths, where the entire film volume is probed, show that the average size distribution of the nanotubes in the entire bulk of the film is not narrow enough to give rise to any detectable diffuse scattering in the corresponding 2D GISANS data. This is due to an accumulation of inhomogeneities over the whole film depth, i.e., length of the nanotubes, as the nanotubes under consideration do not have smooth walls and taper slightly, since they are optimized for application in Li-ion batteries. Moreover, contributions to the scattering from the Ti film and the substrate at lower wavelengths could also unfavorably affect the size distribution.

In order to obtain quantitative information on the average size distributions of lateral structures at varying depths of the nanotubular array, horizontal line cuts are taken from the 2D GISANS data at the Yoneda peak position for each wavelength (see Fig. 2). For TNT-bare, the value of the radius cor-

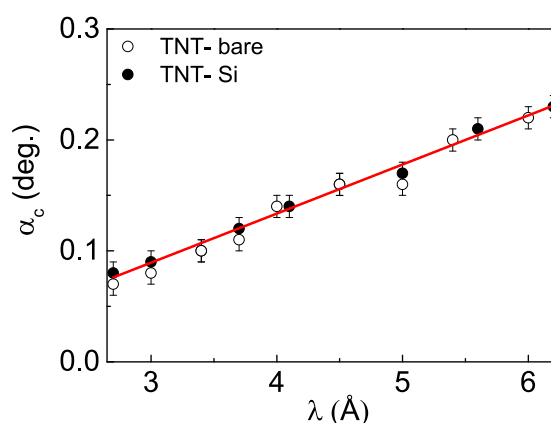


Figure 3: Plot of the critical exit angle positions versus neutron wavelength as obtained from the vertical line cuts for TNT-bare (hollow circles) and TNT-Si (filled circles).

responding to the most prominent cylindrical scattering objects I is (46 ± 5) nm with a corresponding nearest-neighbor distance of (94 ± 6) nm. After silicon coating, the prominent cylinder radius decreases to (23 ± 3) nm, whereas the nearest-neighbor distances between these cylinders remains unchanged (94 ± 6) nm. The dimensions of the cylinders and nearest neighbor distance correspond to the inner nanotube radius (which changes following Si coating) and the intertubular distance (center to center) remains unchanged. In addition to the prominent cylinders, additional scattering objects, II and III, at different lateral length scales are observed for both TNT-bare and TNT-Si. Smaller cylinders II are observed having a radius of (8 ± 2) nm and a nearest-neighbor distance of (38 ± 3) nm (for TNT-bare), and a radius of (6 ± 2) nm with an identical nearest neighbor distance (for TNT-Si). Larger cylinders III have a radius of (60 ± 10) nm, a nearest-neighbor distance of (210 ± 30) nm (TNT-bare) and a radius of (55 ± 10) nm with the same distance (TNT-Si).

Porosity of the nanotube array

The Yoneda peak originates from material-specific scattering at the critical angle, which depends on the scattering length density (SLD) and the neutron wavelength. Thus, it is possible to obtain the SLD from the slope of the linear fit of the critical angle versus the neutron wavelength. If the structure is porous and the pores are filled with air, the SLD is reduced, and the porosity P can also be obtained. From Fig. 3, which plots the critical angle position versus wavelength, the experimental SLD is extracted as $1.26 \times 10^{-6} \text{ \AA}^{-2}$, which gives an average porosity of 46 %.

[1] N. Paul et al., *J. Appl. Crystallogr.* 48, 444 (2015).

[2] J. Brumbarov et al., *J. Power Sources* 258, 129 (2014).

In situ neutron experiments on a sodium metal halide battery

V. Zinth, S. Seidlmayer, M. Schulz, R. Gilles, M. Hofmann

Heinz Maier-Leibnitz Zentrum (MLZ), Technische Universität München, Garching, Germany

High temperature sodium metal halide batteries are attractive alternatives to conventional batteries due to their low cost, high specific energy, rapid charging and discharging capability and long lifetime without the need for maintenance. They are safe in operation and nowadays used in stationary backup systems and mobile applications. We used time and spatially resolved diffraction to investigate the processes occurring in a sodium metal halide cell with mixed Fe/Ni chemistry during cell operation. The large battery dimensions of about $35 \times 35 \times 230 \text{ mm}^3$ mean that it lends itself naturally to neutron scattering experiments as an ideal tool for non-destructive investigation. The in-situ data permitted mapping of the reaction progress in time and space and makes it possible to sketch a simplified mechanism of the processes that occur in the cell during charging.

Chemical processes in the battery

Fig. 1 illustrates the cell setup of a charged sodium halide cell with the help of a tomographic image taken on the imaging station ANTARES. Its cathode consists of a mixture of metal granules ($M = \text{Ni/Fe}$) and NaCl filled in a ceramic β'' -alumina tube which acts as a separator as well as an electrolyte at high temperatures. Here, a surplus of metal is normally used to ensure good electrical contact through the cell. The additional salt NaAlCl_4 in the cathode is

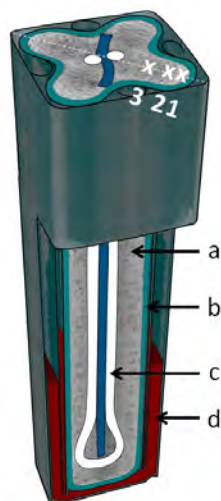


Figure 1: Sketch of a sodium metal halide battery based on a tomographic image (a = cathode, b = β'' -alumina separator, c = current collector and porous wick, d = anode/liquid sodium). The white crosses mark the horizontal positions where the diffraction measurements have been done.

molten at operating temperature ($T = 270 - 350 \text{ }^\circ\text{C}$) and works as a secondary electrolyte, while a nickel wire is used as current collector. The porous wick in the center acts as a further reservoir for additional NaAlCl_4 . The anode is comprised of (liquid) sodium metal.

During cycling, a reaction front propagates from the inner surface of the β'' -alumina separator towards the cathode current collector in the center of the battery [1]. When the battery is charging, NaCl is consumed at the reaction front to form MCl_2 and Na^+ ions. The sodium ions diffuse through the separator and are reduced to sodium metal on the anode side. The reaction is reversed when the battery is discharged. The complete cell reaction can be written as: $2 \text{NaCl} + \text{M} \rightarrow 2 \text{Na} + \text{MCl}_2$ (charging)

In-situ experiments

The reaction process inside a sodium metal halide battery (with mixed Ni/Fe) was studied in-situ using spatial and time resolved neutron diffraction at the diffractometer STRESS-SPEC. The cell was first heated to an operating temperature $T = 280 \text{ }^\circ\text{C}$ with the help of a specially designed furnace to minimize neutron absorption. Then, the battery was charged at a rate of 5A/h and diffraction data were repeatedly taken at short time intervals at three different locations along the cell diagonal (see Fig. 1) at mid-height of the battery using a small measurement gauge volume of $2 \times 2 \times 20 \text{ mm}^3$.

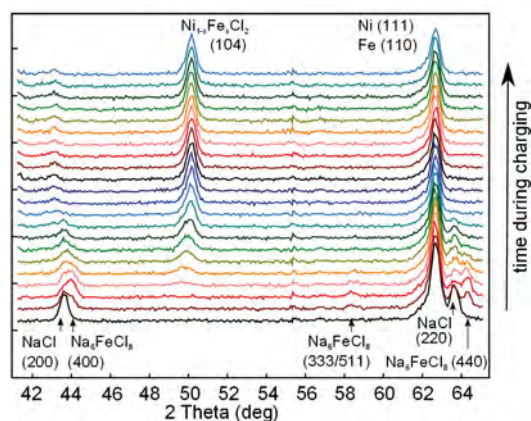


Figure 2: Time resolved diffraction data collected at position 1 (closest to the separator), with all observable crystallographic phases indicated.

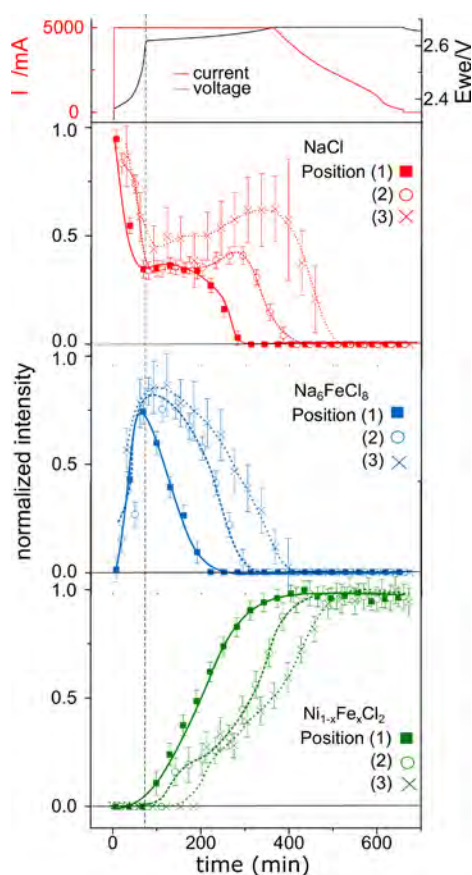


Figure 3: Normalised reflection intensities detected at the three different positions in the cell as a function of charging time. The vertical line depicts the end of Fe/Fe²⁺ oxidation.

Fig. 2 shows a typical time resolved diffraction pattern at position 1 (approx. 1 mm away from the inner surface of the separator) during charging. Reflections from Ni/Fe metals, NaCl and an intermediate Na₆FeCl₈ phase [2, 3] can be identified. The analysis of the Bragg reflection intensities with respect to charging time at the three locations in the cell are summarized in Fig. 3. This makes it possible to identify which reactions take place in the cell and how they progress at the three different positions [1].

Iron is oxidized first because of the lower potential of the Fe/Fe²⁺ redox couple. This oxidation can be associated with the steeper voltage rise to 2.62 V at the beginning of charging. During this period, only the intermediate phase Na₆FeCl₈ is formed, coupled with a substantial NaCl consumption. For instance, at positions 1 and 2 almost 60 % of all NaCl in the discharged cell is consumed. A decrease in the Fe/Ni peak intensity due to Fe consumption is also observed, but not shown here.

After about 76 mins, Ni oxidation sets in, indicated by the change in the slope and slower voltage rise. Fig. 3 shows that shortly afterwards the MCl₂ phase starts to appear. At the same time, Na₆FeCl₈ is consumed while the NaCl phase content remains constant, indicating that at first Ni reacts only with Na₆FeCl₈ to form MCl₂. Finally, when all Na₆FeCl₈ has been used up, NaCl consumption resumes and Ni reacts to form more MCl₂ until all of the NaCl is exhausted. In the course of this reaction, it is interesting to note that only one MCl₂ reflection appears in Fig. 2, indicating that a mixed Ni_{1-x}Fe_xCl₂ phase is formed.

Interpretation of this data indicates that instead of one single reaction front moving through the cell during charge and discharge, separate reaction zones are found for Fe and Ni oxidation as well as for Na₆FeCl₈ and NaCl usage as the Cl⁻ and Na⁺ source during Ni oxidation. The extent of these reaction zones varies with time, depth and the respective reactions.

Model of mechanism

Taking into consideration other factors such as the solubility of the different constituents in the NaAlCl₄ melt, we can sketch a possible mechanism for the reaction processes during charging of the battery [1].

Upon iron oxidation, Na₆FeCl₈ is first formed on the metal backbone structure with Na⁺ and Cl⁻ ions being supplied by the NaAlCl₄ electrolyte and replenished by NaCl going into solution. The second step of the reaction is then Ni oxidation, where nickel reacts with Na₆FeCl₈ to form the mixed Ni_{1-x}Fe_xCl₂ phase as a layer on the metal granules; and only when that reservoir has been exhausted does it further react with Cl⁻ ions from the electrolyte. Again, the Cl⁻ ions are supplied indirectly by NaCl dissolution.

In summary, our study gives the first spatially and time resolved insight into the reaction processes occurring in a sodium metal halide battery during charge (for discharge see also [1]) and provides a basis for future improvements to such a battery through optimization of its main components.

[1] V. Zinth et al., *J. Electrochem. Soc.* 162, A384 (2015).

[2] J. Rijessenbeck et al., *J. Power Sources* 196, 2332 (2011).

[3] M. Hofmann et al., *J. Electrochem. Soc.* 159, A1827 (2012).

Transition metal deposition and capacity fade Li-ion batteries using PGAA, XRD, AC impedance

S. Seidlmayer¹, I. Buchberger², P. Kudejova¹, A. Pokharel², M. Piana², J. Hattendorff², H. A. Gasteiger², R. Gilles¹

¹Heinz Maier-Leibnitz Zentrum (MLZ), Technische Universität München, Garching, Germany

²Chair of Technical Electrochemistry, Technische Universität München, Garching, Germany

We studied the performance degradation of graphite/LiNi_{1/3}Mn_{1/3}Co_{1/3}O₂ (NMC) lithium ion cells, charged and discharged up to 300 cycles at different operating conditions of temperature and upper cut-off potential (4.2 V/25 °C, 4.2 V/60 °C, 4.6 V/25 °C) using a combination of electrochemical (EC) methods with X-ray diffraction (XRD) as well as neutron induced Prompt Gamma Activation Analysis (PGAA). With PGAA we could exactly quantify the amount of transition metals Ni, Co and Mn which dissolve from the cathode and deposit on the anode. Combining the methods we could differentiate between different capacity degradation mechanisms.

Performance research on lithium ion batteries

Lithium ion batteries are widely used in portable electronics and increasingly also in battery electric vehicles [1] or large scale energy storage systems. For batteries in vehicles or local energy storage, life times of >10 years are required. In this scope it is essential to identify, understand and quantify the mechanisms that lead to battery failure in order improve cell lifetime. The interplay of the methods XRD, PGAA and AC impedance and other EC methods in our recent investigation [2] allowed us to determine the main failure mechanisms of NMC/graphite cells. Here we will focus on the neutron methods part, especially the PGAA.

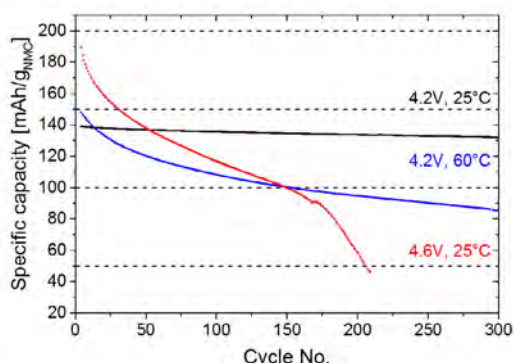


Figure 1: Specific cell capacity plotted against cycle number of different aging parameter sets (depending on upper potential cut-off voltage and cycling temperature).

			Cycling capacity loss	XRD cap. loss	x(Li) (from XRD)
U [V]	T [°C]	# of cycles	[mAh/g _{NMC}]	[mAh/g _{NMC}]	x _{corr.}
4.2	25	300	7	4	0.013
4.2	25	300	7	3	0.012
4.2	60	300	62	57	0.206
4.2	60	300	65	61	0.219
4.6	25	232	120	54	0.194
4.6	25	228	128	59	0.212

Table 1: Comparison of the electrochemically observed capacity loss from cycling data (1st column) vs the established structural capacity loss (by XRD) (2nd and 3rd column). For calculating the XRD capacity loss from x(Li) the theoretical capacity of 278 mAh/g_{NMC} was used (rounded to integer numbers).

Electrochemical capacity degradation study

We investigate the EC aging behavior using Swagelok T-cells consisting of the active electrode materials graphite and NMC, separated by two glass fiber separators as a function of temperature and upper cut-off potential. For our aging studies we use two initial slow formation cycles at C/10 rate with 4.2 V upper (charge) and 3.0 V lower (discharge) cut-off potential. By definition C/10 corresponds to a current which charges or discharges the full cell within 10 h.

The formation process was followed by charging/discharging (cycling) the cells with 1C rate at the different conditions, the results are shown in Fig. 1. Combining in situ and ex situ XRD it is possible to establish the remaining capacity (=amount of active lithium) of the aged cathode from the correlation of the lithium content in NMC with its lattice parameters (*c*, *a*) [2]. Similarly neutron diffraction can be applied and has been reported for other cell chemistries [3]. Two major observations are deduced by comparing the electrochemically obtained capacity losses to the capacity losses obtained from the structure of the aged cathodes (see Tab. 1):

1. 4.2 V/25 °C (black) and 4.2 V/60 °C (blue), mainly loss of active lithium (agreement between structural and EC capacity losses)

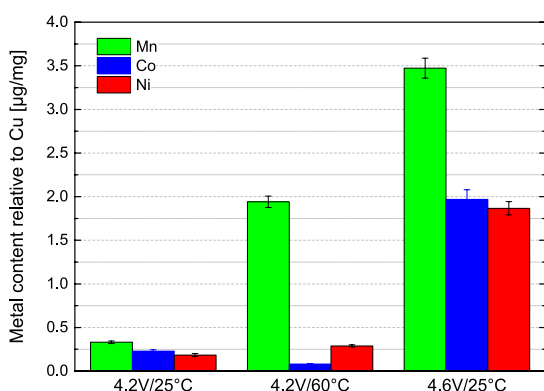


Figure 2: Concentration of Ni, Mn, and Co deposited on harvested aged graphite electrodes as determined by PGAA.

2. 4.6 V/25 °C (red) loss of active lithium and resistance build up at the electrodes occurs (disagreement of structural and EC capacity losses) Accelerated capacity loss at high positive cut-off potentials and/or high temperatures can be caused by the dissolution of transition metals and their subsequent deposition on the graphite anode [2,4,5].

To evaluate this effect, we use the PGAA experiment at the MLZ to examine the extent of transition metal deposition on harvested graphite anodes after long-term cycling in detail [2]. Fig. 2 shows the obtained transition metal concentrations on harvested graphite anodes after long term cycling relative to the copper current collector foil. Using this current collector as an internal standard with known exact mass, we can also calculate the absolute amounts of transition metals relative to the initial amount in the cathode (see Tab. 2).

Cells	Deposited TMS		Loss of TMs
	[µg]	[µmol]	[mol%]
4.2 V/ 25 °C	6.2	0.11	0.08
4.2 V/ 60 °C	19.3	0.35	0.26
4.2 V/ 25 °C	61.2	1.07	0.77

Table 2: Amounts of transition metals (TM) deposited on graphite anodes and relation to the amount of transition metal in the cathode material (right column)

There is a clear trend of increasing transition metal deposition at elevated temperatures (60 °C) and especially at higher cut-off voltages (4.6 V). There is also a preference to the dissolution and deposition of Mn-ions. In the case of high temperature long-term cycling (4.2 V/ 60 °C) the amount of deposited Mn is nearly an order of magnitude larger than the amount of Ni/Co. On the other hand at high cut-off

potential (4.6 V/ 25 °C) all transition metals are significantly transported, but the amount of Mn is still roughly double the amount of Ni/Co. Similar preferential dissolution behavior has been observed by Gallus [4].

Generally, two mechanisms for the transition metal dissolution are suggested. In the lower voltage region, disproportionation reactions are supposed to be the main reason [2]: $2\text{Mn}^{3+} \rightarrow \text{Mn}^{4+} + \text{Mn}^{2+}$. Here trace amounts of Mn^{3+} in the NMC lattice are created due to defects or oxygen vacancies and trigger the dissolution reaction. At higher potentials (like 4.6 V) computational studies showed that the hybridization of electron orbitals between oxygen and transition metals is changing, leading to a reduced effective oxidation state of the metal atoms, causing their dissolution into electrolyte (perhaps also accompanied by oxygen release from the structure) [6]. Mn-dissolution triggered by either of these mechanisms is furthermore enhanced by HF, instantly generated from the decomposition of the LiPF_6 salt and traces of H_2O as shown by Metzger [7].

By combination of our PGAA results with XRD, AC impedance and other EC methods [2] we conclude that the enhanced capacity loss at elevated temperature (4.2 V/60 °C) is most likely caused by an excessive growth of the anodic solid electrolyte interface (SEI) and thereby consuming active lithium. This is triggered by the transition metal dissolution and deposition. Generally SEI growth is vastly accelerated as a result of increased electronic conductivity of the SEI-layer due to the additional precipitation of transition metals into it. Finally, in the case of higher cut-off voltage (4.6 V/25 °C) we show that capacity degradation is caused not only due to active lithium loss but also by a significant impedance growth, cell polarization and possibly particle inactivation.

- [1] D. Andre et al., *J. Mater. Chem. A* 3, 6709 (2015).
- [2] I. Buchberger et al., *J. Electrochem. Soc.* 162, A2737 (2015).
- [3] O. Dolotko et al., *J. Power Sources* 255, 197 (2014).
- [4] D. R. Gallus et al., *Electrochim. Acta* 134, 393 (2014).
- [5] J. Vetter et al., *J. Power Sources* 147, 269 (2005).
- [6] B. J. Hwang et al., *Chem. Mater.* 15, 3676 (2003).
- [7] M. Metzger et al., *J. Electrochem. Soc.* 162, A1227 (2015).

Macroscopic and microscopic residual stresses in friction stir welded metal matrix composites

X. X. Zhang¹, D. R. Ni¹, B. L. Xiao¹, H. Andrä², W. M. Gan³, M. Hofmann⁴, Z. Y. Ma¹

¹Shenyang National Laboratory for Materials Science, Institute of Metal Research, Chinese Academy of Sciences, Shenyang, China

²Fraunhofer Institute for Industrial Mathematics, Kaiserslautern, Germany

³German Engineering Materials Science Centre (GEMS) at MLZ, Helmholtz-Zentrum Geesthacht GmbH, Garching, Germany

⁴Heinz Maier-Leibnitz Zentrum (MLZ), Technische Universität München, Garching, Germany

A new experimental method to determine the macroscopic and microscopic residual stresses in metal matrix composite welds via neutron diffraction has been developed. Friction stir welded 17 vol.% SiCp/2009Al-T4 composite plates were studied as an example. We found that, surprisingly, the profiles of longitudinal (L), transverse (T) and normal (N) components of the total residual stress in the reinforcement are entirely different from those in the matrix. The total residual stress profiles in the matrix are dominated by the macroscopic stress, whereas in the reinforcement the elastic mismatch (microscopic) residual stress prevails. It also turned out that it is better to use the absolute unstrained lattice parameter of SiC powder and the stress equilibrium condition to accurately calculate the thermal and plastic misfit residual stresses in the matrix.

Residual stress in metal matrix composite welds

Metal matrix composites (MMCs) are widely used in advanced industries because of their outstanding properties. However, the poor weldability of MMCs is one of the major factors that limit the widespread application of MMCs. Friction stir welding (FSW) is considered to be a promising technique for joining MMCs. As with other welding processes, residual stresses are generated after FSW. Residual stress in the welds is a crucial issue because it significantly affects the weld properties, such as plastic collapse, fatigue properties and stress corrosion [1], which makes it an essential property that engineers need to assess quantitatively in order to predict the structural integrity of welded components. However, determining residual stresses in MMC welds is quite difficult. On the one hand, residual stresses in MMCs include both considerable microscopic (originating from the elastic mismatch, thermal and

plastic misfit between matrix and reinforcement) and macroscopic stresses [2]. On the other hand, the measurement of the unstrained reference lattice parameters for the metal matrix in MMC welds is especially difficult [2, 3], as lattice parameters vary with the phase transition in the matrix after thermal exposure during welding.

In the past, neutron/synchrotron X-ray diffraction and the Eshelby model were combined to characterize multiscale residual stresses in MMCs. Nonetheless, this method suffers from complexity in calcula-

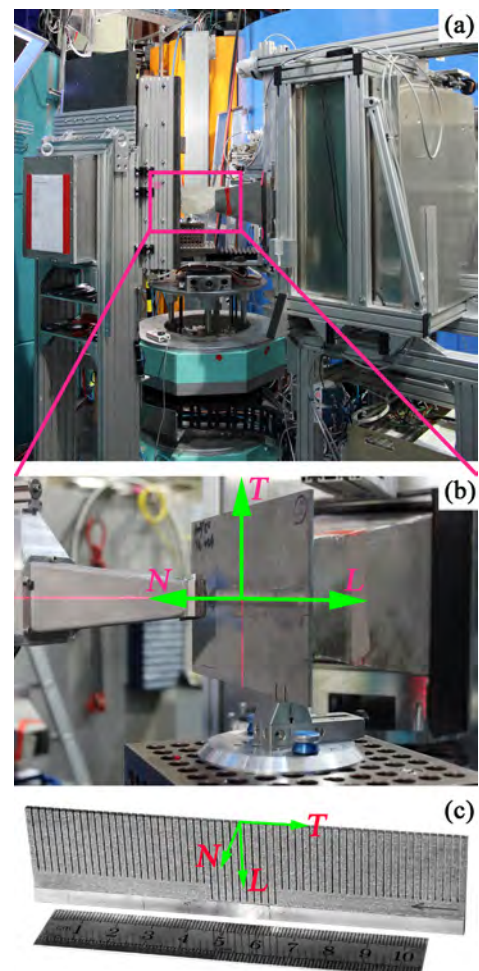


Figure 1: Experimental setup at STRESS-SPEC (a), showing the welded plate (b) and the comb sample (c).

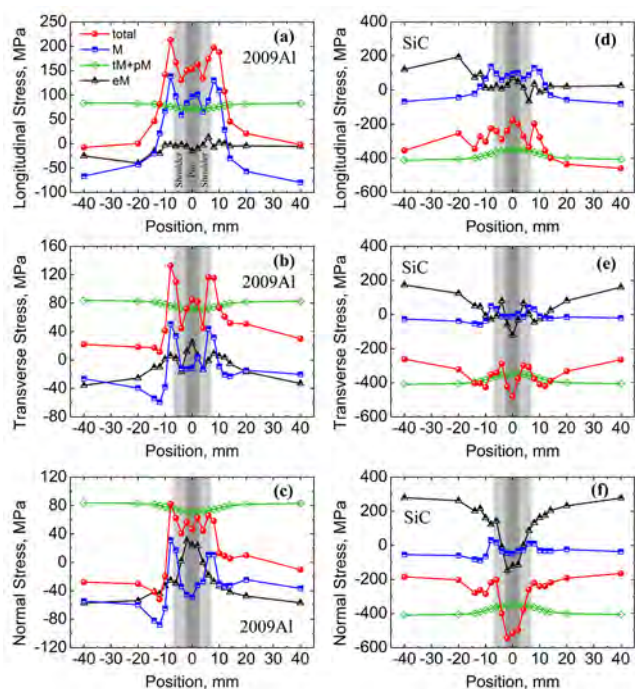


Figure 2: The profiles of the macroscopic (M), elastic mismatch (eM), thermal plus plastic misfit ($tM+pM$), and total residual stresses in both the Al matrix and SiC reinforcements across the weld. The rotation rate is 1500 rpm.

tion, poor applicability and poor accuracy. Our study proposes a new and reliable experimental method to determine multiscale residual stresses in MMC welds via neutron diffraction. Using this method, multiscale residual stresses in FSW SiCp/2009Al-T4 welds have been characterized.

Separation of multiscale residual stresses

First, the phase specific residual strains are measured. To do this, the weld sample, together with a comb sample of the weld and the reinforcement (SiC) powder sample are measured using neutron diffraction at STRESS-SPEC (Fig. 1, [4]). The residual strains are then mapped to multiscale residual stresses via a new proposed calculation method based on the Bragg equation and the stress equilibrium condition [4]. In the course of this procedure, it was found that the calculation of the thermal plus plastic misfit residual stresses in the matrix of the MMC welds is much more accurate when using the absolute unstrained lattice parameter of the SiC powder rather than the unreinforced alloy sample.

The resulting phase specific multiscale residual stresses in the FSW SiCp/2009Al-T4 are plotted separately in Fig. 2. It shows that the profiles and total variations of the L , T and N components of the

total residual stress are determined by those of the macroscopic residual stress in the matrix. The elastic mismatch residual stress has a comparatively minor effect on the total residual stress in the matrix. In contrast, the total residual stress profiles in the reinforcement are totally different from those in the matrix. For instance, the L component of the total residual stress in the matrix in particular has a typical M-shape, whereas that in the reinforcement has three peaks. The N component of the total residual stress in the matrix has an M-shape, whereas that in the reinforcement has a V-shape. Finally, in the reinforcement, the total residual stress is dominated by that of the elastic mismatch residual stress.

Effects of rotation rate on the residual stress

The new method was applied to quantitatively determine the effects of different welding conditions on residual stresses in MMCs. Fig. 3 compares the total residual stress of the metal matrix between R600 (rotation rate 600 rpm) and R1500 (rotation rate 1500 rpm). It indicates that raising the rotation rate has a small effect on the basic profiles of the total residual stress, but increases the width of the profiles, which agrees with previous investigations [5]. The maximum total residual stress in the matrix of R1500 is about 213 MPa, reaching up to $\sim 69\%$ of the yield strength of the 2009Al-T4 alloy, while in the reinforcement the stress with the maximum magnitude is about -550 MPa.

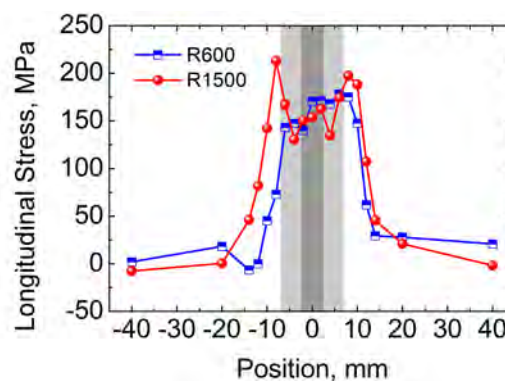


Figure 3: Comparison of the L component of the total residual stress for R600 (rotation rate 600 rpm) and R1500 (rotation rate 1500 rpm) in the Al matrix.

- [1] P. J. Withers, Rep. Prog. Phys. 70, 2211 (2007).
- [2] M. E. Fitzpatrick et al., Acta Mater. 45, 4867 (1997).
- [3] P. J. Withers et al., J. Appl. Crystallogr. 40, 891 (2007).
- [4] X. X. Zhang et al., Acta Mater. 87, 161 (2015).
- [5] A. P. Reynolds et al., Scr. Mater. 48, 1289 (2003).

Scattering influences in fission neutron radiography for in-situ analysis of hydrogen storage tanks

S. Börries¹, O. Metz¹, P. K. Pranzas¹, T. Bücherl², S. Söllradl³, M. Dornheim¹, T. Klassen¹, A. Schreyer¹

¹German Engineering Materials Science Centre (GEMS), Helmholtz-Zentrum Geesthacht GmbH, Geesthacht, Germany

²ZTWB Radiochemie München (RCM), Technische Universität München, Garching, Germany

³Heinz Maier-Leibnitz Zentrum (MLZ), Technische Universität München, Garching, Germany

For the characterization and optimization of metal hydride based hydrogen storage tanks in-situ, Neutron Radiography (NR) exclusively allows for analysis of the spatial distribution of hydrogen stored within the metal hydride bed. However, for a precise quantification of the data, a knowledge of the correlation between beam attenuation and hydrogen content is necessary. To this end, an in-situ NR study of hydrogen absorption by a complex metal hydride was carried out at the fission Neutron Imaging instrument NECTAR. A linear correlation between beam attenuation and the amount of hydrogen absorbed was found, providing the general basis for quantitative investigations of the hydrogen distribution in metal hydride systems and storage tanks. Additionally, the influence of the scattering field on the intensity distributions measured was clarified. [1]

Investigation of hydrogen storage systems by Neutron Radiography

For the development of hydrogen storage systems, metal hydrides offer the highest volumetric densities and, additionally, allow for the safe and reversible storage of hydrogen. In view of future applications, there is a strong need to study and optimize scaled-up metal hydride systems, i.e. sample amounts in-between laboratory samples of a few grams and a full scale tank. NR offers unique analysis possibilities of hydrogen distribution in storage tanks.[2] Still, for an exact quantitative investigation of the time-dependent hydrogen uptake during sorption a precise knowledge of the correlation between beam attenuation and hydrogen content is necessary. Since the neutron interaction cross section of hydrogen is dominated by its elastic scattering cross section, the influence of sample scattering has to be investigated as well.

In-situ absorption studies at NECTAR

An aluminum based storage tank was filled with compacted NaH-Al-0.05TiCl_3 and absorption of hydrogen was performed by continuous increase of the H_2 pressure to a maximum of 100 bar at a temperature of 125 °C. Hydrogen uptake takes place in two steps, with the formation of Na_3AlH_6 and finally NaAlH_4 [3]. The absorption was monitored in-situ by NR using a 10 cm lead filter in combination with a ZnS scintillator embedded in propylene. The time interval between two succeeding images was 252 s. Acquired radiographies are subdivided into different areas to resolve the correlation between beam attenuation and hydrogen content as well as the influence of scattering. The areas are illustrated in Fig. 1.

Area A_0 corresponds to the metal hydride with a total mass of 145.5 g, outer diameter of 77 mm, inner diameter of 11 mm and 25.5 mm thickness. The beam attenuation in area A_0 is time-dependent due to the absorption of hydrogen, where the latter has a final amount of 3 mol. Similarly, the beam attenuation observed for the free tank volume (area A_1) is also time-dependent due to increasing hydrogen gas pressure, corresponding to 0.47 mol of hydrogen for 100 bar. In the outer area, denoted by B, the

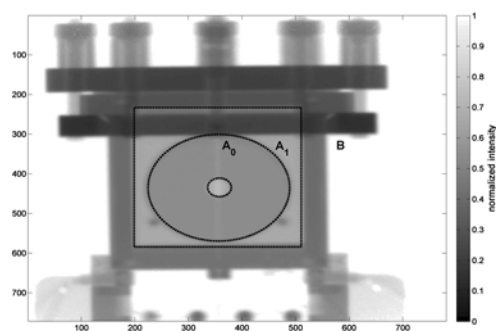


Figure 1: Radiography of an aluminum tank filled with compacted metal hydride. Intensity is normalized to flat field and corrected for dark image. The metal hydride is denoted by area A_0 . Free gas volume is marked by rectangular A_1 . Outer tank area is marked by B.[†]

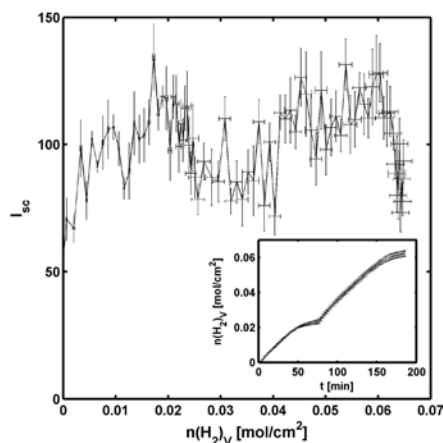


Figure 2: Evolution of scattering field intensity with amount of absorbed hydrogen. The inset shows the time evolution of hydrogen absorption.[†]

beam intensity should carry no time-dependency. Hence, the difference in intensities, $I(t) - I(t_0)$, corresponding to different hydrogen contents, can directly be assigned to a time-dependent scattering field, I_{sc} . It is caused by neutron-hydrogen interaction and contributes in terms of a background to measured intensities in A_0 and A_1 . The evolution of I_{sc} is shown in Fig. 2 for the corresponding absorbed hydrogen content normalized to the pellet area. The inset shows the time evolution of the hydrogen absorption by the metal hydride. As expected, a two-step absorption is observed, indicated by the plateau after approximately 80 min, which is due to two reaction steps of sodium alanate [3]. The scattering intensity I_{sc} already increases rapidly for the first images, followed by a region in which an oscillation around an average of about 100 counts is observed. The reason for the latter is probably due to oscillating beam intensity, but is not yet understood. The initial increase in scattering followed by a rather constant regime originates from the emergence of multiple scattering, broadening the angular distribution of scattered neutrons towards a full sphere. This significantly reduces the correlation between the scattering intensity and hydrogen content and leads to an evolution, as observed in Fig. 2. At a chosen sample-detector distance of 15 cm, the measured scattering field shows no dependency on the horizontal or vertical axis. Thus, it is used to correct the intensities measured in areas A_0 and A_1 for the influence of scattering by simple subtraction.

After correction of the intensity by flat field, dark image and scattering field, its negative logarithm gives the macroscopic attenuation, $\Omega(t) = -\ln(I(t))$. In ideal Neutron Radiography, the attenuation difference

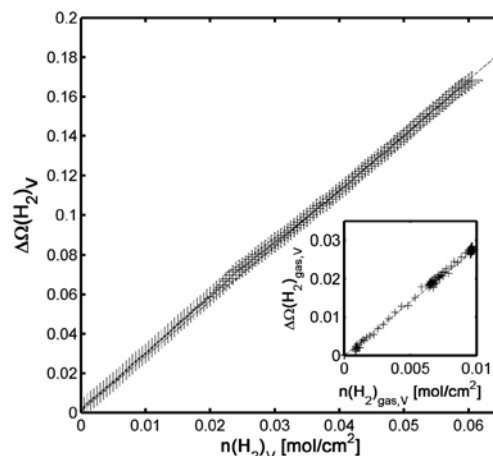


Figure 3: Macroscopic attenuation difference, $\Delta\Omega$, correlated to amount of absorbed hydrogen (referred to area A_0). The inset shows the analogue correlation for gaseous hydrogen (referred to area A_1).[†]

between subsequent images in areas A_0 and A_1 is directly proportional to the change in hydrogen content in these areas, assuming no perturbation by time-dependent scattering after correction using the results shown in Fig. 2. The correlation between the macroscopic attenuation difference, $\Delta\Omega = \Omega(t) - \Omega(t_0)$, and corresponding hydrogen content in the pellet (referred to area A_0) is shown in Fig. 3.

The inset shows the same correlation for the amount of gaseous hydrogen in the free volume. Both correlations are found to be linear with a proportionality factor of $2.8 \pm 0.1 \text{ cm}^2/\text{mol}$. Hence, perturbations by time-constant scattering influences originating from the sample environment as well as an effect of moderation of fission neutrons by hydrogen are negligible.

For sample-detector distances of 15 cm and above, a simple way to correct for the time-dependent scattering field in in-situ NR measurements has been shown. Using this, the correlation between beam attenuation by hydrogen and the corresponding hydrogen content was found to be linear. Thus, even for large samples and hydrogen contents as studied here, the assumption of Beer's law to calculate attenuation coefficients is valid. This paves the way for precise quantitative investigations of hydrogen storage systems using fission neutrons.

[†]Reprinted from [1] with permission from Elsevier

[1] S. Bőrries et al., Nucl. Instrum. Methods Phys. Res. Sect. A-Accel. Spectrom. Dect. Assoc. Equip. 797, 158 (2015).

[2] D. L. Jacobson et al., Int. J. Hydrog. Energy 35, 12837 (2010).

[3] B. Bogdanović et al., J. Alloy. Compd. 36, 302 (2000).

Detection and imaging of the oxygen deficiency in single crystalline $\text{YBa}_2\text{Cu}_3\text{O}_{7-\delta}$ films using NEPOMUC

M. Reiner¹, T. Gigl¹, R. Jany², G. Hammerl², C. Hugenschmidt¹

¹Heinz Maier-Leibnitz Zentrum (MLZ) and Physik-Department E21, Technische Universität München, Garching, Germany

²Experimental Physics VI, Center for Electronic Correlations and Magnetism, University of Augsburg, Augsburg, Germany

In $\text{YBa}_2\text{Cu}_3\text{O}_{7-\delta}$ (YBCO), a variety of exciting phenomena such as high-temperature superconductivity or charge-density wave (CDW) order occurs for certain oxygen deficiencies δ . We have established a linear correlation between the Doppler broadening of the positron-electron annihilation line and δ , as determined by X-ray diffraction (XRD). Our ab-initio calculations reveal the microscopic behavior of the positrons in YBCO crystals as the origin of this dependency. This correlation allows us to use the NEPOMUC positron beam as a sensitive tool for the determination of δ and its spatial fluctuation in YBCO. For a set of laser-deposited single-crystalline YBCO films, we have shown that standard preparation procedures for increasing δ lead to a higher lateral variation and demonstrated the huge potential of positrons for probing the oxygen distribution in YBCO films.

Defect spectroscopy using positrons

Positron Annihilation Spectroscopy (PAS) uses the positron as a probe particle. Positrons in YBCO annihilate rapidly with surrounding electrons after a characteristic lifetime of about 200 ps. Prior to their annihilation, positrons are efficiently trapped in vacancies and other potentially present open volume defects. The trapping in defects is observed by analyzing experimental observables such as the positron lifetime or the Doppler broadening of the electron-positron annihilation line at the characteristic energy of $E_\gamma = 511$ keV. The Doppler broadening is reduced if the overlap of the positron wavefunction with high-momentum core electrons becomes smaller, as it is the case in open volume defects. This leads to an increase in the so-called S-parameter, which is a commonly evaluated lineshape parameter sensitive to the number of counts in the central area of the annihilation line. Doppler Broadening

Spectroscopy (DBS) at a high lateral resolution of up to 0.3 mm (FWHM) and with short measurement times of only one minute per spectrum can be performed at the CDB-spectrometer at NEPOMUC [1].

High-quality YBCO films

High-quality crystals of YBCO are required in technical devices such as superconducting wires, fault current limiters or magnets and for studying the interplay between CDW and superconducting phases [2,3]. A well-defined value of δ and a homogeneous distribution of the oxygen in the films are highly important for applications and fundamental research. The investigated set of carefully grown high-quality YBCO films of 200 nm thickness was prepared at Universität Augsburg [4]. YBCO was deposited onto SrTiO_3 substrates by pulsed laser deposition, which enables growth of single-crystalline layers. In the as-deposited state, δ is around 0.2 as determined by the evaluation of the c-axis lattice parameter from XRD. Subsequent heat treatment at 400 °C after deposition leads to oxygen diffusing out and, hence, allows an increase in δ . Our sample set covered a wide range of $0.191 < \delta < 0.791$ corresponding to $91 \text{ K} > T_c > 24 \text{ K}$.

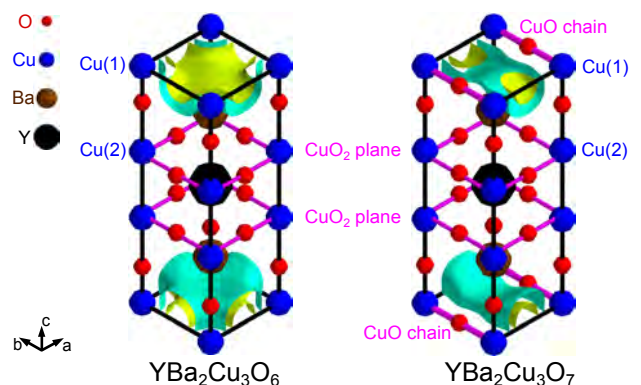


Figure 1: Isosurfaces of the positron density in $\text{YBa}_2\text{Cu}_3\text{O}_6$ and $\text{YBa}_2\text{Cu}_3\text{O}_7$. Positrons occupy a delocalized state in the basal plane with its varying oxygen content.

Positrons and oxygen deficiency in YBCO

In order to investigate the behavior of positrons in YBCO, calculations were performed using the MIKA Doppler software package [5]. Crystals with $\delta = 0$ and $\delta = 1$ were modeled. In the first case, the basal plane is completely oxygen deficient whereas, in oxygen rich samples, the additional atoms form CuO chains in the basal plane along the b-axis. The Schrödinger equation for positrons was solved in both cases. As illustrated in Fig. 1, positrons occupy a delocalized state in the basal plane of the unit cells with varying oxygen content. The reason for this is the large amount of open volume in the vicinity of this plane. The localization of positrons at these planes leads to a strong correlation of PAS observables to δ . The Doppler broadening of the annihilation line decreases with the oxygen content, i.e. $S(\delta)$ increases with higher δ . Our findings indicate that even when positrons are trapped in Cu or Ba vacancies, PAS observables are still sensitive to changes in the oxygen content in the basal plane [5], making PAS an excellent technique for probing δ .

Several experimental approaches can be chosen in order to investigate the YBCO films by DBS at the NEPOMUC positron beam. Depth profiling, i.e. increasing the incident positron energy from 0.5 to 30 keV, allows depth dependent measurements and an adjustment of the incident energy for further experiments. At an energy of 4 keV, the bulk of the YBCO films is probed whereas, at 7 keV, information at the interface to the substrate is obtained. Throughout the whole depth of the layers, a strong correlation between the S-parameter and δ was found. Characteristic S-parameters for the samples with different δ were derived by averaging the results of depth dependent measurements (see S_{YBCO} in Fig. 2). The correlation is well described by a linear fit. Due to the high lateral resolution available at NEPOMUC, the beam can be scanned over the samples, allowing the S-parameter map shown in Fig. 2 to be recorded. For each of the samples, a characteristic S-parameter S_{map} can be extracted by averaging the results of spatially resolved DBS. The correlation between S_{map} and δ is also linear and was used to investigate the lateral variation of δ . A quantitative evaluation [6,7] showed that in the as-deposited sample A1, the lateral variation of S is mainly caused by the statistical error of the measurement and thus, δ is absolutely homogeneous. In

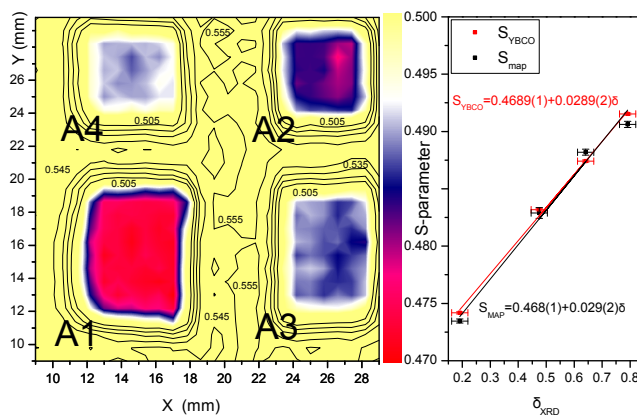


Figure 2 (as published in [6]): Left: S-parameter map of the four investigated YBCO films fixed on an Al sample holder. Right: Correlation between the characteristic S-parameters S_{YBCO} (determined from depth dependent measurements) and S_{map} (determined from the map on the left) as a function of the oxygen deficiency δ . The solid lines were obtained by linear fits yielding the given equations.

the tempered films, δ is higher and shows a larger lateral variation. The latter increases by a factor of around two for the films tempered in vacuum (i. e. A3 and A4) and by a factor of four for the film tempered in a 400 mbar O_2 -atmosphere (A2).

Implications and future experiments

Our results strongly suggest that low residual pressures should be applied during the heat treatment of YBCO films in order to ensure a homogeneous oxygen distribution in the films. In future, we will use the correlation found between the DBS results and δ to observe the oxygen diffusion in-situ at elevated temperatures. In so doing, we will benefit from the unique experimental prospects of NEPOMUC, namely depth dependent DBS measurements within extremely short times in a wide temperature range between -250 and 900 °C.

Acknowledgments

The authors gratefully acknowledge financial support from the projects BMBF 05K13WO1 and DFG TRR 80.

- [1] M. Reiner et al., J. Phys. Conf. Proc. 443, 012071 (2013).
- [2] M. K. Wu et al., Phys. Rev. Lett. 58, 908 (1987).
- [3] J. Chang et al., Nat. Phys. 8, 871 (2012).
- [4] G. Hammerl et al., Nature 407, 162 (2000).
- [5] T. Torsti et al., Phys. Status Solidi B-Basic Solid State Phys. 243, 1016 (2006).
- [6] M. Reiner, PhD Thesis, Technische Universität München (2015).
- [7] M. Reiner et al., Appl. Phys. Lett. 106, 111910 (2015).

Ferrofluid magnetic nanoparticles aggregation driven by electric forces

M. Rajnak¹, V. I. Petrenko^{2,3}, M. V. Avdeev², O. I. Ivankov^{2,3,4}, A. Feoktystov⁵, B. Dolnik⁶, J. Kurimsky⁶, P. Kopcansky¹, M. Timko¹

¹Institute of Experimental Physics SAS, Kosice, Slovakia

²Joint Institute for Nuclear Research, Dubna, Russia

³Kyiv Taras Shevchenko National University, Kyiv, Ukraine

⁴Moscow Institute of Physics and Technology, Dolgoprudniy, Russia

⁵Jülich Centre for Neutron Science (JCNS) at MLZ, Forschungszentrum Jülich GmbH, Garching, Germany

⁶Faculty of Electrical Engineering and Informatics, Technical University of Kosice, Kosice, Slovakia

Ferrofluids, consisting of a base fluid and stabilized magnetic nanoparticles, are known as magnetically controllable fluids. Magnetic control of the ferrofluids' structure and flow originates in the interaction of magnetic nanoparticles with external magnetic fields. The presence of magnetic nanoparticles in a dielectric fluid increases its permittivity and can even lead to the increase in its dielectric breakdown field strength. But what is the structural behavior of such ferrofluids in response to electric fields? We report on an *in situ* small angle neutron scattering (SANS) study of a transformer oil-based ferrofluid exposed to electric fields of various intensities and frequencies. The study proves the reversible formation of anisotropic particle aggregates driven by the electric forces. In low-concentrated ferrofluids, these forces even form macroscopic visible patterns.

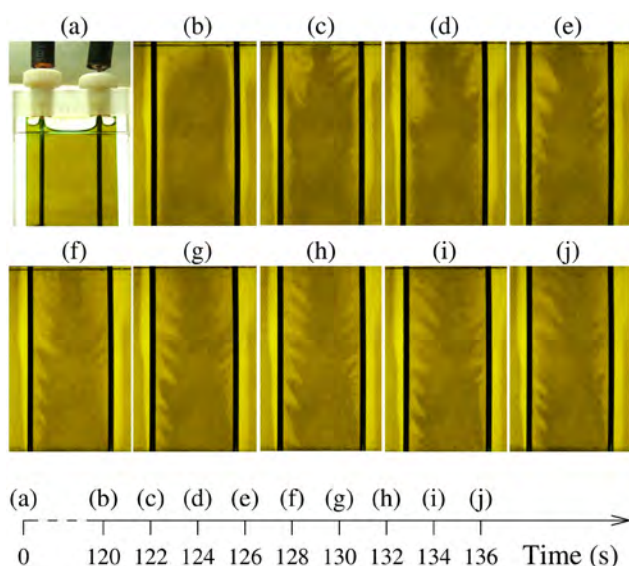


Figure 1: Transformer oil-based ferrofluid in zero electric field (a). Time evolution of pattern formation in the sample exposed to DC electric field of 5 kV/cm (b–j).

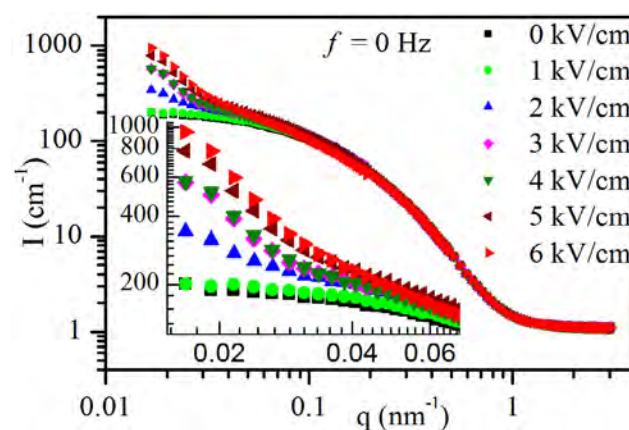


Figure 2: SANS curves for the ferrofluid exposed to various DC electric fields.

Transformer oil-based ferrofluids

Colloidal dispersions of superparamagnetic nanoparticles (SNP) in transformer oils (TO) constitute an important branch of a wide ferrofluid family with respect to technological applications. Their inherent ability to dissipate heat more effectively than pure TO has indicated a potential use in power transformers. As a cooling medium, such a ferrofluid exploits the magnetically controllable flow when exposed to temperature and magnetic field gradients around transformer cores. Much less intuitive than the thermal properties are their dielectric and insulating characteristics. The most promising reason is that the SNP act in the TO as charge scavengers and thus convert free charges (electrons from field ionization) into slow charged SNP [1]. This process can significantly slow down the streamer velocity leading to dielectric breakdown. Hence, the inter-particle interactions and ferrofluid's structural behavior of ferrofluids in electric fields appear fundamental to an understanding of the peculiar breakdown mechanism. Recently, a process of reversible aggregation of SNP in an electric field was deduced from dielectric measurements [2].

Pattern formation

In Fig. 1, we present a visual effect of electric forces on a diluted ferrofluid (0.05 %_{vol}) based on TO and magnetite SNP (10 nm mean diameter) coated with oleic acid. The sample is placed in a quartz Hellma cuvette equipped with two electrodes powered by direct current (DC) voltage (5 kV). After applying the voltage, a gradual transformation of the homogeneous ferrofluid to a state with a separated phase of higher particle concentration was observed. This initial separation is associated with the electric current flowing through the sample. The space charge accumulating onto the electrodes pushes the SNP out of that region, leading to the increase in their concentration between the electrodes. As the ferrofluid with the separated phase exhibits permittivity and conductivity gradients, the further action of the electric field exerts an anisotropic electric force on the transition layer. That force distorts the separated phase in the direction of the electric field gradient and forms the spike-like pattern. We found the pattern formation to be a reversible process, independent of the voltage polarity and gravity. The effect induced was brought on by DC electric fields with intensities from 3 kV/cm to 6 kV/cm [3].

Particle aggregation

Corresponding structural changes in a concentrated ferrofluid (1 %_{vol}) at nanoscale were investigated by KWS-1 small angle neutron scattering diffractometer at MLZ [3]. Fig. 2 shows the scattered neutron intensity I as a function of the scattering vector q measured on the sample exposed to the DC electric field (0–6 kV/cm). While the SANS curve obtained in zero electric field corresponds to a typical system of polydisperse SNP with a mean size of about 8 nm, the increasing field intensity gives rise to the increase in the scattered intensity in the small q region. This effect is considered as a direct evidence of the ferrofluid SNP aggregates induced by the electric forces. Besides the electrohydrodynamic flow, these forces include the polarization forces and subsequent dielectrophoretic SNP interaction. The induced electric dipoles in the SNP appear due to the dielectric contrast between the SNP ($\epsilon > 34$) and the TO ($\epsilon = 2$). Thus, the aggregates are reflected in the SANS profile below 0.1 nm^{-1} . As the profile has not reached the Guinier region, the final aggregate size is greater than 300 nm, as determined from the lowest q value covered in the experiment.

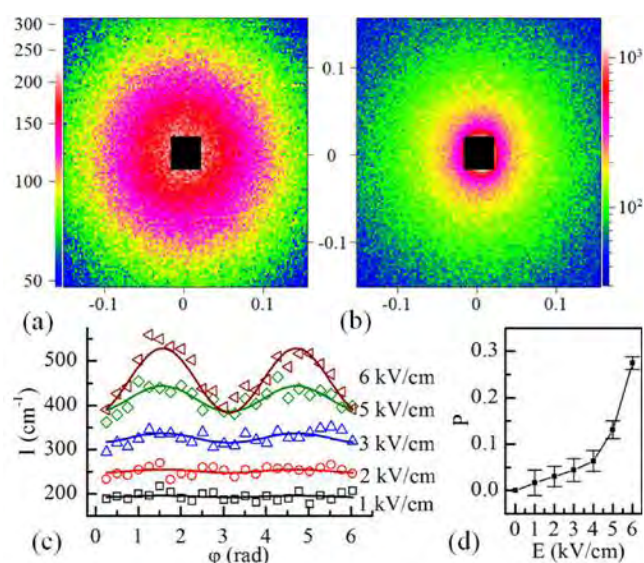
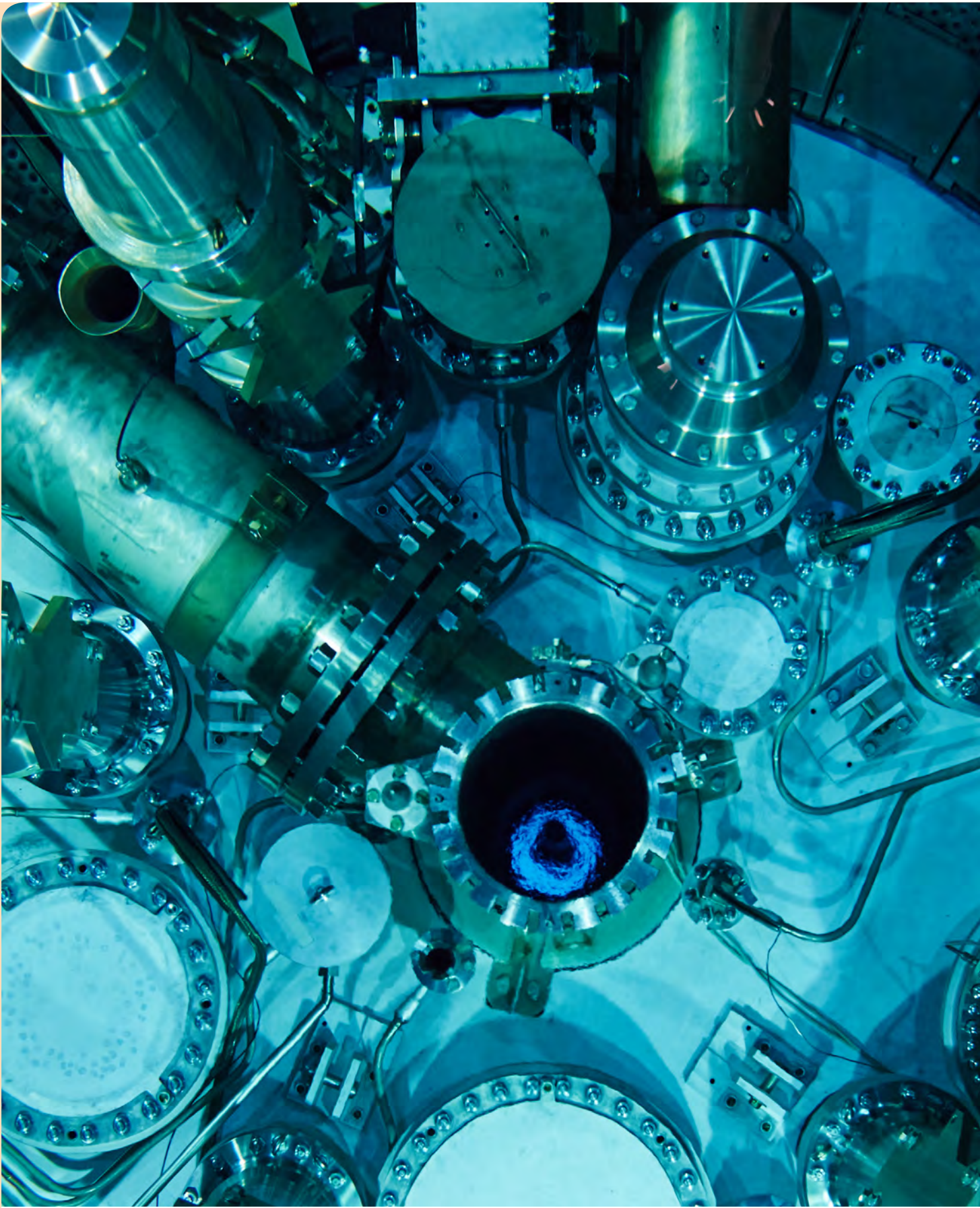


Figure 3: 2D scattering patterns for the ferrofluid in zero (a) and 6 kV/cm DC electric fields (b). Both axes represent $q \text{ (nm}^{-1}\text{)}$. Scattered intensity versus the radial angle ϕ taken at $q = 0.024 \text{ nm}^{-1}$ for different electric field strengths (c). Solid lines are fits according to $A + B \sin^2\phi$. The cut at 4 kV/cm is omitted due to partial overlap with other data. The P -parameter as a function of the electric field strength (d).

Unlike the isotropic scattering in zero electric field (Fig. 3a), SANS in the DC electric fields yields anisotropic patterns (Fig. 3b), thus reflecting the elongated shape of the formed aggregates oriented along the electric field. The development of the scattering anisotropy with the electric field is shown in Fig. 3c, where scattered intensities are plotted as a function of the radial angle ϕ at a constant module of the scattering vector, q . At some form of aggregate shape anisotropy, the structure-factor $S(q)$ can be approximated by $A(q) + B(q)\sin^2\phi$, where $A(q)$ and $B(q)$ are isotropic functions. The corresponding fits, comprising only A and B parameters which describe the intensity oscillations along ϕ , make it possible to estimate the anisotropy of the 2D intensity at a given q -value as $P = B/(A + B)$. In this way one can see that the aggregation and orientation processes in our experiment are far from saturation, as the anisotropy parameter P exhibits a continuous rise with the electric field strength (Fig. 3d).

- [1] J. G. Hwang et al., *J. Appl. Phys.* 107, 1 (2010).
- [2] M. Rajnak et al., *Phys. Rev. E* 90, 032310 (2014).
- [3] M. Rajnak et al., *Appl. Phys. Lett.* 107, 7 (2015).

View into the reactor pool during the replacement of the spent fuel element.



Reactor & Industry

Safe operation and future challenges

A. Kastenmüller

Forschungs-Neutronenquelle Heinz Maier-Leibnitz (FRM II), Technische Universität München, Garching, Germany

Only 171 days of operation had been planned for 2015 due to a scheduled maintenance break to allow for the exchange of the plug at the beam tube SR5. This was required for the new instruments of JCMS in the neutron guide hall east (TOPAS, POWTEX) and the anvil press SAPHIR (University of Bayreuth) as well as the existing instrument TRISP (Max-Planck-Institute Stuttgart), which has to be removed from the experimental hall. In order to facilitate the exchange, relevant subprojects such as the manufacturing and qualification of the new plug for the future three beam tubes by the Forschungszentrum Jülich (institute ZEA-1), the disposal of the previous plug as radioactive waste and the actual exchange process had to be planned and prepared thoroughly. Delays in these subprojects made it necessary to adjust the reactor operation schedule, resulting in a reduction totaling 150 in the number of operating days, and also to postpone the maintenance break until the end of October. In 2015, the neutron source became operational with the second half of cycle 36 and cycles 37 and 38 for a total of 149.2 days. Compared to the 150 days announced, the availability of FRM II to our users and customers corresponds to 99.5 %.

The reactor operation cycles of 2015

In 2015, the FRM II was operated safely with cycles no. 36b, 37 and 38 delivering nuclear energy totaling 2983.7 MWd.

Cycle 36, that began in 2014, was continued from mid - January 2015 and ended, with no interruptions in the meantime, on 11th February 2015 when the control rod reached its upper end position at burnup of the fuel assembly of 1188 MWd.

Cycle 37 started as scheduled on 9th March 2015 and had a total of three interruptions – either short-

term and planned, or unplanned. The first short-term planned reactor shutdown was carried out to replace an ionization chamber of the neutron flux measurement system. The two further breaks were each caused by a reactor fast shutdown due to the failure of the helium compressor of the cold neutron source. The lost operating days were appended at the end of the cycle that was reached on 28th May 2015 at the burnup of the fuel assembly of 1192 MWd.

On 13th July 2015, cycle 38 began as scheduled, but was interrupted just two days later by a renewed failure of the electric motor of the helium compressor of the cold neutron source. A further stop for a planned summer break took place in the period from 7th August 2015 to 7th September 2015. Thereafter, the cycle was continued without further interruptions until the maximum licensed burnup of the fuel assembly was reached on 20th October 2015.

In total, 1820 recurring tests, operability checks, inspections by independent experts from the regulatory body covering 18 different subject areas, as well as maintenance and service measures and around 35 modifications to the facility that had to be referred



Figure 1: Defective helium compressor motor of the cold neutron source.

to the regulatory body, guaranteed that the high safety standards of the FRM II were maintained, or even further improved. There was no reportable incident in 2015.

Maintenance break ahead

Since 20th October 2015, preparations for the exchange of the aforementioned plug of the beam tube SR5 have been ongoing. During the inevitable maintenance break, it is also planned to replace the converter plates of the converter facility. Due to a small leak in a thimble for the temperature measurement in the moderator tank that was detected on 31st October 2015 by the measurement of increased tritium activity in the exhaust air and in the air of the reactor hall, the relevant thimble has to be replaced prior to restarting the reactor. Based on current information, the leakage is at the bottom region of the thimble and is thus surrounded by heavy water. In order to exchange the thimble, the moderator tank has to be emptied and dried completely. Preparations, including the manufacturing of the necessary spare parts, had already started at the end of 2015.

Periodic safety review after 10 years of routine operation

In addition to the various tasks and work within the facility, a periodic safety review (PSR) according to auxiliary condition III.1.6 of the operating license of the FRM II was carried out for the first time after 10 years of routine operation. After the costly and time-consuming preparation of the comprehensive 5400 page document, this was submitted to the St-MUV and its appointed experts from TÜV in time on 30th April 2015. Besides a description of the facility, the document included a deterministic safety status analysis (SSA), a probabilistic safety analysis (PSA) and a deterministic security analysis.

New buildings and decommissioning tasks

In preparation for the planned construction of a new workshop and an office building by the FRM II, as well as a new laboratory and office building by the Forschungszentrum Jülich, extensive measures for the clearance of the construction site and site development took place in 2015. So, the remaining remnants of the "Flachbau II" and the connecting building to the cyclotron building were completely removed. Adjacent to the building USB, the construction of the underground duct for piping and cabling to the new



Figure 2: Cleared construction site for a new workshop, office and laboratory buildings.

building was completed. Furthermore, the storage hall for the radioprotection department west of the supply building USB was constructed and will be usable in the first quarter of 2016.

At the same time, the staff of the FRM II is also partially involved in other projects such as the decommissioning of the old FRM as well as the cyclotron that is located on the premises of FRM II and overall preparations associated with this. In addition, the nuclear fuel lab in the industrial application center (IAZ) needed some support from the staff of the FRM II on account of the license required according to § 9 AtG to handle enriched uranium, which has been granted in the meantime.

These various tasks and related measures present a permanent additional challenge for the reactor operation staff of the FRM II, especially due to the associated and extensive administrative procedures.



Figure 3: Construction of the storage hall for the radioprotection department.

Thermal conductivity of fresh and spent high-density U-Mo fuels

T. K. Huber¹, H. Breitzkreutz¹, D. E. Burkes³, A. J. Casella³, A. M. Casella³, S. Elgeti², W. Petry¹, C. Reiter¹, F. N. Smith³

¹Forschungs-Neutronenquelle Heinz Maier-Leibnitz (FRM II), Technische Universität München, Garching, Germany

²Max-Planck-Institute for Plasma Physics, Garching, Germany

³Pacific Northwest National Laboratory, Richland, Washington, USA

The FRM II is looking into high density U-Mo fuels as a replacement option for its current HEU fuel. For this new fuel, the change in the thermal conductivity during in-pile irradiation plays a significant role in the evolution and performance of the nuclear fuel inside the fuel elements. To correctly simulate the heat fluxes and temperatures in the fuel meat during normal reactor operation, and also for off-normal scenarios, it is necessary to investigate the change in thermal properties, especially the thermal conductivity, which strongly depends on the fission density and temperature. In general, two different U-Mo fuel types are distinguished: dispersion and monolithic. For dispersion fuel, U-Mo powder is embedded in a matrix material, usually Aluminum or an Aluminum alloy. In monolithic fuel, a bulk U-Mo foil without matrix material is used.

Constituents of the thermal conductivity

The thermal conductivity λ cannot be measured directly, but is rather calculated from the thermal diffusivity α , specific heat capacity C_p and density ρ [1]. The specific heat capacity C_p was measured using a Differential Scanning Calorimeter. It is mainly dependent on the atomic, i.e. material composition, and does not vary significantly for the different fuel types, not even during irradiation.

The density ρ was obtained with the Immersion Method and Pycnometry. As well, it does not vary much for the different fuel types, but slightly decreases due to the formation of fission gas bubbles during irradiation.

The thermal diffusivity α was determined by the Laser Flash Method. This quantity is strongly dependent on the material's microstructure and is

the parameter with the largest variation between the different fuels. During irradiation, the material's crystal lattice is destroyed by the highly energetic fission products and fission gas bubbles, drastically decreasing the thermal diffusivity of the irradiated material.

Thermal conductivity: Results

The thermal conductivity of fresh dispersion fuel lies between 25 W/m·K and 70 W/m·K depending on the particle size and shape, matrix material composition and Uranium loading. The thermal conductivity of as-fabricated monolithic fuel is below 17 W/m·K due to the lack of a highly conductive Aluminum matrix [1].

From the beginning of irradiation to a burnup of $4.86 \cdot 10^{21}$ f/cm³, the thermal conductivity of the dispersion fuel decreases drastically from 60 W/m·K down to 19 W/m·K. Irradiation up to $6.12 \cdot 10^{21}$ f/cm³ further decreases the thermal conductivity to 10 W/m·K [1].

The decrease of λ for the monolithic fuel is less rapid. From the beginning of operation to a burnup of $3.25 \cdot 10^{21}$ f/cm³, the thermal conductivity drops from 17 W/m·K down to 12 W/m·K [2].

During irradiation, the highly thermal conductive matrix material of the dispersion fuel is successively consumed by the low thermal conductive interdiffusion layer (IDL) (20 W/m·K) [3] that grows during irradiation between the U-Mo particle and Aluminum matrix, causing a decrease in the thermal conductivity of the fuel of about 70 %. The growth of the IDL is dependent on the fuel meat temperature. Operating the fuel at a higher temperature accelerates the growth of the IDL and the thermal conductivity decreases faster. When all matrix material has been consumed, the thermal conductivity of the disper-

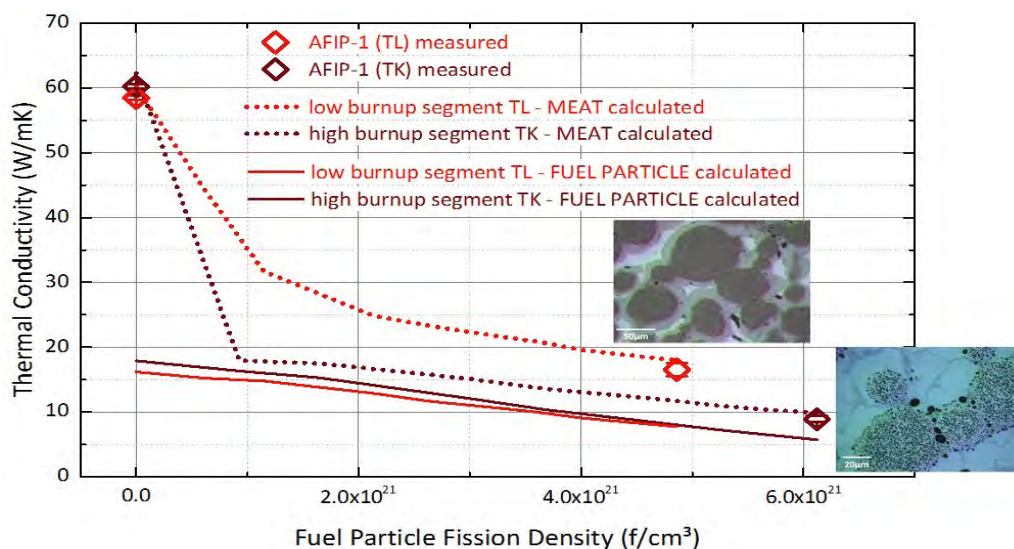


Figure 1: Calculated evolution of the thermal conductivity of the two investigated dispersion fuel segments. The high burnup segment (dark red) was irradiated at higher temperature resulting in faster growth of the IDL and therefore a steeper decrease in the thermal conductivity, compared to the low burn-up segment (light red), where there is still matrix material left after irradiation, as can be seen on the optical microscope images.

sion fuel follows the less steep slope of the thermal conductivity of the monolithic U-Mo. This decrease is mainly caused by the formation of fission gas bubbles and crystal lattice decomposition from the fission products.

Theoretical model

The model of Hsu [4] best describes the thermal conductivity of dispersion fuels with a high Uranium loading, as the model takes into account the fact that the U-Mo particles may touch and, therefore, interact with each other.

The growth of the interaction layer around the fuel particles is taken into account by employing Badrinarayan's model [5] for coated spheres in a one-dimensional heat flow. The thermal conductivity of the coated sphere is then used as the thermal conductivity of the dispersed phase in the model of Hsu.

The evolution of the thickness of the IDL, as well as the thermal conductivity of the U-Mo particle during irradiation, are mainly dependent on the meat temperature and burnup and can be described by an empirical model [3], [2].

Combining these models allows a single model to be used to calculate the thermal conductivity of the fuel meat, depending on the temperature and fission density. The measured and calculated thermal conductivity of the fuel meat show agreement to within $\pm 14\%$ [3].

Comparison to U_3Si_2

For a similar fuel loading, the thermal conductivity of the current U_3Si_2 and UMo dispersion fuels are in about the same range, around 60 W/m·K [6]. Yet, for the much lower U_3Si_2 Uranium loading currently used, a higher thermal conductivity of 80 W/m·K [6] is found due to the higher Aluminum content.

The replacement of the highly enriched U_3Si_2 dispersion fuel by a lower enriched U-Mo solution with a higher Uranium loading therefore reduces the thermal conductivity of the fuel by 25 % at the beginning of life.

- [1] T. K. Huber, Thermal Conductivity of High-Density Uranium-Molybdenum Fuels for Research Reactors, Technische Universität München, PhD Thesis (2016).
- [2] D. E. Burkes et al., J. Nucl. Mater. 464, 331 (2015).
- [3] D. E. Burkes et al., J. Nucl. Mater. – accepted January 2016.
- [4] W. Y. Hsu and T. Berzins, J. Polym. Sci. Pt. B-Polym. Phys. 23, 933 (1985).
- [5] B. Badrinarayan, J.W. Barlow, Prediction of the Thermal Conductivity of Beds Which Contain Polymer Coated Metal Particles, Solid Freeform Fabrication (SEF) Symposium (1990).
- [6] U. S. Nuclear Regulatory Commission, Safety Evaluation Report, Office of Nuclear Reactor Regulation (1988).

N.c.a. Lu-177 as a pharmaceutical drug precursor: From manufacture to new cancer treatment

R. Henkelmann

Isotope Technologies Garching GmbH, Garching, Germany

ITG, Isotope Technologies Garching GmbH, focuses on the development and proprietary production of novel radiopharmaceuticals and radiomedical devices. Today, more than 60 highly trained employees contribute the extensive knowledge and experience they have gained over more than a decade, focusing on next generation radioisotope sourcing and processing for the treatment of numerous serious oncological diseases.

Theranostic Nuclear Medicine

Innovative approaches in cancer treatment to overcome the globally increasing cases of malignant diseases have eagerly been awaited in medicine. Over the past decade, it has been shown that nuclear medicine is destined to play an important role in the future by virtue of its potential for the highly specific treatment of cancer using targeted radionuclide imaging and therapy.

The technique is based on the utilization of small molecules, peptides or antibodies which are able to bind with specificity to tumor cells. These molecules can be tagged with diagnostic radioisotopes to track their distribution and accumulation at the specific disease sites by means of Positron-Emission-Tomography (PET) or Single Photon Emission Computed Tomography (SPECT). Alternatively, therapeutic radionuclides are used to selectively deliver therapeutic doses of ionizing radiation to the malignant tissue.

No carrier added Lu-177

Lutetium-177 is a radioactive isotope of a lanthanide which exhibits a favorable half-life of 6.65 d and decays through the emission of low energy β^- particles to stable Hf-177. The decay mode contains two additional γ -lines perfectly matched to the requirements of SPECT cameras, thereby allowing

the physician in charge to conveniently control the treatment. Currently, Lutetium-177 is used in clinics for the in-house manufacture of novel radiopharmaceuticals.

An innovative small enterprise ITG GmbH and the TUM have developed, at the FRM II, a unique technique for producing Lutetium-177 in pharmaceutical quality, which can effectively be used to manufacture radiolabeled therapeutic agents. The unique procedure allows Lutetium-177 to be manufactured in its particularly pure form and with the highest specific activity, namely as no-carrier-added, via the indirect route from enriched Yb-176 targets.



Manufacture of radiopharmaceuticals at the premises of the FRM II

There are strict regulations governing the preparation of medical radionuclides and radiopharmaceuticals. The agents need to be produced according to the Good Manufacturing Practice (GMP), whereas handling of the radioactivity involves adherence to the regulations on radiation protection. Since 2011, ITG has operated a GMP compliant production facility for manufacturing radiopharmaceutical precursor - no-carrier-added Lu-177 and holds a handling license of 100 TBq Lu-177. The facility is equipped with modern hot-cells and also allows Lutetium-177 radiolabeled drugs to be produced for world-wide centralized distribution.

EndolucinBeta trade mark for n.c.a. Lu-177

In April 2015, ITG successfully submitted a Marketing Authorization Application to the European Medicines Agency (EMA). Following approval, no-carrier-added Lutetium-177 will be commercialized as a radiopharmaceutical precursor under the trade mark EndolucinBeta.



Figure 1: Grade A environment for the production of n.c.a. Lu-177.

The availability of such a high quality innovative medical radionuclide, along with access to modern GMP facilities for the centralized manufacture of radiopharmaceuticals, allows for further development and improvement in cancer treatment.

Lu-177-DOTATOC

DOTATOC is a Somatostatine Receptor binding protein which was designed for use in the PRRT of Neuroendocrine Tumors. In retrospective clinical trials phases I and II, Lu-177-DOTATOC showed excellent results in terms of effectiveness and safety. ITG recently introduced a phase III international clinical trial to achieve final approval for this innovative radiopharmaceutical and provide neuroendocrine cancer patients with the best possible healthcare.

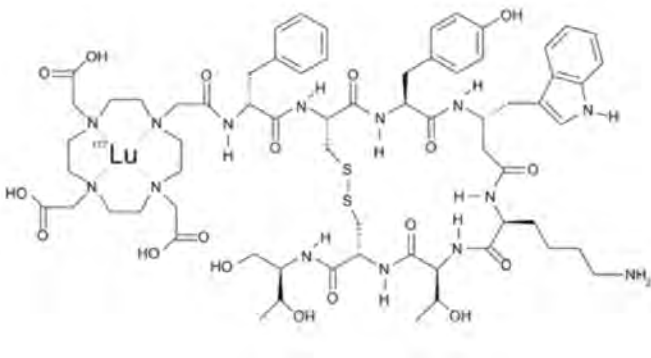


Figure 2: Structure of Lu-177-DOTATOC.

Lu-177-DOTA-Zoledronate

In 2015, ITG in-licensed a DOTA derivative of Zoledronic Acid. This compound is able to combine the favorable pharmacological behavior of bisphosphonate drugs to target bone metastases with the capability of the DOTA chelator to complex n.c.a. Lu-177, transferring the novel PRRT concept to the treatment of skeletal metastases related to breast and prostate cancer.

Ac-225/Bi-213 Generators

α -Particles have a high linear energy transfer with a maximum range of a few cell diameters in tissue. Future applications in radiopharmaceutical oncology focus on the feasibility of α -particle emitters in cancer treatment, since they show superior behavior in cell and animal studies. ITGs global research network is working on concepts for the supply of Bi-213, an α -particle emitter with a short half-life, using a generator system. Bi-213 is one of the last daughter nuclides in the decay chain of Ac-225, which is fixed on a solid phase. By passing an acidic iodide solution over the Ac-225/Bi-213 generator, the therapeutic radioisotope Bi-213 can be obtained in quantities of a few milliliters ready for the labeling of biomolecules.

Amongst others, the chapter “Facts & Figures” provides numbers of visitors, staff, budget, publications, as well as submitted proposals.



Facts & Figures

Ten Years of the User Office

R. Bucher², F. Carsughi², I. Lommatzsch¹, C. Niiranen¹, B. Tonin¹

¹Heinz Maier-Leibnitz Zentrum (MLZ), Technische Universität München, Garching, Germany

²Jülich Centre for Neutron Science (JCNS) at MLZ, Forschungszentrum Jülich GmbH, Garching, Germany

Ten years of user operation – that is quite a long time! A lot of users submitted proposals and reports, applied for visits, needed help to organise their stay in Garching, requested reimbursement of their travel expenses, lost their badges, forgot their dosimetres, and dropped their samples. It is the User Office's task to help each and every one of them – and we did all of this in 2015, as usual!

Let the users meet!

The beginning of the year was devoted to the User Meeting in February. It was our first since 2012 and we planned to make it special. While former meetings were held in the vicinity of the FRM II, this one took place in a conference centre in Ismaning. As well as about 50 posters presenting users' projects, 150 participants listened attentively to three plenary talks and a total of 19 talks in four Science Groups.

Our goal on this occasion: It was hoped that each of these invited talks would initiate discussion between our external users and our in-house Science Groups. We wanted to stimulate our users to tell us what the MLZ could do for them in the future. To which great challenges in our society can we contribute significantly? What are the needs and ex-

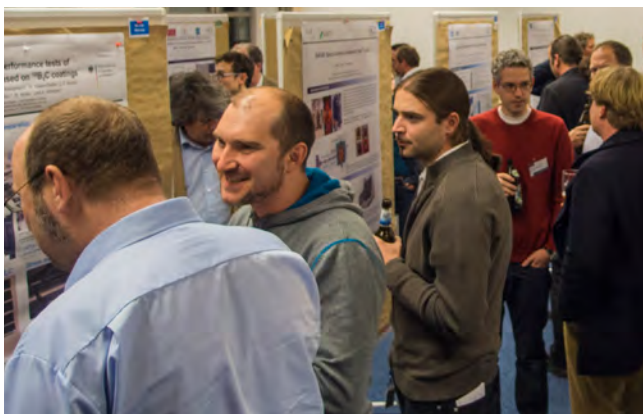


Figure 1: Lively discussion at the poster session.

pectations of our national and international users? We collected scientific topics in order to create a science road map that gathers these requirements and provides a basis for our future instrument and method development activities. This process is supported by our Scientific Advisory Board, as well as our Instrument Advisory Board.

Visiting the capital

The German capital is always worth a visit! And even more so in March 2015 because the 79th DPG Spring Meeting of the Condensed Matter Section was held there. A total of 6055 participants responded to the invitation and bustled about at the Technische Universität Berlin. Most of them – about 81 % – came from Germany, more than 600 were from other European countries, and the USA, Japan, China, Australia, Russia, Canada, South Korea, Taiwan, and Israel were also represented. They listened to 3471 talks and looked at 1658 posters - a lot of work for those few days!



Figure 2: View from the booth during a coffee break.

In between times, the exhibition of literature and equipment deserved a visit – and that was where the MLZ booth waited to greet new and old users. The User Office provided information about neutron and positron applications, the possibilities of getting beam time at Garching, and how to apply for financial support. As always, it was a pleasure for us to meet and chat with everybody!

Heading for the Spanish sun

Between August 30th and September 4th, the neutron scattering community gathered in Zaragoza in the northeast of Spain for the 6th European Conference on Neutron Scattering and enjoyed the high temperatures. A total of 652 participants came from 31 different countries – Germany sported the largest contingent, followed by France and Spain, but there were also a lot of colleagues from Russia, Japan, the USA, Argentina, and even Australia.

More than 200 talks attracted an audience and three poster sessions led to fruitful discussions. These discussion topics changed a little during the conference dinner held in a beautiful location near the river Ebro. This was especially true afterwards, when the in-house disco called for some dancing. It really was great fun!



Figure 3: Staff of MLZ, Forschungszentrum Jülich, and Helmholtz Centers at Berlin and Geesthacht.

At the venue, participants had the opportunity to visit the booths of all the major facilities and several companies. The MLZ organised a joint booth together with the Helmholtz-Zentrum Berlin (HZB) where the German neutron facilities were show-cased. We welcomed a lot of visitors, with even more questions – surprise! surprise!, they dealt mostly with the MLZ proposal deadline one week later!

New material

This year, it was also time for a third revised edition of our Experimental Facilities brochure. It is published roughly every second year and collects the latest information about our instrument suite as well as sample environment and complementary laboratories. In addition to the online version, there is always a printed copy that can be ordered from the User Office. The MLZ flyer was also revised, showing a plan of the experimental halls with all instruments, those running as well as planned.

Some statistics

Two proposal rounds in 2015 and a total of 761 proposals: It was a successful year!

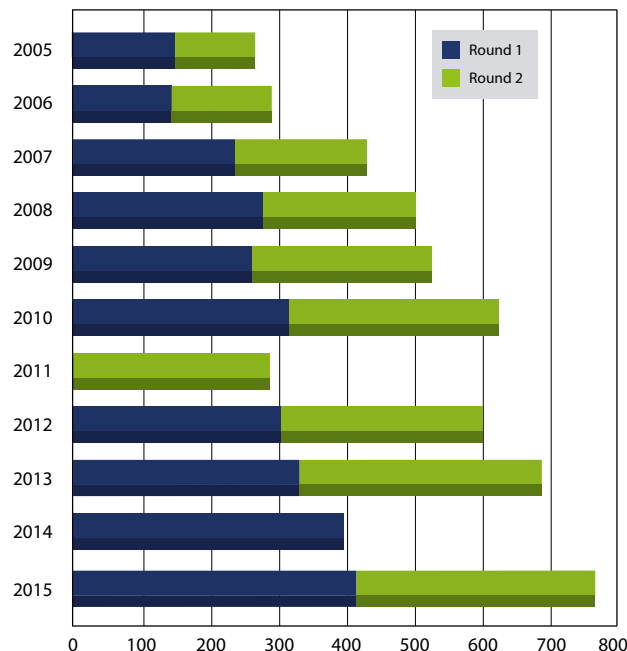


Figure 4: Proposals submitted since the first round in 2005.

Furthermore, the Rapid Access Programme is now into its third year and is flourishing. We began with three instruments (KWS-2, PGAA, and SPODI) before adding BIODIFF to the list this year. Since the start of the programme, 109 proposals have been submitted and a total of 1788 hours of beam time requested. In total, 952 hours of beam time were allocated, of which 945 have been measured. The difference between requested and allocated beam time results in an overbooking factor of 1.9. SPODI is the most widely used instrument within this programme, delivering 42 % of the allocated hours.

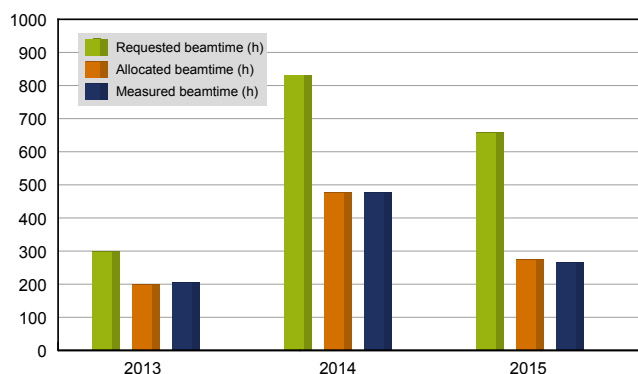


Figure 5: The successful Rapid Access Programme.

From science to media: The public relations office

C. Kortenbruck, A. Voit, C. Niiranen, B. Tonin

Heinz Maier-Leibnitz Zentrum (MLZ), Technische Universität München, Garching, Germany

Compared to 2014 with all the excitement surrounding the 10th anniversary of the FRM II, 2015 was relatively calm but nevertheless packed with interesting projects and guests. We were able to finish the relaunch of the new FRM II webpage; we organized an international workshop within the framework of the Association of European-level Research Infrastructure Facilities, ERF-AISBL, besides our annual events, and we welcomed some illustrious guests over the year. The G7 Presidency of the Federal Republic of Germany brought us some additional VIP visits. At the invitation of the Federal Foreign Office, two working groups came to read up on site about neutron sources, their scientific uniqueness, access rules and different research projects.

Relaunch of the FRM II webpage

At the beginning of 2015, the long-awaited relaunch of the FRM II webpage was finally realized; due to changes in the responsibilities devolved to the press



Figure 1: The first ERF-Workshop on “Public Awareness of Research Infrastructures” in June was an event that begs to be repeated.

officers, it had been delayed several times. The entire content was structured anew, and adapted to current conditions; this process took up a lot of the time available in 2014 and it was not able to be completed until March 2015. Updating the webpages is still a major task for the press office; the new page is now hosted by the TUM.

The international ERF-Workshop at ESO’s

On 18th and 19th June, we organized the first ERF-Workshop on “Public Awareness of Research Infrastructures” together with our partners, nmi3-public relations and ESO. This workshop brought together representatives of funding agencies, facility and project managers, press officers and social researchers to discuss the requirements and expectations of publicity activities. It attracted almost 90 participants from all over Europe and featured over 30 talks. The workshop aimed to answer questions which are crucial for most of the press officers, especially where large-scale facilities are concerned (facility under construction, crisis communication, communication between scientists and politicians ...). Therefore, the sessions which dealt with best practice were the most highly valued and many participants requested that the event be repeated; this is planned for 2017.

Media coverage

More than half of all media items are supported through scientific contributions. 20 % of these are drawn from the foreign media, which highlights the importance of providing consistent English translations. Although for most of the year there was only one part-time employee, the final number of citations more or less matched the average for a normal year. However, the application for corporate approval and the protest movement in Nordrhein-Westfalen produced relatively wide and negative press coverage. During 2016, the press office will be served by two part-time employees.



Figure 2: This photograph, displaying the different flags, testifies to the internationality of the TUM and was very difficult to arrange: It required sun at the right time and an easterly wind.

Special highlights

On the occasion of the 10th anniversary of user operation at the FRM II, “Neutron News” dedicated the first issue, including five long articles and the cover page, to research and instrumentation in Garching. In the summer, a professional photographer asked for permission to take photographs. He was preparing an exhibition on nuclear technology in Germany, which produced first class photos for our photographic data base and which we are allowed to use gratis. As has often been said in the past and according to the motto “a picture tells more than



Figure 3: The weakest magnetic field in the solar system was one of the striking items of news this year and this record-breaking magnetic shielding for high-precision experiments stands in the new guide hall east at the FRM II.

words” excellent photos are a very important part of communication and often make the difference.

Together with the Munich Chamber of Commerce, a breakfast with scientists for some 20 entrepreneurs was organized, which was promptly booked out. The entrepreneurs greatly appreciated having direct contact with the scientists and were very interested in the possibilities offered by the neutron source in solving their problems.

Visitors

At the beginning of the winter semester 2015/ 2016, a new proposal was put into effect together with the physics department of the TUM: There is one special FRM II tour per month exclusively for TUM students; the great advantage is that they can apply online directly through the university calendar. This application procedure turned out to be a resounding success and brings us many more visitors from our most important target groups. So, the 55 % made up only of students and schools demonstrates a keen interest in science and research and is very encouraging.

There were 3128 visitors in total this year, representing an overall increase of 5.8 %. In 2015, there was a Long Night of Science in June instead of the regular Open Day in October and it attracted 373 visitors (12 % of the annual visitor number). This is slightly fewer than the usual number of visitors as the Long Night tends to last at least one hour less. 72 % of all visitors came from Germany, the other 28 % being from Europe, Asia, the Americas and Africa – in fact, from 21 different countries!

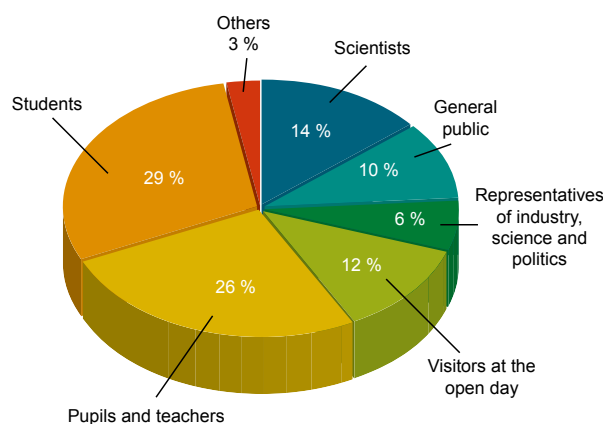


Figure 4: In 2015, a total of 3128 visitors made a guided tour through the FRM II.

Organisation

FRM II and MLZ

The Forschungs-Neutronenquelle Heinz Maier-Leibnitz (FRM II) provides neutrons for research, industry and medicine and is operated as a Corporate Research Centre by the Technische Universität München (TUM). The scientific use of the FRM II, with around 1000 user visits per year, is organized within the "Heinz Maier-Leibnitz Zentrum" (MLZ).

The chart below shows the overall network comprising the neutron source FRM II and the MLZ, as well as the funding bodies and the scientific users performing experiments at the MLZ addressing the grand challenges of our today's society.

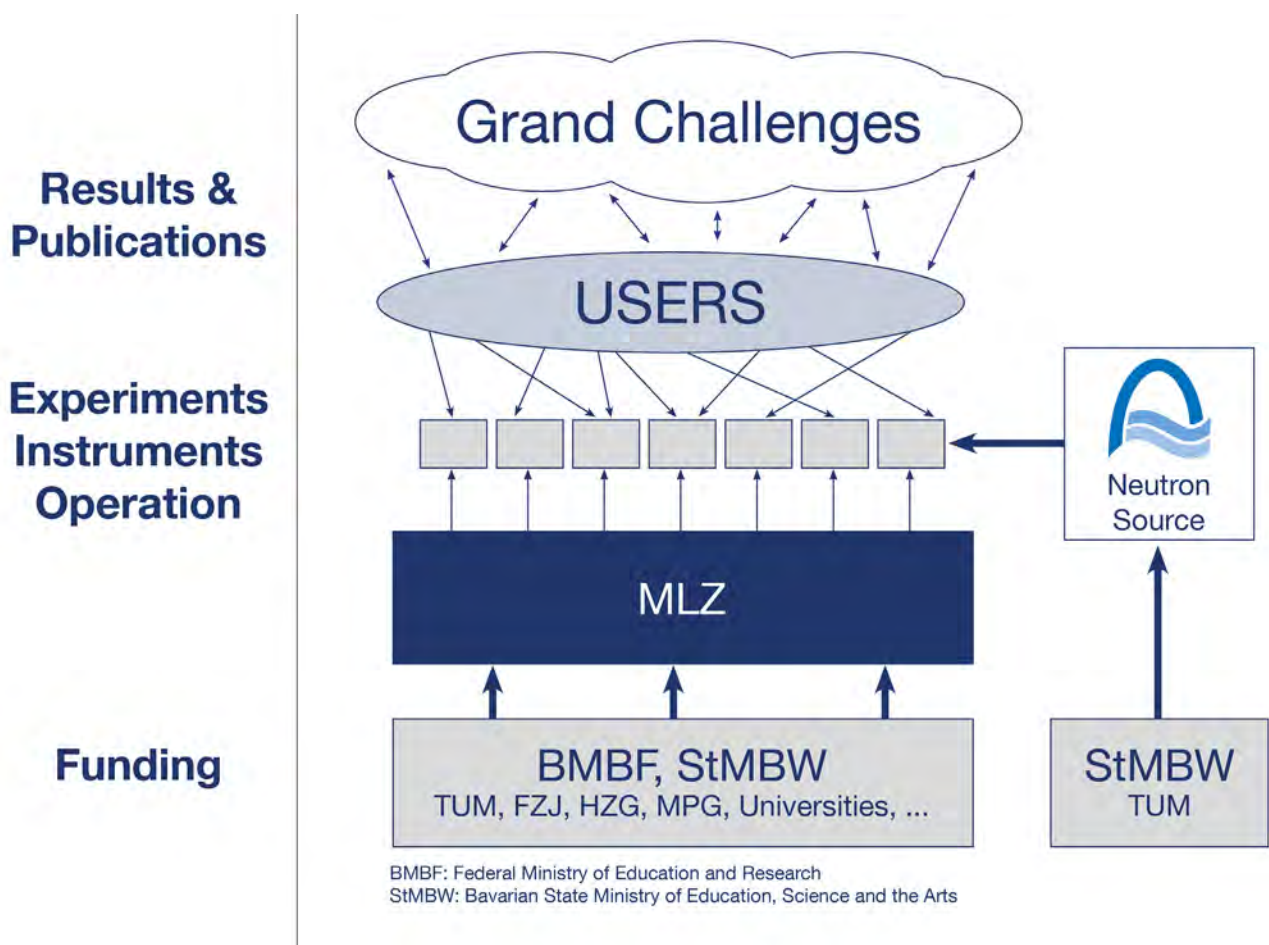


Figure 1: The neutron source FRM II and the user facility MLZ.

Scientific Director MLZ, FRM II

Prof. Dr. Winfried Petry

Technical Director FRM II

Dr. Anton Kastenmüller

Scientific Director MLZ, HGF

Prof. Dr. Thomas Brückel

Administrative Director FRM II

Dr. Klaus Seebach

Scientific Cooperation at the Heinz Maier-Leibnitz Zentrum (MLZ)

The Heinz Maier-Leibnitz Zentrum with its cooperation partners Technische Universität München (TUM), Forschungszentrum Jülich (FZJ) and Helmholtz-Zentrum Geesthacht (HZG) is embedded in a network of strong partners including the Max Planck Society (MPG) and numerous university groups exploiting the scientific use of the Forschungs-Neutronenquelle Heinz Maier-Leibnitz. The organizational chart of the MLZ is shown below.

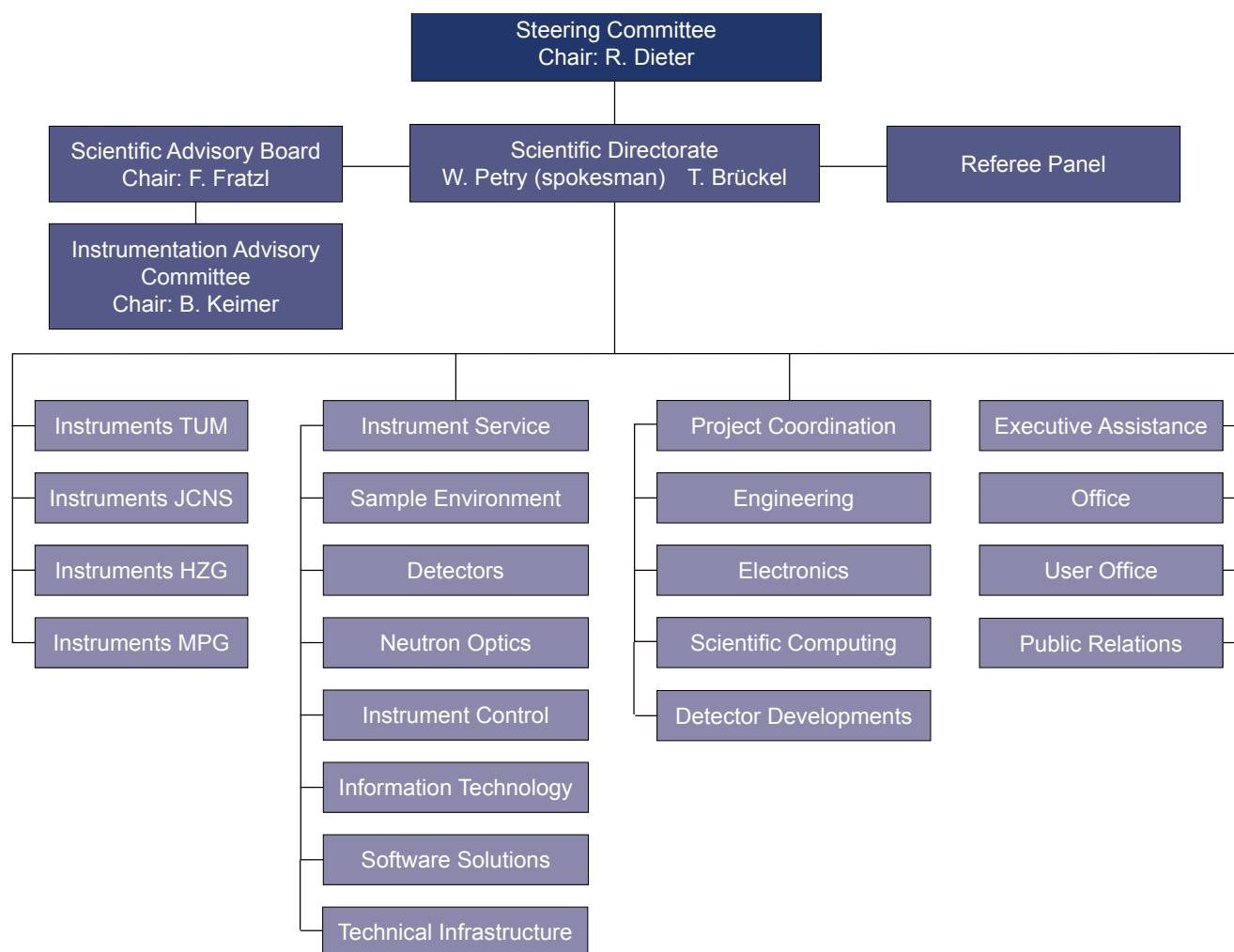


Figure 2: Organisational chart MLZ.

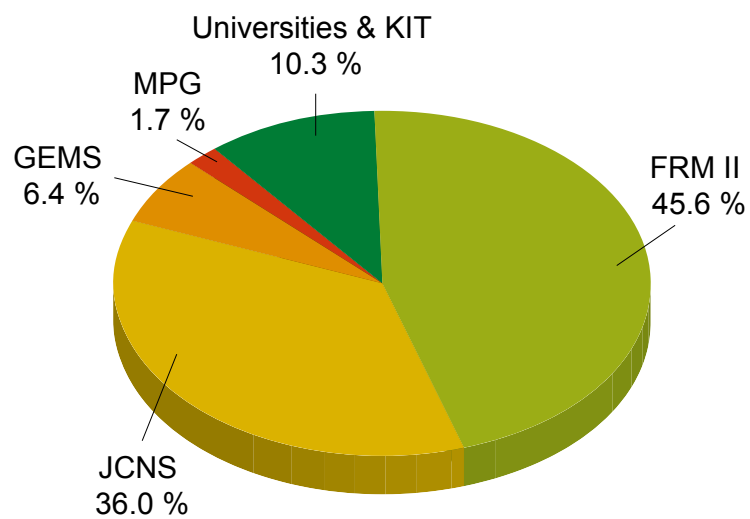
Staff

Staff of the MLZ and the FRM II

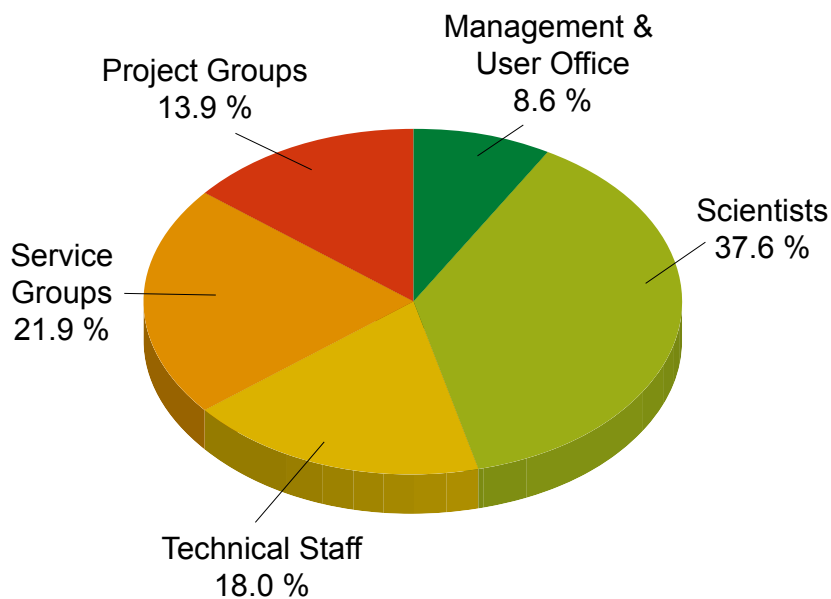
The tables and charts below show the staff of MLZ and FRM II. The staff of MLZ according to its share among the partners with a detailed view according to the function within the MLZ is depicted as well.

MLZ & its Partners	FTE ¹	%
FRM II (Science Division)	106.5	45.6
JCNS	84.0	36.0
GEMS	15.0	6.4
MPG	4.0	1.7
Universities & KIT	24.0	10.3

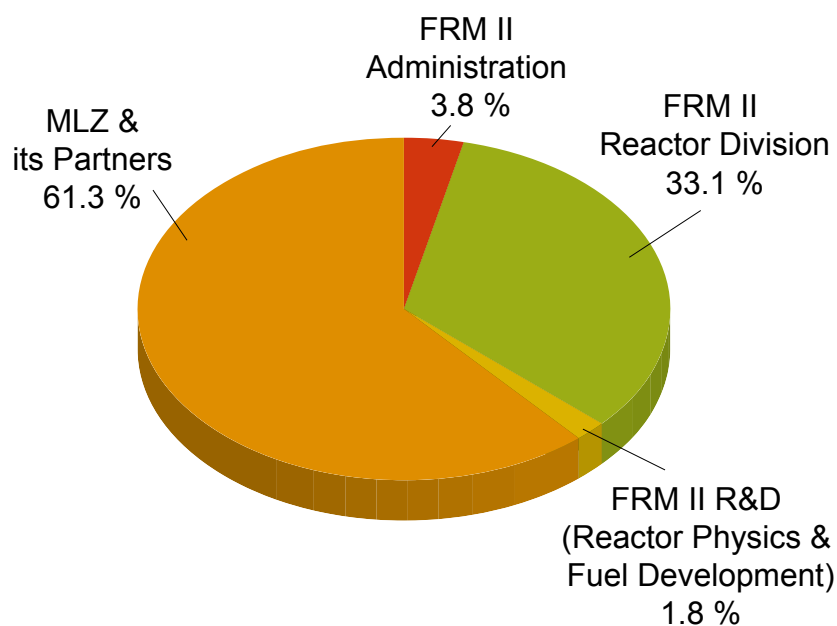
¹FTE (Full Time Equivalent)



MLZ according to Function	FTE	%
Management & User Office	20.0	8.6
Scientists	87.9	37.6
Technical Staff	42.0	18.0
Service Groups	51.1	21.9
Project Groups	32.5	13.9



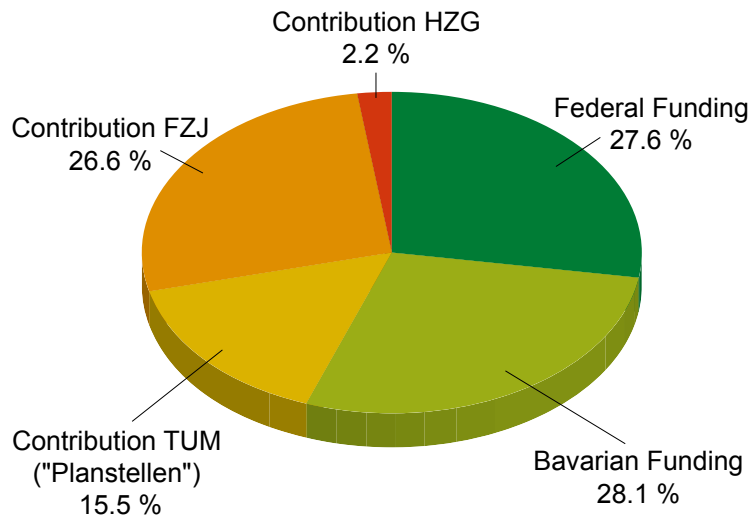
FRM II, MLZ & its Partners	FTE	%
FRM II Administration	14.4	3.8
FRM II Reactor Division	126.0	33.1
FRM II R&D (Reactor Physics & Fuel Development)	7.0	1.8
MLZ & its Partners	233.5	61.3



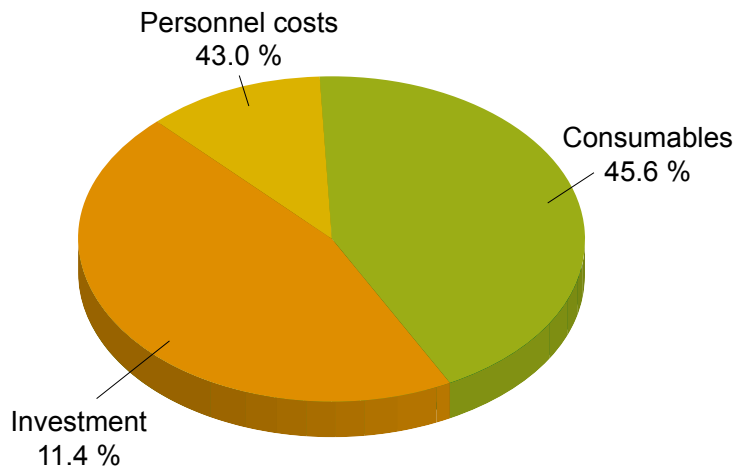
Budget

The table and charts below show the revenue and expenses in 2015.

Revenue 2015	Total (€)	%
Federal Funding	16.700.000	27.6
Bavarian Funding	17.050.000	28.1
Contribution TUM („Planstellen“)	9.420.000	15.5
Contribution FZJ	16.153.339	26.6
Contribution HZG	1.320.000	2.2
Total	60.643.339	100



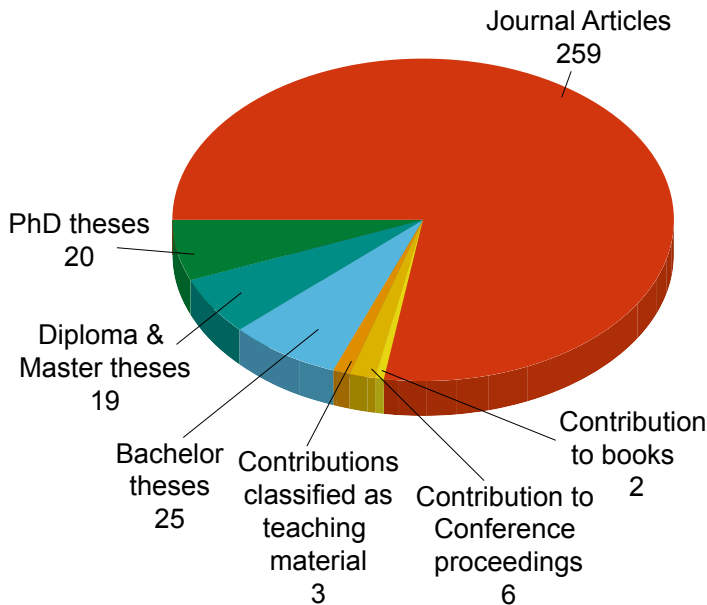
Expenses 2015	TUM (€)	FZJ (€)	HZG (€)	Total (€)	%
Personnel costs	15.050.000	8.739.397	1.310.626	25.100.023	43.0
Consumables	20.080.000	6.070.068	414.348	26.564.416	45.6
Investment	2.100.000	4.160.731	382.439	6.643.170	11.4
Total	37.230.000	18.970.196	2.107.413	58.307.609	100



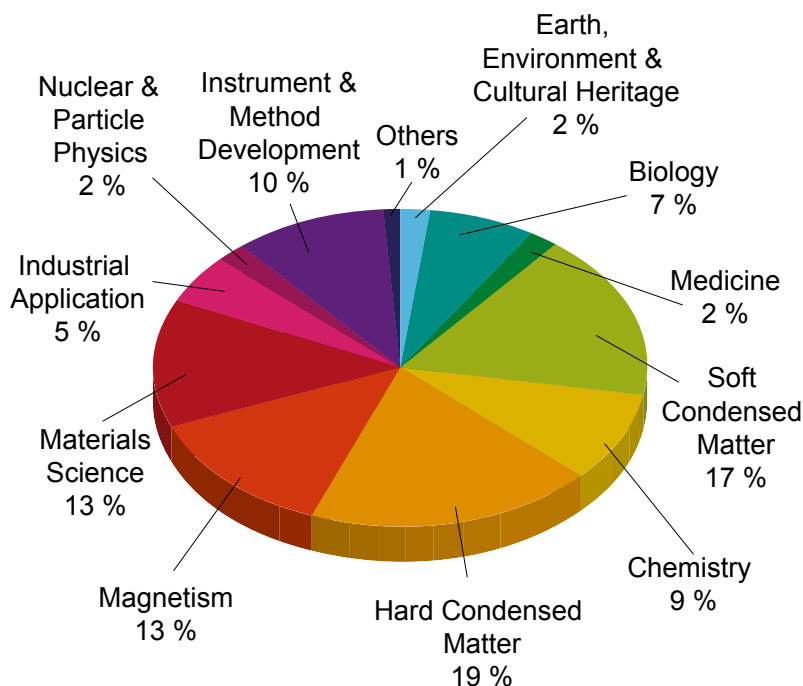
Publications & Theses

In 2015, we received notice of a total of 270 scientific publications, including journal articles, contributions to books and conference proceedings, as well as published teaching material (<https://impulse.mlz-garching.de/> and figure below). Furthermore, in total 64 theses supervised by staff of the scientific cooperation partners were completed in 2015.

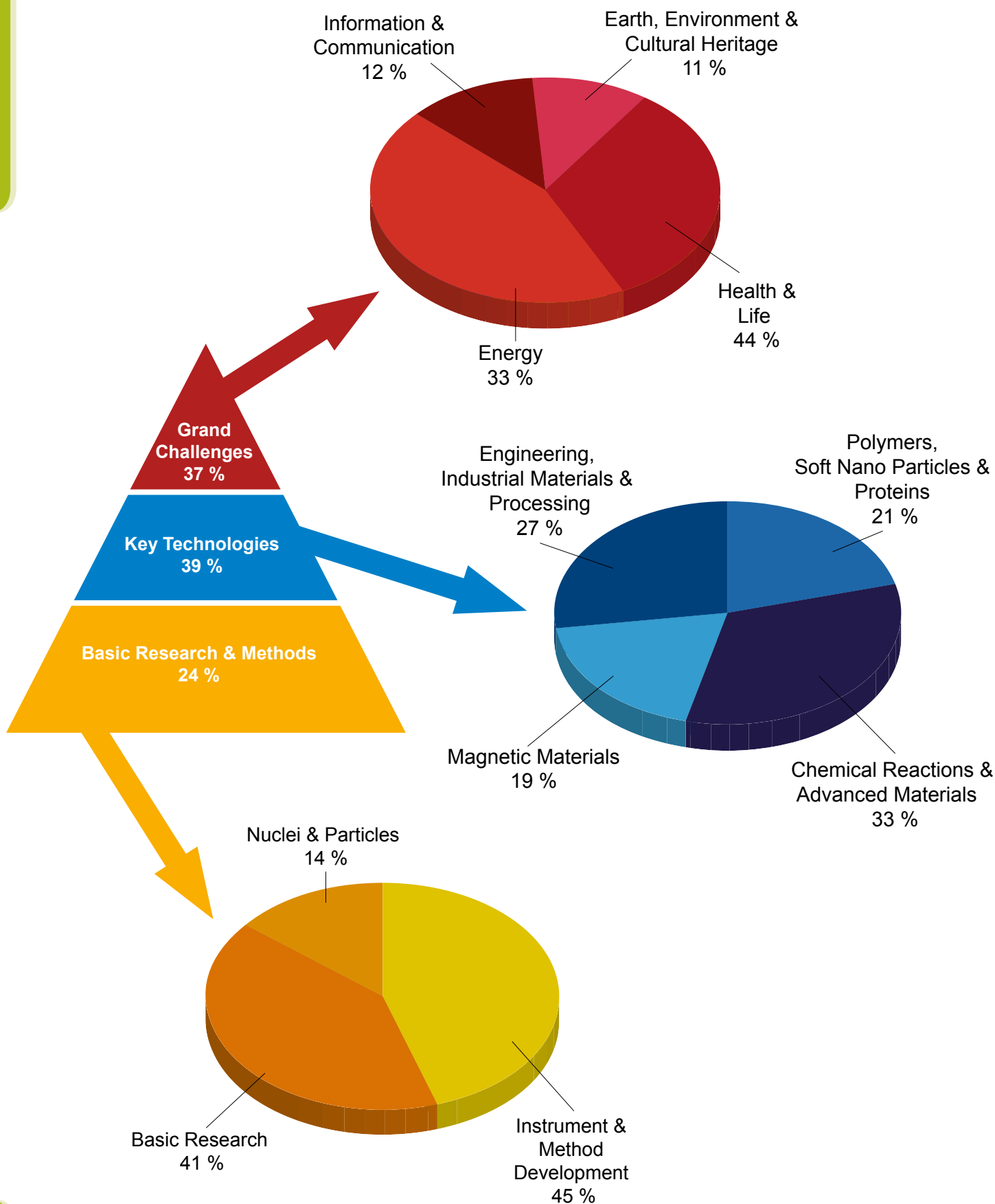
In 2015 more than 200 PhD theses, based on experiments at the MLZ and including external users, were either ongoing or completed. Of these, about 100 are under the direct supervision of staff at the MLZ.



The next figure shows the classification of the journal articles by Scientific Area (several tags per journal article are possible):



The journal articles at the MLZ can be classified according to a pyramid: from Basic Research & Methods (24 %) required to tackle the Key Technologies (39 %), which address directly the Grand Challenges of our today's society (37 %). The pie charts represent the individual subjects being dealt within these three categories.



Committees

Steering Committee

Chairman

Dr. Ralph Dieter
Federal Ministry of Education and Research

Members

MRin Dr. Ulrike Kirste (Vice Chair)
Bavarian State Ministry of Education,
Science and the Arts

Albert Berger
Senior Executive Vice-President
Technische Universität München

Thomas Frederking
Member of the Executive Board of
Helmholtz-Zentrum Berlin
für Materialien und Energie GmbH

Prof. Dr. Dr. h.c. mult. Wolfgang A. Herrmann
President
Technische Universität München
represented by Prof. Dr. Thomas Hofmann
Vice-President
Technische Universität München

Prof. Dr. Wolfgang Kaysser
Member of the Executive Board of
Helmholtz-Zentrum Geesthacht GmbH

Prof. Dr. Stephan Paul
Physik-Department E18
Technische Universität München

Prof. Dr. Sebastian Schmidt
Board of Directors of Forschungszentrum
Jülich GmbH

Guests

Prof. Dr. Winfried Petry
Scientific Director of the MLZ,
representing TUM

Prof. Dr. Thomas Brückel
Scientific Director of the MLZ,
representing HGF institutions

Dr. Anton Kastenmüller
Technical Director ZWE-FRM II
Technische Universität München

Dr. Klaus Seebach
Administrative Director ZWE-FRM II
Technische Universität München

Dirk Schlotmann
Forschungszentrum Jülich GmbH

RDin Steffi Polwein
Head of Central Administration ZA1
Technische Universität München



Figure 1: Steering Committee from left to right: R. Dieter, N. Drewes, S. Polwein, T. Frederking, M. Ganß, A. Berger, U. Kirste, S. Paul, W. Petry, D. Schlotmann, K. Seebach.

Scientific Advisory Board

Chairman

Prof. Dr. Peter Fratzl
Max-Planck-Institut für Kolloid-
und Grenzflächenforschung, Potsdam

Members

Prof. Christiane Alba-Simionesco (Vice Chair)
Laboratoire Léon Brillouin,
CEA, Centre de Saclay

Prof. Dr. Hartmut Abele
Atominstytut der Österreichischen Universitäten
Technische Universität Wien

Prof. Dr. Arantxa Arbe
Centro de Fisica de Materiales,
Material Physics Center, San Sebastián

Alejandro Javier Guirao Blank
Volkswagen AG, Wolfsburg

Prof. Dr. Dirk Johrendt
Department Chemie und Biochemie
Ludwig-Maximilians-Universität München

Prof. Dr. Bernhard Keimer
Max-Planck-Institut für Festkörperforschung,
Stuttgart

Prof. Dr. Joël Mesot
Paul Scherrer Institut, Villigen

Prof. Dr. Joachim O. Rädler
Department für Physik
Ludwig-Maximilians-Universität München

Prof. Dr. Walter Reimers
Institut für Werkstoffwissenschaften
und -technologien
Technische Universität Berlin

Prof. Dr. William Stirling
Institut Laue-Langevin (ILL), Grenoble

Prof. Dr. Metin Tolan
Beschleuniger- & Synchrotronlabor
Technische Universität Dortmund

MLZ Instrumentation Advisory Committee

Chairman

Prof. Dr. Bernhard Keimer
Max-Planck-Institut für Festkörperphysik, Stuttgart

Members

Dr. Laurent Chapon
Institut Laue Langevin, Grenoble

Dr. Ulli Köster
Institut Laue Langevin, Grenoble

Dr. Eberhard Lehmann
Paul-Scherrer-Institut, Villigen

Dr. Frédéric Ott
Laboratoire Léon Brillouin, CEA Saclay

Prof. Dr. Catherine Pappas
Delft University of Technology, Delft

Prof. Dr. Henrik Ronnøw
Ecole Polytechnique Fédérale de Lausanne

Dr. Margarita Russina
Helmholtz-Zentrum Berlin
für Materialien und Energie GmbH

Evaluation of Beam Time Proposals: Members of the Review Panels

Prof. Dr. Arantxa Arbe
Centro de Fisica de Materiales,
Material Physics Center, San Sebastián

Dr. Tamás Belgya
Budapest Neutron Center, Budapest

Dr. Victor Bodnarchuk
Joint Institute for Nuclear Research
Frank Laboratory of Neutron Physics, Dubna

Prof. Dr. Jan Bonarski
Institute of Metallurgy and Materials Science
Polish Academy of Sciences, Cracow



Figure 2: Instrumentation Advisory Committee from left to right: J. Neuhaus, H. Ronnøw, L. Chapon, E. Lehmann, F. Ott, W. Petry, C. Pappas, U. Köster, T. Brückel, B. Keimer.

Dr. Laszlo Bottyan
Institute for Particle and Nuclear Physics,
Hungarian Academy of Sciences, Budapest

Prof. Roberto Brusa
Facoltà di Ingegneria, Dipartimento di Fisica
Università degli Studi di Trento

Prof. Dr. Roberto Caciuffo
Institute for Transuranium Elements
Joint Research Center, Karlsruhe

Dr. Monica Ceretti
Institut Charles Gerhardt
Université de Montpellier 2

Dr. Niels Bech Christensen
Institute of Physics
Technical University of Denmark, Roskilde

Dr. Pascale Deen
European Spallation Source (ESS ERIC), Lund

Dr. Sabrina Disch
Department of Chemistry
University of Cologne

Prof. Dr. Stefan Egelhaaf
Lehrstuhl für Physik der weichen Materie,
Heinrich-Heine-Universität Düsseldorf

Prof. Dr. Helmut Ehrenberg
Institut für Angewandte Materialien
Karlsruher Institut für Technologie (KIT), Karlsruhe

Dr. Tom Fennell
Laboratories for Solid State Physics Neutron
Scattering, Paul Scherrer Institute, Villigen

Dr. Marie Thérèse Fernandez-Diaz
Institut Laue-Langevin (ILL), Grenoble

Dr. Peter Fouquet
Institut Laue-Langevin (ILL), Grenoble

Dr. Victoria Garcia-Sakai
STFC Rutherford Appleton Laboratory, Didcot

Prof. Giacomo Diego Gatta
Dip. Scienze della Terra „Ardito Desio“
Università degli Studi di Milano

Prof. Dr. Rupert Gebhard
Abteilung Vorgeschichte
Archäologische Staatssammlung München

Dr. Jens Gibmeier
Institut für Angewandte Materialien,
Karlsruher Institut für Technologie (KIT), Karlsruhe

Dr. Béatrice Gillon
Laboratoire Léon Brillouin
CEA, Centre de Saclay

Dr. Arsène Goukassov
Laboratoire Léon Brillouin
CEA, Centre de Saclay

Dr. Christian Grünzweig
Paul Scherrer Institute, Villigen

Prof. Dr. Ian William Hamley
Department of Chemistry
University of Reading

Dr. Thomas Hauss
Helmholtz-Zentrum Berlin
für Materialien und Energie GmbH

Prof. Dr. Stephen Hayden
HH Wills Physics Laborator
University of Bristol

Dr. Arno Hiess
Neutron Science Division
European Spallation Source (ESS ERIC), Lund

Dr. Klaudia Hradil
Röntgenzentrum
Technische Universität Wien

Dr. Nikolay Kardjilov
Helmholtz-Zentrum Berlin
für Materialien und Energie GmbH

Dr. Reinhard Kremer
MPI für Festkörperforschung, Stuttgart

Prof. Christian Krempaszy
Fakultät für Maschinenwesen
Technische Universität München

Dr. Eberhard Lehmann
Paul Scherrer Institute, Villigen

Prof. Dr. Martin Lerch
Institut für Chemie
Technische Universität Berlin

Dr. Reidar Lund
Department of Chemistry
University of Oslo

Prof. Dr. Andreas Magerl
Kristallographie und Strukturphysik
Universität Erlangen-Nürnberg, Erlangen

Dr. Andreas Michels
Faculté des Sciences, de la Technologie
et de la Communication
Université de Luxembourg

Prof. Dr. Peter Müller-Buschbaum
Physik-Department E13
Technische Universität München

Prof. Dr. Tommy Nylander
Physical Chemistry
Lund University

Dr. Esko Oksanen
European Spallation Source (ESS ERIC), Lund

Dr. Alessandro Paciaroni
Dipartimento di Fisica
Università degli Studi di Perugia

Prof. Dr. Luigi Paduano
Chemistry Department
University of Naples "Federico II"

Prof. Dr. Catherine Pappas
Delft University of Technology

Prof. Dr. Oskar Paris
Montanuniversität Leoben

Prof. Dr. Wolfgang Paul
Institut für Physik
Martin-Luther-Universität Halle-Wittenberg

Dr. Stéphane Raymond
CEA, Centre de Grenoble

Dr. Simon Redfern
Department of Earth Sciences
University of Cambridge

Prof. Dr. Günther Redhammer
Materialforschung und Physik
Universität Salzburg

Dr. Sarah Rodgers
STFC, Rutherford Appleton Laboratory, Didcot



Figure 3: Welcome of the members of the review panels evaluating beam time at the proposal round in March 2015.

Dr. Matthias Rossbach
Forschungszentrum Jülich GmbH

Dr. Margarita Russina
Helmholtz-Zentrum Berlin
für Materialien und Energie GmbH

Prof. Dr. Michael Sattler
Department Chemie
Technische Universität München

Dr. Harald Schmidt
Institut für Metallurgie
Technische Universität Clausthal

Prof. Dr. Andreas Schönhals
Bundesanstalt für Materialforschung
und -prüfung, Berlin

Dr. Torsten Soldner
Institut Laue-Langevin (ILL), Grenoble

Prof. Dr. Wolfgang Sprengel
Institut für Materialphysik
Technische Universität Graz

Dr. Jochen Stahn
ETH Zürich and Paul Scherrer Institute, Villigen

Dr. Peter Staron
Institute of Materials Research
Helmholtz-Zentrum Geesthacht GmbH

Dr. Oliver Stockert
Max-Planck-Institut für chemische Physik
fester Stoffe, Dresden

Dr. Susana Teixeira
Institut Laue-Langevin (ILL), Grenoble

Prof. Kristiaan Temst
Nuclear & Radiation Physics Section
Katholieke Universiteit Leuven

Prof. Dr. Katharina Theis-Broehl
Hochschule Bremenhaven

Dr. Lambert van Eijck
Department of Radiation, Radionuclides
and Reactors, Delft University of Technology

Prof. Dr. Regine von Klitzing
Institut für Chemie, Stranski-Laboratorium
für Physikalische und Theoretische Chemie
Technische Universität Berlin

Dr. Martin Weik
Institut de Biologie Structurale, Grenoble

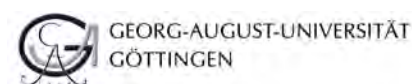
Dr. Andrew Wildes
Institut Laue-Langevin (ILL), Grenoble

Dr. Robert Wimpory
Helmholtz-Zentrum Berlin
für Materialien und Energie GmbH, Berlin

Partner institutions

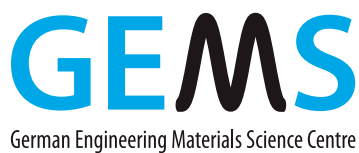


Bayerisches Geoinstitut
Universität Bayreuth
www.bgi.uni-bayreuth.de



Georg-August-Universität Göttingen

- Institut für Physikalische Chemie
www.uni-pc.gwdg.de/eckold
- Geowissenschaftliches Zentrum
www.uni-goettingen.de/de/125309.html



German Engineering Materials Science Centre GEMS
Helmholtz-Zentrum Geesthacht GmbH
www.hzg.de/institutes_platforms/gems/



Jülich Centre for Neutron Science JCNS
Forschungszentrum Jülich GmbH
www.jcns.info



Karlsruher Institut für Technologie

- Institut für Angewandte Materialien –
Energiespeichersysteme (IAM-ESS)
www.iam.kit.edu



Ludwig-Maximilians-Universität München

- Sektion Kristallographie
www.lmu.de/kristallographie
- Fakultät für Physik Physik
www.softmatter.physik.uni-muenchen.de



MAX-PLANCK-GESELLSCHAFT

Max-Planck-Institut für Festkörperforschung, Stuttgart
www.fkf.mpg.de



RWTH Aachen

- Institut für Kristallographie
www.xtal.rwth-aachen.de
- Institut für Anorganische Chemie
www.ac.rwth-aachen.de



Technische Universität Clausthal

- Institut für Werkstoffkunde und Werkstofftechnik
www.iww.tu-clausthal.de



Technische Universität Dresden

- Institut für Festkörperphysik
www.physik.tu-dresden.de/ifp



Technische Universität München

- E13 – Lehrstuhl für Funktionelle Materialien
www.e13.physik.tu-muenchen.de



Technische Universität München

- E18 – Lehrstuhl für Experimentalphysik I
www.e18.ph.tum.de



E21
Arbeitsgebiet stark
korrelierte Elektronensysteme

Technische Universität München

- E21 – Lehrstuhl für Neutronenstreuung
www.e21.ph.tum.de



Technische Universität München

- Exzellenzcluster „Origin and Structure of the Universe“
www.universe-cluster.de



Klinikum rechts der Isar

Technische Universität München

- MRI - Klinikum Rechts der Isar
www.med.tum.de



RCM
Radiochemie München

Technische Universität München

- RCM - Radiochemie München
www.rcm.tum.de



TECHNISCHE
UNIVERSITÄT
WIEN
Vienna University of Technology

Technische Universität Wien

Neutronen- & Quantenphysik
Forschungsbereich am Atominstitut Wien
Arbeitsgruppe Abele

http://ati.tuwien.ac.at/research_areas/neutron_quantum_physics/



Universität der Bundeswehr München

- Institut für Angewandte Physik und Messtechnik
www.unibw.de/lrt2

Universität zu Köln



Universität zu Köln

- Institut für Kernphysik
www.ikp.uni-koeln.de
- II. Physikalisches Institut
www.ph2.uni-koeln.de

Imprint

Publisher

Technische Universität München
 Forschungs-Neutronenquelle
 Heinz Maier-Leibnitz (FRM II)
 Lichtenbergstr. 1
 85747 Garching
 Germany

Phone: +49.89.289.14966
 Fax: +49.89.289.14995
 Internet: www.mlz-garching.de
 EMail: mlz@mlz-garching.de

Editorial Office, Design and typesetting

Ramona Bucher
 Connie Hesse
 Elisabeth Jörg-Müller
 Christine Kortenbruck

Editors

Henrich Frielinghaus
 Robert Georgii
 Michael Hofmann
 Olaf Holderer
 Peter Link
 Wiebke Lohstroh
 Andreas Ostermann
 Björn Pedersen
 Anatoliy Senyshyn
 Olaf Soltwedel
 Yixi Su

Photographic credits

Wenzel Schürmann, TUM:

Cover (1st line, from left to right: 1st, 2nd, 3rd, 5th, 6th;
 2nd line: all; 3rd line: 4th; 5th line: 1st), 8 (bottom, 1st,
 3rd and 4th from left), 12 (top, middle, bottom left),
 13 (bottom), 14 (top), 17 (middle), 18 (middle left),
 21, 23 (top), 27, 33 (left), 120

Astrid Eckert/ Andreas Heddergott, TUM:

Cover (3rd line from left to right: 3rd, 5th; 4th line: 1st,
 2nd, 3rd, 4th; 5th line: 3rd, 4th, 5th), 7, 121

Ernst Graf, TUM:

8 (top)

Forschungszentrum Jülich:

8 (bottom, 2nd from left), 12 (bottom right)

HENN GmbH, Munich:

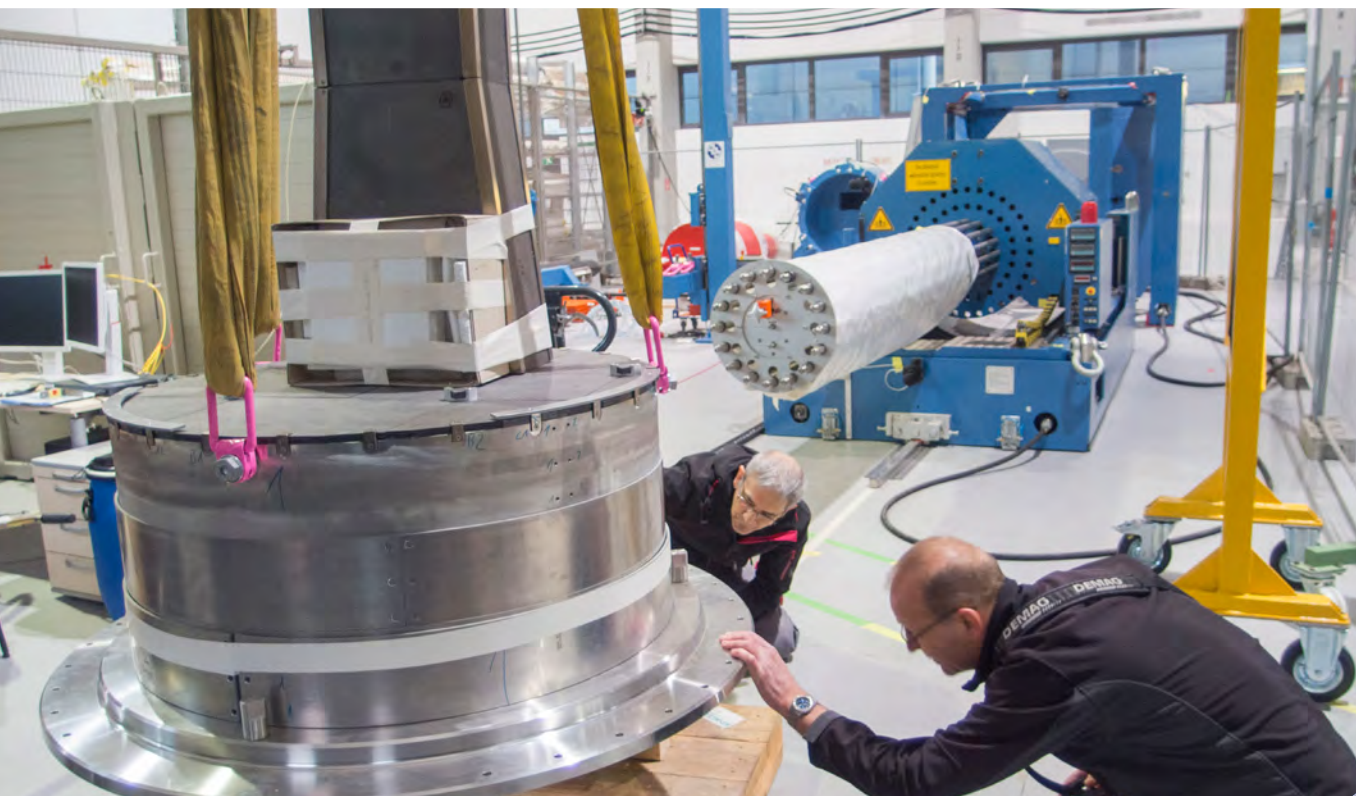
10, 11

Bernhard Ludewig:

108

Editors and authors:

other images



Heinz Maier-Leibnitz Zentrum (MLZ)

www.mlz-garching.de

DOI: 10.14459/2015md1292666

Front page:

10 years of successful user operation

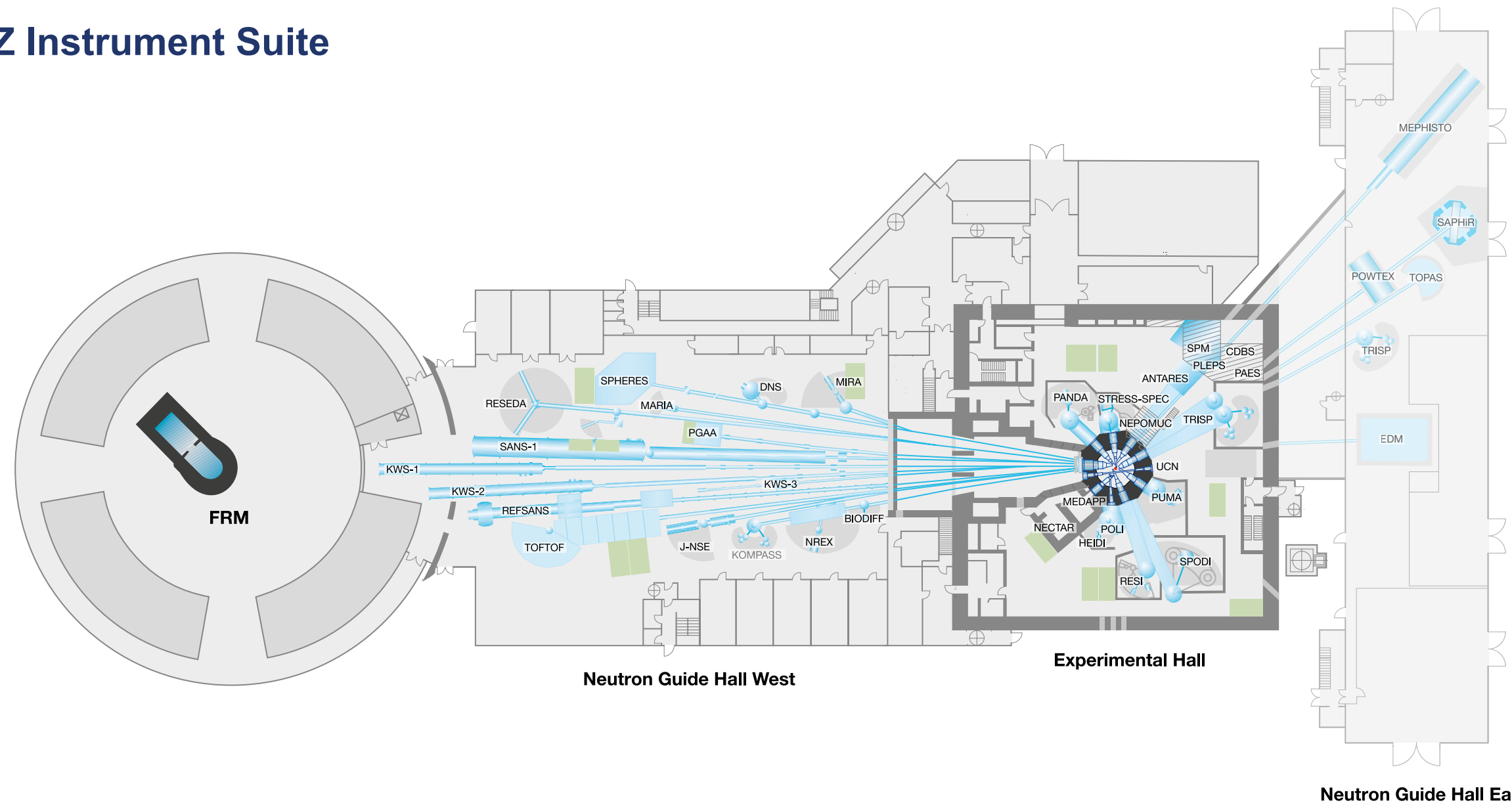
Keeping precious memories: inspired users and curious students, world-class instrumentation, great scientific experiments, many scientific highlights; all made possible by most reliable reactor operation.

Back page:

Delivery of the beam plug for beam tube SR5

It was designed at the Forschungszentrum Jülich by the Central Institute for Engineering, Electronics and Analytics (ZEA) – Engineering and Technology (ZEA-1) and is going to be exchanged at the beginning of 2016 – an important step towards the future neutron supply of the instruments TOPAS, POWTEX and SAPHiR in the guide hall east.

MLZ Instrument Suite



Instrument	Description	Neutrons	Operated by	Funding	Instrument group at MLZ
ANTARES	Radiography and tomography	cold	TUM	TUM	FRM II
BIODIFF	Diffractionmeter for large unit cells	cold	TUM, JCNS	TUM, FZJ	FRM II, JCNS
DNS	Diffuse scattering spectrometer	cold	JCNS	FZJ	JCNS
HEIDI	Single crystal diffractometer	hot	RWTH Aachen	FZJ	JCNS
J-NSE	Spin-echo spectrometer	cold	JCNS	FZJ	JCNS
KOMPASS*	Three axes spectrometer	cold	Uni Köln, TUM	VF	FRM II
KWS-1	Small angle scattering	cold	JCNS	FZJ	JCNS
KWS-2	Small angle scattering	cold	JCNS	FZJ	JCNS
KWS-3	Very small angle scattering	cold	JCNS	FZJ	JCNS
MARIA	Magnetic reflectometer	cold	JCNS	FZJ	JCNS
MEPHISTO**	Instrument for particle physics, PERC	cold	TUM	TUM, DFG	FRM II
MIRA	Multipurpose instrument	cold	TUM	TUM	FRM II
MEDAPP	Medical irradiation treatment	fast	TUM	TUM	FRM II
NECTAR	Radiography and tomography	fast	TUM	TUM	FRM II
NEPOMUC	Positron source, CDBS, PAES, PLEPS, SPM	-	TUM, UniBw München	TUM	FRM II
NREX	Reflectometer with X-ray option	cold	MPI Stuttgart	MPG	MPI Stuttgart
PANDA	Three axes spectrometer	cold	JCNS	FZJ	JCNS

Instrument	Description	Neutrons	Operated by	Funding	Instrument group at MLZ
PGAA	Prompt gamma activation analysis	cold	Uni Köln	TUM	FRM II
PUMA	Three axes spectrometer	thermal	Uni Göttingen, TUM	VF, TUM	FRM II
POLI	Single-crystal diffractometer polarized neutrons	hot	RWTH Aachen	VF, FZJ	JCNS
POWTEX*	Time-of-flight diffractometer	thermal	RWTH Aachen, Uni Göttingen, JCNS	VF, FZJ	JCNS
REFSANS	Reflectometer	cold	GEMS	VF, HZG	GEMS
RESEDA	Resonance spin-echo spectrometer	cold	TUM	TUM	FRM II
RESI	Single crystal diffractometer	thermal	LMU	TUM	FRM II
SANS-1	Small angle scattering	cold	TUM, GEMS	TUM, HZG	FRM II, GEMS
SAPHIR*	Six anvil press for radiography and diffraction	thermal	Uni Bayreuth	VF	FRM II
SPHERES	Backscattering spectrometer	cold	JCNS	VF, FZJ	JCNS
SPODI	Powder diffractometer	thermal	KIT	VF, TUM	FRM II
STRESS-SPEC	Materials science diffractometer	thermal	TUM, TU Clausthal, GEMS	TUM, HZG	FRM II, GEMS
TOFTOF	Time-of-flight spectrometer	cold	TUM	TUM	FRM II
TOPAS*	Time-of-flight spectrometer	thermal	JCNS	FZJ	JCNS
TRISP	Three axes spin-echo spectrometer	thermal	MPI Stuttgart	MPG	MPI Stuttgart
UCN*	Ultra cold neutron source, EDM	ultra-cold	TUM	TUM, DFG	FRM II

*construction
 **reconstruction
 VF: instrument construction funded by "BMBF-Verbundforschung" (Collaborative Projects)